Droplet manipulation

Tristan Gilet

May 15, 2009

Acknowledgments

The following thesis, while an individual work, benefited from the insights and direction of many people. First, I wish to express my gratitude to my supervisor, Prof. Nicolas Vandewalle, who was abundantly helpful and offered me invaluable assistance, support and guidance from the early stages of this research. His truly scientist intuition has made him a constant oasis of scientific ideas, which exceptionally inspire and enrich my growth as a researcher.

I gratefully acknowledge Dr. Stéphane Dorbolo, Prof. Thierry Bastin, Dr. Philippe Brunet and Prof. John W.M. Bush., who have accepted to be members of my reading committee in the midst of all their activity.

I am especially grateful to Stéphane for his advice, supervision and crucial contribution, which made him a backbone of this thesis. He provided me unflinching encouragement and support in various ways. I also wish to thank him for having used his precious time to proofread this thesis and give constructive comments.

I am much indebted to John Bush, first for his hearty welcome at MIT. Armed with persistence, understanding and kindness, John definitely has the wonderful talent to make people give the best of themselves. I am still fascinated by his scientific masterpiece on the amazing interplay between surface tension and biology. Finally, he gave me the marvelous opportunity to continue my research in his lab. I doubt that I will ever be able to convey my appreciation fully, but I owe my eternal gratitude to him. John, I hope that we will keep up our collaboration for a very long time.

I would like to thank the FRIA/FNRS, the federal government of Belgium, the University of Liège and the Massachusetts Institute of Technology for providing the financial means and laboratory facilities. This research would not have been possible without their support.

Many thanks to my colleagues for sharing their invaluable assistance, and for giving me such a pleasant time working with them. A very special thanks goes out to my workmate Denis and my joyful undergrad Ariane for the experimental data they shared me. Denis has also a great talent: he masters the handling of cameras and make them take wonderful pictures, some of which are used in this manuscript. Denis, thank you so much for that; as you can precisely do what I cannot, you are definitely my ideal collaborator.

Finally, I wish to express my deep love and gratitude to my beloved family, my best friends and my dearest wife Christelle, who have always been there with encouragement, understanding and endless love through my studies. Christelle, sei la luce dei miei occhi...

I dedicate this thesis to my father, who instilled in me the desire to observe and understand everything around me.

List of publications

- N. Vandewalle, D. Terwagne, K. Mulleners, T. Gilet and S. Dorbolo, *Dancing droplets onto liquid surfaces*, Phys. Fluids **18**, 091106 (2006).
- T. Gilet, K. Mulleners, J.P. Lecomte, N. Vandewalle and S. Dorbolo, *Critical parameters for the partial coalescence of a droplet*, Phys. Rev. E **75**, 036303 (2007).
- T. Gilet, N. Vandewalle and S. Dorbolo, *Controlling the partial coalescence of a droplet on a vertically vibrated bath*, Phys. Rev. E **76**, 035302(R) (2007).
- T. Gilet, D. Terwagne, N. Vandewalle and S. Dorbolo, *Dynamics of a bouncing droplet onto a vertically vibrated interface*, Phys. Rev. Lett. **100**, 167802 (2008)
- D. Terwagne, T. Gilet, N. Vandewalle and S. Dorbolo, *From bouncing to boxing*, Chaos **18**, 041104 (2008)
- S. Dorbolo, D. Terwagne, N. Vandewalle and T. Gilet, *Resonant and rolling droplet*, New J. Phys. **10**, 113021 (2008)
- F. Ludewig, S. Dorbolo, T. Gilet and N. Vandewalle, *Energetic approach for the characterization of taps in granular compaction*, Europhys. Lett. **84**, 44001 (2008)
- T. Gilet and J.W.M. Bush, *Chaotic bouncing of a droplet on a soap film*, Phys. Rev. Lett. **102**, 014501 (2009)
- T. Gilet and J.W.M. Bush, *The fluid trampoline: droplets bouncing on a soap film*, J. Fluid Mech. **625**, 167 (2009)
- N. Vandewalle, D. Terwagne, T. Gilet, H. Caps and S. Dorbolo, *Antibubbles, liquid onions and bouncing droplets*, Colloid Surf. A: Physicochem. Eng. Aspects, in press (2009)
- D. Terwagne, T. Gilet, N. Vandewalle and S. Dorbolo, *Metastable bouncing droplets*, Phys. Fluids, in press (2009)
- T. Gilet, N. Vandewalle and S. Dorbolo, *Completely inelastic ball*, Phys. Rev. E, in press (2009)
- T. Gilet, D. Terwagne and N. Vandewalle, *Digital microfluidics on a wire*, Appl. Phys. Lett., in revision (2009)
- T. Gilet and N. Vandewalle, *A method and an apparatus for separating a first amount of liquid*, submitted to the European Patent Office - EP09154128 (2009)

Contents

Introduction

Goutte nf *Très petite quantité d'un liquide qui se détache avec une forme sphérique.*

Droplet: small amount of liquid that breaks away with a spherical shape. This is the definition given by the famous French dictionary Larousse [1]. The droplet is definitely a daily encountered concept. Strings of raindrops that fall and slide on our windows, small pearls observed on spider webs in the early morning, oily droplets that spread everywhere and make these so feared grease stains, the drip-drip of syringes, spatters, tears... but also fog, sprays, spindrift, ink drops in printers, fuel drops injected in motors, etc. Finally, we must not forget the emulsions (e.g. dairy products, beauty creams) obtained when two immiscible liquids are forced to blend together: one of them forms a myriad of tiny droplets into the other, resulting in an usually opaque material.

A droplet... an outwardly simple object... which has no reason to captivate ? The definition proposed by dictionaries do not stand the test of daily observation. The oily stains are not removed without cleaning agents, and the small droplets on our windscreens cannot fly away unless a powerful wind blows them out. Regarding the sphericity, it is only encountered in a very special case: a droplet floating in weightlessness. On the contrary ! The atypical shapes of droplets in "normal" conditions have often inspired artists and poets. The physics hidden behind this concept of "droplet" is in fact extremely rich and complex. A countless number of questions have been raised by scientists during the last century, that remain currently unanswered.

On a technological point of view, the droplet seems to be the absolute must in microfluidics, i.e. the miniaturization of fluid processes. Many applications make use of the manipulation of very small amounts of liquid. Nevertheless, to deal with droplets is not as simple as it seems: let's leave a water droplet on the table and try to pick it up back entirely to put it elsewhere. Impossible to collect the whole volume all at once! The droplet inevitably leaves on the table a significant part of its contents, no matter how priceless it is. Hopefully, the droplet physics has a trick or two up its sleeve.

In this thesis, we propose to explore various techniques that would "skillfully" handle droplets, and to study the related physical phenomena. By "skillful" manipulation, we mean that a simple rule is satisfied: the more a droplet is touched by solid surfaces, the more its properties (volume, chemical composition, physical properties) are likely to be affected. Therefore, in droplet handling, we must avoid contact with solid parts, so far as we can.

We start with two introductory chapters; the first one sets the scene and gives the physical background required to understand this thesis, while the second one is a non-exhaustive review of the current technological advances and improvements related to the droplet physics. The manuscript is then divided in two parts. In the first, we discuss the behavior of droplets in the

vicinity of another liquid interface. In particular, the bouncing of liquids is deeply investigated through several examples. We explain how the observed phenomena may be useful to handle individual droplets without touching them. The second part is dedicated to the study of droplets on fibers. We show that many elementary microfluidic operations can be performed thanks to simple fiber networks. Finally, the main conclusions and the numerous perspectives of this thesis are summarized.

Chapter 1

At droplet scale...

I have often been impressed by the scanty attention paid even by original workers in physics to the great principle of similitude. It happens not infrequently that results in the form of "laws" are put forward as novelties on the basis of elaborate experiments, which might have been predicted a priori after a few minutes' consideration. However useful verification may be, whether to solve doubts or to exercise students, this seems to be an inversion of the natural order. Lord Rayleigh, in Nature (1915) [2]

It is surprising to see how liquids behave differently according to the scale they are observed. Indeed, the forces that drive these liquids and shape them usually depend on the characteristic size of the system. For example, the Coriolis force, which is due to the Earth rotation, is responsible for various phenomena related to the atmospheric and oceanic circulations at planet scale. On the other hand, contrary to a common misconception, its impact is negligible on the direction of the vortex observed when we drain our sink. Time and length scales involved in the Earth rotation (one day and several thousands kilometers) have nothing in common with the scales of a sink draining (one minute and a few tens of centimeters). So each physical phenomenon, each force, each influence has its own range of scales on which it is efficient. At droplet scale (say from micrometer to millimeter), the dominant forces are often due to capillarity. As an example, the small water insect in Fig. 1.1(a) relies on capillary forces to move on water and climb on plants. Nevertheless, other forces (gravity, viscosity, inertia, ...) may also be important at this scale and counteract capillary effects. In order to evaluate the relative impact of each force on the system, we define dimensionless numbers that correspond to the ratios between these secondary forces and capillarity [3, 4] .

1.1 Surface tension

Capillary effects shape the microscopic world like no other force can do. Indeed, they are among the rare forces in physics that exert on a surface and not in bulk. Although gravity attracts objects downwards, capillary forces have no favorite direction: they only tend to reduce the surface of a liquid exposed to the neighboring. The resulting complexity is well illustrated in Fig. 1.1(b-c).

Capillarity results from the cohesion of liquids (to be general, every condensed phase). Molecules in the bulk experience an isotropic attraction from their neighbors which self-

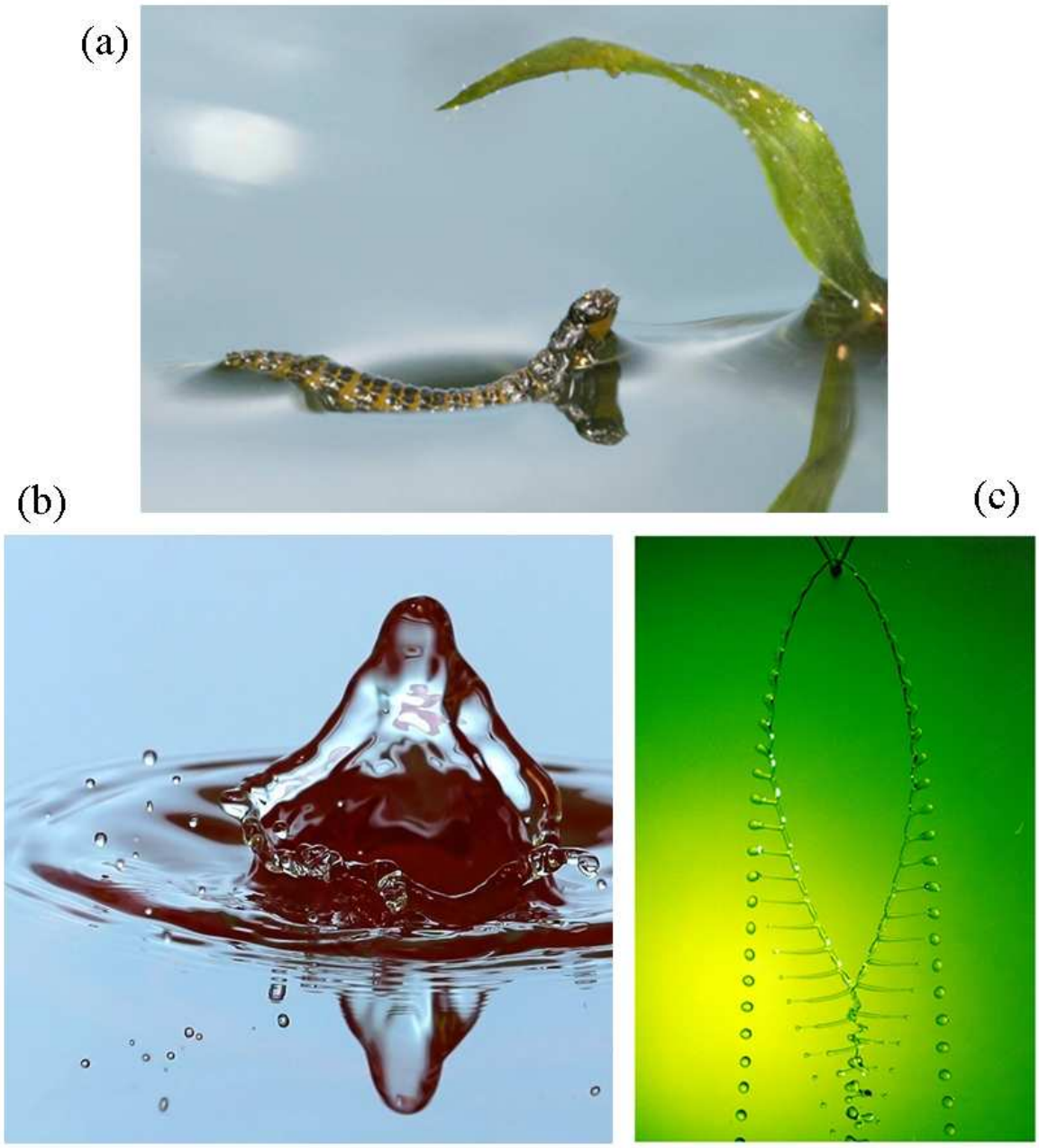

Figure 1.1: (a) This water insect has to climb on the liquid interface curved by surface tension in order to reach the leaf. To proceed, it bends its back so it also curves the surrounding water surface. The excess surface of water between the insect and the plant spontaneously resorbs, exerting a force that pulls the animal onto the leaf [5] - (Credit J.W.M. Bush, MIT). (b) Water droplet taking an ephemeral, uncommon and relatively evocative shape during a splash on a water bath [6] - (Credit : www.liquidsculpture.com). (c) The collision between two jets is able to generate complex structures such as this "backbone" [7] - (Credit J.W.M. Bush, MIT).

balances, while molecules located at the liquid boundary are only attracted toward the center, resulting in a net force inwards. This latter corresponds to a potential energy higher for surface molecules than for others. The excess of surface potential energy E_σ is proportional to the surface S of the liquid object

$$E_\sigma = \sigma S, \tag{1.1}$$

the proportionality factor is called surface tension σ. It also corresponds to a (conservative) force per unit length, exerted tangentially to the liquid interface.

When the liquid surface is curved, surface tension creates a discontinuity in the stress normal to the interface. If the liquid is at rest, this discontinuity results in an overpressure Δp inwards, given by Laplace law

$$\Delta P = \sigma \boldsymbol{\nabla} \cdot \vec{n} = 2\sigma \mathcal{C}, \tag{1.2}$$

where $\boldsymbol{\nabla} \cdot \vec{n}$ is the divergence of the normal vector of the interface, equal to twice the mean curvature $\mathcal{C}$. For a spherical droplet of radius R, $\mathcal{C} = 1/R$ and $\Delta P = 2\sigma/R$.

Surface tension is mainly modified by two factors; it decreases when the temperature increases and when surfactant molecules are added. Inhomogeneities in temperature or surfactant concentration correspond to surface tension gradients. These latter are responsible for the discontinuities in tangential stress, that can set the liquid into motion [8].

1.2 Gravity, Bond number and the capillary length

Gravity attracts objects towards the Earth center with a force proportional to the object mass M, the proportionality constant being the acceleration of gravity $g = 9.81$ m/s^2. The potential energy related to this conservative force is $E_g = MgZ$, where Z is here the height of the mass center of the object. A spherical droplet has thus an additional gravity energy MgR compared to a configuration where the liquid completely spreads on the table. This excess may be compared to the surface energy of the droplet $E_s = 4\pi\sigma R^2$, which defines the Bond number

$$Bo = \frac{Mg}{4\pi\sigma R} = \frac{\rho g R^2}{3\sigma} \sim \frac{\text{Gravity}}{\text{Surface tension}}. \tag{1.3}$$

The capillary forces are more important than gravity for length scales smaller than the capillary length

$$\lambda_\sigma = \sqrt{\frac{\sigma}{\rho g}}. \tag{1.4}$$

This length only depends on the liquid physical properties. For usual liquids, $\sigma \in [20, 70]$ mN/m while $\rho \sim 1000$kg/m^3 : the capillary length is about a few millimeters. Both the height of the meniscus formed at contact between a bath and its container and the maximal size of a droplet are of the order of the capillary length. When a droplet is dipped into an immiscible liquid of similar density ρ_s, the capillary length is considerably larger and the Bond number smaller, namely

$$Bo_s = \frac{|\rho - \rho_s| g R^2}{3\sigma_s} \text{ and } \lambda_{\sigma s} = \frac{\sigma_s}{|\rho - \rho_s| g}, \tag{1.5}$$

where σ_s the interfacial tension between both liquids.

1.3 Inertia, Weber number and capillary time

Inertia may be seen as the ability of objects to resist external forces. The inertial force is given by the product of mass and acceleration. Inertia is often opposed to surface tension in impact problems [6]. For a droplet of mass M impacting an object at speed V, the corresponding kinetic energy is given by $K = MV^2/2$. We define the Weber number as the ratio between this kinetic energy and the surface energy E_σ:

$$We = \frac{3MV^2}{4\pi\sigma R^2} = \frac{\rho V^2 R}{\sigma} \sim \frac{\text{Inertia}}{\text{Surface tension}}. \tag{1.6}$$

When $We \ll 1$, the droplet is hardly deformed by the kinetic energy released at impact. On the other hand, when $We \gg 1$, the excess kinetic energy turns into enough surface energy to make the droplet blow up into a myriad of microdroplets.

1.3.1 Capillary waves on a droplet

Capillary waves at the surface of a liquid result from a combination of inertia and surface tension. Inertia is here related to internal flows inside the liquid. At the surface of a droplet, small amplitude waves may be described as a sum of eigenmodes called spherical harmonics Y_ℓ^m. These deformation modes of a sphere are made of a number of hollows and humps. Those regions are separated by meridian and parallel imaginary circles corresponding to the zero-deformation points of the sphere (Fig. 1.2). Spherical harmonics are denoted by two integers: the degree ℓ is the total number of zero-deformation circles, and the order m is the number of meridians among these circles. Harmonics with $m = 0$ are always symmetric around the vertical axis. For example, mode Y_2^0 corresponds to a spheroid, i.e. an ellipsoid of revolution.

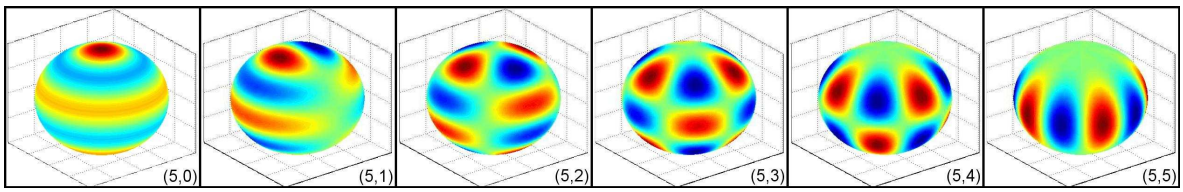

Figure 1.2: Spherical harmonics of degree $\ell = 5$ for various values of the order m. Regions of hollows and humps, always alternated, are separated by 5 zero-deformation circles, m of which are vertical and $5 - m$ horizontal.

The dispersion relation of waves at the surface of a floating droplet yields the natural frequency $f_{(\ell,m)}$ of each mode Y_ℓ^m,

$$f_{(\ell,m)}^2 = \frac{\ell(\ell-1)(\ell+2)}{3\pi}\frac{\sigma}{M}. \tag{1.7}$$

Initially obtained by Lord Rayleigh (App. C), this relation suggests that the frequency does not depend on m; there is a degeneracy according to this parameter. The wave period is proportional to the capillary time

$$\tau_\sigma = \sqrt{\frac{M}{\sigma}}. \tag{1.8}$$

This time is characteristic of surface-tension-driven motions at droplet scale. We show in next chapters that the bouncing of a droplet and its fusion with a liquid bath both occur at

timescales close to τ_σ. A millimetric oil droplet corresponds to $\tau_\sigma \sim 10$ ms, so fast imaging (up to thousands of frames per second) is often required to observe these phenomena [9].

1.4 Viscosity, Ohnesorge number and the viscous length

The fluid viscosity is related to the momentum diffusion. Two nearby fluid particles (separated by a distance $\mathrm{d}x$) with slightly different velocities (u and $u+\mathrm{d}u$) exert a stress $\mu \mathrm{d}u/\mathrm{d}x$ on each other, μ being the dynamic viscosity. The diffusion coefficient ν, also called kinematic viscosity, satisfies $\nu = \mu/\rho$. Viscosity leads to dissipative forces that do not derive from any potential energy. Moreover, as in every diffusion process, the viscosity transfers information over a distance that increases with time. The viscous time $\tau_\nu = R^2/\nu$ is the time needed to transfer momentum over the droplet scale R by diffusion. The Ohnesorge number is defined as the ratio between capillary and viscous times,

$$Oh = \frac{\nu\sqrt{\rho}}{\sqrt{\sigma R}} \sim \frac{\tau_\sigma}{\tau_\nu} \sim \frac{\text{Viscosity}}{\text{Surface tension}}. \tag{1.9}$$

Among others, this number is proportional to the damping factor of capillary waves on the droplet (App. C). Viscosity invalidates the inertia/capillary balance at scales smaller than the viscous length

$$\lambda_\nu = \frac{\rho\nu^2}{\sigma}. \tag{1.10}$$

Like the capillary length, the viscous length only depends on the liquid properties. For $\sigma \sim 40$ mN/m and $\rho \sim 1000$ kg/m^3, the viscous length is 25 nm for a liquid as viscous as water ($\nu \sim 1$ cS), and 250 μm for a $\nu = 100$ cS liquid. In that case, viscous effects are always significant at droplet scale. In particular, capillary waves are fully damped at the surface of such viscous liquids.

Chapter 2

Droplets in science and engineering

Practical applications of the droplet physics are numerous, and we are unable to list them all. This chapter gives an overview of some scientific and engineering problems involving droplets. In particular, we explain how droplets can be useful in microfluidics, and we discuss the various technical solutions that are currently investigated in this field.

Droplet physics is found everywhere, in everyday life, from the formation of raindrops to the sprays (paintings, fuel injection, plant treatment), the emulsions, the ink-jet printing, etc. More exotic applications are found in the scientific litterature; e.g. the aeration of lakes (an absolute requirement for life inside) which is mainly made by an air bubble trapping mechanism that occurs each time a raindrop impacts the lake surface [6]. Scientists have also observed that some meteorites, named tektites, have a shape somewhat similar to droplets, which suggest that they were formed thanks to analog physical processes [10].

The use of droplets is also promising in micro-technologies. For example, they can serve as bearing structures [11]. Glue and welding droplets can perform self-micro-assembly [12], e.g. through elasto-capillarity [13]. Nowadays, droplets are already used as optical lenses in our mobile phone cameras ((Fig. 2.1a-b). Two immiscible liquids of different refracting index are placed in a small tube, the walls of which are covered with an hydrophobic coating. The first liquid, an aqueous solution, is a good electrical conductor, while the second liquid (an oil) is a bad conductor. By tuning the voltage across the system, the hydrophobicity of the coating is changed (electrowetting), which modifies the shape of the water/oil interface and so the focal length of this fluidic lens. Advantages of this technique patented by Philips [14] are numerous: the micro-lens focal length is tuned from 5 cm to infinity in less than 10 ms, with a quasi-zero electric consumption. The lifetime of this lens is estimated at more than one million focusing operations without any loss of performance; the lens resists well to shocks and temperature variations. Droplets may be used as lenses in several other opto-fluidic operations [15]. But the main current interest in droplet physics comes from microfluidics, as discussed here below.

2.1 Microfluidics

Microfluidics is the emergent part of fluid dynamics that studies how to handle amounts of liquid smaller than 1 μL. It was born about two decades ago, when researchers began discussing the intriguing idea of shrinking the equipment needed for everyday chemistry and biology procedures to fit on a centimetric chip. These procedures involve many elementary operations on fluids: displacement, injection, division, fusion, mixing, dosage, extraction,

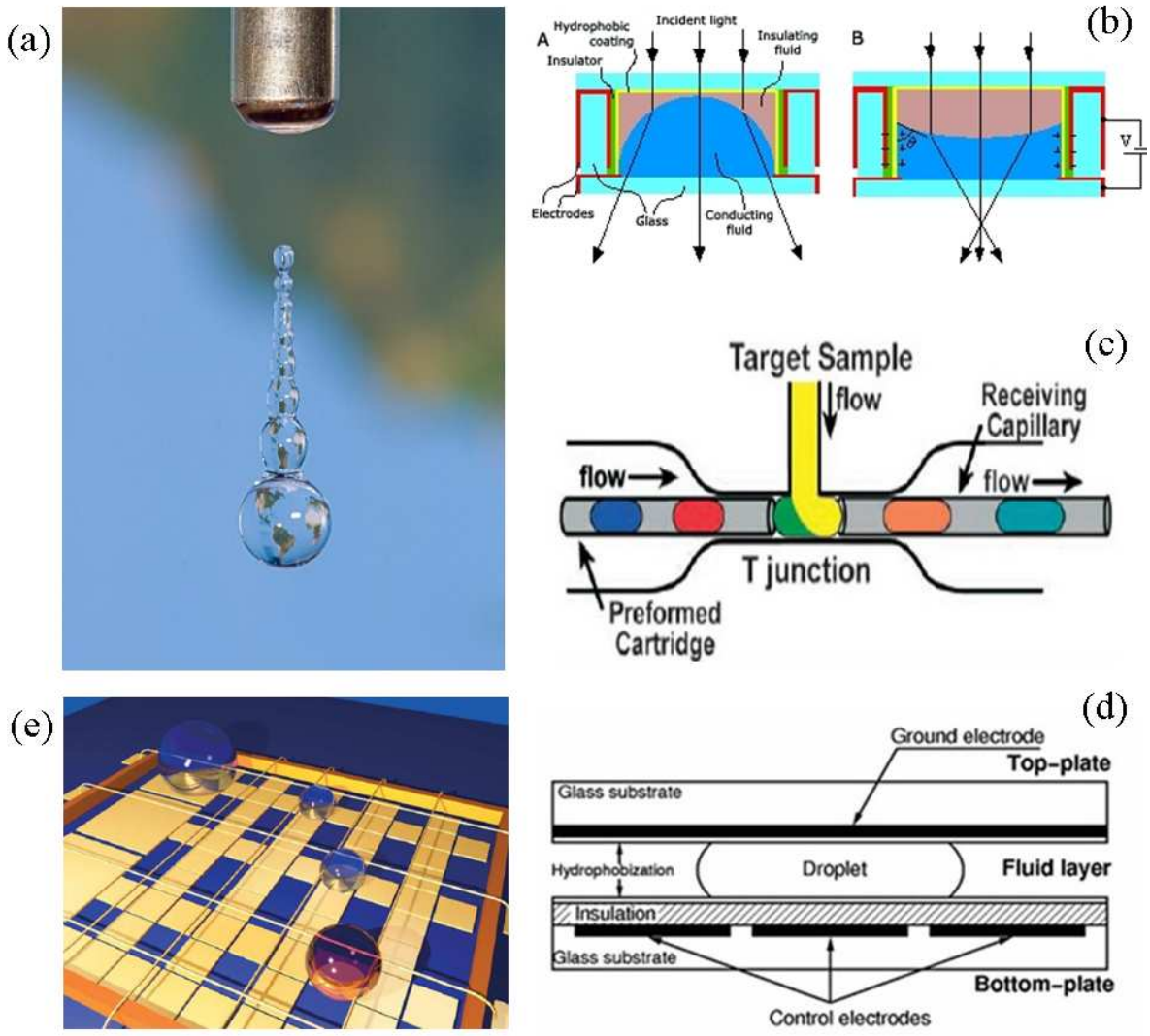

Figure 2.1: (a) Lens-effect of a droplet. - Credit : www.liquidsculpture.com (b) Optical lens with variable focusing patented by Philips [14]. (c-e) Various techniques in digital microfluidics : (c) Droplets are released in a multiphasic flow inside a micro-channel network [16]. (d) Droplets are sandwiched between two solid substrates covered with printed circuits, and handled by electrowetting. - Credit : http://microfluidics.ee.duke.edu (e) Droplets are placed on a printed circuit and moved by electrowetting, the guiding is ensured by catenary fibers [17].

identification, recovery, storage, etc. The results of the biochemical reactions are commonly brought back by using fluorescence techniques [18]. Microfluidics benefits from the experience in microfabrication of electronic systems acquired during the twentieth century. For example, many microfluidic systems are built in PDMS thanks to soft lithography, which is an adaptation of the techniques used in microelectronics [19]. But while this latter brilliantly follows the Moore's law, the shrinking of fluidics has to face much more fundamental issues. Indeed, contrary to electromagnetism, the physics of fluids widely depends on the system length-scale and seems not so easy to miniaturize [18].

In twenty years of research, scientists have brought a large panel of techniques, described hereafter, that are more or less suitable for given applications. Nowadays, the greatest challenge is to integrate these techniques into smart microfluidic systems that may be used by people who are not experts in fluid physics. Those systems must be widely and inexpensively available [19].

2.1.1 Continuous vs. digital microfluidics

Current microfluidic systems may be sorted in two main categories: continuous and digital. In continuous microfluidics, historically the first, liquids travel into complex micro-channel networks through electromechanical pumps, gates and mixers. The pumps are not as conventional, though air pressure could push samples through channels. But the channel walls would exert a drag on the liquid, so that fluid at the center of the channel would move faster than that at the edge and concentrated samples would quickly become smeared. The most commonly used alternative makes use of a phenomenon called electro-osmosis: the channel wall ionizes water molecules in its vicinity and, when an electric field is applied along the channel, these ions flow towards the negative pole and drag the rest of the fluid along with them; the liquid moves as a plug flow [20]. Continuous microfluidics is already used for microscale heat transfer, display, ink-jet printing, etc. [21]. Nevertheless, it is taking a long time to use continuous microfluidics for bio-chemical applications, the main reason is that reagents are not confined and may diffuse through the entire network. Moreover, air bubble entrapment frequently occurs when solvents do not perfectly wet the channel surface, resulting in drastic changes of the device response dynamics [18].

In digital microfluidics, small droplets are used as containers in which the liquid of interest is placed. Droplets are almost ideal biochemical reactors because they create homogeneous controlled conditions without any hydrodynamic dispersion; the high surface-to-volume ratio grants very fast thermal transfer and internal recirculations inside the droplet allow efficient mixing. One of the main goals is thus to handle the many droplets that can be generated with only a minute amount of material, and to divide and recombine them in a multiplicity of nanoreactors so as to perform multiplexing. This requires the control and reproducibility of many droplet operations: fabrication, sorting, storage, fusion and breakup among others. Potential applications of digital microfluidics are numerous [16, 17, 21, 22]. For example, genomics and proteomics, i.e. sequencing of the human genom (DNA) and the various proteins it produces, may advantageously make profit from the high rates and indexing capabilities of digital microfluidics. Low-cost, simple to use and reusable diagnostic tools should be designed for medical, food and environmental applications. In these cases, robustness is the main requirement, since the physico-chemical properties of the samples to analyze are not known a priori. Digital microfluidics is also of interest for synthesizing proteins, organic molecules or nanoparticles. Cellular cultures may be parallelized through encapsulation inside droplets; this

confined environment allows an accurate determination of what is absorbed/rejected by the cell. Researchers also think about using droplets as a support to reproduce some networks of functional biological reactions, such as enzyme cycles. Finally, advances in microfluidics could be very useful for both pharmaceutic [23] and food industries [24]. Indeed, it is currently the only technology that can produce 100%-success encapsulation of an active substance by means of a one-step process [25]. For example, one can dissolve the desired molecules or polymers into an organic phase and let the latter flow into an aqueous stream to generate droplets. To dry the resulting emulsion, the organic solvent is either exchanged with the aqueous phase or slowly evaporated through it. A last step of ultraviolet-induced cross-linking or polymerization can then be used to solidify the colloids. The polydispersity of the particles can be as low as a few percent, far better than what is achievable with classical means of generating emulsions. Many technical solutions have been explored to perform microfluidic operations, the main ones are discussed here below.

2.1.2 Levitation

Levitation consists in applying a force to the droplet that makes it float into the air by exactly balancing gravity. The force may result from aerodynamical, acoustical [26, 27], optical [28] or electromagnetical effects [29]. Although appealing at first sight for specific applications [30], levitation is unwieldy to implement and is therefore inappropriate for most microfluidic issues.

2.1.3 Multiphasic flow through micro-channel networks

Nowadays, the most prominent microfluidic technology [16] consists in making use of an immiscible carrying liquid (usually oil) to convey nanoliter aqueous droplets through a micro-channel network (Fig. 2.1c). This technique is advantageous in many respects. First of all, droplets cannot evaporate, which is appreciated when dealing with tiny amounts of aqueous solutions. Thanks to the well-defined velocity in channels, it is possible to convert temporal variations (e.g. the kinetics of a chemical reaction) into a spatial variation in the flow direction. A typical flow of 0.1 m/s convecting 1 mm droplets allows a temporal resolution of 10 ms. To avoid the collision between two successive droplets in the channel, one can separate them with plugs made of a third immiscible phase (e.g. a gas) [31]. The T-junctions between channels are considered as one of the elementary blocks of the network, on the basis of which it is possible among others to create the droplets: one branch of the T brings water, and both others convey the oil (Fig. 2.1c). This results in droplets of sizes comparable to the channel diameter [16]. T-junctions are also used as logical gates that may be combined to perform complex operations such as counting [32]. The droplet size is currently controlled by tuning the input flow rates. Unfortunately, this affects simultaneously the frequency, composition and speed of the droplets, whereas one would want to control each of these parameters independently [25]. A natural microfabrication strategy is to integrate actuators in order to achieve a local control of the droplet motion. This gain in control may unfortunately result in somewhat sophisticated, specialized and expensive chips with limited flexibility and versatility. It must be necessary to standardize a few basic on-chip functions, with a drift toward passive strategies that combine simplicity and robustness. For example, as an alternative to the complex microfabrication by lithography, microfluidic circuits can already be created on a support as simple as a paper sheet thanks to a desktop plotter and some special inks [33].

2.1.4 Electrowetting

Microchannel networks suffer from an evident lack of flexibility. In other words, it is hard to make different operations on successive droplets. Moreover, these networks are usually not reprogrammable and are consequently designed for a single specific application. The handling by electrowetting could be an interesting alternative to that issue: operations are indeed driven by electronic circuits that can be programmed.

The sandwich technique [17, 34] consists in placing droplets in between two parallel solid planes distant from about a few tenths of millimeter. The first plane is an insulator while the second is usually made of glass; both are covered with an hydrophobic coating (Fig. 2.1d). Under the insulating layer, a series of electrodes are placed that pilot the droplet; the conducting glass is connected to the ground. Droplets thus behaves as capacitors, their capacity varies with the interface shape. Droplets are moved by successively activating the electrodes: a droplet lying simultaneously on two contiguous electrodes moves towards the activated one. Although fusion between droplets is obviously performed, division of a single droplet is harder: the droplet may cover at least three electrodes, the middle one is switched off, so dividing the droplet in two parts. We perfectly understand that such a process cannot perform division in hundreds of micro-droplets, which is though required for high-throughput multiplexing operations. Moreover, the walls are never perfectly hydrophobic, so the liquid may adhere on them [35]. Droplets thus lose some mass by coating everything behind them [36, 37], so contaminating other next droplets that have to pass the same points.

In order to minimize losses by coating, one can use only a single solid insulating surface on which droplets are also driven by electrowetting [17, 38]. A micro-catenary may serve as the second electrode, as well as a guide for droplets (Fig. 2.1e). Another option consists in having two parallel conducting strips on the insulating surface [39]. Nevertheless, we note that droplet division is even an harder issue with these technical solutions.

2.1.5 Spontaneous motion on active surfaces

Droplets can be driven by the physical properties of the solid surface on which they are released. For example, spontaneous motion is observed on surfaces with a wettability gradient due to thermic, optical [21] or chemical effects [40]. Hydrophobicity is also tuned by changing the micro-texture [41]. Like lotus leaves [42], the surface may ally roughness to chemical hydrophobicity to offer the minimum of surface to water droplets. Contact angles up to 160° are observed and surfaces acquire a kind of self-cleaning property : droplets roll on them, taking dust away [43].

To definitely avoid contact, one may use the Leidenfrost effect: when a droplet is placed on a very hot surface, its bottom evaporates and the vapor creates a gas cushion on which the droplet floats. On an asymmetrically textured surface, Leidenfrost droplets experience spontaneous motion [44]. Although there is no contact between the droplet and the substrate, there is still an important mass loss through evaporation. Another solution to prevent contact is to texture the droplet itself, namely to cover it with an hydrophobic powder [45, 46]. So coated, the droplet is moved without any friction or mass loss. It can also float on the surface of a water bath. Some insects walk on water by using a similar technique; their textured hydrophobic legs offer them a minimal contact with water [47].

Finally, we note that droplets can be moved by inertial forces, e.g. by shaking the solid substrate on which they are placed. Under given conditions, droplets may climb on inclined

vibrated surfaces [48, 49]. Such technique has also been exploited in nature: some shorebirds fish by striking the water surface with their long thin beak, so extracting a droplet containing the prey. The droplet climbs along the beak and reaches the mouth thanks to a quick and efficient succession of opening/closing cycles [50].

2.2 A need for alternatives

It is obvious, there is no technical solution without drawbacks: impossibility to perform some basic operations, expensiveness, difficulty to use, lack of flexibility and robustness, etc. Nevertheless, the droplet physics is far from being fully explored. One of the goals of this thesis is to propose some new alternatives that would complete this range of existing techniques. The first part discusses an elegant variant of levitation, in which droplets bounce indefinitely on a liquid bath though they never touch each other. A much more promising solution is presented in part two: droplets slide down fibers. The basics in microfluidics is advantageously transposed on simple fiber networks. In particular, the division and multiplexing operations are performed very efficiently.

Part I

Droplets on liquid interfaces

Chapter 3

Bouncing or coalescence, life or death

The collision of two distinct streams of drops presents points of interest which have been made subject of examination. [...] When the angle of collision is small, the disposition of the files of drops may be made such that they rebound without crossing (fig.3). More often, however, the drops shoulder their way through after one or more collisions, somewhat as in fig.4. [...] At a somewhat higher angle of collision amalgamation will usually occur. The streams do not usually join into one, as we might perhaps expect, but appear to pass through one another, much as if no union of drops had occurred. With the aid of the revolving disk the course of things is rendered evident. The separating layer is indeed ruptured at contact and, for a short time, the drops move as one mass. There is, however, in general, considerable outstanding relative velocity, which is sufficient to bring about an ultimate separation, preceded by the formation of a ligament (fig.5). Lord Rayleigh, 1882 (reference to Fig. 3.1).

Lord Rayleigh (1879) was in the first physicists to investigate the interactions between several droplets [51]. In his experiment [52], two jets destabilized in a series of falling droplets collide with each other. The very fast motion of droplets is seen through stroboscopic effect. Rayleigh observed various behaviors depending on the collision parameters (angle, velocity): the droplets may bounce on each other, or fuse together (coalescence) and possibly after split into many droplets. The pictures from Rayleigh (Fig. 3.1) are remarkably accurate and realistic. He also discussed the significant impacts of many factors, including viscosity, surface tension, solubility of the interstitial gas, electric charge, addition of surfactant molecules and dusts. His work has been completed by many authors [53, 54]. Some of them have also studied droplets interacting with a liquid bath [55, 56]; again, the droplet may bounce onto or coalesce into the bath.

At the same time as Rayleigh, Worthington [57] was publishing his beautiful observations of droplets impacting a bath at high velocity; this violent fusion is often called a splash. The droplet usually turns into a crown that breaks up in a myriad of tiny droplets, as if the initial droplet was blowing up. A powerful vertical jet is formed at the impact point, which usually destabilises into many droplets as in the experiment of Rayleigh. The transition between coalescence and splash is described in [58]. During impact, a small air bubble may be trapped under the bath surface. This bubble is mainly responsible for the noise made by raindrops [59]. The air trapping is even greater when a liquid jet impacts a bath. The jet can also bounce onto the bath [60] or penetrate inside [61] and possibly turn into antibubbles [62], i.e. water droplets surrounded by an air layer, the whole immersed in the bath. Droplet impacts

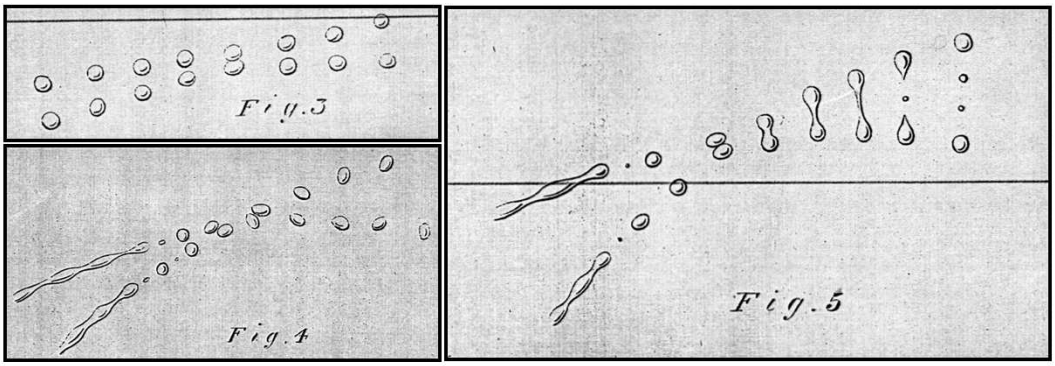

Figure 3.1: Drawings made by Lord Rayleigh in 1882 to describe his observations on interacting droplets. These latter may bounce onto or brush against each other, fuse together and possibly split again.

have been studied in many configurations, on other kind of surfaces, e.g. on a liquid film [63], on a dry solid surface [6], into another immiscible liquid [64], etc. Recently, impacts on super-hydrophobic surfaces have been investigated [65, 66, 67].

Introduced in that way, the droplet physics seems infinitely complex; each experiment has a number of variations, each one bringing qualitatively new phenomena. However, the behavior of a single droplet in the vicinity of another liquid/gas interface (droplet or bath) is nearly dichotomic: it bounces or it coalesces. In the case of bouncing, both liquid masses never touch each other, the contact is only apparent. On a microfluidic point of view, where the droplet is considered as an individual entity containing information (e.g. the active principle of a medication), bouncing is equivalent to survival. A straight contact between two miscible liquids implies coalescence, i.e. the death of the microfluidic entity by dilution. Nevertheless, this fusion may be partial and give birth to new smaller droplets.

3.1 Birth and death of a droplet

There are many ways to create a droplet, i.e. to extract a small amount of liquid from a container. The most common and straightforward is dripping, i.e. letting droplets slowly escape from a tap or a syringe. At a given time, a pinch occurs and the droplet is definitely separated from the rest. Droplets produced by this way have a relatively calibrated volume, provided the creation is quasi-static, i.e. infinitely slow [68]. Conversely, when finite-amplitude dripping are considered, the physics quickly becomes complex [69, 70, 71], even chaos is encountered [72]. Droplets can also be born from the destabilization of a jet [73] since, for a given volume, their surface is less than the jet surface. This instability was first discovered by Plateau and Rayleigh [74, 75] (Chap. 8, App. G).

Droplets may be as well directly extracted from a bath. For example, a toothpick tip dipped into a bath and quickly taken out pulls a thin thread of liquid out from the bath, which turns into a droplet thanks to the Rayleigh-Plateau instability and falls onto the bath surface [76]. Droplet are also formed when the bath is violently shaken up and down (Faraday instability [77]) or when it is excited by powerful acoustic waves [30]. Finally, scientists from MIT have recently discovered an original way to extract droplets, by using an elastic sheet (Fig. 3.2). This latter behaves as a clamp whose opening is driven by surface tension [13].

Finally, as already mentioned, droplets may result from a partial coalescence of other droplets.

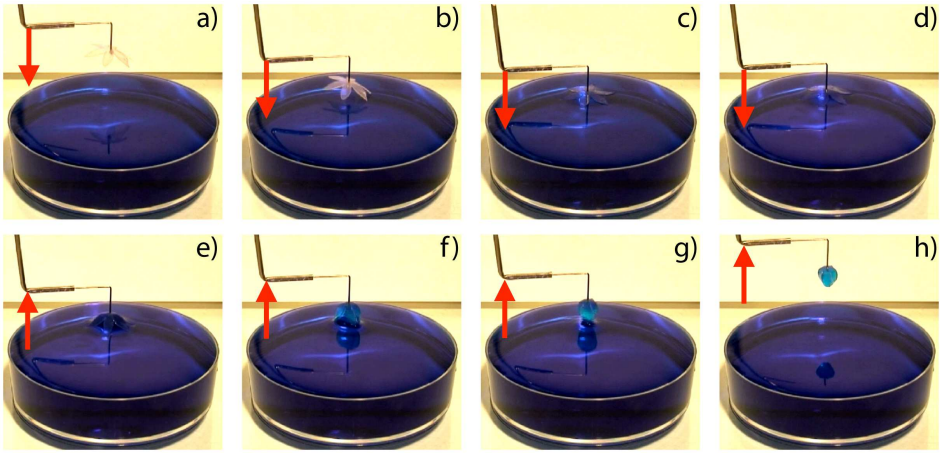

Figure 3.2: A flexible millimetric flower-shaped plastic sheet is used as a elasto-capillary pipette. Driven by a balance between surface tension and elasticity, it is able to extract droplets from a bath and release them into another one (Credit: Pedro M. Reis, MIT).

Both the fusion and the separation of liquid objects involve a topological change of the liquid interfaces, with the occurrence of singularities which satisfy to universal self-similarity laws [78]. For example, when two low-viscosity liquid objects coalesce together, the radius of the effective contact zone increases as the square root of time [79], whatever the considered geometry.

3.2 Delaying coalescence

A droplet falling on a bath behaves as a ball thrown on the ground; it bounces some times, less and less higher, before it eventually comes at rest on the bath surface. Starting from that point, the coalescence is not necessarily immediate; the droplet rests for a short time. The thin layer of surrounding fluid (e.g. air) between the droplet and the bath must be drained outwards for coalescence to occur. The film thickness is estimated from the interference fringes that are seen when the droplet is lightened with a monochromatic source (Fig. 3.3a); it is typically micrometric [80]. This momentary live of droplets on a bath was first reported by Lord Rayleigh in 1879 [51], then in 1881 by Osborne Reynolds[81]. Five years later, Reynolds came with the explanation, a theory called lubrication (App. D). This theory does not only explain the delayed coalescence of droplets [82] but also rationalizes the flows in every thin films, e.g. among others, the spreading of pancakes in a pan, the slipping of an object on another, the lava flows in an erupting volcano, the dynamics of soap films, bubbles [83] and antibulles [84].

The lubrication equations are obtained starting from the Navier-Stokes equations, in which the length scale in a given direction (namely the film thickness) is set much smaller than in other directions. Consequently, the pressure is constant along the thickness, resulting in a 2-D Poiseuille-like flow (Fig. 3.3b). The overpressure in the film gives rise to a force F_L that

opposes further thinning. A film of size R corresponds to a lubrication force of

$$F_L \sim \mu R \dot{h} \left(\frac{R}{h} \right)^3, \tag{3.1}$$

where $\dot{h}$ is the thinning rate of the film. Due to the factor $(R/h)^3$, the lubrication force becomes gigantic when the film is very thin. Nevertheless, lubrication effects are considerably attenuated when the film boundaries are set into motion (e.g. pulled by the liquid inside the droplet or bath). The resulting flow inside the film is a combination of a Poiseuille flow and a Couette flow, the latter might increase the drainage rate without modifying the lubrication force (Fig. 3.3c).

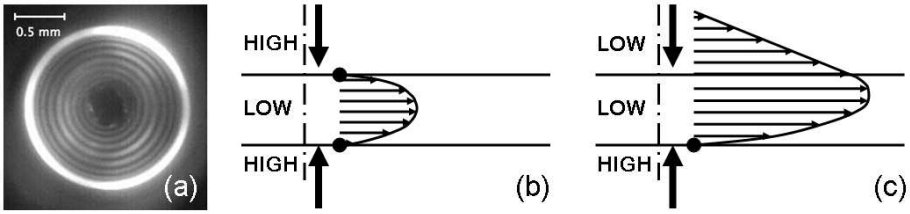

Figure 3.3: (a) Interference fringes visible through the droplet when the air film is micrometric. (b) A low-viscosity film is surrounded by high-viscosity liquids at rest; interfaces are motionless and the drainage is slow. (c) The low-viscosity film is pulled by the motion of the upper liquid; drainage is significantly increased by this additional flow.

When a droplet is tactfully placed on a bath in such a way that the liquids remain at rest, the air drainage may be considered as a pure Poiseuille flow. The lifetime t_L of the droplet corresponds to the drainage time of the film when the lubrication force is balanced by the weight. This yields

$$t_L \sim \frac{\mu_a R^4}{Mgh^2}, \tag{3.2}$$

where $\mu_a \simeq 18 \cdot 10^{-6}$ kg/m.s is the dynamic viscosity of air. The film breaks when a sub-micrometric thickness is reached, thanks to the cohesive forces (Van Der Waals) exerted by the liquids on each side. The large curvature of the interface next to the rupture point causes the film to quickly retract. According to Eq. (3.2), the lifetime of a millimetric droplet placed at 1 μm from the bath is $t_L \sim 0.3$ s. Practically, droplets experience much lower lifetimes due to residual flows inside [85]. Moreover, a number of factors significantly affect the result: temperature, electrostatic fields, surfactant molecules [86, 87], vapor concentration, rheologic properties, presence of stabilizing polymers [88], etc. The coalescence time of droplets is of crucial importance for many industrial processes involving emulsions [89]: dairy products in food industry, petrol demulsification, cosmetics, etc. Nevertheless, in spite of the tremendous efforts made by scientists since the sixties [90], the lifetime of droplets is hardly predicted with accuracy and reproducibility.

For the problem we are interested in, we need not to slow down the air drainage, but to cancel it so droplets can be handled without this time constraint. Many techniques have been proposed in the last ten years to prevent coalescence [91]. For example, a horizontal relative motion between the droplet and the bath can maintain the air film; a lift force balances the

weight. The motion may be a rotation [92, 93] or a hydraulic jump [94]. It may also be due to thermocapillary flows [93]. A water droplet placed in the vicinity of a very hot source (a solid surface [95, 96] or a bath [97]) is observed to float on a gas cushion, as already noted by Leidenfrost in 1756. The air film transfers the heat to the bottom of the droplet which evaporates; the released vapor balances the losses due to drainage.

In 1978, Jearl Walker [98] proposed an astonishing way to maintain a droplet alive on a bath surface. The bath is simply vibrated vertically, e.g. by fixing the container on the membrane of a loud-speaker. This forcing makes the droplet bounce indefinitely on the bath, exactly as a ball can be kept bouncing on a racket by swinging it up and down (App. E). The air film is regenerated at each bounce and the energy dissipated by viscosity is balanced by the incoming energy from the vibration. We note that an horizontal oscillation of the bath [99] may also delay the coalescence, but cannot enable sustained bouncing. In this thesis, we concentrate specifically on this technique of vertically vibrating the liquid substrate in order to provide the energy required for periodic bouncing. To understand it, we need first to investigate the physics of bouncing.

3.3 The physics of bouncing

Bouncing objects are subject to universal mechanisms which, qualitatively, are weakly dependent on the considered configuration. To get bouncing, the system object/substrate must have at least one efficient spring mechanism. At impact, the translational kinetic energy is converted into deformation potential energy (through surface tension for liquids, and elasticity for solids). This energy is then partly given back to the translational motion. The other part feeds waves, oscillations and internal motions. The apparent contact time t_c between the object and the substrate is similar to the energy transfer characteristic time

$$t_c \sim \sqrt{M/k}, \tag{3.3}$$

where M is the mass of the bouncing object and k the stiffness of the spring mechanism. For a droplet [65, 100], we find the capillary time $\tau_\sigma = \sqrt{M/\sigma}$. For rigid beads on an elastic membrane under tension $\mathcal{T}$, $t_c \sim \sqrt{M/\mathcal{T}}$ [101]; and for elastic balls of Young modulus $\mathcal{E}$ and radius R on a rigid ground, $t_c \sim \sqrt{M/\mathcal{E}R}$. As universal as the spring mechanism is the dissipative process, whose final effect is to damp the bouncing: viscosity for fluids, shear/friction for solids. Depending on the case, some dissipations are more significant than others - e.g. the dissipation of micro-flows inside the droplet, or the dissipation in the intervening air layer.

Despite its universal features, the bouncing dynamics is difficult to model in a general case. Consider for example a 10 cS millimetric droplet bouncing on a bath made of the same liquid. At impact, both the droplet and the bath are deformed and store surface energy. The resulting flow in the bath is hardly described mathematically. A crater is formed at impact, which can be represented by nonlinear capillary waves. Owing to its mass, the bath has inertia; it reacts to the droplet in a finite time with its own dynamics. In these conditions, bouncing is really hard to model.

Two specific bouncing configurations are discussed in this thesis. Each one corresponds to a limit in which the bath dynamics is overly simplified, even neglected. In the first case (Chap. 4), the droplet bounces on a soap film. This special bath is much lighter than the droplet, it has a negligible inertia and it reacts quasi-instantaneously to external solicitations, it lets itself be shaped by the droplet. In the second case (Chap. 5), the liquid bath is highly

viscous, bath deformations are limited and the stored energy cannot be given back. Therefore, we suppose in first approximation that the bath behaves as a rigid surface of infinite inertia. The main difference with a solid surface is that the bath is perfectly smooth down to atomic scale. This quality is required for bouncing droplets, since any micrometric rugosity in the surface would prematurely break the air film and lead to coalescence.

3.4 Summary

In this chapter, we have discussed the various interactions between a droplet and another liquid object. The droplet usually bounces or coalesces into the other liquid. The bouncing is a priori complex since both the bath and the droplet dynamics influence each other. The next chapters concentrate on limit cases in which these interactions are simplified.

The bouncing may be seen as a way to prevent coalescence, i.e. the inevitable death of a droplet in the vicinity of a liquid bath. This coalescence is delayed thanks to the intervening air layer between the droplet and the bath, that must first be drained out for fusion to occur. This drainage obeys to the lubrication theory; it can be slowed down and even stopped by many techniques. Among others, a droplet can bounce indefinitely without coalescing when the liquid bath is vertically vibrated.

Chapter 4

A droplet on a soap film

A soap film is a liquid film of micrometric thickness covered on each side with a monolayer of surfactant molecules. This latter considerably decreases the surface energy of the film, so it is expected to deform much more easily. When the film is very thin, both surfactant layers may interpenetrate and repulse each other, which yields additional stability to the soap film.

The impact of a droplet on a soap film was described for the first time by Courbin and Stone [102] in 2006. These authors observed that small objects (liquid or solid) intercepting the film at high speed are able to cross it without breaking it. For smaller impact velocity, solid particles have a different behavior from liquids. Owing to its roughness, the bead immediately touches the soap film, which reacts by applying a force upwards at the contact line. This force slows down the bead fall and, if the velocity is not sufficient, the bead is trapped by the soap film [103]. Conversely, as we have seen in Chap. 3, a droplet may avoid touching the soap film thanks to the existence of a thin lubricating air layer. Nevertheless, the soap film is highly deformed by the droplet. The deformation energy of the film is taken from, then given back to the translational energy of the droplet. As a gymnast on a trampoline, the droplet bounces on the iridescent soap film (Fig. 4.1). Although not encountered in nature or in industrial processes, the bouncing of a droplet on a soap film has two major particularities that make its understanding and quantitative modeling much easier than other bouncing configurations:

- The soap film stores practically all the energy of the incoming droplet.
- The soap film inertia is negligible compared to the droplet inertia.

It is therefore a perfect case study to first understand the physics of bouncing.

4.1 Experimental setup

We have studied the bouncing of droplets on a horizontal soap film through two series of experiments, both performed at the Massachusetts Institute of Technology in collaboration with Professor John W.M. Bush [104, 105].

In the first series, a droplet impacts a soap film of thickness $h_{sf} \sim 1$ μm fixed on a thin metallic ring of radius $R_{sf} = 8$ mm (Fig. 4.2a). In the second experiment, the soap film is vertically vibrated in order to provide additional energy to the droplet; sustained bouncing is observed exactly as in Walker's experiment [98]. The vibration is ensured by pinning the soap film on the edge of a plexiglas tube of radius $R_{sf} = 16$ mm. The tube is fixed to a

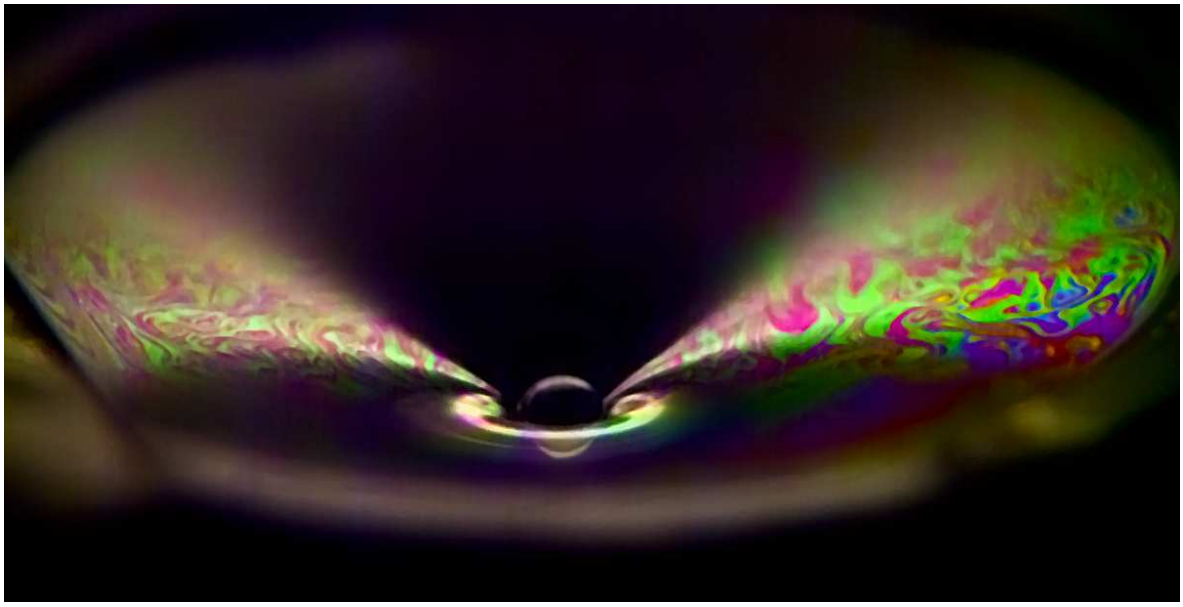

Figure 4.1: A millimetric droplet bouncing on an iridescent soap film pinned on a ring.

loud-speaker membrane that vibrates sinusoidally with an amplitude A and a frequency f between 20 and 80 Hz (Fig. 4.2b). To avoid the practical difficulties of leveling the soap film, the tube is put in a larger concentric tube (Fig. 4.2b) that is partially filled with water and fixed to the speaker. The soap film is created on the inner tube while the tube is immersed in the fluid reservoir, so that an air column is trapped between the soap film and the liquid bath. The inner tube is then moved slightly upwards before fixing it to the outer cylinder with screws. The low pressure in the air column deflects the soap film downwards at its center and the resulting film curvature stabilizes the bouncing droplet.

Droplets of constant radius $R = 0.8$ mm are released above the soap film from an insulin syringe. The impact speed V is varied between 0.1 and 1 m/s by changing the release height. The liquid used for both the droplet and the soap film is a mixture of water, glycerol and commercial soap (Dove®). The concentration of soap is 1 % by volume. The viscosity of the liquid is altered by varying the concentration of glycerol (App. B). Most of the experiments were performed with a mixture of 80 % water and 20 % glycerol, which corresponds to a viscosity $\nu \simeq 2$ cS, a density $\rho = 1050$ kg/m^3 and a surface tension $\sigma \simeq 22$ mN/m. Experiments are recorded from the side with a high-speed video camera with acquisition rate 1000 fps and resolution 256 $\times$ 256 pixels. For our typical field of view, the characteristic pixel size is 50 μm. Measurements of drop position and film shape are made via image processing.

The droplet impact on a vibrating soap film is characterized by 12 physical variables (R, R_{sf}, h_{sf}, ρ, ν, σ, ρ_a, ν_a, g, V, f and A - Fig. 4.2), so nine independent dimensionless numbers can be formed. Nevertheless, we choose to only vary four parameters V, R_{sf}, f and A, which are related to four dimensionless numbers:

- the Weber number $We = \rho V^2 R/\sigma \in [1, 30]$, which corresponds to the ratio between the kinetic energy of the incoming droplet and its surface energy,

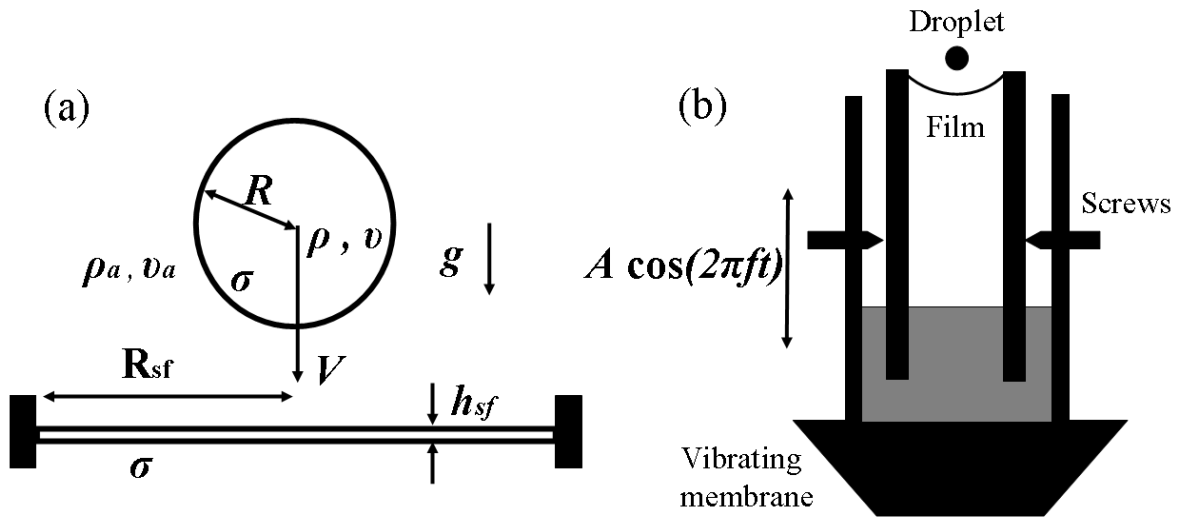

Figure 4.2: Experimental set-up. (a) Without vibration: a droplet strikes a horizontal soap film fixed on a thin ring. (b) With vibration: the soap film is pinned at the end of the inner tube, which is vertically vibrated by a speaker. The arrangement with the outer cylinder ensures a downward curvature of the film, and so stabilizes the bouncing droplet.

- the ratio between the soap film and droplet radii

$$\xi = \frac{R_{sf}}{R}, \tag{4.1}$$

- the forcing acceleration

$$\Gamma = \frac{4\pi^2 A f^2}{g} \in [0.15, 3], \text{ and} \tag{4.2}$$

- the reduced frequency

$$\omega = 2\pi f \sqrt{\frac{M}{k}} \in [0.7, 3], \text{ where} \tag{4.3}$$

$$k = c_k \sigma \tag{4.4}$$

  is the stiffness of the soap film. The exact value of c_k is deduced latter.

In our experiments, $\xi = 10$ when the film is at rest, and $\xi = 20$ when it is vibrated. Other dimensionless numbers, such as $Bo = 0.1$ and $Oh = 0.015$, are not varied.

4.2 From bouncing to crossing: the soap film shape

As previously observed by [102], the droplet bounces on the soap film for low We while, at high We, it crosses the soap film without breaking it. In this section, we discuss the transition between both behaviors as a function of We.

During a bouncing event (Fig. 4.3a-b), the kinetic energy of the falling droplet is primarily converted into surface energy of the distorted soap film; thereafter, the bulk of this energy

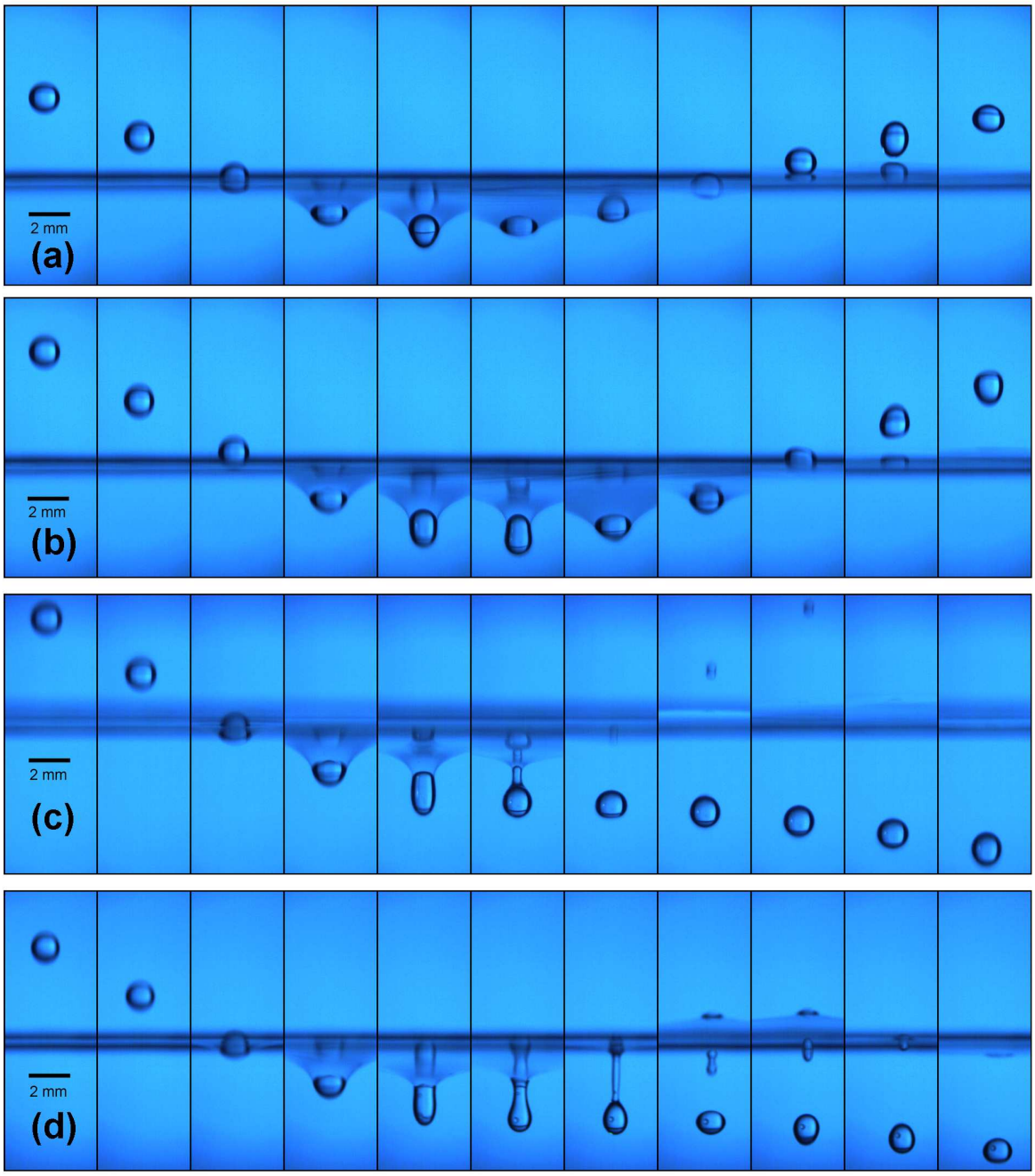

Figure 4.3: Various behaviors of a droplet impacting a soap film. Snapshots are taken every 4 ms. (a) Bouncing at $We \simeq 7$. (b) Bouncing at $We \simeq 12$. (c) Partial crossing at $We \simeq 16$. (d) Full crossing at $We \simeq 15$.

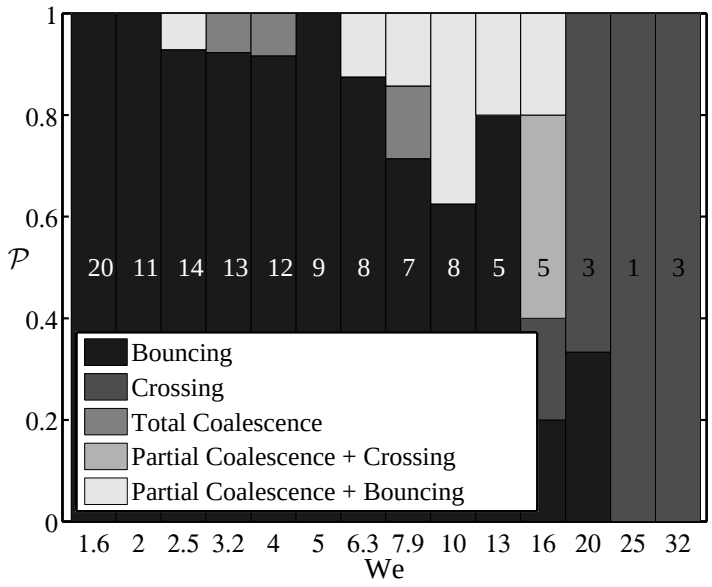

Figure 4.4: Transition from bouncing to crossing for impact on a stationary film. The probability $\mathcal{P}$ of different events is represented as a function of We. The number of events in each class is reported in the middle of the columns. The transition between bouncing and passing occurs for a critical Weber number $We_{th} \simeq 16$.

is restored to the droplet kinetic energy. To avoid coalescence, the droplet must never touch the soap film: the thin intervening air layer must persist. As this layer thins, the resulting lubrication pressure deforms the underlying film. At impact, the droplet becomes oblate, but recovers a roughly spherical shape when the soap film deflection is maximal. As the drop is ejected, it again becomes oblate. For the sequence illustrated in Fig. 4.3(a), the contact time t_c, during which the droplet is in the immediate vicinity of the soap film, is about 20 ms.

In a crossing event (Fig. 4.3d), the soap film is not able to absorb the initial kinetic energy of the droplet: as the droplet passes through, the film self-heals. How the passage from one side to the other does occur ? Here is a plausible scenario: the air layer is so compressed by the incoming droplet that it breaks, the droplet coalesces into the soap film. Nevertheless, the residual kinetic energy allows the droplet to keep going downwards and eventually separate from the film. After coalescence, a part of the droplet may possibly be ejected upwards (Fig. 4.3c). The formation of droplets after coalescence is also observed on a bath and called partial coalescence (Chap. 7).

In Fig. 4.4, the likelihood of bouncing and crossing is represented as a function of We. The transition between bouncing and crossing regimes occurs at $We_{th} \simeq 16$. The probability of a coalescence increases with the Weber number since the air layer becomes thinner. The threshold Weber is high relative to other configurations. For example, when a droplet impacts a liquid film on a solid substrate [63], the transition between bouncing and coalescence occurs at $We_{th} \simeq 7$.

In order to rationalize this experimental result, we first model the shape of the soap film, so we deduce a relation between the drop position and the force generated by the soap film. The soap film reacts to the external forcing associated with the impacting droplet at a timescale determined by the speed of capillary waves on the soap film, $u_{cw} \sim \sqrt{\sigma/(\rho h_{sf})}$ [106]. For

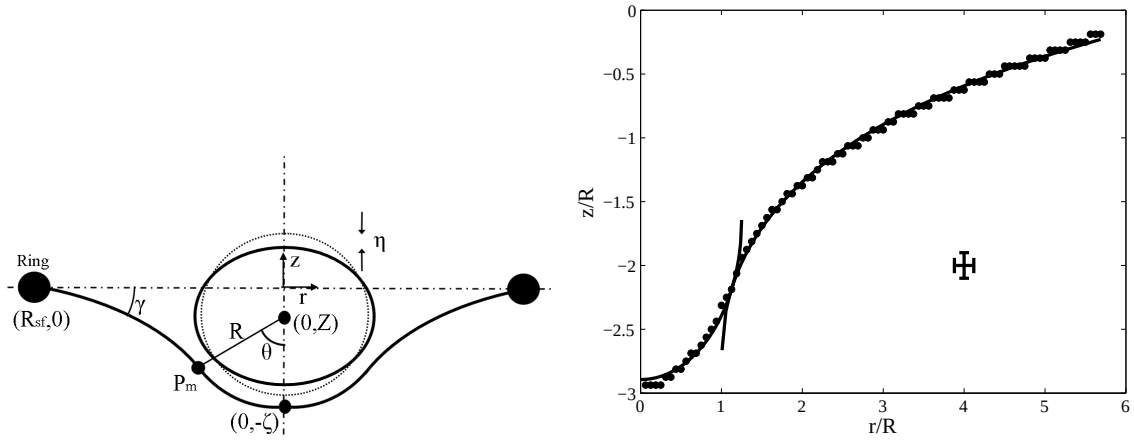

(a) (b)

Figure 4.5: (a) Hypothetical shape for the soap film: the region of curvature $1/R$ below the droplet matches onto an exterior region of zero curvature at the point P_m corresponding to an inclination angle θ. The soap film is pinned at $(r, z) = (R_{sf}, 0)$, while its point of maximum centerline deflection reaches $(0, -\zeta)$. The center of mass of the droplet is at $(0, Z)$, and its vertical deflexion is denoted by η. (b) Observed shape of the soap film at $We = 9.7$. The solid curves represent the "sphere plus catenoid" model.

a film of thickness $h_{sf} = 1\,\mu$m, the wave speed, $u_{cw} \sim 5$ m/s, is approximately 10 times larger than the characteristic droplet impact speed. The soap film thus adjusts rapidly to the applied forcing, the information being transmitted by capillary waves [107]. For the relatively low-impact speeds considered in our study, the film shape may be described as quasi-static: there is a univocal relation between the soap film deformation ζ and the resulting vertical force F_σ applied to the droplet through the air layer. As seen below, this relation does neither depend on time, nor on the loading history of the soap film which has no memory.

The shape expected for the soap film is in perfect agreement with experimental observations (Fig. 4.5). We assume that the droplet remains roughly spherical and that, near the droplet, the soap film is a spherical cap lying tangent to the droplet with constant mean curvature $1/R$. Beyond the droplet, the soap film has zero curvature since the air pressure is atmospheric on both sides (Fig. 4.5a). The only non-planar axisymmetric surface that has zero mean curvature is the catenoid:

$$\frac{z}{r_m} = -\mathrm{acosh}\left(\frac{R_{sf}}{r_m}\right) \pm \mathrm{acosh}\left(\frac{r}{r_m}\right), \tag{4.5}$$

where r_m is the minimum radius of the catenoid. We must match this catenoid to the spherical cap at a point P_m prescribed by the angle θ: $r_m/R = \sin^2\theta$. The maximum vertical deformation ζ of the soap film may be expressed as a function of θ through

$$\frac{\zeta}{R} = 1 - \cos\theta + \sin^2\theta\left[\mathrm{acosh}\left(\frac{1}{\sin\gamma}\right) - \mathrm{sign}(\cos\theta)\mathrm{acosh}\left(\frac{1}{\sin\theta}\right)\right], \tag{4.6}$$

where $\sin\gamma = r_m/R_{sf} = (\sin^2\theta)/\xi$. The anomalous surface generated by the film deformation,

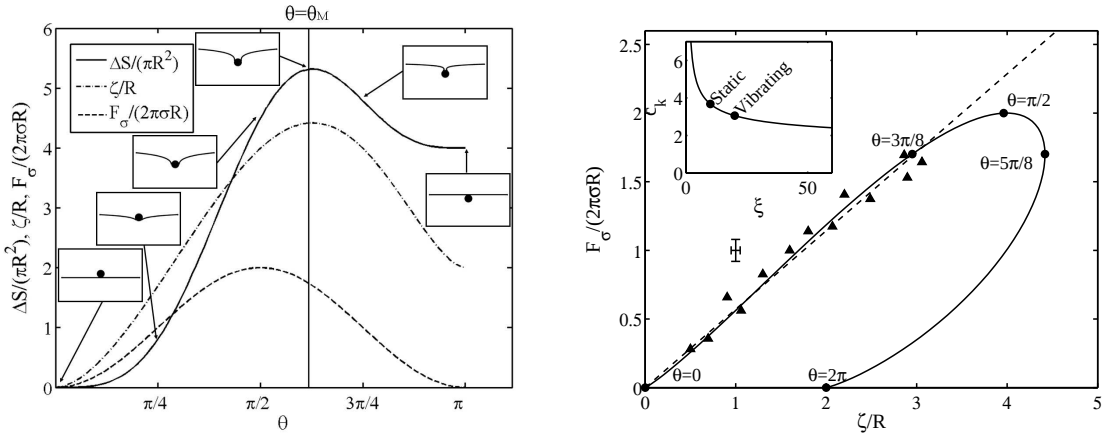

Figure 4.6: Theoretical model of the soap film shape for $\xi = 10$. (a) Variation of $\Delta S/(\pi R^2)$, ζ/R and $F_\sigma/(2\pi\sigma R)$ with θ. The surface is maximum in $\theta = \theta_M$. Insets represent the shape of the film. (b) Theoretically predicted force–displacement curve for a spherical drop impinging on a soap film. The solid line represents the variation of the force $F_\sigma/(2\pi\sigma R)$ with respect to the maximum film deflection ζ/R for $\xi = 10$. The dashed line represents the linear spring approximation (4.9) and the (▲) are the experimental measurements. (Inset) Stiffness coefficient $c_k = k/\sigma$ as a function of ξ. Our static soap film ($\xi = 10$) has a stiffness coefficient $c_k \simeq 8\pi/7$ while for the vibrated soap film ($\xi = 20$), $c_k \simeq 24\pi/25$.

ΔS, is given by

$$\begin{aligned} \frac{\Delta S}{\pi R^2} &= (1-\cos\theta)^2(2+\cos\theta) - \frac{\sin^4\theta}{1+\cos\gamma} \\ &+ \sin^4\theta\left[\operatorname{acosh}\left(\frac{1}{\sin\gamma}\right) - \operatorname{sign}(\cos\theta)\operatorname{acosh}\left(\frac{1}{\sin\theta}\right)\right]. \end{aligned} \tag{4.7}$$

The vertical force F_σ required to produce a vertical displacement ζ is given by

$$\frac{F_\sigma}{2\sigma\pi R} = \frac{\partial_\theta \Delta S/(\pi R^2)}{\partial_\theta \zeta/R} = 2\sin^2\theta. \tag{4.8}$$

Of course, this force is obtained more easily by integrating the vertical component of the surface tension over the circle formed by revolving the point of matching P_m about the vertical axis $r = 0$.

The dependence on θ of $\Delta S/(\pi R^2)$, ζ/R and $F_\sigma/(2\pi\sigma R)$ is illustrated in Fig. 4.6(a) for $\xi = 10$. The anomalous surface ΔS reaches a maximum for a critical angle $\theta_M \simeq 5\pi/8$. For $\theta < \theta_M$, the system tends to the $\theta = 0$ state (droplet above the soap film), while for $\theta > \theta_M$ it tends to the $\theta = \pi$ state (droplet fully enclosed by the soap film). The maximum deflection $\zeta/R \simeq 4.4$ is also reached for $\theta = \theta_M$. The force F_σ exerted by the soap film on the droplet remains directed upwards, whatever the value of θ. The maximum force generated by the soap film, $F_\sigma = 4\pi\sigma R$, occurs when $\theta = \pi/2$. The force is represented as a function of the maximum centerline deflection ζ in Fig. 4.6(b). Four distinct regimes are apparent.

- When $0 < \zeta < 3R$ ($0 < \theta < 3\pi/8$), the soap film reacts like a spring, exerting a force that grows roughly linearly with the deformation

$$F_\sigma = k\zeta, \tag{4.9}$$

where the stiffness k is given by $k = c_k\sigma$. The dependence of c_k on ξ is illustrated in Fig. 4.6(b): $c_k \simeq 8\pi/7$ when $\xi = 10$ (static soap film in our experiments) while $c_k \simeq 24\pi/25$ when $\xi = 20$ (vibrated soap film in our experiments). Agreement with experimental data is excellent. In particular, we confirm that there is no hysteresis; the deformation does not depend on the direction of the droplet.

- When $3R < \zeta < 4R$ ($3\pi/8 < \theta < \pi/2$), the spring law becomes nonlinear as the force saturates. The stiffness vanishes when $\zeta = 4$.

- When $4R < \zeta < 4.4R$ ($\pi/2 < \theta < \theta_M$), the stiffness is negative: increasing the deformation results in decreasing the force. The stiffness diverges when $\theta \to \theta_M$ and the system switches equilibrium states.

- When $\theta > \theta_M$, ζ decreases towards $2R$ and the stiffness is again positive. Here, the system tends towards the $\theta = \pi$ configuration, where the droplet is wrapped by the film. We note that for $\theta > \theta_M$, the film shape is poorly described by the model: the last frames of Fig. 4.3(d) clearly indicate that the film does not wrap the drop as it passes through.

Finally, we apply this quasi-static model for the film shape to estimate the minimum Weber number We_{th} required for a droplet to pass through the soap film. Supposing that the whole initial kinetic energy is converted into surface energy of the film, the energy balance is written $\frac{2\pi}{3}\rho R^3 V^2 = 2\sigma \max(\Delta S)$, so

$$We_{th} = 3\frac{\max(\Delta S)}{\pi R^2}. \tag{4.10}$$

In our experiments, the static soap film has a radius of R_{sf} =8 mm and corresponding $\xi = 10$; we thus anticipate $We_{th} = 16$. This value is in good agreement with the experiments reported in Fig. 4.4. We note that the prediction (4.10) neglects energy dissipated during impact as well as the droplet deformation. Nevertheless, it does provide a good leading-order criterion for droplet breakthrough.

4.3 Bouncing on a film at rest

We proceed by characterizing two important bouncing parameters: the apparent contact time t_c and the energy dissipated during a single bounce. Both quantities were measured for various We. As seen in Fig. 4.7(a), t_c is proportional to the capillary time τ_σ and independent of We:

$$t_c \simeq 1.86\tau_\sigma. \tag{4.11}$$

This result is similar to those reported by [101] for beads bouncing on elastic membranes and by [65] for droplets bouncing on hydrophobic surfaces. In that latter case, the proportionality constant is much lower, $t_c \simeq 1.27\tau_\sigma$.

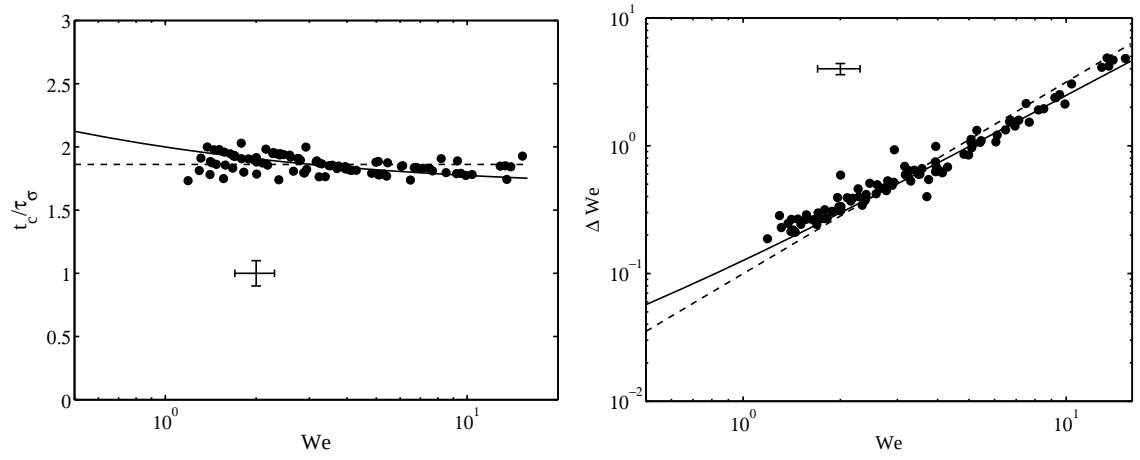

Figure 4.7: (a) Contact time t_c normalized by τ_σ. (b) Difference in We before and after the bounce as a function of We. Dashed lines in (a) and (b) represent fits of Eq. (4.11) and (4.14), respectively. Solid lines were deduced by integrating (4.31) with $c_T = 0.028$ (best fit).

In the previous section, we have concluded that the soap film behaves as a linear spring of stiffness $k \simeq 8\pi/7\sigma$, which corresponds to a natural frequency

$$f_{sf} = \frac{1}{2\pi}\sqrt{\frac{k}{M}} = \frac{0.3}{\tau_\sigma} \simeq 30 \text{ Hz}. \tag{4.12}$$

One expects the contact time to be approximately half a period of oscillation of the soap film, i.e. $t_c = 1.66\tau_\sigma$, which is coherent with the experimental results.

During each bounce, a droplet loses a fraction of its initial translational energy through viscous dissipation. In dimensionless terms, the Weber number is decreased by an amount ΔWe at each bounce owing to dissipation inside the droplet, soap film or intervening air layer. The coefficient of restitution, specifically the ratio of take-off and landing speeds, is given by

$$\epsilon = \sqrt{1 - \frac{\Delta We}{We}}. \tag{4.13}$$

The dependence of ΔWe on We is reported in Fig. 4.7(b). The experimental data collapse onto a single curve corresponding to a power law close to

$$\Delta We \simeq 0.09\, We^{3/2}. \tag{4.14}$$

The dissipation is markedly different from that observed by [108], i.e. $\Delta We \simeq 0.2\, We$, for droplets bouncing at $We \ll 1$ on a hydrophobic surface.

We proceed by developing a simple theoretical model to rationalize Eq. (4.14). The center of mass of the droplet Z evolves according to

$$M\ddot{Z} = F_\sigma(\zeta) - Mg. \tag{4.15}$$

If η denotes the vertical deformation of the droplet (Fig. 4.5), we can write $Z = -\zeta + R + \eta$. Equation (4.15) can then be recast in terms of energy as

$$\frac{\mathrm{d}}{\mathrm{d}t}\left[\frac{M\dot{Z}^2}{2} + MgZ + E_{\sigma sf}(\zeta)\right] = F_\sigma(\zeta)\dot{\eta} \tag{4.16}$$

where $E_{\sigma sf}(\zeta)$ is the surface energy stored in the soap film, so that $\mathrm{d}E_{\sigma sf}(\zeta)/\mathrm{d}\zeta = F_\sigma(\zeta)$. The only remaining non-conservative term in (4.16) is $F_\sigma(\zeta)\dot{\eta}$, the work done by the soap film in deforming the droplet. This term describes the transfer of energy between the translational and vibrational motions of the droplet. The total energy removed in this fashion during impact necessarily scales as $F_\sigma \dot{\eta} t_c$. We thus need to know how F_σ, $\dot{\eta}$ and t_c scale with We.

The maximum centerline deflection of the soap film, ζ, was measured for various We. When $\zeta < 4$ (i.e. $\theta < \pi/2$), the maximum force $F_{\sigma M}$ exerted by the soap film occurs at the point of maximum deflection and can be calculated from (4.6) and (4.8). As shown in Fig. 4.8(a), the maximum force is linearly proportional to We.

$$\frac{F_{\sigma M}}{\sigma R} \simeq 1.11\, We. \tag{4.17}$$

The droplet deformation rate during impact $\dot{\eta}$ scales as η_M/τ_σ, where η_M is the maximum droplet deformation. The droplet reacts rapidly to the impact; it is already highly compressed by the time the soap film begins to deform. Indeed, the natural frequency of the soap film is given by Eq. (4.12), while according to Rayleigh (Eq. 1.7), the natural frequency of the droplet oscillating in the mode Y_2^0 is

$$f_{(2,0)} = \frac{0.92}{\tau_\sigma} \simeq 90 \text{ Hz}, \tag{4.18}$$

so the droplet reacts three times faster than the soap film. For an experiment at $We \simeq 9$ corresponding to a kinetic energy $K \simeq 2.60\ \mu\mathrm{J}$, the maximum drop deformation is estimated to be $\eta_M \sim 0.41R$. The corresponding surface energy is

$$E_\sigma \simeq \frac{8\pi}{5}\sigma\eta_M^2 \simeq 0.13\ \mu\mathrm{J}, \tag{4.19}$$

which represents a fraction $\Lambda \simeq 5$ % of the kinetic energy K. This lost energy at impact cannot account for the characteristic value $\Delta We/We \sim 0.25$ observed in Fig. 4.7(b), from which we infer that some additional energy is transferred after impact. Substituting $E_\sigma = \Lambda K$ into Eq. (4.19) yields a scaling for η_M

$$\left(\frac{\eta_M}{R}\right)^2 \simeq \frac{5\Lambda}{8\pi}\frac{K}{\sigma R^2} = \frac{5}{12}\Lambda\, We. \tag{4.20}$$

This scaling is similar to that observed by [109] for droplets striking a hydrophobic surface.

Equations (4.11), (4.17) and (4.20) together yield

$$\Delta We = \frac{3}{2\pi}\frac{\Delta K}{\sigma R^2} = \frac{3}{2\pi\sigma R^2}\int_0^{t_c} F_\sigma \dot{\eta}\mathrm{d}t \sim \frac{3}{2\pi}\frac{F_{\sigma M}\dot{\eta}t_c}{\sigma R^2} \simeq 0.63\Lambda^{1/2}\, We^{3/2}. \tag{4.21}$$

For $\Lambda = 5$ %, we thus obtain

$$\Delta We \approx 0.14\, We^{3/2}, \tag{4.22}$$

which is close to the observed scaling (4.14). While the coefficient deduced (0.14) is 50% higher than that observed (0.087), this estimate has not taken into account the variations of the sign of $F_\sigma\dot{\eta}$ over the integration period. Nevertheless, since t_c/τ_σ is independent of We, it is reasonable to suppose that the time correlation of F_σ and $\dot{\eta}$ remains unchanged with increasing We, which lends further credibility to this scaling. In summary, the translation energy is converted into

deformation energy, only a part of which is transferred back to translation. The remaining part is dissipated through internal motions in the droplet. This dissipation mechanism is also observed for droplets bouncing on hydrophobic surfaces [108], though the scaling is different.

Some energy is also inevitably dissipated in the air layer and the soap film. Both film and droplet are coated by a commercial surfactant whose precise surface properties are not easily quantified. The extent to which a surfactant-laden surface is rigidified depends on both the type and concentration of surfactant. In general, soap films lie between the "rigid" and "free" limits, in which the internal flows correspond, respectively, to Poiseuille and plug flows. The Poiseuille regime is more dissipative since velocity gradients arise across the thickness of the film. Conversely, in plug flow, transverse velocity gradients are negligible and the dissipation results from velocity gradients in directions parallel to the film, which are necessarily much smaller. Therefore, for the sake of bounding the dissipation in the soap film, only the Poiseuille case is considered here. Lubrication equations write

$$\frac{\partial h}{\partial t} + \boldsymbol{\nabla} \cdot \vec{Q} = 0 \tag{4.23}$$

$$\vec{Q} + \frac{h^3}{12\mu} \boldsymbol{\nabla} P = 0 \tag{4.24}$$

where $\vec{Q}$ is the flow rate and $\boldsymbol{\nabla} P$ the pressure gradient, both parallel to the air film. The energy dissipation ΔK in the whole film (surface S) during t_c is given by

$$\Delta K = -\int_0^{t_c} \int_S \vec{Q} \cdot \boldsymbol{\nabla} P \mathrm{d}S \mathrm{d}t \tag{4.25}$$

These equations are scaled to yield

$$\left.\begin{array}{l} \dfrac{h}{t_c} \sim \dfrac{Q}{R} \\ Q \sim \dfrac{h\Delta P}{12\mu R} \end{array}\right\} \Rightarrow \left\{\begin{array}{l} Q^2 \sim \dfrac{12\mu R^4}{t_c^3 \Delta P} \\ h^2 \sim \dfrac{12\mu R^2}{t_c \Delta P} \end{array}\right. \tag{4.26}$$

and

$$\Delta K \sim t_c (2\pi R^2) \frac{\Delta P}{R} Q \sim 4\pi \sqrt{\frac{3\mu R^6 \Delta P}{1.86\tau_\sigma}} \tag{4.27}$$

The overpressure ΔP, i.e. the pressure at center of the air film below the droplet, should scale as $F_{\sigma M}/(\pi R^2) \sim 0.35(\sigma/R)\, We$, which gives a scaling for the dissipated energy

$$\Delta We \sim 3 Oh^{1/2} We^{1/2}. \tag{4.28}$$

Assuming that the constant of proportionality is relevant, the range of energy loss due to dissipation in a soap film with $Oh = 0.015$ is $\Delta We \in [0.37, 1.5]$, while the observed range of dissipation is $\Delta We \in [0.2, 5]$. So, for $We \lesssim 1$, we expect the resulting dissipation in the soap film to be relevant for the case of rigid films. This additional source of dissipation might explain the fact that the observed dissipation is systematically higher than the scaling law (4.14) for $We \sim 1$. Nevertheless, the scaling $\Delta We \sim We^{1/2}$ is not observed experimentally for $We \gtrsim 1$. The observed loss of translational energy mainly results from a transfer to the vibrational motion of the droplet.

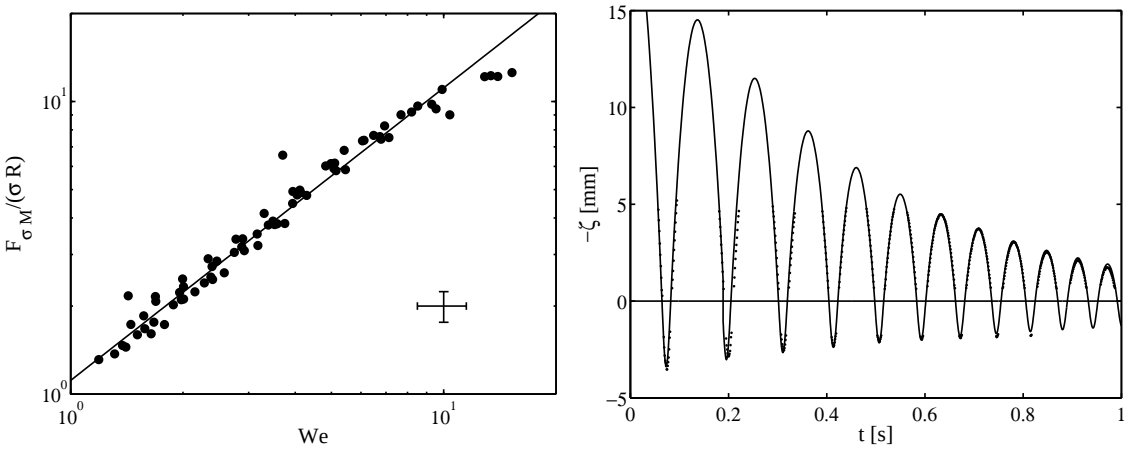

(a) (b)

Figure 4.8: (a) Dependence on *We* of the maximum force $F_{\sigma M}$ applied by the soap film on the droplet. The solid line corresponds to Eq. (4.17). (b) Observed (dots) and simulated (solid line) trajectories of a droplet released at $We = 15.24$ and bouncing on a stationary soap film. Experimental data could only be obtained in the apparent field of view, that was partially obscured by the frame of the soap film and also limited from above.

Although Eq. (4.16) seems to correctly describe the energy transfer between the droplet and the film, it cannot be solved unless an evolution equation for the drop deformation η is written. Instead, for the sake of mathematical simplicity, we model the dissipative transfer term $F_\sigma(\zeta)\dot{\eta}$ as a function of $\dot{\zeta}$, specifically

$$F_\sigma(\zeta)\dot{\eta} = -c_T \frac{M}{R}\mathcal{H}(\zeta)|\dot{\zeta}|^3, \tag{4.29}$$

where $\mathcal{H}(\zeta)$ is the Heaviside function and c_T is the transfer constant. The transfer is zero when $Z > 0$ (the droplet is flying), but is negative definite and scales as $We^{3/2}$ when $Z < 0$. We further simplify the system by assuming that $|\eta| \ll |\zeta|$: the droplet deformation is much smaller than the amplitude of vertical motion, so that $Z \simeq R - \zeta$. Finally, consistent with (4.9), we assume that the soap film has a linear force–displacement law $F_\sigma(\zeta) = \mathcal{H}(\zeta)k\zeta$. We thus obtain

$$\frac{\mathrm{d}}{\mathrm{d}t}\left[\frac{M\dot{\zeta}^2}{2} - Mg\zeta + \mathcal{H}(\zeta)\frac{k\zeta^2}{2}\right] = -c_T\frac{M}{R}\mathcal{H}(\zeta)|\dot{\zeta}|^3, \tag{4.30}$$

so

$$M\ddot{\zeta} = Mg - k\zeta\mathcal{H}(\zeta) - c_T\frac{M}{R}\mathcal{H}(\zeta)\dot{\zeta}|\dot{\zeta}|. \tag{4.31}$$

The constant $c_T = 0.028$ is determined by fitting the solutions of (4.31) to the experimental data in Fig. 4.7(b). The results from (4.31) with the c_T value so deduced represent an improvement over the scaling law (4.14). The predicted contact time t_c/τ_σ is also in good agreement with experimental data reported in Fig. 4.7(a). As seen in Fig. 4.8(b), the model produces a remarkably accurate picture of the damped bouncing on a stationary film.

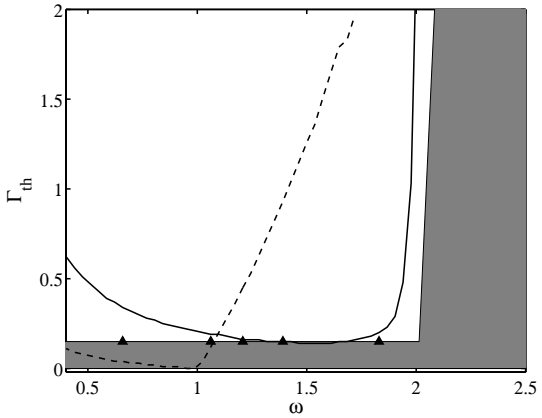

Figure 4.9: Threshold acceleration for bouncing, Γ_{th}, as a function of the dimensionless forcing frequency ω. For a given frequency, a droplet was released onto a film vibrating at $\Gamma > \Gamma_{th}$; subsequently, Γ was decreased until the droplet coalesced. The experiment was repeated several times to capture both modes (1,1) and (2,1): the minimum measured value of Γ corresponds to the threshold reported by (▲). When forcing parameters (Γ, ω) are located inside the shaded area, no periodic bouncing is observed and the droplet coalesces. Solid (resp. dashed) line represents the threshold computed by solving (4.33) numerically and corresponds to the mode (2,1) (resp. (1,1)). The lower threshold solution roughly corresponds to our experimental data.

4.4 Sustained bouncing on a vibrating soap film

On a stationary soap film, the *We* decreases at each bounce, until the droplet settles onto and ultimately merges into the film. To counter dissipative losses, a vertical vibration is applied to the frame of the soap film: energy is thus transferred from the frame to the film to the droplet. Provided the mechanical energy so supplied balances dissipative losses, the droplet is re-energized during impact and may bounce indefinitely, as in Walker's experiment [98]. Thanks to our simple model (4.31), it is possible to deeply understand this sustained bouncing.

First, we measure the acceleration threshold $\Gamma_{th}(\omega)$, which is the minimal acceleration Γ that can sustain periodic droplet trajectories, as a function of the dimensionless forcing frequency ω (Fig. 4.9). For $\omega < 2$, Γ_{th} is roughly constant (about 0.15 ± 0.04). When $\omega > 2$, bouncing droplets cannot be sustained. We note that this critical frequency corresponds to a period of 18 ms, a value roughly equal to the measured contact time.

A striking characteristic of droplet bouncing on soap films is the coexistence of multiple periodic solutions for given forcing parameters (Γ, ω), or, in the parlance of dynamical systems theory, multi-periodicity. Bouncing modes are denoted by two integers (p, q) such that one period of the trajectory corresponds to p forcing periods and q bounces of the droplet. For example, modes (1,1), (2,1) and (3,1) are displayed in the spatiotemporal diagrams of Fig. 4.10(a-c). All these solutions are observed to be stable, at least during the 8 seconds of recording corresponding to 240 forcing periods. Depending on initial conditions, specifically the impact speed and phase, the droplet locks onto one particular mode. Note that the amplitude of the jumps experienced by modes (2,1) and (3,1) is much larger than the forcing amplitude. Weber numbers at impact are about 0.06, 1.5 and 3.9 for modes (1,1), (2,1) and

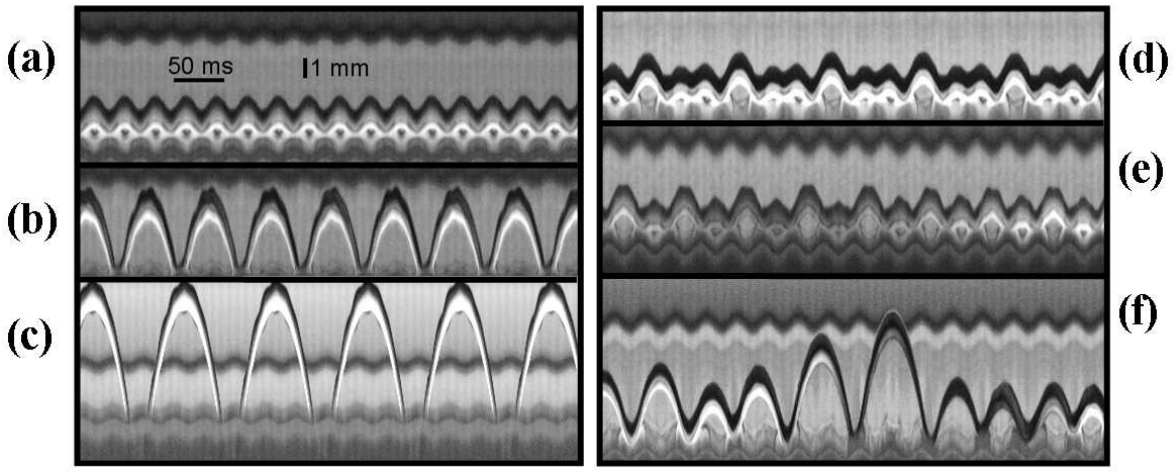

Figure 4.10: Spatiotemporal diagrams of a droplet bouncing on a soap film vibrating at $f = 33$ Hz ($\omega = 1.21$). The dark low-amplitude oscillation at the top of these pictures represents the vertical motion of the ring to which the soap film is pinned. (a) Mode (1,1) at $\Gamma = 0.6$ - $We \simeq 0.06$. (b) Mode (2,1) at $\Gamma = 0.6$ - $We \simeq 1.5$. (c) Mode (3,1) at $\Gamma = 0.6$ - $We \simeq 3.9$. (d) Mode (3,3) at $\Gamma = 0.7$. (e) Period-doubling transition, from mode (1,1) to mode (2,2) at $\Gamma = 1.2$. (f) Chaotic bouncing trajectory at $\Gamma = 1.1$.

(3,1), respectively. According to (4.14), with each bounce these modes lose kinetic energy such that ΔWe is approximately 10^{-3}, 0.16 and 0.67, respectively. For periodic solutions, this energy loss has to be perfectly balanced by the energy input from the forcing. In the following, we shall demonstrate that the same forcing can deliver three different amounts of energy according to the impact phase of the droplet.

We also observed more complex periodic bouncing states, where the periodicity appears only after several jumps ($q > 1$). For example, the mode (3,3), observed at $\Gamma = 0.7$ and $\omega = 1.21$ (Fig. 4.10d), is characterized by three successive jumps of different amplitude. At higher accelerations, a period-doubling transition may occur spontaneously (at fixed forcing parameters), transforming a mode (1,1) into a mode (2,2) as seen in Fig. 4.10(e). Chaotic trajectories are also observed (Fig. 4.10f), with episodic periods of high-amplitude bouncing. The chaotic bouncing is usually unstable and the air film ultimately breaks, typically after a particularly vigorous impact.

The sustained bouncing may be modeled by adding to Eq. (4.31) a fictitious inertial force $Mg\Gamma\cos(2\pi ft + \phi)$, since Newton's law is expressed in a frame moving with the vibrating film. Defining dimensionless variables

$$y = \frac{-kZ}{Mg}, \qquad \tau = \sqrt{\frac{k}{M}}t \quad \text{and} \quad U = \frac{V}{g}\sqrt{\frac{k}{M}} \tag{4.32}$$

yields

$$\ddot{y} + \mathcal{H}(-y)y + 1 = -\frac{4\pi c_T}{c_k} Bo\mathcal{H}(-y)|\dot{y}|\dot{y} + \Gamma\cos(\omega\tau + \phi). \tag{4.33}$$

which may be solved subject to initial conditions $y(0) = 0$ and $\dot{y}(0) = -U$ at impact. The multi-periodicity is observed as in the experiments (Fig. 4.11a). The droplet in the high-energy mode (3,1) lands before that in low-energy mode (1,1), thereby increasing the amount

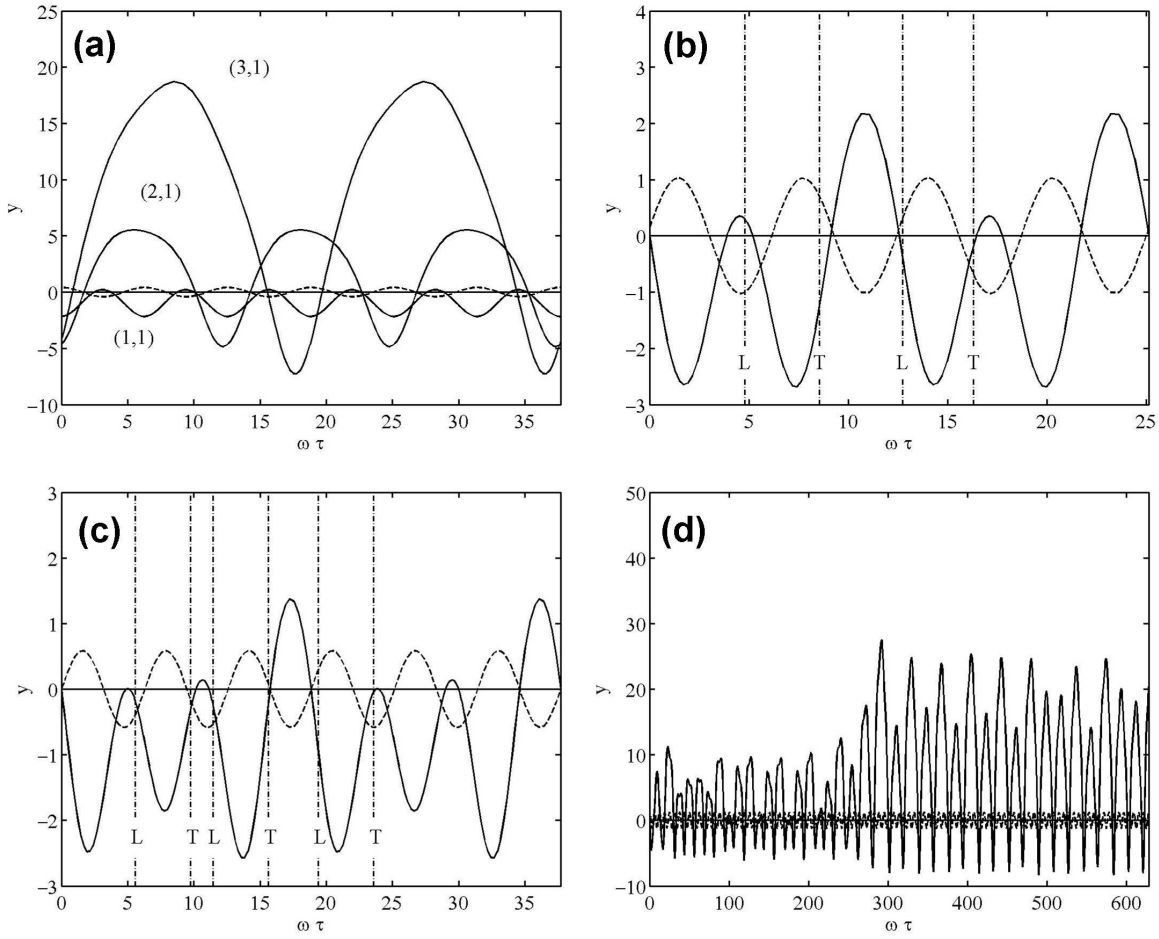

Figure 4.11: Numerical solution of Eq. (4.33) at $\omega = 1.21$. Solid lines correspond to trajectories $y(\omega\tau)$ in the frame of the ring; dashed lines correspond to the ring motion; vertical dash–dotted lines represent the landing (L) and take-off (T) phases measured experimentally. (a) Modes (1,1), (2,1) and (3,1) at $\Gamma = 0.6$. (b) Mode (3,3) at $\Gamma = 0.8545$. (c) Mode (2,2) at $\Gamma = 1.5$. (d) Chaotic bouncing at $\Gamma = 1.82$.

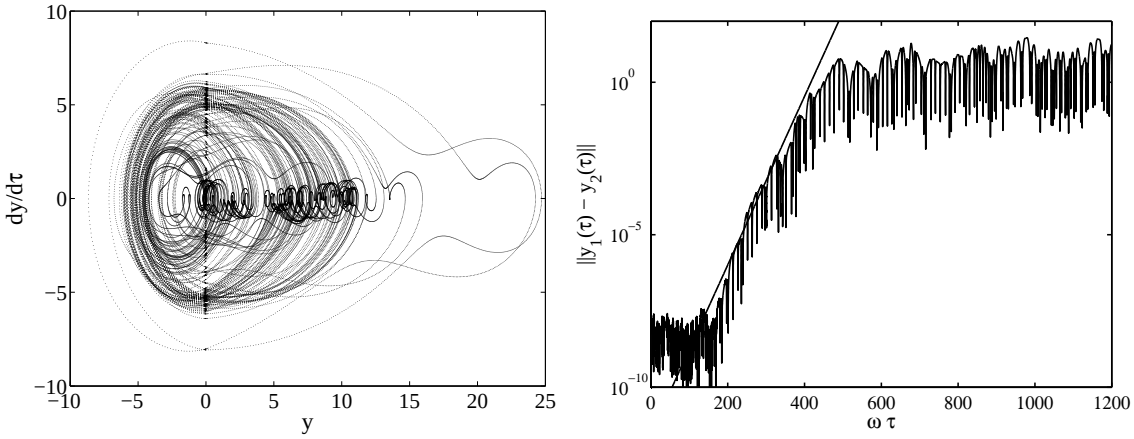

Figure 4.12: Chaotic solutions for $(\Gamma, \omega) = (1.82, 1.21)$. (a) Chaotic attractor in the phase diagram. (b) Positive Lyapunov exponent $\simeq 0.4$. Initially neighboring trajectories diverge exponentially, indicating sensitivity to initial conditions.

of energy extracted during impact. The model also reproduces complex modes (3,3) and (2,2), as seen in Fig. 4.11(b-c). The measured phases of landing and take-off are in good agreement with the model predictions, though these complex modes are not observed at precisely the same forcing parameters as in the experiments. Many other complex periodic solutions are generated by the model for different forcing parameters (Γ, ω) and initial conditions (U, ϕ).

The system (4.33) is similar to that arising from the Duffing equation and the vertically oscillated pendulum [110]; it thus supports chaotic solutions (Fig. 4.11d), as many other bouncing systems [111, 112]. The trajectory rolls up on a strange attractor (Fig. 4.12a) and corresponds to a positive Lyapunov exponent deduced by calculating the rate of exponential divergence of two initially adjacent trajectories (Fig. 4.12b). The model (4.33) exhibits chaos starting from $\Gamma = 1.76$, a value much higher than observed in experiments ($\Gamma = 1.1$). This discrepancy is presumably due to the shortcomings of our simple model for the dissipation in the system; in particular, details of the droplet deformation are not modeled in Eq. (4.33).

We proceed by solving (4.33) with $\omega = 1.21$ fixed for various accelerations $\Gamma \in [0, 2]$ to develop a bifurcation diagram of our system (Fig. 4.13a). Modes (p, q) are represented by q different branches corresponding to the dimensionless impact velocity U of the q different bounces. Many complex bifurcation events appear on the bifurcation diagram, analysis of which is beyond the scope of this thesis. For $\Gamma < 0.18$, no periodic bouncing is possible. $\Gamma_{th}^{(2,1)} = 0.18$ corresponds to the lower bouncing threshold, at which mode $(2, 1)$ appears. At the upper bouncing threshold $\Gamma_{th}^{(1,1)} = 0.47$, the static solution completely disappears and transforms into a periodic bouncing $(1, 1)$. Both thresholds are computed for various forcing frequencies ω (Fig. 4.9), the lower of which is in good agreement with experiments. In particular, the threshold remains roughly constant and less than 0.2 until $\omega = 2$; thereafter, it increases drastically, consistent with the observed absence of bouncing for $\omega \gtrsim 2$. We note that the minimum in the upper threshold curve corresponds to the resonant frequency of the soap film $\omega = 1$, as defined in (4.12). As Γ is increased, the principal modes $(p, 1)$ branch to $(2p, 2)$ states through period-doubling events. The transition to chaos occurs via a number of

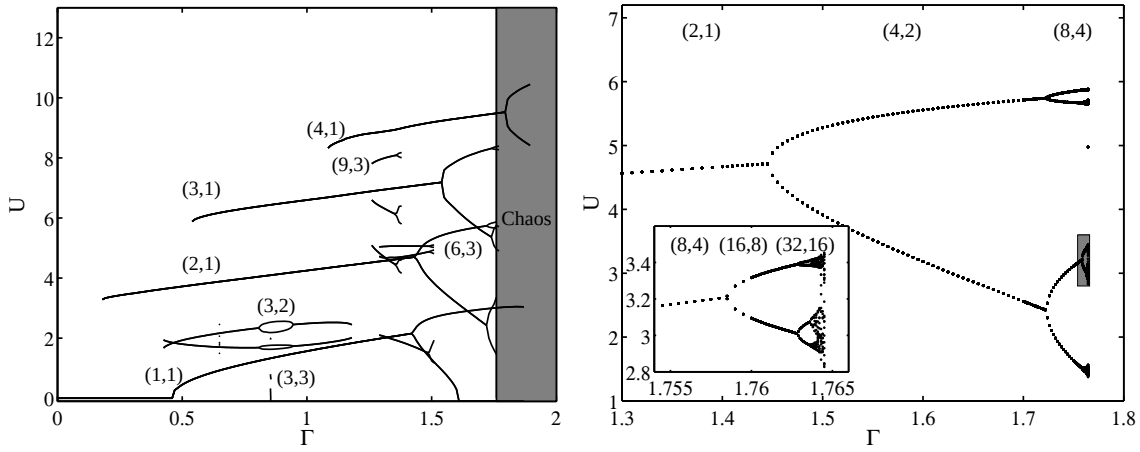

(a) (b)

Figure 4.13: (a) Bifurcation diagram of the impact speed U as a function of Γ for $\omega = 1.21$. Each mode (p, q) is represented by q branches. (b) Period-doubling cascade from mode $(2, 1)$ to mode $(64, 32)$. The cascade converges in $\Gamma = 1.764$ where a chaotic attractor is created. The inset represents a zoom on the shaded region.

such branching events, known as a period-doubling cascade (Fig. 4.13b).

Solutions of (4.33) can be displayed on a Poincaré section made at impact (Fig. 4.14). The net energy ΔK gained by the drop during the ith bounce is computed for each (U, ϕ), and contours of iso-values are plotted. For impact in the grey and white regions, the drop experiences a net energy gain and loss, respectively. On the intervening curve, the energy transferred to the drop precisely balances that dissipated, $\Delta K = 0$. Modes $(p, 1)$ are stationary states in this iterative map corresponding to single points that necessarily fall on this zero contour. Complex modes $q > 1$ are represented by closed circuits of q points, the energy of which necessarily sums to zero. In mode $(3, 3)$, two bounces increase the energy, the velocity and the phase until the droplet leaves the shaded region. The third bounce dissipates energy, thereby restoring the initial conditions of the first bounce. The Poincaré section of the chaotic attractor emerging at $(\Gamma, \omega) = (1.82, 1.21)$ is structured as a spiral-like fractal shape (Fig. 4.14b) in polar coordinates.

4.5 Summary

In this chapter, we have mainly discussed the bouncing mechanisms of a droplet on a soap film. Although this configuration may seem exotic, it is a good start for our investigation of bouncing since the corresponding model is overly simple and accurate. Indeed, the soap film has a negligible inertia and is thus in quasi-static equilibrium; it may be described through a scalar relation between its vertical deformation and the force it exerts on the droplet. By modeling the soap film as the combination of a spheroid and a catenoid, we have succeeded in rationalizing the transition between the bouncing and crossing behaviors at $We_{th} \simeq 16$. For smaller We, the film behaves as a linear spring, the contact time between the bouncing droplet and the film is shown to be independent on the impact velocity. At each bounce, the droplet loses a part ΔWe of its incoming translation energy that increases as $We^{3/2}$.

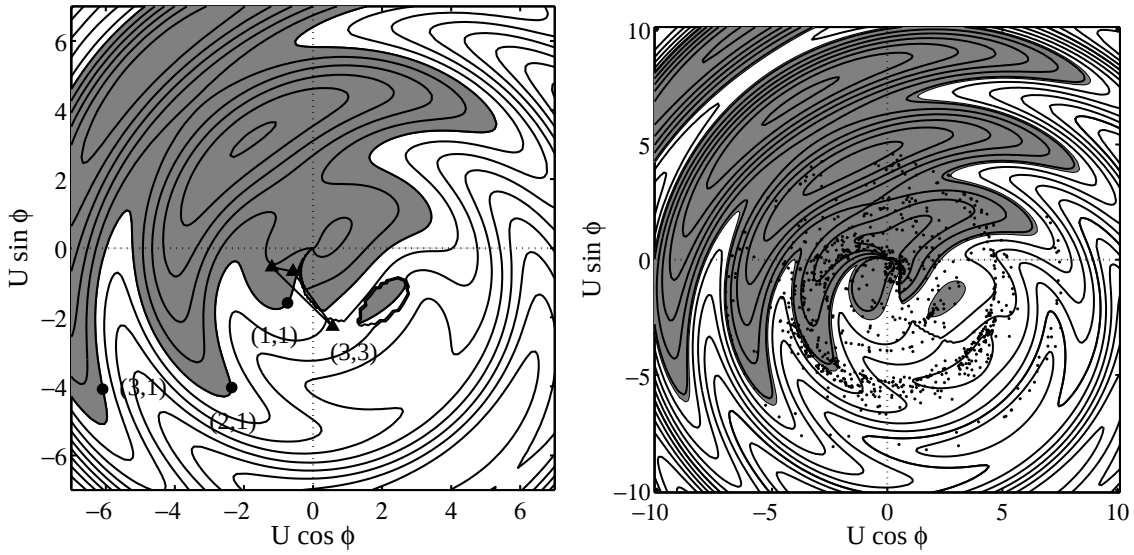

Figure 4.14: Poincaré sections representing the impact parameters (U, ϕ) in polar coordinates, computed from (4.33) with $\omega = 1.21$. Contours correspond to the net energy transferred to the drop during impact. In the shaded area, the droplet gains more energy during impact than it loses to dissipation; in the white area, the opposite occurs. (a) Simple modes ($q = 1$ - •) and complex modes ($q > 1$ - ▲) at $\Gamma = 0.82$. (b) Chaotic attractor at $\Gamma = 1.82$.

Theoretical arguments suggest that this energy is in reality transferred to the vibrational and internal motions of the droplet, before being dissipated through viscous effects. This loss of energy can be balanced by vertically vibrating the soap film, so the droplet bouncing becomes periodic. Multiperiodicity is observed; namely, for a given forcing, the droplet may bounce in several different ways depending on the initial conditions. The droplet adjusts its impact phase in order to extract from the forcing the exact amount of energy to balance its losses. Complex periodic motions (i.e. sequences of several different bounces) and chaotic trajectories are also observed. Experiments are in excellent agreement with the solutions of a single ordinary differential equation of order 2, deduced from the second Newton's law.

Chapter 5

Periodic bouncing on a high-viscosity vibrating bath

In this chapter, we discuss the bouncing mechanisms in a second limit case, probably closer from potential microfluidic applications, namely droplets bouncing on a viscous bath. Here, the bath cannot efficiently store surface energy and the droplet has to bounce by itself. Like in the soap film experiment (Chap. 4), we observe a threshold forcing acceleration Γ_{th} above which sustained bouncing is possible. The threshold measurements from Denis Terwagne and Stéphane Dorbolo [113] are rationalized through a model similar to Eq. (4.33).

5.1 Experimental results : bouncing threshold and droplet deformations

A container is filled with about 8 mm of silicon oil (Dow Corning 200, $\nu = 1000$ cS) and fixed on an electromagnetic shaker that vibrates according to $A\cos 2\pi ft$. Droplets of radius $R \in [0.73, 0.93]$ mm made of a less viscous silicon oil ($\nu \in [0.65, 100]$ cS) are released from a syringe in the vicinity of the bath. The threshold acceleration $\Gamma_{th} = 4\pi^2 Af^2/g$ is measured as described in Chap. 4: droplets are created when $\Gamma > \Gamma_{th}$, then Γ is decreased until coalescence.

The threshold Γ_{th} is measured as a function of the forcing frequency f for various droplet viscosity (Fig. 5.1a). At 100 cS, Γ_{th} monotonically increases with f, starting from $\Gamma_{th} \to 1$ in $f \to 0$. At lower viscosity, regularly spaced extrema are seen on the threshold curve. Bouncing is easier around some specific frequencies, which suggests that the system behaves as a resonating damped oscillator. Viscosity is obviously the damping mechanism, since the extrema disappear at high viscosity. On the other hand, the bouncing seems to be ensured through the droplet deformation. Indeed, as seen in Fig. 5.2, the droplet shape changes as the frequency is increased, we may recognize some of the droplet eigenmodes, i.e. the axisymmetric spherical harmonics Y_ℓ^0 already introduced in Chap. 1. The droplet selects the deformation mode used to bounce as a function of the forcing frequency, and each minimum in the threshold curve $\Gamma_{th}(f)$ corresponds to a mode Y_ℓ^0.

The dispersion relation of capillary waves (1.7) suggests to scale the forcing frequency with the frequency $f_{(2,0)}$ of the spherical harmonic Y_2^0. The droplet is thus seen as a spring of stiffness $k = c_k\sigma$ with $c_k = 32\pi/3$, and the dimensionless frequency writes again $\omega = 2\pi f\sqrt{\frac{M}{k}}$. The thresholds corresponding to different droplet radii collapse on a single curve (Fig. 5.1b).

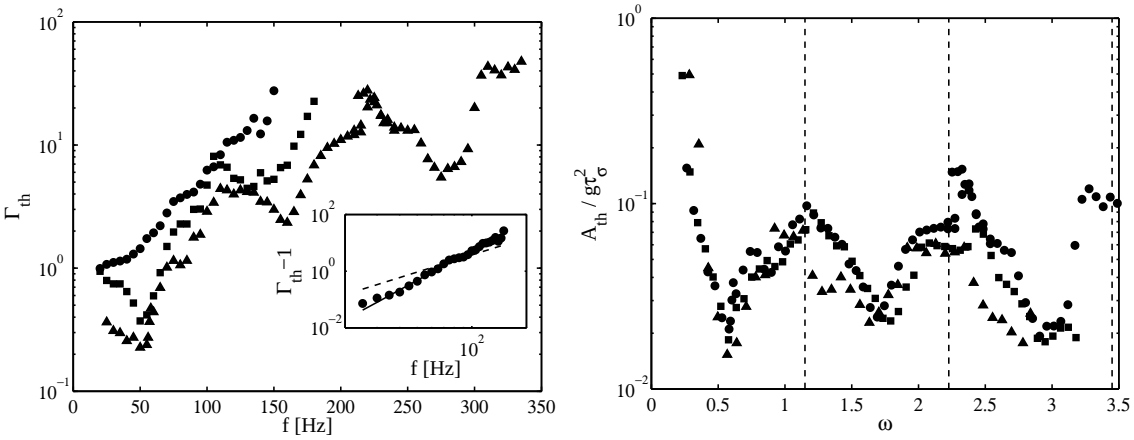

Figure 5.1: (a) Threshold acceleration Γ_{th} as a function of the forcing frequency f for a droplet of $R = 0.765$ mm. (•) $\nu = 1.5$ cS; (■) $\nu = 10$ cS; (▲) $\nu = 100$ cS. The inset represents the threshold curve in logarithmic scale, for $\nu = 100$ cS. The solid (resp. dashed) line is a power law of exponent 3.5 (resp. 2, as proposed in [114]). (b) Normalized threshold amplitude as a function of the dimensionless frequency ω for various droplet sizes ($\nu = 1.5$ cS): (•) $R = 0.765$ mm; (■) $R = 0.812$ mm; (▲) $R = 0.931$ mm. The vertical dashed lines correspond to the droplet natural frequencies (Eq.5.1).

By replacing Γ_{th} by a more appropriate dimensionless number based on the threshold amplitude A_{th}, namely $A_{th}/(g\tau_\sigma^2)$, the extrema are all located at the same dimensionless forcing level, whatever the selected mode.

The dimensionless natural frequencies $\omega_{(\ell,m)} = f_{(\ell,m)}/f_{(2,0)}$ of a droplet floating in microgravity (Eq.1.7) do neither correspond to the minima, nor to the maxima of the threshold curve. Indeed, several authors have already observed that the dispersion relation of capillary waves depends on the considered geometrical configuration, e.g. a droplet placed on a hydrophobic surface vibrated vertically [115, 116] or horizontally [117], a large droplet significantly flattened by gravity [118], or simply a droplet highly deformed in the nonlinear regime [119, 120]. On the other hand, these frequencies $\omega_{(\ell,m)}$ multiplied by a factor 1.15 correspond to the maxima $\omega_M(\ell)$ of the threshold curve,

$$\omega_M^2 = (1.15\omega_{(\ell,m)})^2 = 0.165\ell(\ell-1)(\ell+2). \tag{5.1}$$

Therefore, it is more difficult to make a droplet bounce when forcing the system at one of the droplet natural frequencies. Moreover, the droplet is observed to select the mode Y_ℓ^0 when the forcing frequency ranges in $[\omega_M(\ell-1), \omega_M(\ell)]$. These results may seem contradictory; since the bouncing is due to the droplet deformation, an increased deformation would facilitate the bouncing and the natural frequencies of the droplet should correspond to the minima of the threshold curve. The model developed in the next section explains this apparent paradox.

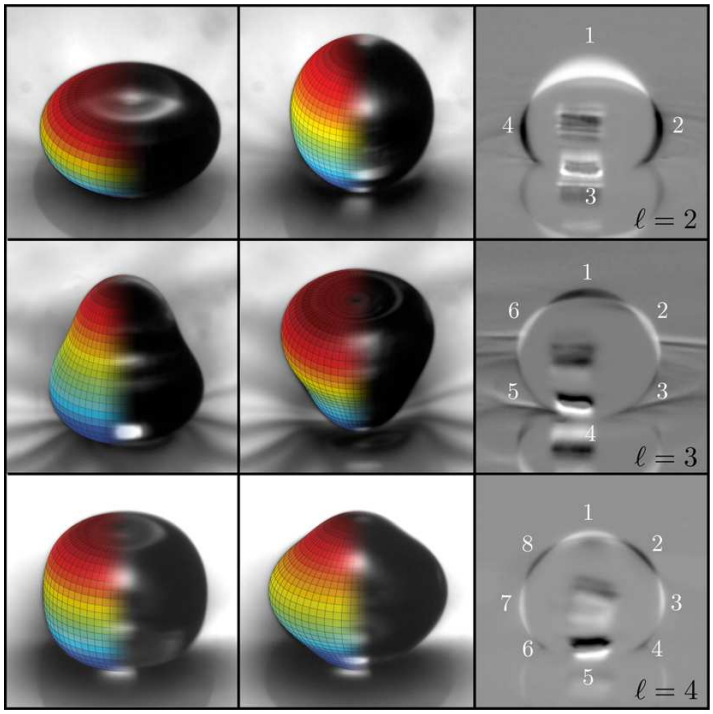

Figure 5.2: Axisymmetric spherical harmonics Y_ℓ^0 observed when a droplet bounces on a vibrated high-viscosity bath. The ellipsoidal mode Y_2^0 is obtained at $f = 50$ Hz and $\Gamma = 0.3$; the mode Y_3^0 at $f = 160$ Hz and $\Gamma = 2$; and the mode Y_4^0 at $f = 275$ Hz and $\Gamma = 6$. Modes are better recognized in the third column, corresponding to the difference between images from both firsts.

5.2 Modeling the bouncing on a bath

5.2.1 The model of Couder

The first modeling of the sustained bouncing of a droplet on a vertically vibrating bath was proposed by Couder and coworkers in 2005 [114]. These authors have studied the bouncing of highly viscous droplets ($\nu = 500$ cS) on a bath made of the same liquid. They suggest the following mechanism [1]:

Stability requires that the air film resists squeezing during the half period of upward motion and that, during the downward half period, air has time to penetrate the film to allow lift-off. We must thus consider the dynamics of the thin air film, and seek if it can sustain the drop bouncing and be renewed. At a given time the thickness of this film is h and its radius r_L. In the following, we assume that the viscosity of the liquid μ is much larger than that of air μ_a, so that the airflow does not entrain the liquid. At the drop landing, the film of air resists squeezing only when a viscous regime is reached, i.e. the Reynolds number becomes small enough: $Re = \rho_a h^2 f/\mu_a < Re_{th}$, with ρ_a and μ_a being the density and viscosity of air. This condition sets a scale for a typical film thickness h. Reynolds lubrication theory shows that the film resists squeezing with a force of magnitude $F_L \sim \mu_a r_L^4 f/h^2$ (using the vibration period as a time scale). Let M be the drop mass and Γ the imposed acceleration. At landing the balance of forces gives $-Mg + F_L = Mg\Gamma$, and at lift-off $Mg + F_L = Mg\Gamma$. The lift-off condition being more restrictive determines the critical acceleration Γ_{th} needed for bouncing (using the scale for the film thickness found above):

$$\Gamma_{th} = 1 + \frac{1}{Re_{th}} \frac{\rho_a}{\rho} \frac{r_L^4}{R^3} f^2. \tag{5.2}$$

Qualitatively, this means that a larger acceleration is needed to squeeze or fill the air film at a higher frequency or for a more extended film. [...]

The model correctly describes several experimental observations; e.g. for viscous droplets, the threshold $\Gamma_{th}(f)$ increases monotonically with the forcing frequency starting from $\Gamma_{th}(0) = 1$. Nevertheless, it has some major shortcomings that are addressed in the following section.

1. The power law $\Gamma_{th} - 1 \sim f^2$ is approximately correct for 500 cS droplets on a 500 cS bath, but it is already not valid anymore for 100 cS droplets on a 1000 cS bath (inset of Fig. 5.1a) where the exponent of the power law is closer to 3.5.

2. Neither the viscosity nor the surface tension and the deformation of the droplet are taken into account. So the model cannot catch the bouncing physics of less viscous droplets.

3. The force balance is only written at a given instant, namely the take-off, so the whole trajectory cannot be computed.

4. The choice of that Reynolds number to estimate the typical film thickness may be contested. Indeed, it is based on the vertical velocity of the droplet, of the order of $h \cdot f$. Another (maybe better) choice would have been the horizontal drainage velocity of the air film, which is about $R \cdot f \gg h \cdot f$ and leads to the scaling $\Gamma_{th} - 1 \sim f^3$.

[1] Notations have been adapted from the original manuscript in order to be coherent with our notations.

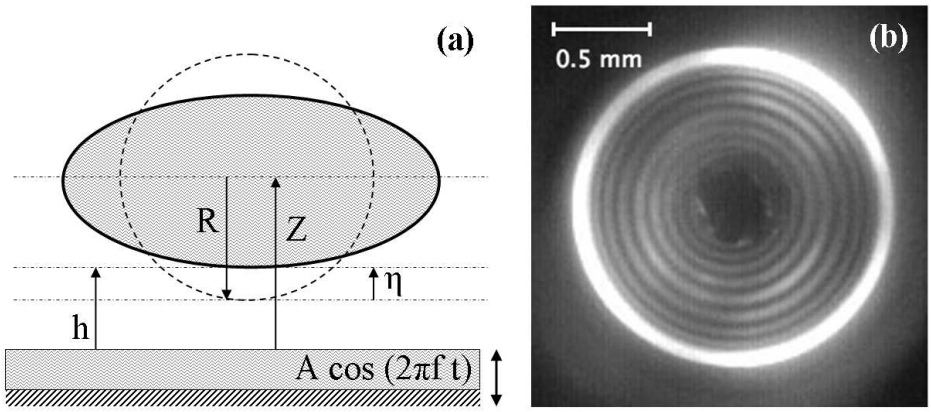

Figure 5.3: (a) Geometrical variables: R is the radius of the undeformed droplet, η is its vertical deformation about the axis of symmetry, h is the thickness of the intervening air film and Z is the position of the droplet mass center relative to the bath. (b) Interference fringes observed through the thin air layer when the droplet is lightened by a monochromatic light.

5.2.2 Taking the droplet deformation into account

The proposed model [121] consists in two differential equations, one describing the motion of the droplet center of mass (vertical position Z, as for the soap film), and one for the droplet vertical deformation η. The droplet is supposed to select the Y_2^0 ellipsoidal mode (Fig. 5.3a); the bath deformation is neglected. During its flight, the droplet experiences the apparent gravity $Mg(\Gamma \cos 2\pi ft - 1)$ in the frame of the vibrating bath. The air layer is described through the lubrication theory; a vertical lubrication force F_L is applied on the droplet. The deformations are responsible for micro-flows within the droplet that may help the air drainage and modify the resulting F_L. At leading order, the drainage is considered as a Poiseuille-Couette flow between two parallel plane interfaces. The bottom interface (bath) is at rest, while the top interface moves with a velocity proportional to $\dot{\eta}r/R$, where r is the radial horizontal coordinate (cylindrical). Calculations (App. D) yield

$$F_L = c_{L1}\mu_a R^4 \left(c_{L2}\frac{\dot{\eta}}{h^2 R} - \frac{\dot{h}}{h^3} \right), \tag{5.3}$$

where c_{L1} and c_{L2} are positive constants. The lubrication theory suggests that $c_{L1} = 3\pi/2$. On the other hand, the parameter c_{L2}, representing the effect of deformation on drainage, cannot be estimated through simple arguments.

The second Newton's law in a frame moving with the bath writes

$$M\ddot{Z} = Mg\left(\Gamma \cos 2\pi ft - 1 \right) + F_L. \tag{5.4}$$

For practical purposes, we use the thickness of the air layer $h = Z - R - \eta$ instead of Z. The evolution of η is prescribed by an energy balance in the frame of the mass center of the droplet,

$$\frac{\mathrm{d}(K + E_\sigma)}{\mathrm{d}t} = -P_D - \dot{\eta} F_L, \tag{5.5}$$

where K is here the kinetic energy of the motion inside the droplet, E_σ is the interfacial energy and P_D is the viscous dissipative power inside the droplet. In order to close the system, variables K, E_σ and P_D must be estimated as functions of η. Scaling arguments yield

$$K = c_K M \frac{\dot{\eta}^2}{2}, \quad E_\sigma = c_\sigma \sigma \frac{\eta^2}{2}, \quad P_D = c_D \nu M \frac{\dot{\eta}^2}{R^2}, \tag{5.6}$$

where constants c_K, c_σ and c_D depend on the flow inside the droplet. For example, the potential flow related to the spherical harmonic Y_2^0 leads to $c_K = 3/10$, $c_\sigma = 16\pi/5$ and $c_D = 3$, so $c_k = c_\sigma / c_K$ (App. C).

The whole system is written in dimensionless form by using

$$y = \frac{k}{Mg} h, \qquad x = \frac{k}{Mg} \eta \quad \text{and} \quad \tau = \sqrt{\frac{k}{M}} t. \tag{5.7}$$

$$\begin{cases} \ddot{x} + \ddot{y} = \Gamma \cos \omega\tau - 1 + \dfrac{F_L}{Mg}, \\ c_K \ddot{x} + c_D \sqrt{\dfrac{4\pi}{3c_k}} Oh \dot{x} + \dfrac{c_\sigma}{c_k} x = -\dfrac{F_L}{Mg}, \\ \dfrac{F_L}{Mg} = \dfrac{\sqrt{3}}{(4\pi)^{7/2}} c_k^{5/2} c_{L1} \dfrac{\mu_a}{\mu} \dfrac{Oh}{Bo^3} \left(4\pi \dfrac{c_{L2}}{c_k} Bo \dfrac{\dot{x}}{y^2} - \dfrac{\dot{y}}{y^3} \right). \end{cases} \tag{5.8}$$

Moreover, the second equation is replaced by the sum of both first in order to remove the lubrication term.

$$\begin{cases} \ddot{x} + \ddot{y} = \Gamma \cos \omega t - 1 + \dfrac{\sqrt{3}}{(4\pi)^{7/2}} c_k^{5/2} c_{L1} \dfrac{\mu_a}{\mu} \dfrac{Oh}{Bo^3} \left(4\pi \dfrac{c_{L2}}{c_k} Bo \dfrac{\dot{x}}{y^2} - \dfrac{\dot{y}}{y^3} \right), \\ (c_K + 1) \ddot{x} + c_D \sqrt{\dfrac{4\pi}{3c_k}} Oh \dot{x} + \dfrac{c_\sigma}{c_k} x = \Gamma \cos \omega\tau - 1 - \ddot{y}. \end{cases} \tag{5.9}$$

Terwagne *et al.* [122] observed the dynamics of the air film located between the droplet and the bath using a monochromatic light. Concentric fringes of interference appear when the air film is squeezed (Fig. 5.3b). When the droplet bounces, the motion of the fringes is perfectly periodic. No attenuation or phase drift take place and the bouncing is stationary. On the other hand, the number of fringes decreases when the droplet does not bounce; the film thins and finally breaks, leading to coalescence. The periodicity of the fringes motion suggests periodic solutions from Eq. (5.9). Conditions for such solutions are obtained by integrating Eq. (5.9) over a period $2\pi/\omega$. Under the assumption of periodicity, many terms vanish, giving

$$\int_0^{2\pi/\omega} x \mathrm{d}\tau = -\frac{2\pi}{\omega} \frac{c_k}{c_\sigma} \quad \text{and} \quad c_{L2} \int_0^{2\pi/\omega} \frac{\dot{x}}{y^2} \mathrm{d}\tau = \frac{64\pi^{7/2}}{\sqrt{3} c_{L1} c_k^{3/2}} \frac{\mu}{\mu_a} \frac{Bo^2}{Oh\omega}. \tag{5.10}$$

Terms on the right-hand side are always strictly positive. According to the first relation, a mechanism of potential energy storage (here, the droplet deformation) should be taken into account ($x \neq 0$). The droplet has to spend more time in an oblate state ($x < 0$) than in a prolate state ($x > 0$). According to the second equation, internal movements in the liquid phase, related to the deformation rate, must have a significant influence on the film drainage and the resulting lubrication force ($c_{L2} \neq 0$). Moreover, a significant phase shift between the minimum film thickness and the maximum compression must be observed.

Indeed, $\int_0^{2\pi/\omega} \dot{x} dt = 0$, while $1/y^2$ is strictly positive and vanishes when the film thickens. To have a positive left hand side in the second equation, we expect the film to be the thinnest when the droplet begins to recover its spherical shape ($\dot{x} > 0$). All these required conditions show us that this model is minimal: if the model does not take into account all above listed conditions, its prediction fails and no periodic bouncing solutions can be found.

We proceed by computing typical trajectories of this model, for an oil droplet ($R = 0.8$ mm, $\nu = 50$ cS, $\sigma = 20$ mN/m) released on a bath at $f = 50$ Hz. The various coefficients are obtained through a fitting procedure detailed here after. Experiments suggest a coalescence at $\Gamma = 0.5$ and a sustained bouncing at $\Gamma = 1.5$. These observations are well-rendered by the model (Fig. 5.4a-d). Below the bouncing threshold ($\Gamma = 0.5$ - Fig. 5.4a-b), the droplet deformation x and film thickness y (in log scale) oscillate sinusoidally and in-phase. The dimensional thickness corresponding to y ranges in [0.1,1] μm, which foretells a near coalescence: the air film is not fully regenerated and its mean thickness significantly decreases on the long run. Above the threshold ($\Gamma = 1.5$ - Fig. 5.4c-d), the deformation is not sinusoidal anymore, and the film thickness reaches about 100 μm every period. The droplet is seen to take-off and the motion is perfectly periodic. On the phase diagram (y, x), the trajectory at $\Gamma = 0.5$ consists in a series of quasi-parallel straight lines (y and x are in-phase), while a limit cycle appears at $\Gamma = 1.5$.

The acceleration threshold Γ_{th} required for periodic bouncing may be estimated starting from Eq. (5.9). When $\Gamma < \Gamma_{th}$, the droplet does not bounce, the air film remains thin and $\ddot{y} \ll 1$. The second equation in Eq. (5.9) does not depend on y anymore. The droplet behaves as a simple forced oscillator

$$x(\tau) = G\Gamma \cos(\omega t + \phi) - \frac{c_k}{c_\sigma} \tag{5.11}$$

where G and ϕ are functions of ω defined as

$$\begin{cases} G^{-2} = \left[\dfrac{c_\sigma}{c_k} - (c_K + 1)\omega^2\right]^2 + \dfrac{4\pi}{3c_k} c_D^2 Oh^2 \omega^2, \\ \tan\phi = c_D \sqrt{\dfrac{4\pi}{3c_k}} \dfrac{Oh\omega}{(c_K+1)\omega^2 - \frac{c_\sigma}{c_k}}. \end{cases} \tag{5.12}$$

The resonance frequency related to this oscillator is given by

$$\omega_{res}^2 = \frac{c_\sigma}{c_k(c_K+1)} \left[1 - \frac{2\pi c_D^2}{3c_\sigma(c_K+1)} Oh^2\right]. \tag{5.13}$$

To find y with the first equation of Eq. (5.9), it is convenient to define the amplitude $Y(\tau)$ of its variation (i.e. the short-term average) as

$$y(\tau) = Y(\tau) \mathrm{e}^{4\pi \frac{c_{L2}}{c_k} Bo G\Gamma \cos(\omega t + \phi)}. \tag{5.14}$$

Calculations yield

$$\begin{aligned} \sqrt{\frac{3}{(4\pi)^7}} c_{L1} c_k^{5/2} \frac{\mu_a}{\mu} \frac{Oh}{Bo^3} \frac{\dot{Y}}{Y^3} &= \left\{ G\Gamma \left[\left(\frac{c_\sigma}{c_k} - c_K\omega^2\right) \cos(\omega t + \phi) \right.\right. \\ &- \left.\left. c_D \sqrt{\frac{4\pi}{3c_k}} Oh\omega \sin(\omega t + \phi) \right] - 1 \right\} \mathrm{e}^{8\pi \frac{c_{L2}}{c_k} Bo G\Gamma \cos(\omega t + \phi)} \end{aligned} \tag{5.15}$$

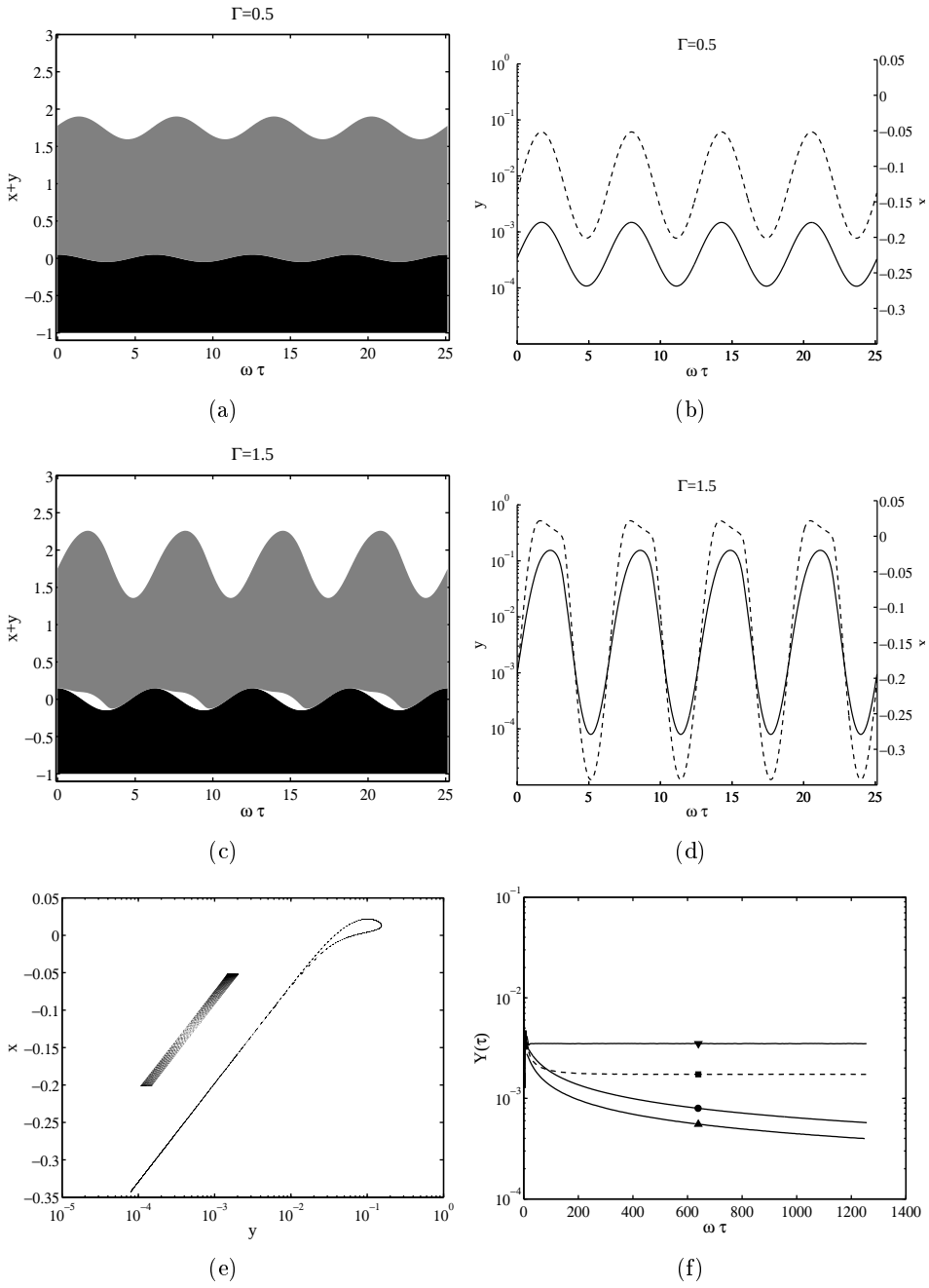

Figure 5.4: Droplet trajectory obtained by numerically integrating Eq. (5.9). Physical parameters are $R = 0.8$ mm, $\nu = 50$ cS, $\sigma = 20$ mN/m and $f = 50$ Hz. (a-b) The droplet does not bounce and the film thins at $\Gamma = 0.5$. (c-d) The droplet bounces periodically at $\Gamma = 1.5$. (a-c) The solid line is the film thickness y and the dashed line is the droplet deformation x, both as functions of time τ. (e) Phase diagram (y, x) on which trajectories at $\Gamma = 0.5$ (left) and $\Gamma = 1.5$ (right) are plotted. (f) Evolution of the short-term averaged thickness of the air layer $Y(\tau)$. The dashed line corresponds to the bouncing threshold. (●) $\Gamma = 0$, (▲) $\Gamma = 0.5$, (■) $\Gamma = 1.1$, (▼) $\Gamma = 1.5$.

By integrating this equation over a long time τ and by only keeping secular terms, we obtain:

$$Y(\tau) = \left[Y(0)^{-2} - 2\sqrt{\frac{(4\pi)^7}{3}} \frac{1}{c_{L1} c_k^{5/2}} \frac{\mu}{\mu_a} \frac{Bo^3}{Oh} C\tau \right]^{-1/2}, \tag{5.16}$$

where the function $C(\Gamma, \omega)$ is defined as

$$\begin{cases} C = \left(\dfrac{c_\sigma}{c_k} - c_K \omega^2 \right) G\Gamma I_1 \left(8\pi \dfrac{c_{L2}}{c_k} BoG\Gamma \right) - I_0 \left(8\pi \dfrac{c_{L2}}{c_k} BoG\Gamma \right), \\ I_j(x) = \dfrac{1}{\pi} \displaystyle\int_0^\pi \mathrm{e}^{x \cos t} \cos(jt) \mathrm{d}t. \end{cases} \tag{5.17}$$

When $C < 0$, the averaged film thickness Y decreases with time and the droplet finally coalesces. Conversely, when $C > 0$, Y diverges and the solution is not longer valid. The droplet takes off, $\ddot{y}$ cannot be neglected anymore in Eq. (5.9) and bouncing occurs. The threshold acceleration for bouncing Γ_{th} can thus be defined as the value of Γ such that $C = 0$.

$$\left(\frac{c_\sigma}{c_k} - c_K \omega^2 \right) G\Gamma_{th} I_1 \left(\frac{8\pi c_{L2}}{c_k} BoG\Gamma_{th} \right) = I_0 \left(\frac{8\pi c_{L2}}{c_k} BoG\Gamma_{th} \right). \tag{5.18}$$

This equation has one positive solution when $c_\sigma - c_K c_k \omega^2 > 0$, and no solution in the other case. There is a cut-off frequency

$$\omega_{co}^2 = \frac{c_\sigma}{c_k c_K} \tag{5.19}$$

above which the model cannot predict bouncing based on the deformation mode Y_2^0 (C is always negative). This frequency corresponds to the natural resonance $\omega_M(\ell = 2)$ of the droplet (Eq.5.1), and to the first maximum of the $\Gamma_{th}(\omega)$ curve (Fig. 5.1b). Beyond ω_{co}, the droplet does not select the mode Y_2^0 anymore. The cut-off frequency is always higher than ω_{res}, which may be seen as the resonance frequency of the system "droplet + air film" and the first minimum of Fig. 5.1(b). This minimum is shown to disappear when ω_{res} is complex, i.e. when $Oh^2 > 3c_\sigma(c_K + 1)/(2\pi c_D^2)$ which corresponds to high viscosity, as observed experimentally. At this stage, I would like to thank the first of my faithful and careful readers by offering him a billion of freshly handled 1 nL droplets of a delicious Belgian beer, provided he can reconstruct by heart the model from the beginning to this point. Finally, as in Couder's model, the predicted threshold curve $\Gamma_{th}(\omega)$ tends asymptotically to a constant value > 1 when $\omega \to 0$.

In order to compare the model predictions to the experimental data shown in Fig. 5.5, a single fit has been made on coefficients c_{L2} and c_K, while the nominal value of mode Y_2^0 is taken for other coefficients, namely $c_\sigma = 16\pi/5$, $c_k = 32\pi/3$ and $c_D = 3$. The coefficients resulting from the fitting procedure are $c_{L2} \simeq 17.5$ and $c_K \simeq 0.1$. The comparison with experiments is acceptable, both qualitatively and quantitatively. In particular, the minima for low viscosities and the divergence for high frequencies are reproduced. According to the fit, $\omega_{res} = 0.52$, which perfectly corresponds to the first minimum of Fig. 5.1(b). Nevertheless, there are some significant discrepancies between the model and experiments. First, the value of c_K obtained through fitting is much lower than predicted by theory ($c_K = 0.3$). And second, the predicted cut-off at $\omega_{co} = 1.73$ is far beyond the first maximum of Fig. 5.1(b). These shortcomings might be due to several reasons: The experimental threshold is very sensitive to the droplet size, which is not systematically measured. Moreover, the model only takes mode Y_2^0 into account and supposes that the droplet deformation is symmetric with respect to the mid-horizontal plane.

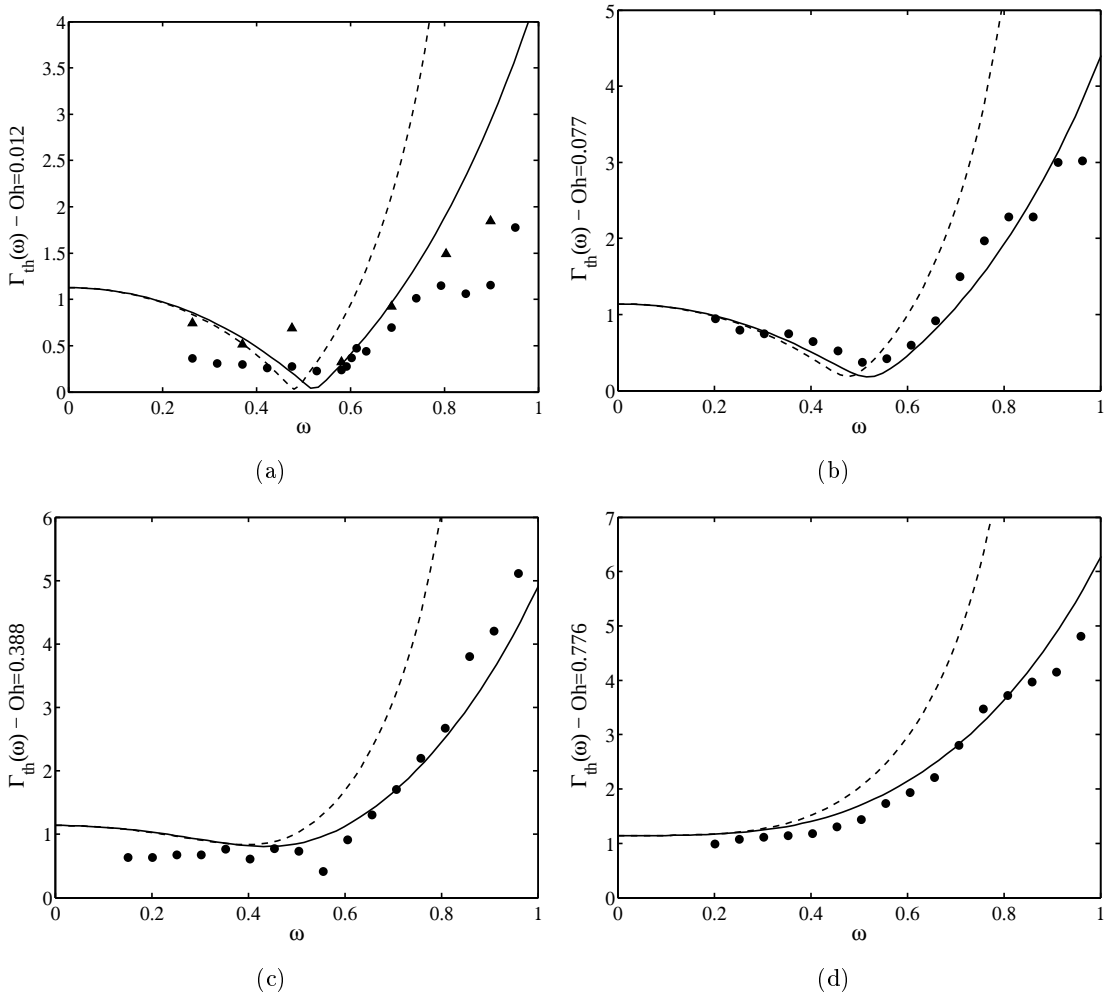

Figure 5.5: Acceleration threshold $\Gamma_{th}(\omega)$ for droplets of $R = 0.765$ mm and various viscosities, i.e Ohnesorge numbers: (a) $Oh = 0.012$, (b) $Oh = 0.077$, (c) $Oh = 0.388$ and (d) $Oh = 0.776$. For $Oh = 0.012$, thresholds are different according to whether the acceleration is increased (▲) or decreased (●). The solid (resp. dashed) line corresponds to the model prediction (5.18) with the fitting value $c_K = 0.1$ (resp. the theoretical value $c_K = 0.3$).

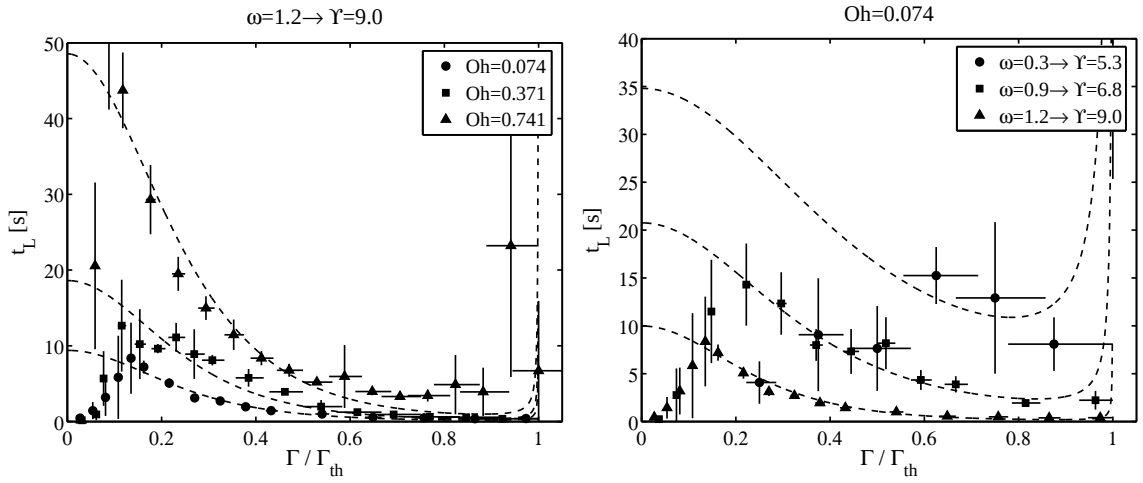

(a) (b)

Figure 5.6: Lifetime t_L of bouncing droplets of radius $R = 0.84$ mm as a function of the normalized acceleration Γ/Γ_{th}, (a) for various viscosities and (b) forcing frequencies. The dashed curves correspond to Eq. (5.22).

5.3 Delayed coalescence below the bouncing threshold

Although droplets cannot bounce periodically when $\Gamma < \Gamma_{th}$, their lifetime t_L seems to be significantly increased by the vibration [123]. Indeed, droplets on under-vibrated bath may float for near to a minute while they last a few tenths of seconds on a static bath. Surprisingly, the lifetime is observed to be important for small Γ and to decrease with increasing Γ, until increasing again and diverging when $\Gamma \to \Gamma_{th}$ (Fig. 5.6). Moreover, the dispersion of measurements is important for small Γ, while the lifetime seems more reproducible at larger Γ. We proceed by rationalizing these observations thanks to the model (5.9) developed in the previous section.

First, for practical purpose, we define the function $\Upsilon(\omega) = 8\pi\frac{c_{L2}}{c_k}BoG\Gamma_{th}$ and write

$$\left(\frac{c_\sigma}{c_k} - c_K\omega^2\right)\frac{c_k}{8\pi c_{L2}Bo}\Upsilon I_1(\Upsilon) = I_0(\Upsilon), \tag{5.20}$$

so

$$C = \frac{I_0(\Upsilon)}{I_1(\Upsilon)}\frac{\Gamma}{\Gamma_{th}}I_1\left(\Upsilon\frac{\Gamma}{\Gamma_{th}}\right) - I_0\left(\Upsilon\frac{\Gamma}{\Gamma_{th}}\right). \tag{5.21}$$

In this mathematical expression of C, the frequency information is fully contained in Υ and the forcing acceleration is always compared to the threshold Γ_{th}.

Now, suppose that the air film breaks in at time t_L such as $Y = Y_{th}$. Then, Eq. (5.16) yields

$$t_L = -\frac{t_0}{C} \tag{5.22}$$

where t_0 is the hypothetic lifetime at $\Gamma = 0$ ($C = -1$). Equation (5.22) is fitted on the experimental curves of Fig. 5.6 thanks to this single fitting parameter t_L. The agreement is good, especially for the deterministic part of the data. The model correctly catches the variations of t_L with the forcing parameters Γ and ω. The influence of other droplet-related factors is unfortunately hidden in t_0.

5.4 Summary

In this chapter, we have discussed the bouncing of droplets on a high-viscosity bath. Contrary to the bouncing on a soap film, the droplet deformation is shown to play a key role in this case. Different natural modes of the droplets (spherical harmonics) can be excited depending on the forcing frequency. The threshold in forcing acceleration Γ_{th} is shown to be maximum when the system is excited at one of the natural frequencies of the droplet, while it is minimum in between these frequencies. The model we have proposed is based on two differential equations, the first being the Newton law applied to the droplet mass center (like for the soap film) and the other describing the droplet deformation. The model predictions are in good agreement with the experiments in the range of frequency covered by the spherical harmonic Y_2^0. In particular, the model correctly reproduces the transition from the film thinning regime (that leads to coalescence) to the periodic bouncing regime (that prevents coalescence). The threshold Γ_{th} obeys to an implicit equation, the solution of which fits well the experimental data. A minimum in Γ_{th} (and so in the energy to provide for the droplet through the forcing) is observed at the same frequency as in experiments. It corresponds to a resonance of the system "air layer + droplet" where the incoming energy is efficiently used to make the droplet bounce. On the other hand, a divergence is predicted when the forcing frequency corresponds to the natural frequency of the droplet alone. In that case, the energy is fully absorbed by the droplet deformation. The model suggests that bouncing is not possible anymore in mode Y_2^0 when this frequency is exceeded. Finally, it gives an accurate picture of the lifetime experienced by droplets before coalescence when the forcing is below the threshold. The main shortcoming of the proposed model is that it only takes the mode Y_2^0 into account, while other deformation modes are observed at higher frequency.

Chapter 6

Movements and interactions on a vibrated bath

At this stage, we are able to maintain droplets for hours in a bouncing configuration onto a vibrated liquid bath. The next step in our approach of handling is to move these droplets horizontally on the bath surface, or more specifically to make them move by themselves. In other words, we need to break the horizontal symmetry of the bouncing mechanism. There are two different ways to achieve this goal, depending on what is deformed: the droplet (rollers) or the bath (walkers). Both motions are discussed here below. The walkers have some very interesting interaction properties that are especially studied on a statistical point of view.

6.1 The rollers

As noted in the previous chapter, a low viscosity droplet makes use of its deformation in order to bounce on a high viscosity bath. The deformation is expressed in terms of spherical harmonics Y_ℓ^m, which are axisymmetric when $m = 0$. Depending on the forcing frequency, the droplet selects a specific deformation mode. As seen in Eq. (1.7), for a droplet in free-fall, the natural frequency $f_{(\ell,m)}$ of the mode Y_ℓ^m only depends on ℓ, not on m. This degeneracy is observed to break down when the droplet bounces. For example, modes Y_2^0 and Y_2^1 are excited on distinct frequency ranges. The Y_2^1 mode is preferentially selected when the frequency is close to the first maximum $\omega \simeq 1$ in the threshold curve (Fig. 5.1), i.e. between about 100 Hz and 140 Hz for droplets of radius 0.765 mm. The asymmetric motion of droplets in the Y_2^1 mode makes them roll on the bath surface (Fig. 6.1a), which gives birth to a slight but robust horizontal translation perpendicular to the rotation axis. These self-propelled droplets are called rollers.

The roller velocity v_r has been measured for various forcing parameters (Γ,f). Data roughly collapse on a single curve (Fig. 6.1b), whose equation is determined empirically

$$v_r = 0.82(A - A_{th})(f - f_0), \tag{6.1}$$

where A_{th} is the threshold amplitude given by $\Gamma_{th} g/(4\pi^2 f^2)$ and $f_0 \simeq 103$ Hz is the lowest frequency for which rollers are observed.

On a flat bath, the roller trajectory is a straight line whose direction is selected initially. The trajectory is sensitive to bath deformations. For example, due to the meniscus, roller droplets bounce back on the bath walls. They can therefore be guided between two parallel

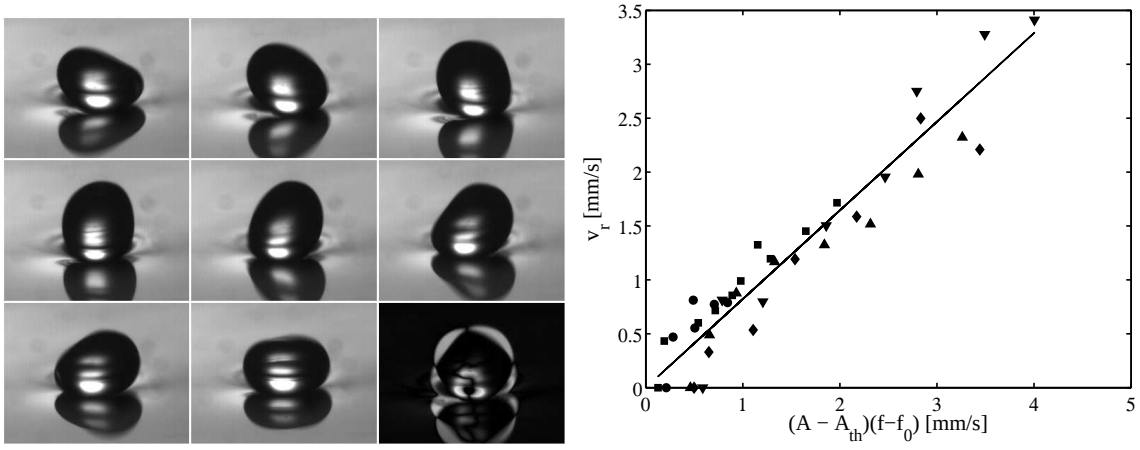

(a) (b)

Figure 6.1: (a) At $f = 115$ Hz and $\Gamma = 4.5 > \Gamma_{th}$, a droplet of radius $R = 0.765$ mm deforms asymmetrically and rolls on the bath surface. The spherical harmonic Y_2^1 is clearly identified on the last snapshot, corresponding to the subtraction between the images 1 and 6. (b) Horizontal velocity of the roller droplet as a function of the forcing parameters. The solid line corresponds to Eq. (6.1).

walls forming a channel. Since each droplet makes a slight hollow on the bath surface, the rollers are also attracted by each other, which may promote their coalescence. Both guiding and attraction are interesting operations for potential droplet handling.

6.2 The walkers

On a low viscosity bath (typically 50 cS or less), the bouncing is also ensured by the bath deformation. Couder and coworkers [124] have shown that under specific conditions, a symmetry breaking can also set the droplet into a permanent horizontal motion. Indeed, the impact deflects the bath surface and a capillary wave is emitted (Fig. 6.2a). At next bounce, the droplet may thus fall on the slope of the wave it has previously created, which gives it a small horizontal impulse (Fig. 6.2b); the droplet turns into a walker.

A vertically vibrated bath is subject to the Faraday instability [125, 126, 127] when the forcing acceleration is higher than a threshold value Γ_F [128, 129, 130]. Below this threshold, capillary waves are quickly damped while above Γ_F, a pattern of standing capillary waves covers the bath surface (Fig. 6.2c). The frequency of these waves is half the forcing frequency (App. F).

As Γ_F is approached from below, the damping factor of capillary waves progressively vanishes and emitted waves propagate over a longer distance. For this reason, the walking droplets are observed just below the Faraday threshold. Indeed, their horizontal impulse comes from the waves they have emitted on the bath at the previous bounce. These waves must not have been damped meanwhile. Couder's team [131, 76] has located the range of physical parameters (Γ,f,R,ν) in which walkers are observed (Fig. 6.3a-b).

We investigated the behavior of an assembly of walkers on a bath made of 50 cS silicon oil vibrated at $\Gamma = 4.2$ and $f = 50$ Hz. These experimental conditions are kept through the whole

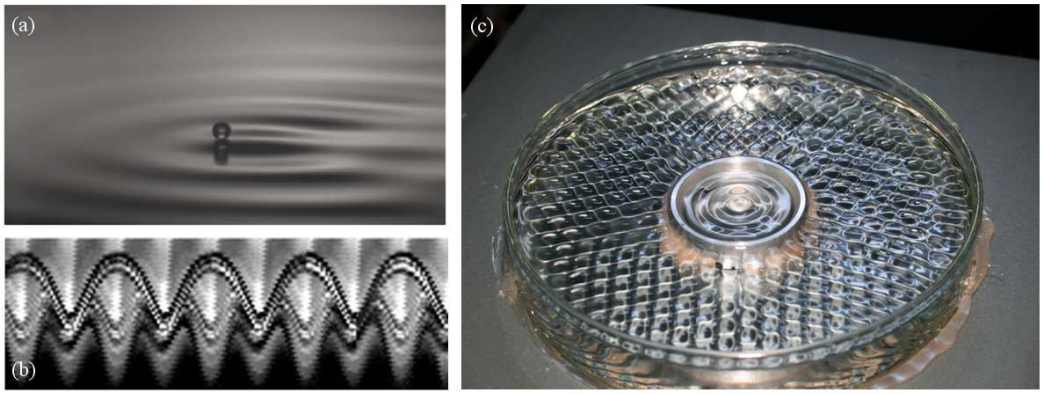

Figure 6.2: (a) A walker bounces on the wave it has created on the bath at previous impact (Credit: S. Protière [76]). (b) Spatiotemporal diagram of a walking droplet (Credit: S. Protière [76]). (c) Standing Faraday waves observed when $\Gamma > \Gamma_F$ (Credit: H. Caps).

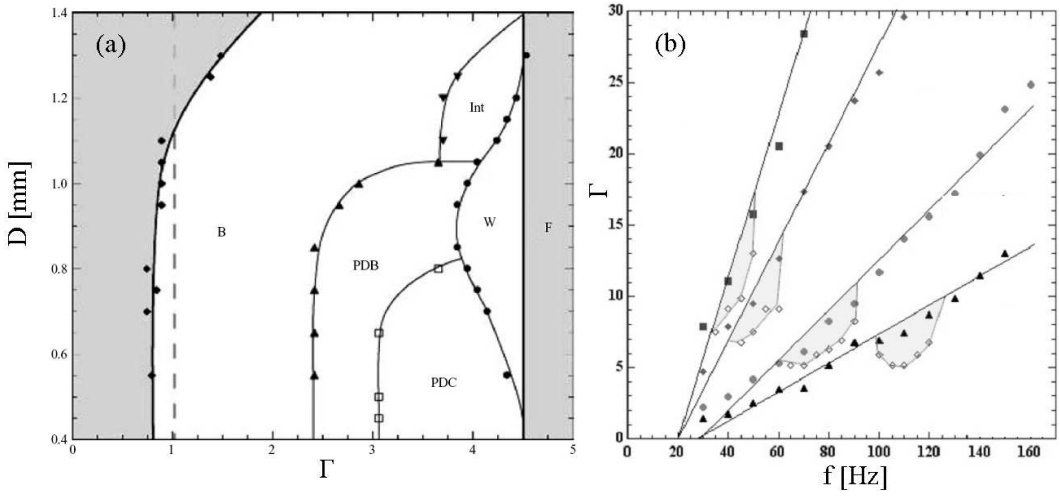

Figure 6.3: Identification of the walker zone in the phase diagrams of the bouncing droplet. (a) In the (Γ, D)-diagram, where $D = 2R$ is the droplet diameter, the walking zone (resp. Faraday instability zone) is indicated by W (resp. F). Other parameters are $f = 50$ Hz and $\nu = 50$ cS. (b) In the (f, Γ)-diagram, the shaded walking zone is slightly under the Faraday threshold (solid line), for various viscosities: (■) $\nu = 100$ cS, (⧫) $\nu = 50$ cS, (●) $\nu = 20$ cS and (▲) $\nu = 10$ cS. (Credit: S. Protière [131, 76])

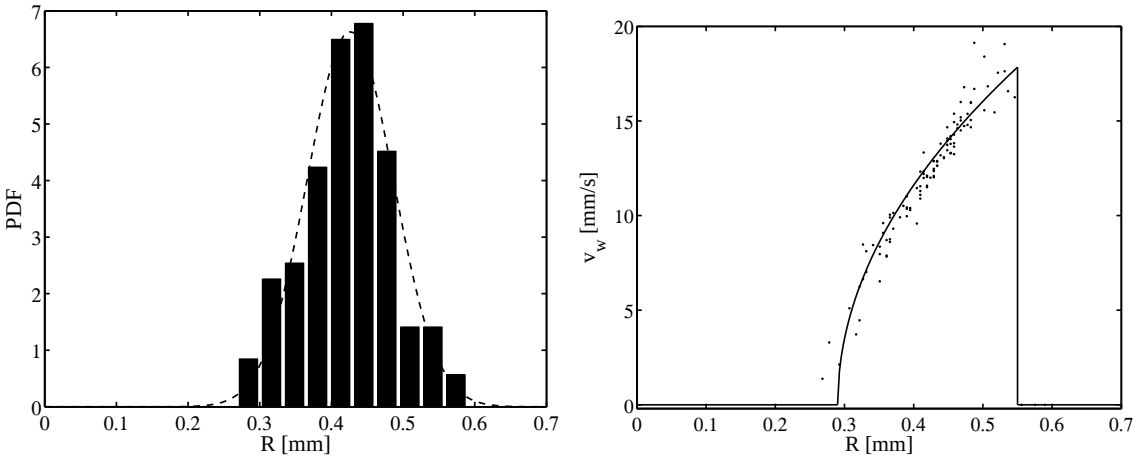

(a) (b)

Figure 6.4: (a) Probability Distribution Function of the radius R of droplets created with a nail tip. The dashed line is a normal distribution of mean 0.43 mm and standard deviation 0.06 mm. (b) Velocity v_w of the walkers as a function of their size R. The solid line corresponds to Eq. (6.2).

section. Walking droplets ($R \sim 0.4$ mm) are about twice smaller than droplets usually made with a syringe and a needle ($R \sim 0.8$ mm), so they need to be produced by another way, here with a nail tip dipped into a bath and quickly taken out (cf. sec.3.1). The droplets and the bath are thus made from the same liquid (so they have the same viscosity). With this method of creation, the droplet size R is not perfectly reproducible; it follows a normal distribution of mean 0.43 mm and standard deviation 0.06 mm (Fig. 6.4a). The walker horizontal velocity v_w has also been measured as a function of its radius R (Fig. 6.4b). Droplets start walking at $R \geq 0.29$ mm, through a pitchfork bifurcation. The velocity increases as the square root of the distance to the threshold size, until it abruptly vanishes for $R \geq 0.55$ mm (Fig. 6.4b). The average velocity is about 10 mm/s;

$$v_w[\text{mm/s}] = \begin{cases} 35\sqrt{R[\text{mm}] - 0.29} & \text{if } R \in [0.290.55] \text{ mm}, \\ 0 & \text{otherwise.} \end{cases} \tag{6.2}$$

6.2.1 Non-local interactions

The walker and the surface wave on the bath are interlocked. Indeed, the wave was born from the droplet bouncing, and the walking ability is only due to the wave. The walker is therefore a marvelous and unique example of wave-particle duality at macroscopic scale [124].

Droplets use their wave to probe the surroundings. The wave extension around the droplet varies with the damping rate, which decreases as the distance to the Faraday threshold Γ_F is decreased. On the other hand, the threshold Γ_F significantly increases when the bath depth is decreased below 5 mm. So a droplet cannot walk where the bath is not sufficiently deep, the associated wave being fully damped. By immersing objects of height 8 mm in a bath of depth 9 mm, we observe that the waves propagate everywhere but on these objects. As a consequence, incoming walkers feel the submarine objects and stay away from them [76];

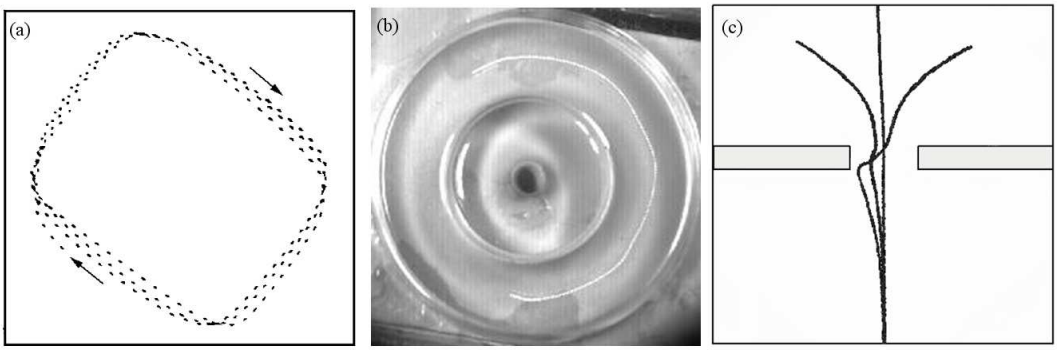

Figure 6.5: (a) A droplet probes the surrounding thanks to the wave it emits. Consequently, it is reflected from a distance by the walls (Credit: S. Protière [76]). (b) A droplet may be guided through a circular channel. (c) A droplet is randomly deviated when passing through a slit between two submarine objects (Credit: Y. Couder [133]). In (a,b,c), the successive images taken by the camera are superposed in order to reveal the trajectory of the droplet; black line in (a) and (c), white line in (b).

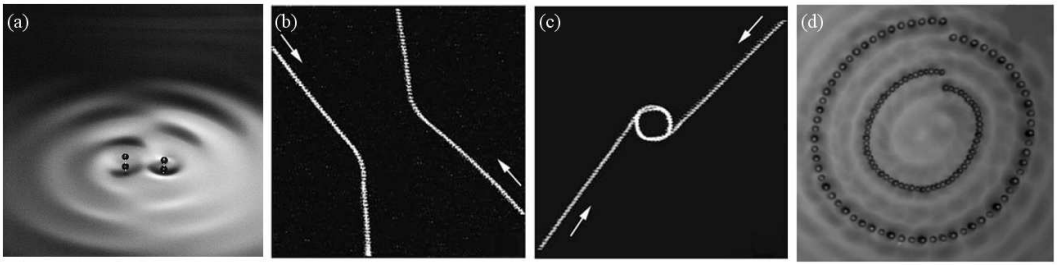

Figure 6.6: (a) Two walking droplets interact through the wave they emit. These walkers may repulse (b) or attract (c) each other, resulting in complex orbital motions. As an example (d), two droplets may orbit around a virtual center of rotation (Credit: S. Protière [76, 134]).

they are reflected by the walls (Fig. 6.5a). Thanks to this property, walkers may be guided through channels, exactly as rollers do (Fig. 6.5b). Nevertheless, it is better here to only use submarine walls than emersed walls. Indeed, the meniscus that matches the bath surface to the wall may emit parasite Faraday waves [132]. The duality between a wave and a particle is highlighted in the brilliant following experiment, made by Couder and coworkers in 2006 [133]. Two submarine objects are placed next to each other with a small gap between both. A droplet that enters the gap seems to be deviated randomly (Fig. 6.5c). Nevertheless, when repeating the experiment a large number of times, it appears that the Probability Distribution Function of the deviation angle forms a diffraction pattern perfectly similar to those observed with photons or electrons!

When two walkers come in the vicinity of each other, they interact through their waves [76]. Indeed, the wave pattern on which they bounce is the sum of individual waves emitted by both (Fig. 6.6a). The incoming droplets may repulse or attract each other, depending on the distance between them (Fig. 6.6b-c). Attraction leads to the formation of complex orbital motions and epicycles [134], as those observed in celestial mechanics (Fig. 6.6d).

When more than two walkers interact together, they usually form a crystalline structure

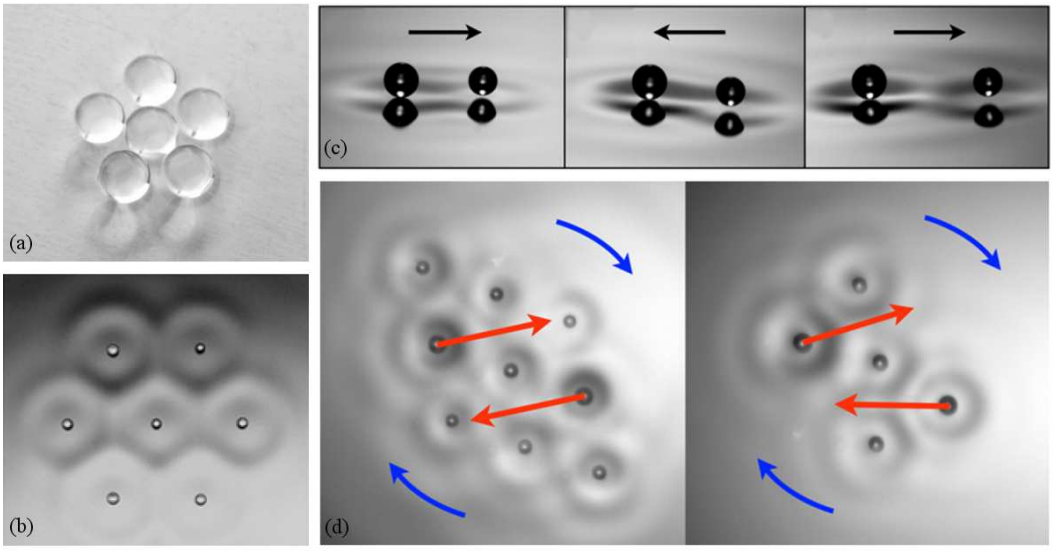

Figure 6.7: (a) Large bouncing droplets agglomerate together and form rafts, even at low forcing acceleration. (b) Several walkers form a crystalline structure (often hexagonal) where the distance between particles is close to the wavelength of the emitted waves (Credit: S. Protière [76]). (c) Two unequal walkers form a spontaneously moving ratchet, the direction being prescribed by the forcing conditions. (d) Larger droplets are able to set a whole crystalline structure of small droplets into motion.

(Fig. 6.7b), where the distance between two droplets is close to the wavelength of the emitted capillary waves [131]. At lower forcing, larger bouncing (but not walking) droplets have a similar behavior [135, 136], but the distance between them is now next to nothing (Fig. 6.7a). Indeed, two particles (even solid spheres or bubbles) placed on a bath attract each other to minimize the excess surface created by the meniscus around each particle [137, 138, 139, 140]. Two walkers with a different size form a ratchet [141]; the symmetry is broken and the resulting system experiences a net translational motion (Fig. 6.7c). One or several larger droplets placed in a crystal of small droplets can drive the whole structure, i.e. give it a translational/rotational motion (Fig. 6.7d).

Walker structures can also be moved by using virtual droplets (D. Caballero, private communication). A pulsed laser locally heats the bath surface periodically, which creates a capillary wave due to a Marangoni effect. This capillary wave interacts with the walker waves exactly as if it was also coming from another walker. Therefore, the walkers can be driven by the controlled motion of the laser beam. This way to manipulate droplets is also of great interest for possible applications in microfluidics.

6.2.2 A gas of droplets

Our main contribution to research on walkers consists in studying the statistical behavior of a large number of them bouncing onto a bath of surface $S = 4900$ mm^2. In particular, we want to know to which extent this set of droplets behaves as a gas (Fig. 6.8). The initial number N_i of droplets is varied from 10 to 50, five recordings of about 130 s are made in each case. Droplets are observed to strongly interact with each other, using every mechanism

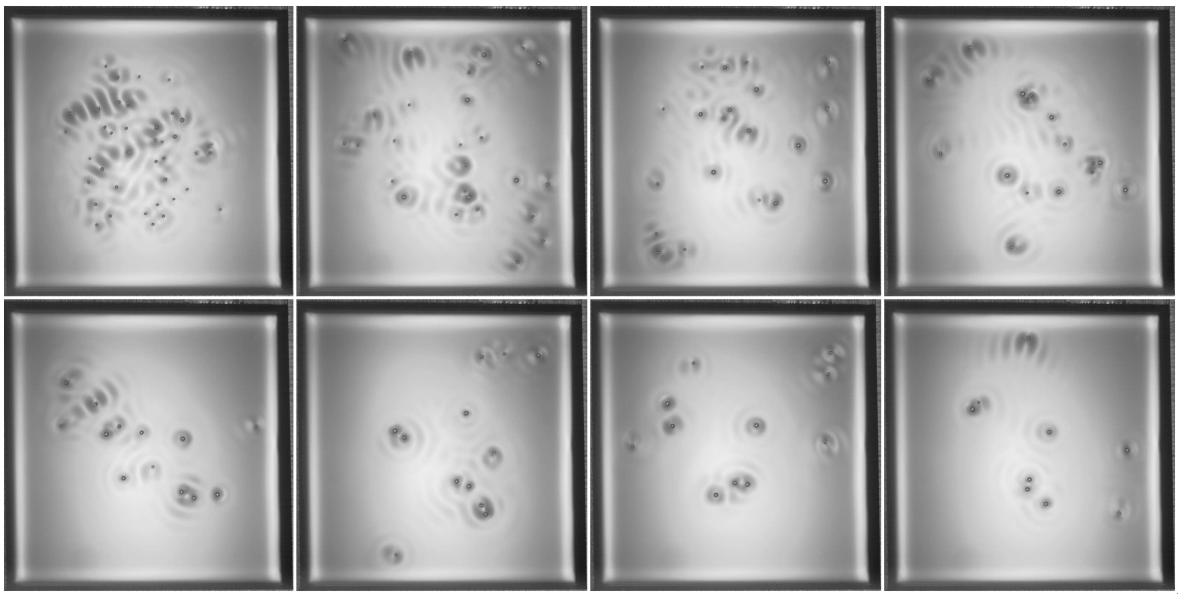

Figure 6.8: Time evolution of a gas of droplets. Snapshots are taken every 16 s.

detailed here above: repulsions, orbits, crystals, ratchets... Sometimes, two walkers collide and fuse together. The resulting droplet may be too large to keep walking.

As a consequence, the number of droplets $N(t)$ decreases with time and the walkers progressively turn into a motionless population (Fig. 6.9a). The number of droplets is relatively well fitted by a decreasing exponential

$$N(t) = N_f + (N_i - N_f)\mathrm{e}^{-t/t_N}, \tag{6.3}$$

which corresponds to a relaxing process from the initial number of droplets N_i to the equilibrium final state N_f with a characteristic time t_N. The final number N_f increases with N_i (Fig. 6.9b) while t_N decreases (Fig. 6.9c). We note that t_N is also much more reproducible when N_i is sufficiently large for statistical tools to apply. The increase of N_f with N_i may be rationalized by a simple model based on the following hypotheses coming from observations:

- There are two distinct populations of droplets, N_w walkers and N_{nw} not walking droplets, such as the total number of droplets is $N = N_w + N_{nw}$.
- When a walker coalesces with another droplet, the result is a motionless droplet. The probability of coalescence does not depend on the nature of this other droplet (walker or not).
- Two motionless droplets cannot coalesce together.

The probability $\mathcal{P}_{w/w}$ for a walker/walker coalescence and the probability $\mathcal{P}_{w/nw}$ for a coalescence between a walker and a droplet at rest are respectively

$$\mathcal{P}_{w/w} = \frac{N_w - 1}{N_w - 1 + N_{nw}} \quad \text{and} \quad \mathcal{P}_{w/nw} = \frac{N_{nw}}{N_w - 1 + N_{nw}}. \tag{6.4}$$

Starting from N_i walkers and zero motionless droplet, the probability $\mathcal{P}_{(N_w,N_{nw})}$ of each scenario (N_w, N_{nw}) may be evaluated until $N_w = 0$. An example is given in Fig. 6.9(d) for

$N_i = 6$. The mean number of resulting motionless droplets is given by

$$N_f(N_i) \simeq \sum_{j=0}^{N_i/2} j\mathcal{P}_{(0,j)}. \tag{6.5}$$

The standard deviation is also computed

$$\Delta N_f(N_i) \simeq \sqrt{\sum_{j=0}^{N_i/2} \left(j^2\mathcal{P}_{(0,j)} - N_f^2 \right)}. \tag{6.6}$$

This solution, plotted in Fig. 6.9(a), roughly fits the experimental data. Nevertheless, according to the distribution of droplet sizes (Fig. 6.4a), there is a significant probability that two coalescing walkers form a walker again. So the model has been generalized to three populations: small walkers, large walkers and droplets at rest (Fig. 6.9a). A more accurate model could be a combination of both scenarios that would take into account the initial size distribution.

We have also investigated the velocity distribution of droplets. These distributions are obtained by measuring the instantaneous velocity of every droplets during a short interval of time (here 4 s, which corresponds to 100 images). Examples of Cumulative Distribution Functions (CDF) are plotted in Fig. 6.10 for $N_i = 30$. The distribution is seen to significantly evolve with time. In any case, it is well fitted by a Weibull distribution, for which PDF (Probability Density Function) and CDF are given by:

$$PDF(v_w) = \frac{b}{a}\left(\frac{v_w}{a}\right)^{b-1} \mathrm{e}^{-\left(v_w/a\right)^b} \quad \text{with } v_w > 0, \tag{6.7}$$

$$CDF(v_w) = 1 - \mathrm{e}^{-\left(v_w/a\right)^b} \quad \text{with } v_w > 0. \tag{6.8}$$

The Weibull distribution has two parameters, the scale a and the shape b. For specific values of b, it is equal to some well-known distributions; the exponential distribution is obtained when $b = 1$, $b = 2$ leads to the Rayleigh distribution and $b = 3.4$ is very close to a normal distribution. The Rayleigh distribution is of importance in this context since it is the 2-dimensional analog of the Maxwell-Boltzmann distribution followed by the velocity of molecules in an ideal gas.

Each experimental sequence is divided into segments of 4 s on which the velocity distribution is evaluated and fitted by a Weibull distribution. The resulting parameters a and b are measured on each sequence as a function of time (Fig. 6.11). Various sequences corresponding to the same N_i are averaged together. Although data are scattered, the scale parameter a does not seem to depend on N_i. It seems to decrease from $a_i = 12.12$ mm/s, which corresponds to the mean velocity of a single walker. The final value is $a_f = 5.56$ mm/s and the characteristic time $t_a = 63.2$ s roughly corresponds to twice the relaxation time t_N of $N(t)$. The shape parameter b also decreases with time, and seem to converge towards $b = 1$ (exponential distribution). The initial value decreases with increasing N_i.

These results may be explained with physical arguments. At the beginning, the walkers start with a velocity distribution around $b = 2$ which roughly corresponds to an ideal gas, though the distribution is expected to be close to the one presented in Fig. 6.4(b). Then, due

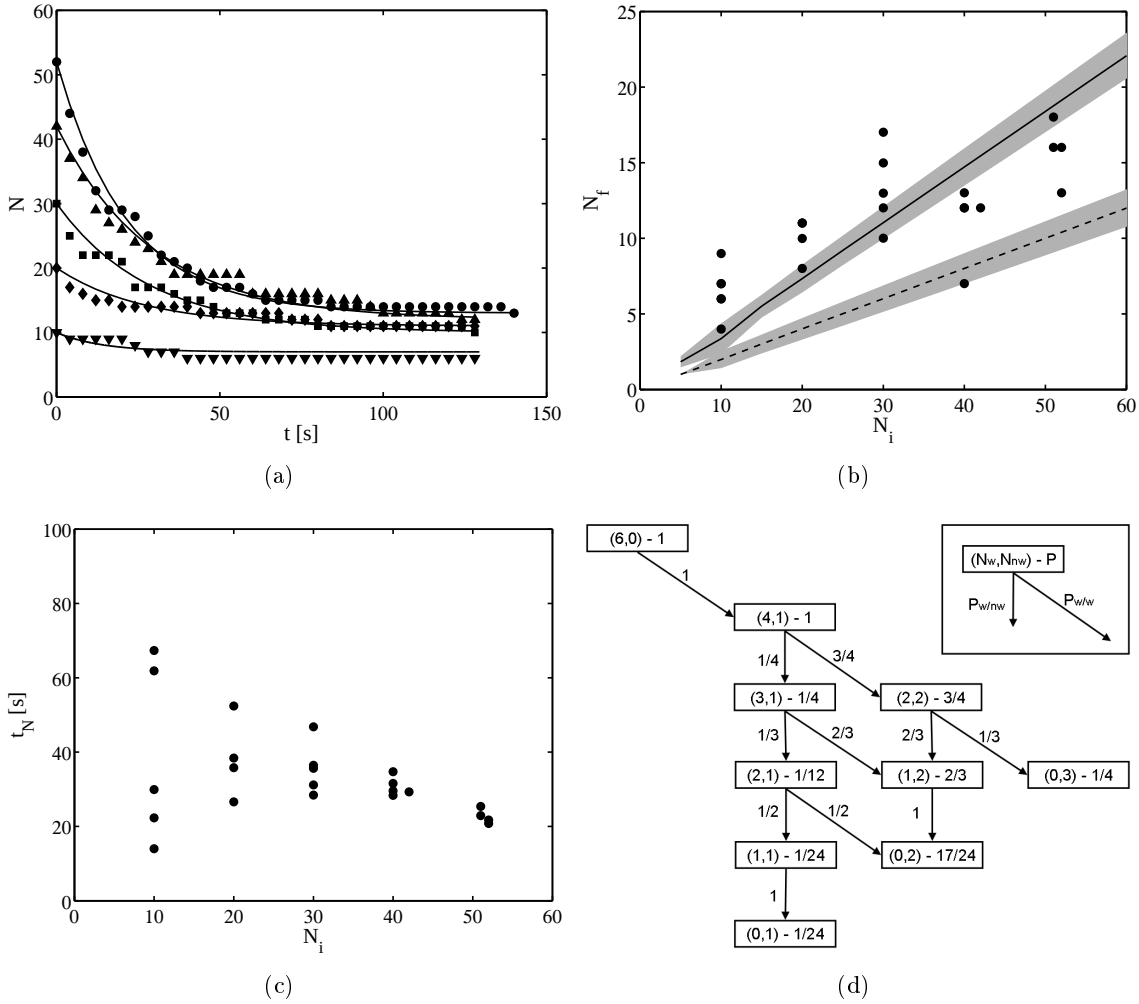

Figure 6.9: (a) Evolution of the number $N(t)$ of droplets for various initial numbers: (●) $N_i = 52$, (▲) $N_i = 42$, (■) $N_i = 30$, (♦) $N_i = 20$ and (▼) $N_i = 10$. The solid lines correspond to Eq. (6.3). (b) Final (equilibrium) number of droplets N_f as a function of the initial number N_i. The solid line (resp. dashed line) corresponds to the mean number of motionless droplets predicted by the 2-populations model (resp. 3-populations). The shaded zone represents the standard deviation. (c) Characteristic time t_N of the relaxing process as a function of N_i. (d) Example of evolution predicted by the 2-populations model for $N_i = 6$. In each box, the number of both populations is indicated in brackets (walkers, droplets at rest), followed by the probability to reach this state. Next to the arrows is the conditional probability to go from one box to another. The process ends when the number of walkers is zero.

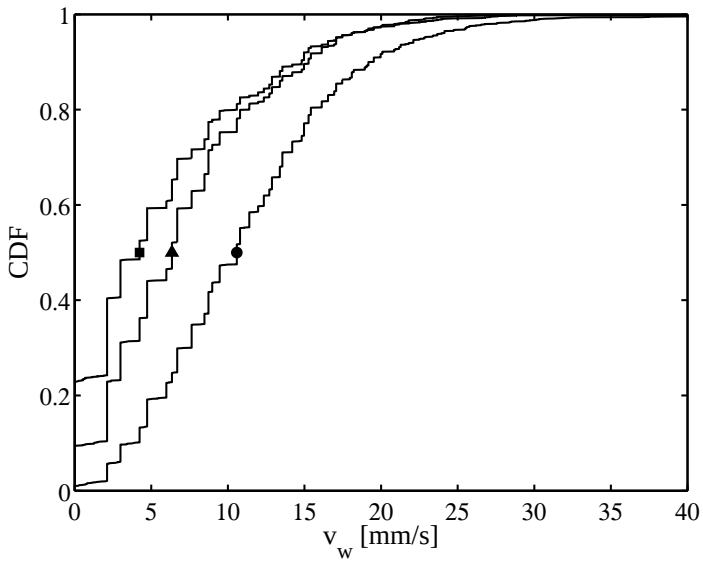

Figure 6.10: Cumulative Distribution Function (CDF) of the droplet velocity v_w at various times t. (●) $t = 0$ s, (▲) $t = 36$ s, and (■) $t = 90$ s.

to the coalescences between walkers, b decreases and tends towards unity, which corresponds to the exponential distribution. In this regime, the major part of droplets result from coalescence and are at rest, while there are still a few walkers with high velocity. A similar velocity distribution is encountered for large assemblies of young fishes, e.g. Nile Tilapia alevins [142]. Indeed, these alevins are generally at rest, and only a few individuals explore the surroundings through brief sequences of high-speed motion.

The characteristic time of the decreasing of b may be related to the mean free path of the walkers. Indeed, in a 2-dimensional gas, the mean time between two successive collisions is given by

$$t_{coll} \simeq \frac{S}{v_w N_i R}, \tag{6.9}$$

where $S = 4900$ mm^2 is the bath surface, $v_w \simeq 9$ mm/s is roughly the mean velocity, and $R \simeq 0.45$ mm is the droplet radius, which approximately corresponds to the cross section of the droplet. Therefore, $t_{coll} \simeq 1210/N_i$, which is is good agreement with the observed characteristic time for the decreasing of b.

6.3 Summary

In this chapter, we have discussed two configurations in which bouncing droplets experience a self-propelled horizontal motion, namely the rollers and the walkers. The first is due to the droplet deformation while the second relies on the waves emitted at the bath surface. Both rollers and walkers are reflected on the walls of the container, so they can be guided in channels. The walkers can also be handled with a laser beam. The self-propelled motion occurs in a specific range of forcing parameters, so it can be started and stopped by only tuning the forcing : the controlled manipulation of droplets onto a vibrating bath is possible. The walkers experience long-range interactions through the waves they emit, so they may

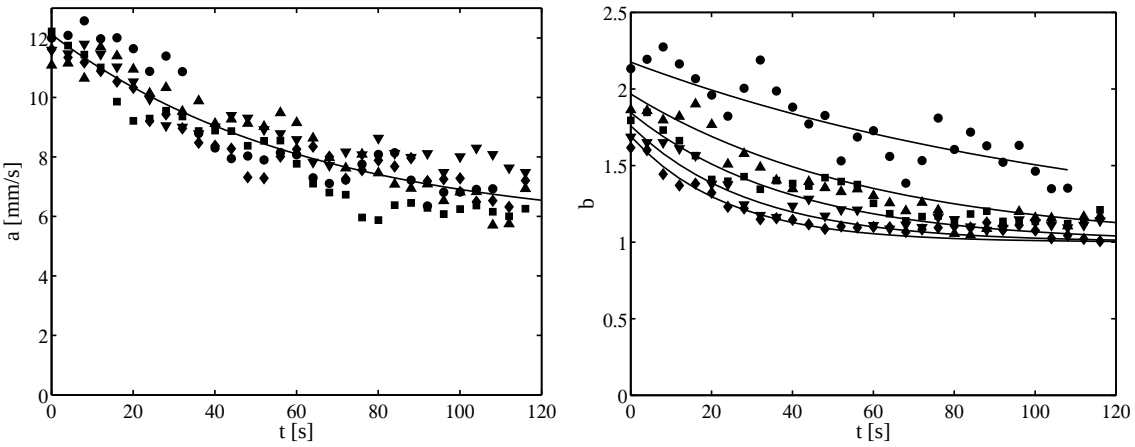

(a) (b)

Figure 6.11: (a) Scale parameter a and (b) shape parameter b of the velocity distribution as a function of time. (●) $N_i = 50$, (▲) $N_i = 40$, (■) $N_i = 30$, (▼) $N_i = 20$ and (⧫) $N_i = 10$. The solid lines are guides for the eyes.

form complex orbits or crystalline structures. Moreover, droplets are attracted by each other, which promote their coalescence.

We have mainly investigated the collective behavior of a large number of walkers from a statistical point of view. Due to the unavoidable collisions and coalescences between the walkers, the number of them decreases with time. The system tends to an equilibrium state in which droplets are too big to keep walking. The velocity distribution is correctly described by a Weibull distribution. Initially close to that of an ideal gas, it turns into an exponential distribution in which the major part of droplets is at rest while only a few individuals are still walking. This distribution is also observed in other systems of collective behaviors, such as the Nile Tilapia alevins. Therefore, the gas of walking droplets could be a promising model for statistical physics of collective motions and self-organization.

Chapter 7

Partial coalescence

In previous chapters, we have seen that a droplet can be sustained onto a bath as long as there is a thin air layer separating both liquids. When the air is completely drained out, the droplet quickly coalesces into the liquid bath. Nevertheless, the fusion is not always in one go, and may result in a droplet of radius about half the initial droplet: the coalescence is said to be partial (Fig. 7.1). This daughter droplet also stays on the bath, drains its air layer and coalesces. Again, the coalescence may be partial, thus giving birth to a grand-daughter droplet. Up to seven successive generations have been observed during the coalescence of a single mother droplet. When the daughter droplet is sufficiently small, it coalesces totally, thus ending this cascade of partial coalescences. The whole process lasts about 200 ms (each partial coalescence is only a few milliseconds), so it is hardly visible to the naked eye.

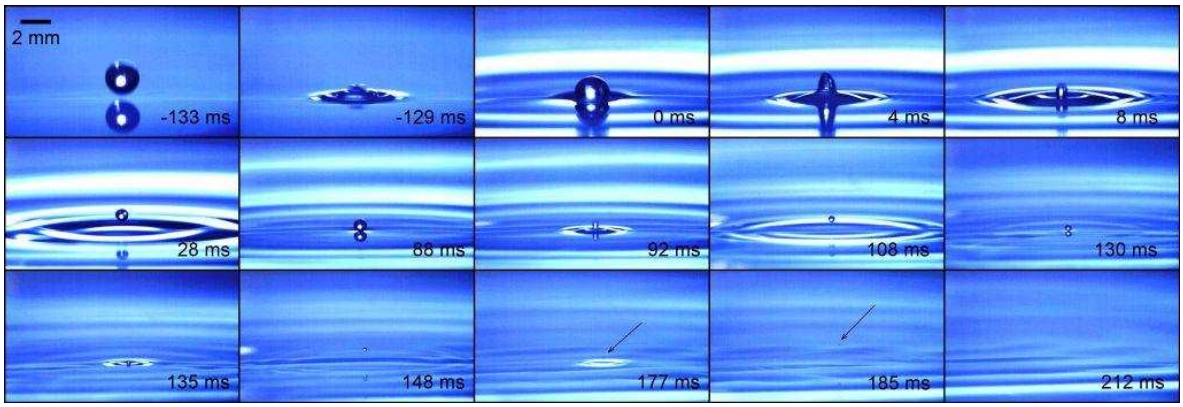

Figure 7.1: Cascade of partial coalescences of a 5 μL oil droplet ($\nu = 1.5$ cS). Four successive partial coalescences are observed, each of them halving the droplet radius; the last daughter droplet is about 1/10000th of the initial mother droplet in volume !

The detail of a partial coalescence is seen in Fig. 7.2(a). Coalescence only begins when the air film breaks. This rupture usually occurs asymmetrically at the boundary of the apparent contact zone between the droplet and the bath [143, 144]. The hole quickly opens due to high pressure gradients resulting from the Laplace law (1.2). Indeed, the film thickness at rupture is micrometric, so the related curvature near the break point is about $\mathcal{C} \sim 10^6$ m^{-1}. During the retraction, a part of the bath comes up into the droplet [145, 146], as seen when colorless droplet coalesces into a colored bath. Next, the emptying droplet takes a column shape that

may pinch off and form a daughter droplet (partial coalescence), or alternatively collapse into the bath (total coalescence). Finally, the liquid below the pinch is violently ejected downwards and forms a powerful vortical ring in the bath [147, 148, 149].

Partial coalescence was reported by Mahajan in 1930 [150], but the first systematic investigation was only made by Charles and Mason in 1960 [151], thanks to the recent developments of high-speed photography. These authors considered the partial coalescence of water droplets at the planar interface between an oil layer and a water layer. Since the water droplet is surrounded by oil instead of air, the lifetime t_L between two successive coalescences is increased, so each daughter droplet is visible to the naked eye. Charles and Mason thought that the formation of the daughter droplet is due to a Rayleigh-Plateau instability that reshapes the column of fluid formed by the fusing mother droplet. Nowadays, this scenario is invalidated. In 1993, the French PhD-student Y. Leblanc [89] studied the sensitivity of partial coalescence to variations in size, surface tension, and viscosity of both fluids. Unfortunately, his results were never published in international journals; they were rediscovered by others [152, 153, 154] several years later. But the main breakthrough occurs in 2006, due to Blanchette and Bigioni [155, 156] who discovered the main mechanism of partial coalescence. According to these authors, the column shape formed by the coalescing mother droplet is mainly due to the propagation of capillary waves on the droplet surface. These latter are created by the air film retraction at the bottom of the droplet [89, 152, 153]. They climb on the droplet and converge at the top. This greatly lifts the droplet interface and delays its vertical collapse, thus giving advantage to the horizontal pinch. Other works on partial coalescence have been published since [157, 158, 159, 160, 161]. Unfortunately, they rarely take into account the very recent results of Blanchette.

In this chapter, we present a deeper investigation of partial coalescence at the interface between two immiscible liquids [162]. After a dimensional analysis, we study the influence of the physical properties of both fluids on the coalescence outcome. We discuss the exact role played by capillary waves in the partial coalescence mechanism. Finally, we show that a cascade of partial coalescence can be stopped on a vibrated bath.

7.1 Experimental setup

Partial coalescence is robust and easy to observe experimentally. A container is partly filled with an aqueous solution. Then, an oil layer ($\nu < 50$ cS) denoted (s) is poured on it, as seen in Fig. 7.2(a). A water droplet (mother) is released from a syringe in the oil phase. Thanks to gravity, it migrates towards the water/oil interface and finally coalesces into its homophase. The mother droplet radius is varied by changing the needle diameter. The viscosity of both liquids is tuned between about 1 and 100 cS (various silicon oils and water/glycerol/ethanol mixtures - App. B). The interfacial tension between water and oil has been measured. It is approximately 40 mN/m for (water+glycerol)/oil interfaces, and it sharply decreases with an addition of ethanol (down to 9 mN/m for a mixture made of 40% ethanol for 60% water). More than 150 partial coalescences have been filmed thanks to a high-speed camera (2000 fps, pixel size 30 μm). The interface position (supposed axisymmetric) is detected as a function of time by post-processing the images.

Many experimental precautions have been taken in order to ensure the data reproducibility:

- A glass container is easier to clean.

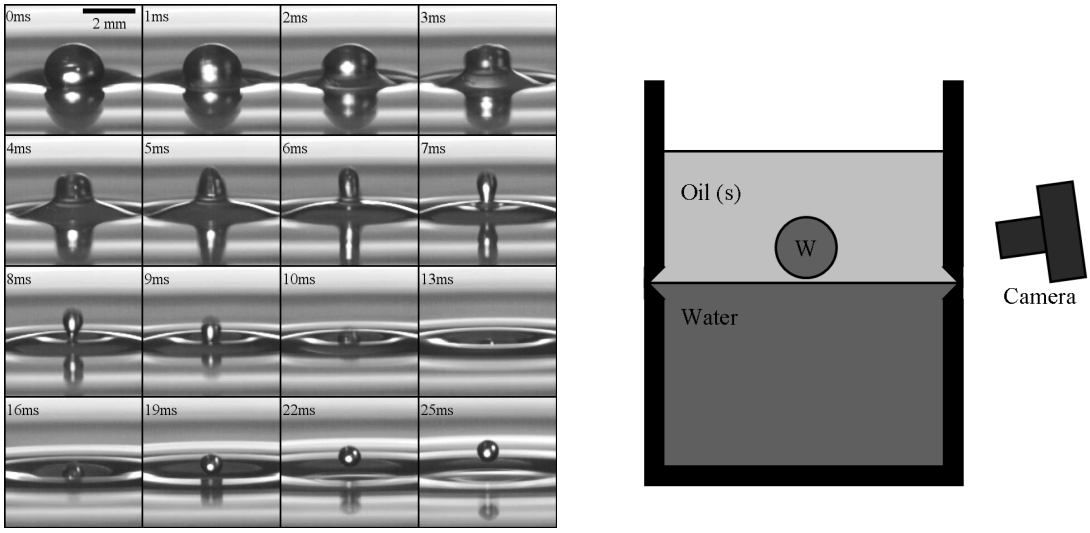

(a) (b)

Figure 7.2: (a) Sequence of events in a partial coalescence of an oil droplet ($\nu = 1.5$ cS) in air. (b) Experimental setup: a container is filled with an aqueous mixture (water + glycerol + ethanol) and a layer of silicon oil (s). An aqueous droplet crosses the (s) layer and coalesces into its bulk phase.

- The curvature of the liquid-liquid interface may affect the coalescence outcome [155], so the interface needs to be as planar as possible. To prevent unexpected curvatures, a horizontal groove is made, in which the liquid/liquid interface is pinned.
- The droplet may be at rest on the interface (no internal flows) at the beginning of the coalescence. Therefore, experiments are not taken into account when the drainage time is less than 1 s.
- The container is sufficiently large to avoid parasite reflections of capillary waves on the walls during the coalescence.

7.2 Invariant scalings in coalescence

How much time is a coalescence ? Do partial and total coalescence share some common features, or are they completely different since their beginning ? To answer these questions, we started by measuring the time evolution of two variables that characterize the coalescence. The first is the excess surface energy $E_\sigma = \sigma \Delta S$, compared to the final state where the droplet has fully coalesced (Fig. 7.3a). The second quantity is the volume Ω of the droplet that is still above the mean level of the liquid/liquid interface (Fig. 7.3b). These measurements are made for every observed coalescence, whatever its outcome, and both ΔS and Ω are normalized by their initial value.

The coalescence was already observed to scale on the capillary time τ_σ [146, 152]. Surprisingly, all the $\Delta S(t)$ and $\Omega(t)$ curves collapse when the time is scaled by τ_σ, no matter the outcome. The difference between partial and total coalescence only appears in the later stages of coalescence. The possible pinch-off occurs between 0.7 and 0.8 τ_σ after the beginning. The

decrease in ΔS is remarkably linear; the power released by surface tension to set the liquids into motion is roughly constant during the main part of the coalescence. The emerged volume decreases as the cube of time, so the emptying is relatively slow until $t = 0.3\tau_\sigma$. The corresponding flow rate evolves as the square of time. These scaling laws are only observations, and still need to be rationalized.

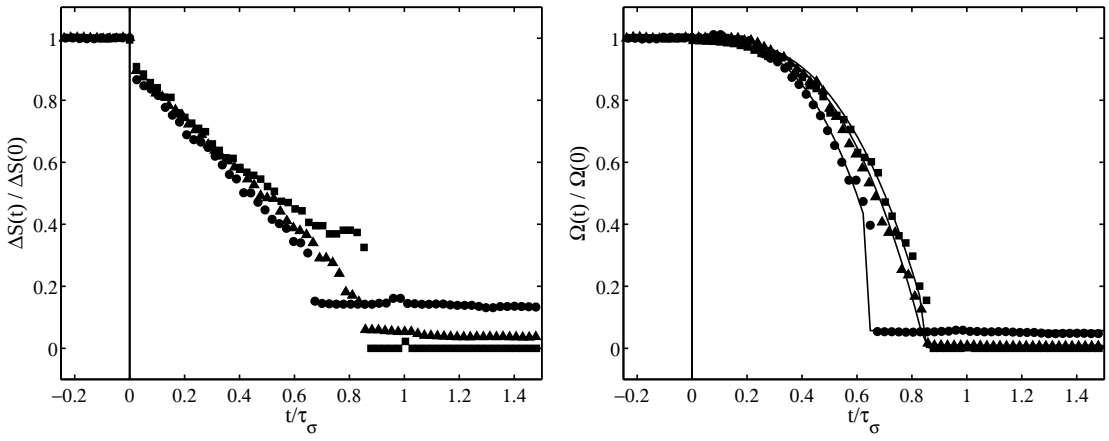

(a) (b)

Figure 7.3: Evolution of the global quantities for a total (▲) and two partial coalescences (● and ■) with various liquids. (a) Excess of surface ΔS. (b) Volume Ω above the mean interface level. The vertical solid line indicates the start point of coalescence (i.e. the film breaking). The solid curves in (b) correspond to a fit by the equation $1 - \Omega(t)/\Omega(0) \sim (t/\tau_\sigma)^3$.

7.3 Dimensional analysis

Once the coalescence has started, the dynamics is macroscopically governed by three forces resulting from surface tension, gravity and viscosity respectively. Therefore, seven dimensional parameters are relevant: the interfacial tension σ, both densities ρ, ρ_s and viscosities ν, ν_s, the droplet radius R and the gravity g. According to the Π-theorem (Vaschy-Buckingham), four independent dimensionless numbers can be built that entirely determine the coalescence outcome. Any dimensionless quantity that describes the partial coalescence must be a function of these four numbers only. Since the coalescence timescale is shown to be τ_σ, surface tension must be the driving mechanism. Indeed, no other force (neither gravity nor viscous forces) could explain the complex shapes encountered in partial coalescence.

If partial, the coalescence is roughly self-similar: it repeats identically, no matter the size of the initial droplet. On the other hand, the competition between two forces gives rise to a length scale at which both forces balance each other. For example, as seen in Chap. 1, gravity and surface tension have the same order of magnitude when the system is close to the capillary length. In these conditions, the process cannot be self-similar since the dominant force is gravity for larger droplets while it is surface tension for smaller droplets. Therefore, self-similarity requires surface tension to be the only dominant force at the considered scale. When the droplet size is about the capillary length (resp. the viscous length), i.e. when the Bond (resp. the Ohnesorge) number is of the order of unity, surface tension is not dominant anymore and the self-similarity of partial coalescence is compromised. Bond (Bo_s) and both

Ohnesorge numbers (Oh and Oh_s) are thus pertinent dimensionless numbers. The fourth dimensionless number may be the relative difference in density

$$\Delta\rho = \frac{\rho_1 - \rho_2}{\rho_1 + \rho_2}. \tag{7.1}$$

The validity of this dimensional analysis may be contested when significant residual micro-flows are present within the initial droplet. In that case, additional parameters (and dimensionless numbers) are required to describe the coalescence. Since these micro-flows directly enhance the drainage, their characteristic timescale must be of the order of the drainage time. When this time is measured to be much higher than the coalescence time, residual micro-flows can be neglected.

7.3.1 The Ψ function

What kind of transition separates partial and total coalescences ? To answer this question, the most relevant parameter may be the the ratio between radii of the daughter R_f and mother R_i. Obviously, this latter is a function Ψ of the four independent dimensionless numbers only;

$$\frac{R_f}{R_i} = \Psi(Bo_s, Oh, Oh_s, \Delta\rho). \tag{7.2}$$

When $Bo_s, Oh, Oh_s \ll 1$, surface tension is the only dominant force and the coalescence is partial and self-similar (Fig. 7.4a). The ratio Ψ only depends on the relative difference in density $\Delta\rho$, which is constant during a single cascade. In this regime, we observe $\Psi \simeq 0.45 \pm 0.05$ in average. Unfortunately, the liquid density is always close to water, so our experiments do not cover a range of $\Delta\rho$ sufficiently large to assess about the variation of Ψ with $\Delta\rho$.

The Bond number increases with the droplet size, and large droplets are influenced by gravity. This latter significantly accelerates the droplet emptying [89, 155], which is in favor of total coalescence. As checked experimentally (Fig. 7.5a), the Ψ function decreases with an increase in Bo_s. According to the present data, it is not possible to state that Ψ is 0 (total coalescence) for Bond numbers larger than a critical value $Bo_{s/th}$.

A decrease in droplet size corresponds to an increase in both Ohnesorge numbers. The flows responsible for the partial coalescence (e.g. capillary waves) are progressively damped by viscosity in both fluids [89, 152, 155]. This results in a decrease of the Ψ function, which ends up vanishing when $Oh \geq Oh_{th} \simeq 0.02 \pm 0.005$ or $Oh_s \geq Oh_{s/th} \simeq 0.3 \pm 0.05$ (Fig. 7.5b). Variations of Oh induce a sharp and premature transition from partial to total coalescence, while variations of Oh_s result in a smoother and delayed transition. Both viscosities do not have the same role in inhibiting the partial coalescence mechanisms. As seen in Fig. 7.4(c-d), the interface switches from a column shape to a cusp-like shape for high Oh_s values.

We have also studied the behavior of Ψ with a combined variation of both Ohnesorge numbers, the Bond number being negligible (Fig. 7.6). The boundary curve between partial and total coalescence has been modeled by Leblanc, as

$$Oh + 0.057 Oh_s = 0.02. \tag{7.3}$$

Although this equation is in relatively good agreement with the experimental results when $Oh_s \sim 1$, it fails catching the boundary close to $Oh = Oh_s$: partial coalescence is observed for much greater Ohnesorges than predicted.

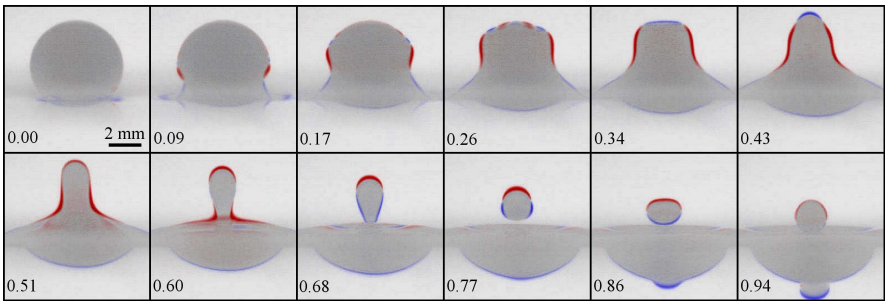

(a)

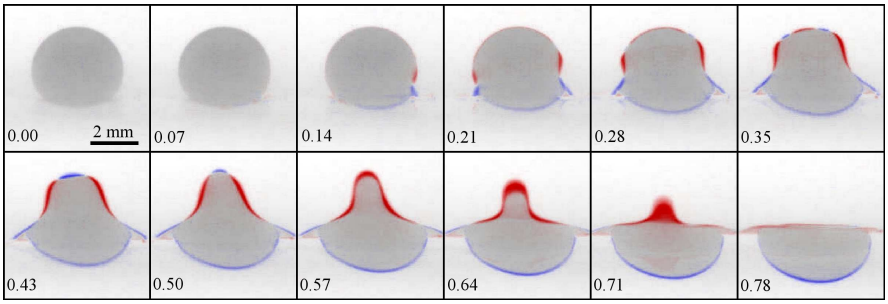

(b)

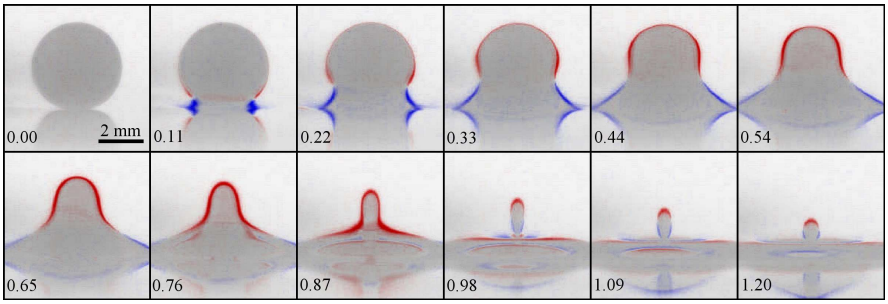

(c)

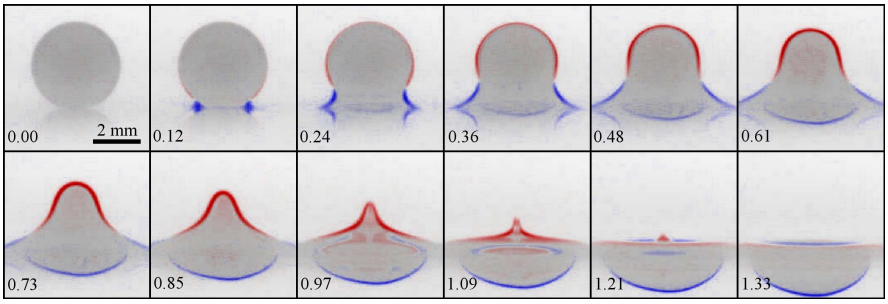

(d)

Figure 7.4: Partial and total coalescences for various values of Bo_s, Oh and Oh_s. (a) Partial coalescence for small Ohnesorges ($Bo_s = 0.049$, $Oh = 0.0025$, $Oh_s = 0.013$). (b) Total coalescence due to a high Ohnesorge on the aqueous side ($Bo_s = 0.079$, $Oh = 0.018$, $Oh_s = 0.0049$). (c) Intermediate partial coalescence due to a high Ohnesorge on the oil side ($Bo_s = 0.011$, $Oh = 0.0030$, $Oh_s = 0.16$). (d) Total coalescence when the oil side Ohnesorge is very high ($Bo_s = 0.0095$, $Oh = 0.0031$, $Oh_s = 0.34$). The time is indicated in capillary time units in the lower left corner. Images are obtained by subtracting two successive images in order to highlight the interface motion; the blue interface is advancing while the red is receding.

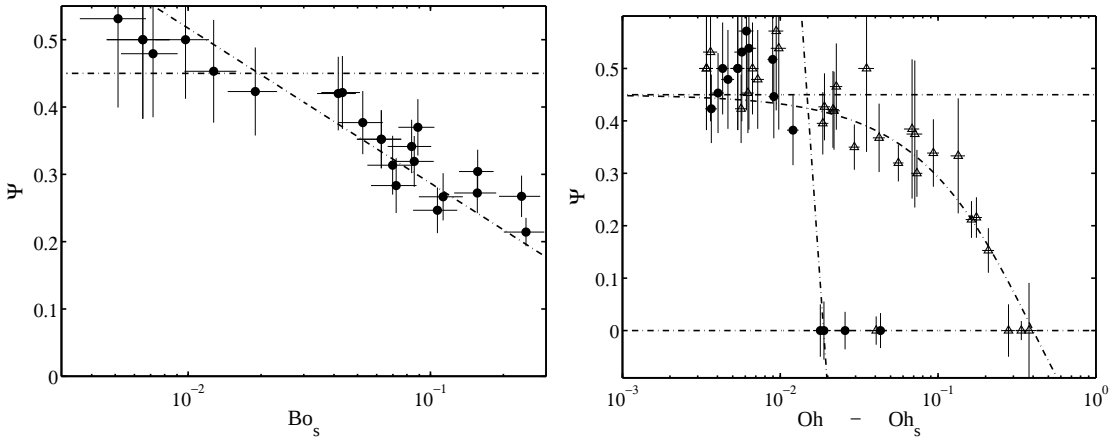

Figure 7.5: (a) Radii ratio Ψ as a function of Bo_s. The corresponding Ohnesorge numbers are always smaller than 7.5×10^{-3}. (b) Variation of the Ψ function with respect to Oh (•) and Oh_s (△). The Bond number is always smaller than 0.03, and the other Ohnesorge number smaller than 7.5×10^{-3}. Dashed lines are guides for the eyes.

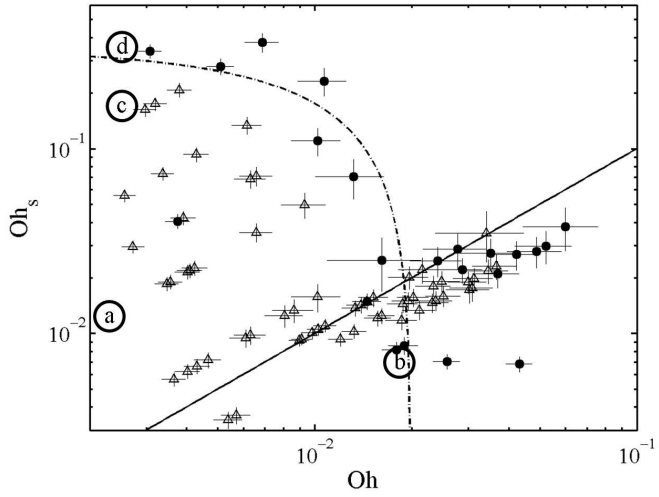

Figure 7.6: Combined influence of both Ohnesorge numbers on the coalescence outcome: partial (△) or total (•). The Bond number is always smaller than 0.03. The solid straight line corresponds to $Oh = Oh_s$, while the dashed curve is Eq. (7.3). Circled letters correspond to the snapshots of Fig. 7.4.

7.4 Capillary waves

According to Blanchette [155], the convergence of capillary waves at the top of the droplet is responsible for the partial coalescence. The motion of the droplet interface is highlighted by subtracting successive images of the snapshots (Fig. 7.4). The progression of capillary waves is clearly seen in Figure 7.7, which represents a time zoom on Fig. 7.4(a).

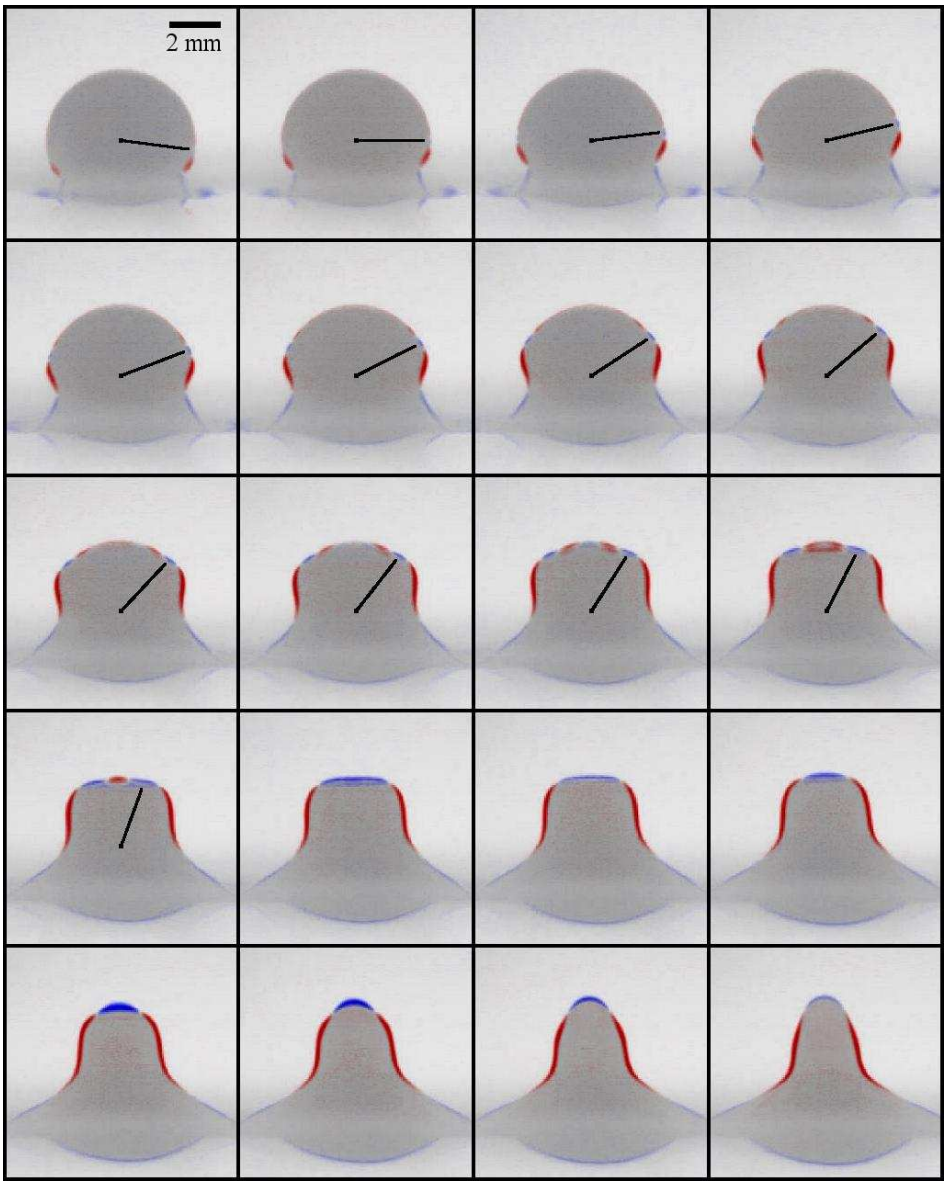

Figure 7.7: Time zoom on Fig. 7.4(a), revealing the capillary wave propagation. The time step is $0.021\tau_\sigma$; the lines help locating the wavefront.

The dispersion relation of capillary waves (Eq.1.7) may be extended to the case of a droplet immersed in another immiscible liquid (App. C):

$$(f_{(\ell,m)}\tau_\sigma)^2 = \frac{\ell(\ell^2-1)(\ell+2)(1+\Delta\rho)}{3\pi(2\ell+1+\Delta\rho)}. \tag{7.4}$$

According to Fig. 7.7, the dominant mode is $\ell = 11 \pm 1$. The wave is created at about 7.5° below equator, at the beginning of the coalescence, when the hole expands below the droplet. Its phase velocity u_{cw} is 5.27 radians per unit of capillary time, in excellent agreement with the velocity calculated through

$$\frac{u_{cw}\tau_\sigma}{R_i} = \frac{2\pi f_{(\ell,m)}\tau_\sigma}{\ell}, \tag{7.5}$$

when $\ell = 11$. The propagation time t_{cw} of the waves from the bottom to the top of the droplet is proportional to $\ell^{-1/2}$. So modes $\ell > 8$ arrive more or less at the same time, while modes $\ell < 8$ come later, separately, and cannot participate to the convergence.

The capillary waves are damped by viscosity effects on both sides of the interface. This damping may be quantified by measuring the amplitude of waves as they converge at the top. The height of the top $H(t)$ is measured as a function of time (Fig. 7.8a). The maximum H_M occurs in $t = t_{cw} \simeq 0.4\tau_\sigma$ and corresponds to the convergence of capillary waves. We see in Fig. 7.8(b) that the damping does not significantly depend on which viscosity is increased (inside or outside the droplet). For similar viscosities, damping is only 1.5 times more efficient within the droplet. The critical Ohnesorge for waves to be damped before reaching the top of the droplet is about 0.08. The viscous dissipation can be estimated theoretically (App. C). The wave amplitude at the top is

$$H_M = H_{M0} e^{-\beta t_{cw}/\tau_\sigma}, \tag{7.6}$$

where the damping factor is defined as

$$\beta = \sqrt{\frac{\pi}{3}} \frac{2\ell+1}{2\ell+1+\Delta\rho} \left[(\ell^2-1)Oh + \ell(\ell+2)\sqrt{1-\Delta\rho^2}\, Oh_s \right]. \tag{7.7}$$

This solution is close to the measured damping (Fig. 7.8b). Again, the factors that weight both Ohnesorge numbers in Eq. (7.7) are not significantly different for $\ell = 11$ and $\Delta\rho \ll 1$.

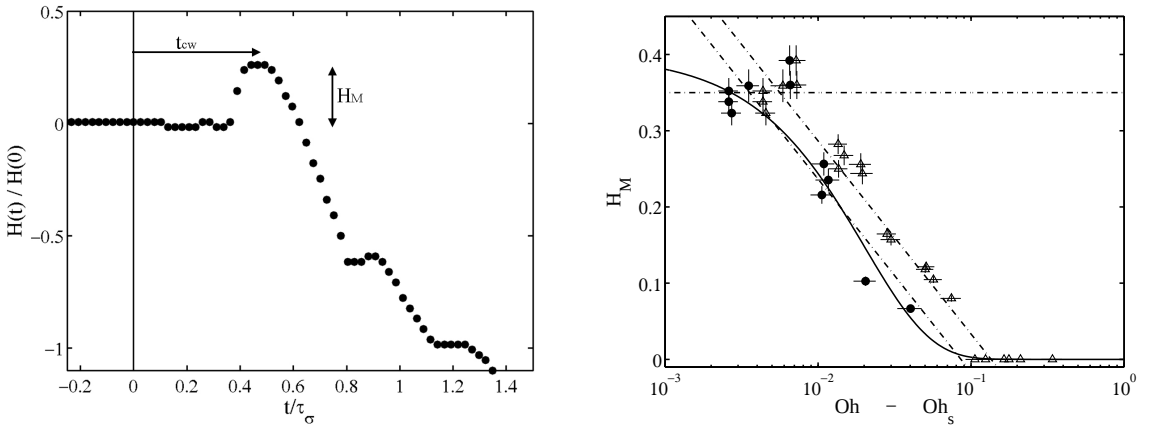

Figure 7.8: (a) Time evolution of the height of the droplet summit $H(t)$ for a partial coalescence. (b) Normalized maximal height of the interface, as a function of Oh (•) and Oh_s (△). Dashed lines are guides for the eyes, while the solid line corresponds to Eq. (7.6).

7.4.1 Capillary waves and the partial to total transition

As seen in previous sections, the transition between partial and total coalescence does depend on which Ohnesorge is increased, while the capillary wave damping are not so much influenced by that. In particular, capillary waves may be observed in a total coalescence (Fig. 7.4b), while being fully damped in a partial coalescence (Fig. 7.4c). Capillary waves are fully damped when one of both Ohnesorge numbers exceeds 0.08. On the other hand, the critical Ohnesorge values for the partial/total transition are $Oh_{th} \simeq 0.02$ and $Oh_{s/th} \simeq 0.3$, so 4 times less and 4 times mode than the critical Ohnesorge for wave damping, respectively. So the link between partial coalescence and capillary waves presented by Blanchette [155] must be revised. There must be an additional mechanism, antisymmetric in relation to both viscosities, that promotes total coalescence for high Oh and partial coalescence for high Oh_s. Moreover, this mechanism should not be efficient when $Oh \sim Oh_s$, which would explain the outgrowth of the partial coalescence zone in the (Oh, Oh_s) diagram of Fig. 7.6.

During a coalescence, the main fluid flow is a powerful rotation that ejects the droplet liquid into the underlying bath (cf. PIV experiments of [153], and numerical simulations of [155, 161]). This motion, represented by thick arrows in Fig. 7.9, originates from the conversion of interfacial energy into kinetic energy, which has been observed to occur at a constant rate, regardless of the coalescence outcome. This kinetic energy is unequally distributed to both liquids, though continuity conditions are satisfied at the interface.

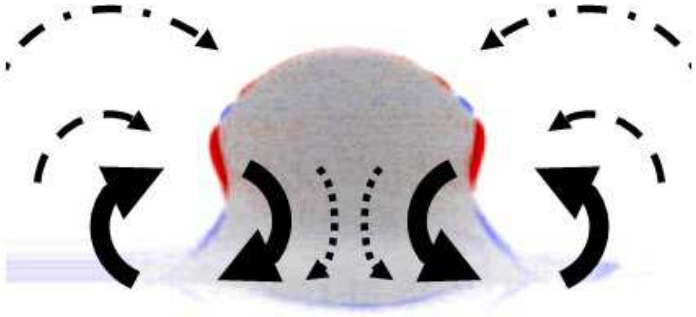

Figure 7.9: Schematic view of hypothetical motions occurring in a coalescence. Thick solid arrows represent the nominal rotation (low viscosity). Dotted arrows (resp. dashed and dash-dot) correspond to an favored rotation due to an increase in Oh (resp. Oh_s).

The viscosity is known to diffuse momentum, and so kinetic energy; zones with high velocity gradients (next to the interface among others) significantly spread when the viscosity is increased. Since the motion is driven by the interface dynamics, the constantly released kinetic energy preferentially goes into the most viscous fluid. So when $Oh > Oh_s$, the rotation within the droplet is accentuated (dotted arrows in Fig. 7.9), which promotes the droplet emptying, a quick collapse of the fluid column and a resulting total coalescence. Conversely, when $Oh_s > Oh$, the horizontal collapse is favored by the reinforcement of the external rotation, which explains the cusp-like shape observed at latter stages of the process (Fig. 7.4c-d). For moderate Oh_s, the viscous diffusion of the external rotation is limited and the horizontal collapse occurs below the equator, the coalescence is partial (dashed arrows in Fig. 7.9). At higher Oh_s, the external rotation reaches the top of the droplet, thus also promoting the vertical collapse; the coalescence is total (dash-dot arrows in Fig. 7.9). When $Oh_s = Oh_{s/th} \simeq 0.32$, the distance over which momentum is diffused is about $0.5R_i$ during the whole coalescence ($t = 0.8\tau_\sigma$),

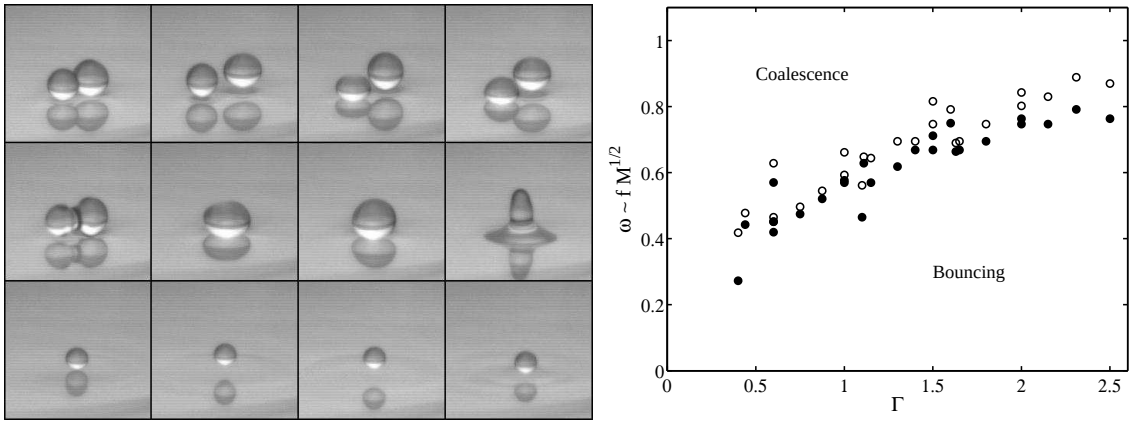

(a) (b)

Figure 7.10: (a) Two droplets are periodically bouncing on a vibrated bath, when they meet and coalesce together. The resulting droplet is too heavy to bounce, so it coalesces partially with the bath. The daughter droplet has a suitable mass for permanent bouncing. (b) Maximum size for bouncing as a function of the forcing acceleration Γ, for various frequencies. (•) Stable bouncing droplets, and (∘) unstable bouncing droplets that ends up partially coalescing.

which is coherent with the proposed mechanism. Although this latter is still hypothetical and must be confirmed by experiments and numerical simulations, it can rationalize the role played by each viscosity on the partial/total transition.

7.5 Stopping a cascade of partial coalescences

In a microfluidic perspective, the partial coalescence might be of interest for tuning the volume of a droplet, provided that the resulting daughter can be retrieved. In other words, the cascade of partial coalescences must be stopped before the ultimate total coalescence. This goal is naturally achieved by vibrating the bath on which the droplet coalesces [163]. Indeed, as seen in Chap. 5, a droplet of mass M bounces on a bath vibrated with a forcing frequency f provided the forcing acceleration is larger than a threshold $\Gamma_{th}(\omega)$ where $\omega = 2\pi f\sqrt{M/k}$ and $k = 32\pi\sigma/3$. Therefore, for given forcing parameters (Γ, f), there is a critical droplet mass $M_{th} \sim (\omega/f)^2$ above which droplets coalesce and below which they can bounce. Droplets heavier than M_{th} thus coalesce partially until their daughter reaches a mass suitable for bouncing (Fig. 7.10a). In some sense, the system behaves as a low-pass filter that only selects droplets smaller than a critical mass M_{th}. Droplets of different sizes have been released on a bath vibrated with various forcing parameters (Γ,f). Figure 7.10(b) indicates which ones were observed to bounce and which ones coalesced partially. Data from different f collapse when ω is considered instead of M. For each Γ, there is a threshold ω_{th}, tuned by the forcing parameters, that prescribes the maximum size for permanent bouncing.

7.6 Summary

Low viscosity droplets are seen to partially coalesce into a static bath; a smaller droplet is formed at the end of the coalescence process. This daughter droplet may also partially coalesce

and so on and so forth until the droplet reaches a critical size below which it totally coalesces. The exact conditions for partial coalescence have been investigated for droplets crossing an interface between two immiscible liquids. Partial coalescence is possible when both Bond and Ohnesorge numbers are smaller than some critical values. Capillary waves may be observed at the surface of the droplet. The exact relation between them and the partial coalescence has been discussed. Finally, we have shown that a cascade of partial coalescences can be stopped by vibrating the underlying bath; the droplet partially coalesces until it reaches a suitable size for bouncing. The vibrating bath is thus considered as a low-pass filter that only selects small droplets. Large droplets are reduced through partial coalescence until their size is appropriate.

Part II

Droplets on fibers

Chapter 8

A droplet on a vertical fiber

In the early morning, the spider webs in our gardens are often covered with a myriad of dew pearls. At dawn, the fresh and humid air condenses into a thin water film on the threads. Quickly, this film turns into a string of droplets, the smallest of which stay on the web and wait for the first sunbeams to evaporate again. The biggest slide and roll along the web (Fig. 8.1), collide and fuse together, leave pearls in their wake, and sometimes fall from the web due to a possible overweight.

Droplets on fibers are omnipresent in nature and everyday life. The first work that explores the subject is probably the book of the belgian physicist Joseph Plateau, published in 1873 [74]. Since, a relatively small number of studies were dedicated to the interactions between individual droplets and fibers. Physicists have rather investigated the flows of liquid films on threads [164, 165, 166]. However, "fusion", "sliding", "micro-droplets" are words commonly used in digital microfluidics. In these chapters, we show how the droplet behavior on those "arachnidean" buildings can indeed inspire new ways for microfluidics.

8.1 Experimental method

The method explained here below is shared by experiments from both chapters 8 and 9. Fibers made of nylon (fishing thread) are tight on a metallic frame. The tension in fibers is supposed of negligible influence on the droplet motion. Unless otherwise stated, droplets are made of silicon oil (Dow Corning 200), though the results may be generalized to any liquid that wets nylon. Experiments involve droplets made of six different viscosities (1.5, 5, 10, 20, 50 and 100 cS) and fibers of 5 different diameters (80, 100, 140, 200 and 250 μm). Droplets are directly released on the fibers with a syringe. The droplet size is varied by changing the needle diameter. Moreover, by moving the release point on the fiber, one can tune the volume of the droplet when it enters a specified region of interest. Indeed, as explained below, the droplet loses some mass by coating the fiber; so the greater the distance between the release point and the region of interest, the smaller the resulting droplet (Fig. 8.2a). About 500 droplets have been filmed from the side with a high-speed camera (recording frequency up to 1000 fps). Measures are made by image processing (Fig. 8.2b).

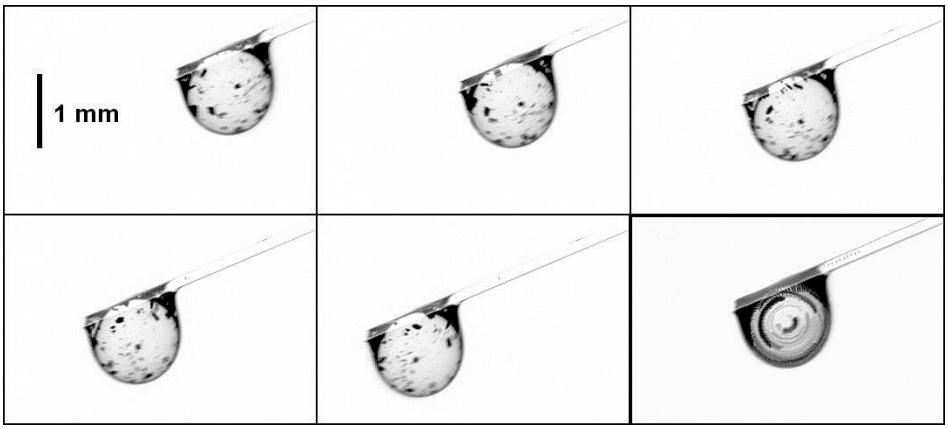

Figure 8.1: An oil droplet ($\nu = 100$ cS) slides and rolls along a fiber of diameter 140 μm. Snapshots are taken every 50 ms. The background, including the originally dry fiber, is subtracted in order to reveal the micrometric coating film left in the wake of the droplet. The last picture corresponds to the sum of formers; particles within the droplet follow circular paths, indicating that the droplet rolls on the fiber.

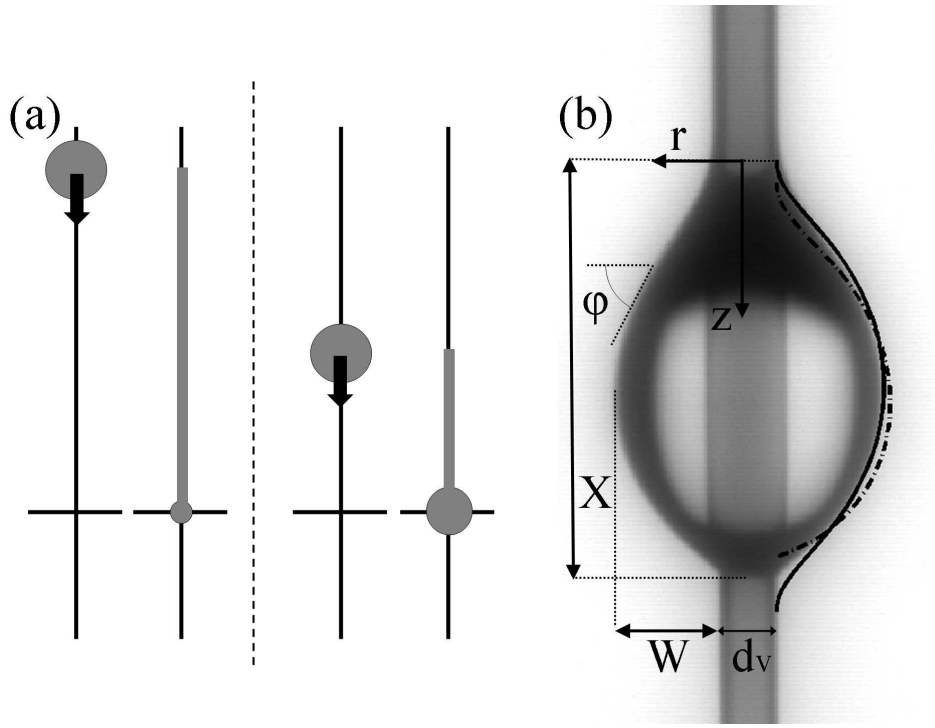

Figure 8.2: (a) The droplet size is tuned by changing the release point, and so the distance to the region of interest. (b) Axisymmetric shape of a droplet on a vertical fiber. The dash-dot (resp. solid) line corresponds to the numerical solution of Eq. (8.1) with (resp. without) gravity.

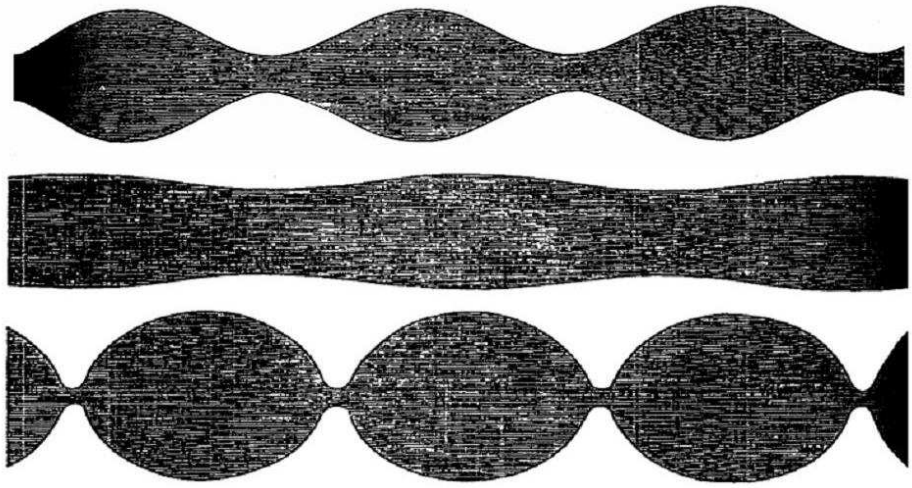

Figure 8.3: Drawings of Joseph Plateau [74]: the liquid form a string of pearls called unduloid on fibers of various diameters.

8.2 Geometry

Joseph Plateau has already observed that, due to surface tension only, a liquid covering a fiber spontaneously turns into a string of pearls (Fig. 8.3) called unduloid. This instability has been rationalized a few years later by Lord Rayleigh [75]. Nevertheless, droplets may take other shapes than the one proposed by Plateau. For example, the axisymmetry of the shape is broken down by gravity for large droplets on a horizontal fiber. If the liquid does not perfectly wet the fiber (e.g. pure water on nylon), the droplet cower on one side of the fiber, without wrapping it [167, 168]. Such droplets often hang at rest on a vertical fiber [169]; their weight is balanced by a bottom-up difference in contact angle. In this thesis, we mainly study droplets that perfectly wet fibers and slide on them.

On a vertical fiber of diameter d_v, wetting droplets take an axisymmetric shape of volume Ω, close to the unduloid of Plateau (Fig. 8.2b), dimensions (width W and extension X) of which are represented as a function of Ω in Fig. 8.4(a-b). This shape is computed theoretically as $[r(s), z(s), \varphi(s)]$, where s is the curvilinear coordinate along a meridian of the interface (Fig. 8.2b). If supposing a balance between gravity and surface tension, the Laplace equation (1.2) yields

$$\left\{ \begin{array}{l} \dfrac{\mathrm{d}r}{\mathrm{d}s} = \cos\varphi, \\ \dfrac{\mathrm{d}z}{\mathrm{d}s} = \sin\varphi, \\ \dfrac{\mathrm{d}\varphi}{\mathrm{d}s} = \dfrac{\Delta P}{\sigma} - \dfrac{\sin\varphi}{r} + \dfrac{z}{\lambda_\sigma^2}, \end{array} \right. \tag{8.1}$$

where ΔP is the overpressure within the droplet, at location $z = 0$. Nevertheless, if this balance gravity / surface tension was effective, the droplet would stay at rest on the fiber. The observed sliding of the droplet suggests that viscous stresses have to be taken into account. Therefore, we may suppose that these stresses balance gravity, and that surface tension forces balance themselves. To assess this hypothesis, Eq. (8.1) is solved numerically, successively with and without the gravity term z/λ_σ^2. The comparison with experimental observations

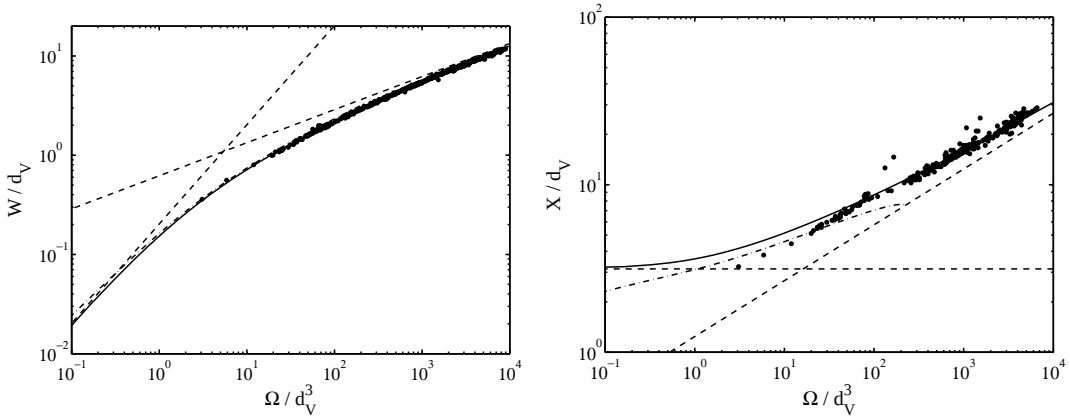

(a) (b)

Figure 8.4: (a) Width W and (b) extension X of a droplet of volume Ω on a fiber of diameter d_v. The dashed line represents the asymptotic scalings (G.3) and (G.6). The solid line (resp. dash-dot line) corresponds to the numerical solution of (8.1) without (resp. with) considering the gravity term z/λ_σ^2.

(Fig. 8.2b and 8.4b) clearly confirms this second scenario; gravity can be neglected in the Laplace equation and the droplet indeed takes an unduloidal shape. Although this unduloid cannot be described with a simple explicit equation, it is possible to find analytical expressions in the asymptotic regimes $\Omega \gg d_v^3$ and $\Omega \ll d_v^3$ (App. G).

8.3 Short-term steady motion

The motion of a droplet on a vertical fiber involves several effects with specific timescales. Starting from rest, the droplet first accelerates and quickly reaches (in less than 0.1 s) a limit speed where viscous effects balance gravity, as shown indirectly in the previous section. On the other hand, the droplet leaves some mass in the coating film; the mass loss becomes significant after several seconds. Therefore, only the (not too) short-term velocity may be considered as constant. The gravity/viscosity balance has already been encountered in other related systems, such as the propagation of a slug in a tube [36], or the droplet motion on horizontal fibers induced by thermal effects [170], geometry [171] or aerodynamic forces [172]. The friction is due to velocity gradients within the droplet, that are estimated by $c_{\nu 1} v/W \cdot X/2z$. Here, z is the distance to the nearest contact line and $c_{\nu 1}$ a proportionality factor that may depend on surface tension among others. The resulting viscous force is

$$F_\nu = 2 \cdot \pi d_v \int_0^{X/2} c_{\nu 1} \frac{\mu v}{z} \frac{X}{2W} \mathrm{d}z. \tag{8.2}$$

This integral diverges due to the singularity at contact point ($z = 0$). In order to solve this paradox, one may begin to integrate from $z = \Xi \sim 10^{-9}$ m - the characteristic length of the molecular film covering the fiber - instead of $z = 0$. This yields

$$F_\nu = \pi c_{\nu 1} \alpha \nu \rho d_v \frac{X}{W} v, \tag{8.3}$$

where

$$\alpha = \ln(X/2\Xi) \simeq 15. \tag{8.4}$$

Balancing this force with the droplet weight $\rho g \Omega$ gives

$$\frac{\nu v}{g d_v^2} = \frac{1}{\pi c_{\nu 1} \alpha} \frac{W}{X} \frac{\Omega}{d_v^3}. \tag{8.5}$$

As previously seen (Fig. 8.4), the dependence of W/X on Ω/d_v^3 is complex in the general case, but droplets sufficiently large compared to the fiber tend to be spherical, so $W/X \to 0.5$. Equation 8.5 is in excellent agreement with experimental results (Fig. 8.5), whatever the fiber diameter d_v, provided that $c_{\nu 1}$ satisfies

$$c_{\nu 1} = c_{\nu 2} \sqrt{\frac{\lambda_\sigma}{d_v}} \Rightarrow \frac{\nu v}{g d_v^2} = \pi c_{\nu 2} \alpha \sqrt{\frac{d_v}{\lambda_\sigma}} \frac{W}{X} \frac{\Omega}{d_v^3}. \tag{8.6}$$

The factor $\sqrt{d_v/\lambda_\sigma}$ clearly indicates that gravity is not perfectly balanced by viscous effects, and that surface tension also plays a role in the droplet limit velocity. The coefficient $c_{\nu 2}$ is of the order of unity; it slightly depends on the viscosity when this one is lower than 10 cS. The following empirical law is proposed (inset of Fig. 8.5):

$$c_{\nu 2} = 0.33 \left(1 + 0.01 \frac{\sqrt{g \lambda_\sigma^3}}{\nu} \right). \tag{8.7}$$

We can now estimate the acceleration time of the droplet

$$t_{acc} \sim \frac{v}{g} = \frac{1}{\pi c_{\nu 2} \alpha} \sqrt{\frac{d_v}{\lambda_\sigma}} \frac{W}{X} \frac{\Omega}{d_v \nu}, \tag{8.8}$$

and check that, for a typical velocity of 1 m/s, the steady regime is reached after 0.1 s.

8.4 Long-term mass loss

The coating of a solid by a liquid has been deeply investigated since the pioneering work of Landau, Levich and Derjaguin [173]. The LLD theory rationalizes the coating of a fiber slowly pulled out of a liquid bath. The thickness δ of the coating film is given by

$$\frac{\delta}{d_v} = c_{we} Ca^{2/3} \quad \text{with} \quad Ca = \frac{\mu v}{\sigma}, \tag{8.9}$$

where Ca is the capillary number and the wetting constant $c_{we} = 0.67$ according to the authors. Many corrections (gravity, inertia, geometry, wetting, etc.) can be implemented by simply changing this factor c_{we} [174]. For example, $c_{we} = 1.07$ when the fiber crosses the interface between two immiscible liquids [175, 36].

Sliding droplets are observed to coat fibers exactly as if these latter were pulled out of a bath. Consequently, the droplets lose some mass through coating as they move on the fiber. Equation (8.9) may be applied to predict the mass loss and be coupled to (8.6) in order to get the long-term trajectory of the droplet. Denoting by Z the vertical position of the droplet mass center, the volume variation $\dot{\Omega}$ is

$$\dot{\Omega} = -\pi d_v \delta \dot{Z} = -\pi c_{we} d_v^2 \left(\frac{\mu}{\sigma} \right)^{2/3} \dot{Z}^{5/3}. \tag{8.10}$$

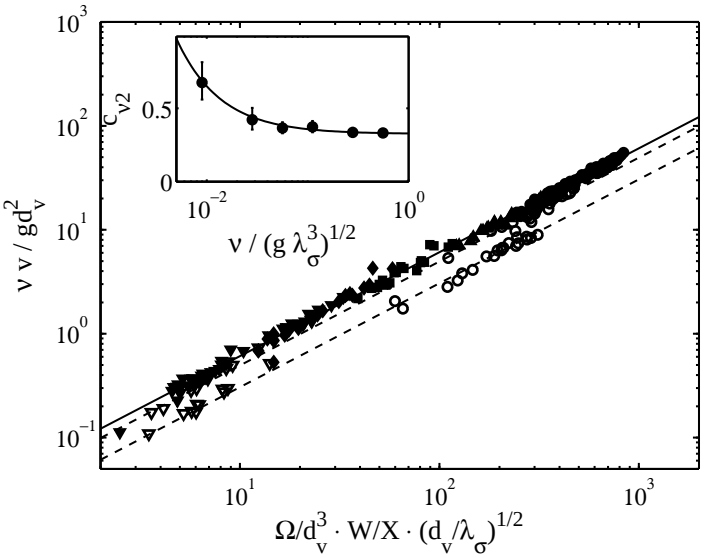

Figure 8.5: Short-term balance: normalized velocity $\nu v/gd_v^2$ as a function of the normalized volume Ω/d_v^3. Black (resp. white) symbols correspond to viscosity $\nu \geq 10$ cS (resp. $\nu < 10$ cS). ($\circ$,$\bullet$) $d_v = 80$ μm, ($\blacktriangle$) $d_v = 100$ μm, ($\blacksquare$) $d_v = 140$ μm, ($\blacklozenge$) $d_v = 200$ μm, ($\blacktriangledown$,$\triangledown$) $d_v = 250$ μm. The solid line represents Eq. (8.6) where $c_{\nu 2}$ takes its high-viscosity value (0.33). The dashed line is Eq. (8.6) in the low-viscosity regime, i.e. $c_{\nu 2} > 0.33$. (Inset) Coefficient $c_{\nu 2}$ as a function of the normalized viscosity $\nu/\sqrt{g\lambda_\sigma^3}$. The solid line corresponds to Eq. (8.7).

We proceed by deriving (8.6) according to time, supposing that W/X is constant:

$$\dot{\Omega} = \pi c_{\nu 2} \alpha \frac{X}{W} \sqrt{\frac{\lambda_\sigma}{d_v}} \frac{\nu d_v \ddot{Z}}{g}. \tag{8.11}$$

Both equations yield

$$\begin{aligned} \ddot{Z} &= -\frac{c_{we}}{c_{\nu 2}\alpha} \frac{W}{X} \sqrt{\frac{d_v}{\lambda_\sigma}} \left(\frac{\mu}{\sigma}\right)^{2/3} \frac{g d_v}{\nu} \dot{Z}^{5/3}, \\ &= -w \dot{Z}^{5/3} \quad \text{with} \quad w = \frac{-c_{we}}{c_{\nu 2}\alpha} \frac{W}{X} \sqrt{\frac{d_v}{\lambda_\sigma}} \left(\frac{\mu}{\sigma}\right)^{2/3} \frac{g d_v}{\nu}, \end{aligned} \tag{8.12}$$

where the parameter w only depends on physical constants. This equation is integrated twice;

$$Z = \frac{{\dot{Z}_i}^{1/3} - \left({\dot{Z}_i}^{-2/3} + \frac{2}{3} w t\right)^{-1/2}}{w/3}, \tag{8.13}$$

where $\dot{Z}_i$ is the initial velocity of the droplet. Predictions of Eq. (8.13) are compared to the observed long-term trajectories (Fig. 8.6). The initial velocity $\dot{Z}_i$ is fitted on the experiments, and w is computed by successively taking $c_{we} = 0.67$ and $c_{we} = 1.5$. This second value gives an accurate description of the trajectory, whatever the droplet viscosity or size. Finally, we check a posteriori that the ratio W/X is approximately constant over a trajectory. Typically, W/X variations become significant when Ω is varied by a factor 10, which happens after about $5.5/(w{\dot{Z}_i}^{2/3})$, so 89 s for the ($\blacktriangledown$)-curve in Fig. 8.6.

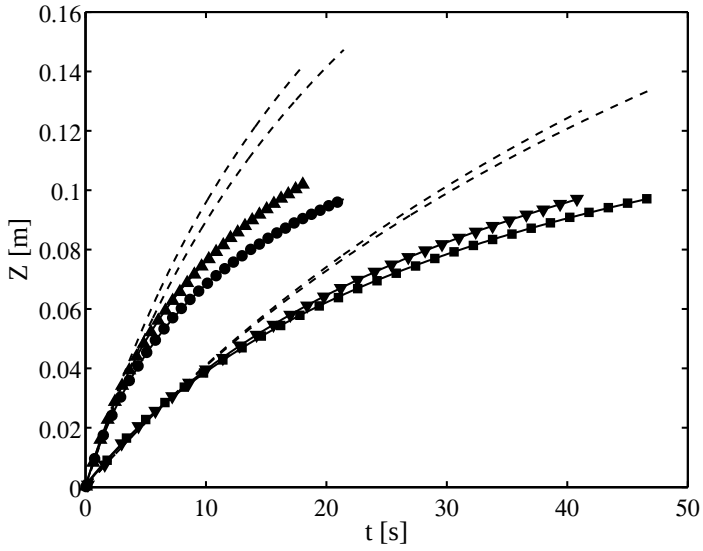

Figure 8.6: Long-term trajectories $Z(t)$ of droplets with various viscosity and size on a fiber of diameter $d_v = 250$ μm. The solid line (resp. dashed line) corresponds to Eq. (8.13) with $c_{we} = 1.5$ (resp. $c_{we} = 0.67$).

8.5 Shape transition

The droplet shape on a fiber is not always axisymmetric and unique; several equilibrium configurations may coexist, some being more stable than others [168]. We have seen that some 100 cS droplets sliding on a vertical fiber can remain in a metastable asymmetrical shape. At any moment, these droplets quickly switch to the well-known axisymmetrical configuration. By the way, the friction is considerably increased and the droplets immediately slow down (Fig. 8.7a). The inverse transition has never been observed and is likely impossible.

The velocity v_f of the final symmetrical shape has been measured as a function of the initial velocity v_i before the transition, for 100 cS droplets on various fibers (Fig. 8.7b). Data suggest

$$v_f = 0.30 v_i, \tag{8.14}$$

so the friction coefficient $c_{\nu 2}$ is about 3.3 times less in the asymmetrical configuration.

We have observed a similar transition on inclined fibers, though both configurations are asymmetric in that case (Fig. 8.8). The velocity is only decreased by a factor 2.

8.6 Summary

In this chapter, we have characterized the shape and motion of a droplet on a vertical fiber. Provided that the droplet wets the fiber, it takes an axisymmetric shape and starts sliding down the fiber. After a short acceleration, the droplet reaches its terminal velocity, that results from a balance between its weight and the viscous friction on the fiber. As the droplet slides, it coats the fiber and loses some mass. Consequently, the terminal velocity slowly decreases. Finally, we have observed that the droplet may keep a metastable asymmetric shape for seconds before axisymmetry is recovered.

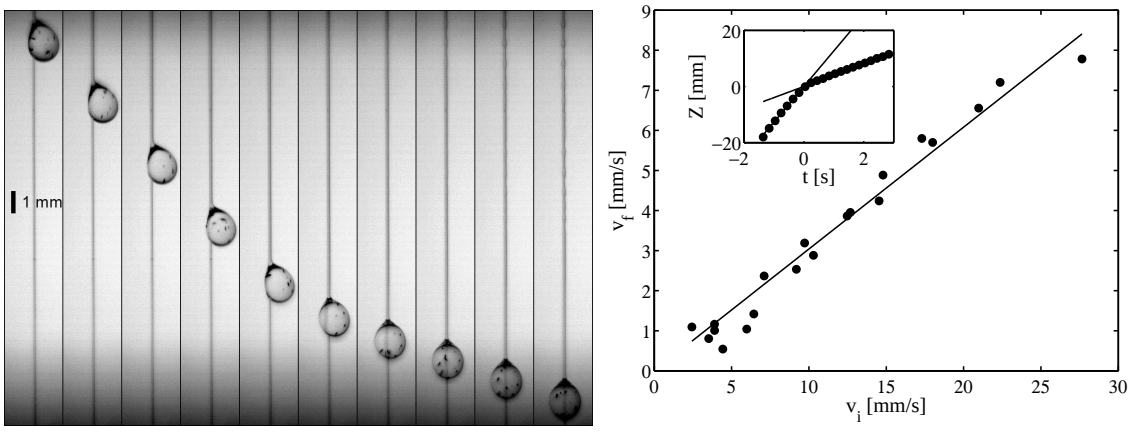

(a) (b)

Figure 8.7: (a) A 100 cS droplet slides along a vertical fiber of diameter $d_v = 160$ μm. Snapshots are taken every 160 ms. The initially asymmetrical shape suddenly becomes symmetric, which decreases the droplet velocity from 18 mm/s to 5.7 mm/s. (b) Velocity of the symmetrical shape v_f as a function of the velocity of the corresponding asymmetrical shape v_i. The solid line corresponds to Eq. (8.14). (Inset) Typical trajectory $Z(t)$ of a droplet experiencing a shape transition in $t = 0$. The solid lines represent constant velocity trajectories.

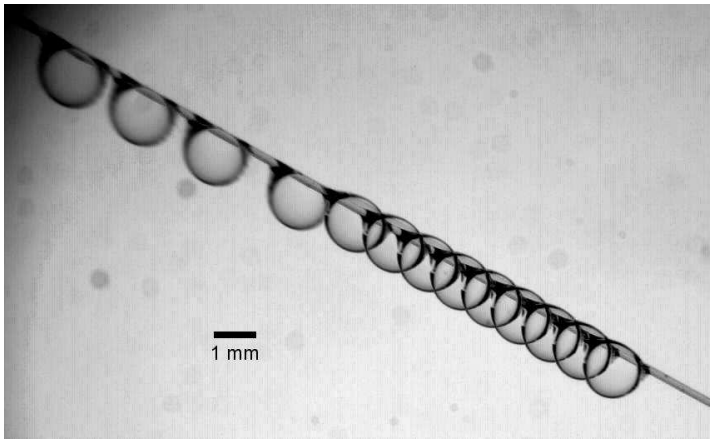

Figure 8.8: A 100 cS droplet slides along an inclined fiber of diameter $d_v = 140$ μm. Snapshots are taken every 320 ms and superposed together. The shape transition increases the friction, so decreasing the velocity from 6 mm/s to 3 mm/s.

Chapter 9

Intersection between two fibers

In chapter 8, we have studied droplet motion on a single fiber. We naturally proceed by discussing the behavior of droplets as they encounter an intersection between two fibers. The junction is simply made by placing a horizontal fiber next to the vertical one, so they just touch each other; contact is ensured by the tension between fibers.

9.1 Blocking/crossing transition

Droplets are released on the vertical fiber, upstream from the intersection. As they approach, two scenarios are observed: small droplets remain pinned on the node (Fig. 9.1a) while larger droplets cross the intersection and keep sliding downwards (Fig. 9.1b). The trapping of small droplets is mainly due to the capillary forces developed by the horizontal fiber. On the other hand, large droplet are likely too heavy to hang on the horizontal fiber. Lorenceau and Quéré have already investigated problems that involve the same mechanism, namely falling droplets that impact a sieve [176] or a horizontal fiber [177]. The balance between gravity and surface tension is the Bond number related to the fiber, defined as

$$Bo = \frac{Mg}{2\pi\sigma d_h}, \tag{9.1}$$

where d_h is the diameter of the horizontal fiber. A sharp transition is observed between blocking and crossing regimes (Fig. 9.2a); there is a critical Bond number $Bo_{th} \sim 1$ above which droplets cross the node and below which they are blocked. The intersection behaves as a fluidic diode. This Bo_{th} depends on the droplet viscosity ν, at least when this latter is small.

When crossing, a tiny amount of liquid is still trapped by the horizontal fiber, so the droplet mass (and corresponding Bond number Bo_f) after crossing is slightly lower than before (Bo_i). Although this volume cannot be accurately measured, it should be about a few times the "volume" of the intersection, namely $d_h d_v (d_h + d_v)$.

Large high viscosity droplets may experience significant delays (sometimes as long a several seconds) when they cross the intersection (Fig. 9.3). These delays are shown to diverge as $Bo \to Bo_{th}$, as often in physics when a potential barrier is just crossed (Fig. 9.2b). The divergence is not observed for low viscosity droplets, whose crossing time remains small.

As already seen in Fig. 9.2, the threshold Bond number Bo_{th} increases with the droplet viscosity, and saturates to a limit value in the high viscosity regime where delays are observed.

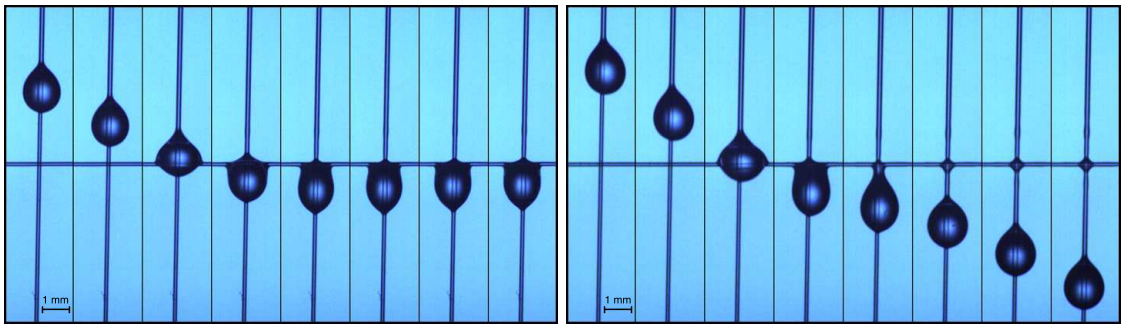

(a) (b)

Figure 9.1: A 5 cS oil droplet interacts with a junction between two nylon fibers (diameter 140 μm). Snapshots are taken every 10 ms. The intersection behaves as a fluidic diode: (a) A small droplet is pinned on the junction, while (b) a large droplet crosses it. In that latter case, a tiny amount of liquid is left at the intersection.

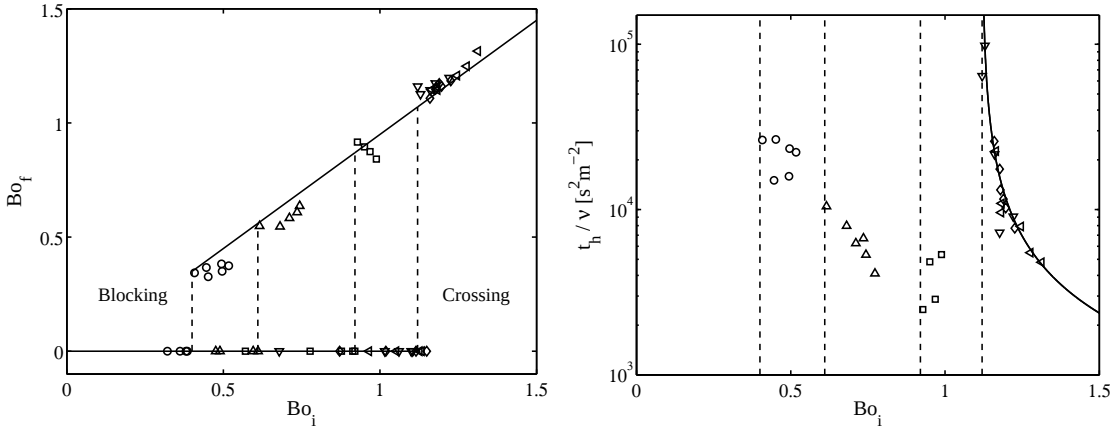

(a) (b)

Figure 9.2: (a) Relationship between the volume of liquid allowed to cross the node and the initial droplet volume, expressed in terms of Bond numbers $Bo_f(Bo_i)$. The solid lines correspond to equations $Bo_f = 0$ when $Bo_i < Bo_{th}$ (blocking) and $Bo_f = Bo_i - 0.05$ when $Bo_i > Bo_{th}$ (crossing). (b) Time t_h needed by the droplet to cross the intersection, as a function of Bo_i. The solid line is the empirical law $t_h/\nu = 900/(Bo_i - Bo_{th})$. (a-b) Experimental data for $d_h = 250$ μm and $d_v = 80$ μm: ($\circ$) $\nu = 1.5$ cS, ($\triangle$) $\nu = 5$ cS, ($\square$) $\nu = 10$ cS, ($\triangledown$) $\nu = 20$ cS, ($\Diamond$) $\nu = 50$ cS and ($\triangleleft$) $\nu = 100$ cS. Error bars typically correspond to the symbol size. The dashed lines correspond to the Bo_{th} values.

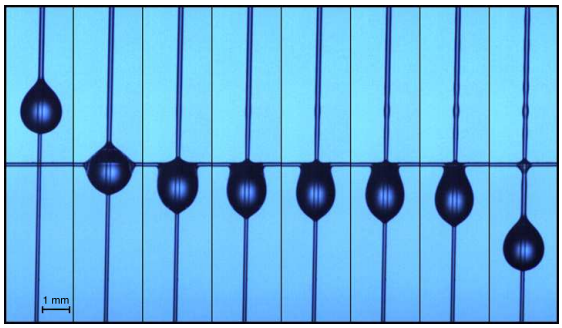

Figure 9.3: A delay of nearly 0.2 s is observed when a 50 cS droplet with $Bo \rightarrow Bo_{th}$ crosses the intersection between two fibers of diameter 140 μm. Snapshots are taken every 34 ms.

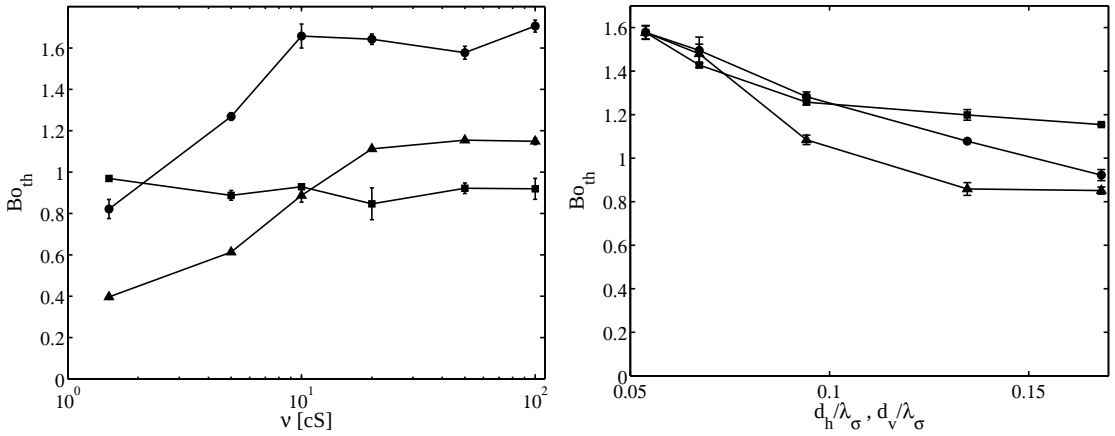

(a) (b)

Figure 9.4: (a) Variation of Bo_{th} with the droplet viscosity ν for (•) $d_h = d_v = 80$ μm, (■) $d_h = 80$ μm and $d_v = 250$ μm, and (▲) $d_h = 250$ μm and $d_v = 80$ μm. (b) Variation of Bo_{th} with the fiber diameters, for $\nu = 50$ cS. (•) $d_h = 80$ μm and d_v is varied, (■) $d_v = 80$ μm and d_h is varied, and (▲) $d_h = d_v$ are both varied.

The critical viscosity above which Bo_{th} is constant depends on the fiber diameter (Fig. 9.4a). In general, Bo_{th} decreases with increasing fiber diameter (Fig. 9.4b) in a non-obvious way.

9.1.1 Modeling

In order to model the behavior of a droplet interacting with a junction between two fibers, we have first to measure and analyze the droplet trajectory. Observations are again qualitatively different depending on the viscosity regime. As already mentioned, high viscosity droplets cross the junction with a delay time that increases as they approach the threshold Bo_{th} (Fig. 9.5a). Small droplets are smoothly blocked, and the trajectory is always monotonic. Low viscosity droplets do not experience any significant delay when crossing is allowed. Moreover, small blocked droplets largely oscillate before coming at rest on the node (Fig. 9.5b).

These results strongly suggest to model the droplet as a damped harmonic oscillator whose

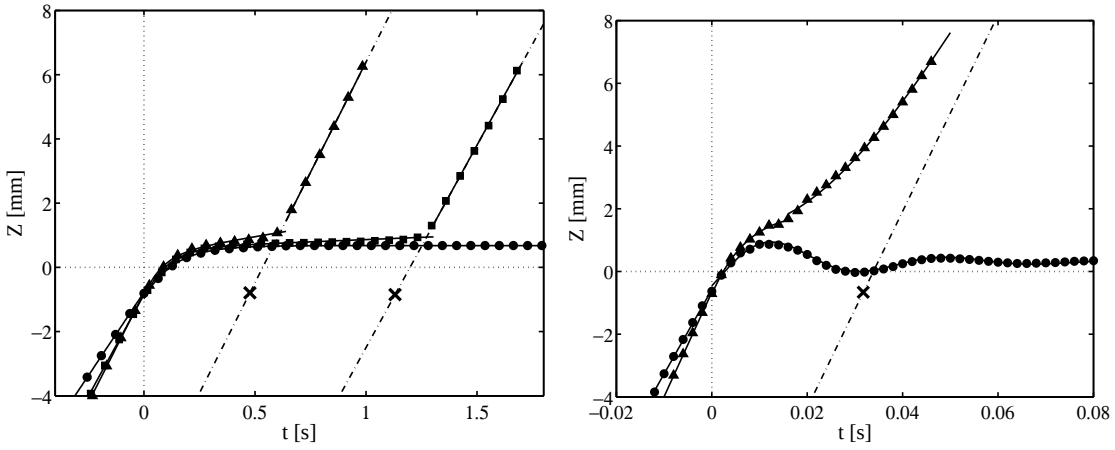

(a) (b)

Figure 9.5: (a) Droplet trajectory in the high-viscosity regime, namely for $d_h = d_v = 80\,\mu$m and $\nu = 100$ cS, so $Bo_{th} \simeq 1.67$. (•) Blocking for $Bo_i = 1.54$, (▲) crossing for $Bo_i = 1.87$, and (■) crossing with delay for $Bo_i = 1.68$. (b) Droplet trajectory in the low-viscosity regime, namely for $d_h = 250\,\mu$m, $d_v = 80\,\mu$m and $\nu = 1.5$ cS, so $Bo_{th} \simeq 0.41$. (•) Blocking for $Bo_i = 0.38$, and (▲) crossing for $Bo_i = 0.52$. In both (a) and (b), the solid line corresponds to the fit of Eq. (9.2), while the dash-dot line represents the linear trajectory that the droplet would have taken if it had not been delayed by the horizontal fiber. The cross indicates the delay time t_h.

restoring force is truncated to the neighborhood of the node, i.e.

$$M\ddot{Z} + c_{\mu 1}\mu\Omega^{1/3}\dot{Z} + kZ\chi_{[-Z_1,Z_2]}(Z) = Mg, \tag{9.2}$$

where $c_{\mu 1}$ is the friction coefficient, $\chi_{[-Z_1,Z_2]}(Z)$ is the characteristic function equal to 1 when $-Z_1 < Z < Z_2$ and 0 otherwise, and k is the stiffness of the spring mechanism related to the horizontal fiber, so

$$k = c_k\sigma = c_\sigma \frac{d_h}{\Omega^{1/3}}\sigma. \tag{9.3}$$

The position Z of the droplet mass center is counted from the intersection, thus corresponding to $Z = 0$. Equation (9.2) is put in a dimensionless form by using

$$y = Z/Z_1 \tag{9.4}$$

and $\tau = \sqrt{k/M}t$;

$$\ddot{y} + 2\beta\dot{y} + y\chi_{[-1,\kappa]}(y) = \Theta, \tag{9.5}$$

where

$$\kappa = Z_2/Z_1, \qquad 2\beta = \frac{c_{\mu 1}}{\sqrt{c_\sigma}}\frac{\mu}{\sqrt{\rho\sigma d_h}} \quad \text{and} \quad \Theta = \frac{Mg}{kZ_1} = \frac{2\pi\Omega^{1/3}}{c_\sigma Z_1}Bo. \tag{9.6}$$

We note that the damping factor β is equivalent to an Ohnesorge number based on d_h, and the forcing parameter Θ is proportional to the Bond number.

This equation may be solved starting from the initial condition $y(0) = -1$ and $\dot{y}(0) = \Theta/2\beta$, i.e. when the droplet, evolving at the limit speed $\Theta/2\beta$ as described in Chap. 8,

touches the horizontal fiber. Like in the classical damped oscillator, two regimes are observed in Eq. (9.5) according to the value of β. For $\beta > 1$, the system is overdamped and corresponds to the high-viscosity regime, while it is underdamped otherwise.

In the overdamped regime $\beta > 1$, the solution is

$$y(\tau) = \Theta - \mathrm{e}^{-\beta\tau}\left[(1+\Theta)\cosh(\Phi\tau) + \frac{2\beta^2(1+\Theta)-\Theta}{2\beta\Phi}\sinh(\Phi\tau)\right], \tag{9.7}$$

where

$$\Phi = \sqrt{|\beta^2 - 1|}. \tag{9.8}$$

The solution always tends monotonically towards $y = \Theta$. Nevertheless, the solution is not valid anymore when $y > \kappa$ due to the truncation; $\Theta_{th} = \kappa$ is therefore the threshold that separates blocking ($\Theta < \kappa$) and crossing ($\Theta > \kappa$) behaviors. The crossing time obviously diverges when $\Theta \to \kappa^+$, as in experiments.

In the underdamped regime $\beta < 1$, the solution is

$$y(\tau) = \Theta - \mathrm{e}^{-\beta\tau}\left[(1+\Theta)\cos(\Phi\tau) + \frac{2\beta^2(1+\Theta)-\Theta}{2\beta\Phi}\sin(\Phi\tau)\right]. \tag{9.9}$$

The solution also tends towards $y = \Theta$, but with damped oscillations. The critical point $y = \kappa$ is necessarily reached at the first oscillation, so the crossing delay cannot be larger than the oscillator period. The blocking/crossing threshold Θ_{th} is obtained when the first maximum of Eq. (9.9) coincides with $y = \kappa$, which yields

$$y(\tau_{th}, \Theta_{th}) = \kappa \quad \text{with} \quad \tan(\Phi\tau_{th}) = \frac{-\Theta_{th}\Phi}{\beta(\Theta_{th}+2)}, \tag{9.10}$$

where τ_{th} is the time of first maximum when $\Theta = \Theta_{th}$. This system of implicit equations with unknowns (τ_{th}, Θ_{th}) cannot be solved analytically. Nevertheless, it can be shown that $(\tau_{th}, \Theta_{th}) \to (\pi, 0)$ when $\beta \to 0$.

When crossing occurs and y passes the κ-point in τ_κ, the droplet starts accelerating again until it reaches its terminal velocity:

$$y(\tau) = \kappa + \frac{\Theta}{2\beta}(\tau - \tau_\kappa) - \frac{\Theta - 2\beta\dot{y}(\tau_\kappa)}{4\beta^2}\left[1 - e^{-2\beta(\tau-\tau_\kappa)}\right], \tag{9.11}$$

where $\dot{y}(\tau_\kappa)$ is the velocity at the exit point $y = \kappa$.

Equations perfectly fit experimental trajectories (Fig. 9.5). As seen in Fig. 9.6, the fitting parameters $c_{\mu 1}$ and c_σ approximately satisfy

$$\begin{cases} c_{\mu 1} = c_{\mu 2}\left(\frac{d_h}{\lambda_\sigma}, \frac{d_v}{\lambda_\sigma}\right)\frac{\lambda_\sigma^3}{\Omega}, \\ c_\sigma = c_\sigma\left(\frac{d_h}{\lambda_\sigma}, \frac{d_v}{\lambda_\sigma}\right). \end{cases} \tag{9.12}$$

More precisely, we obtain for $d_v = 80$ μm, Dimensionless parameters Θ and β are computed for each experiment, starting from these values of $c_{\mu 2}$ and c_σ. The agreement with the theoretical equation (9.10) is rather good (Fig. 9.7), considering the significant error made by converting the measured physical parameters into dimensionless quantities β and Θ.

	$d_h = 80\ \mu$m	$d_h = 250\ \mu$m
$c_{\mu 2}$	$13 \pm 20\%$	$27 \pm 12\%$
c_σ	$16 \pm 18\%$	$9.9 \pm 22\%$

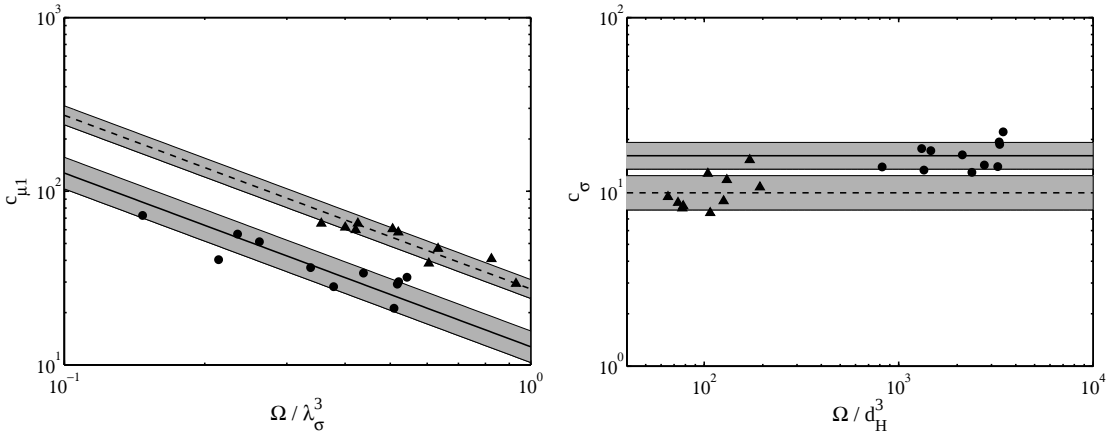

(a) (b)

Figure 9.6: Coefficients $c_{\mu 1}$ and c_σ of the dimensional model (9.2). Symbol data are obtained by fitting this model to the experimental trajectories. The lines correspond to Eq. (9.12), the shaded areas represent standard deviations. The (•) and solid line (resp. (▲) and dashed line) correspond to $d_h = 80\ \mu$m (resp. $d_h = 250\ \mu$m), while $d_v = 80\ \mu$m in both cases.

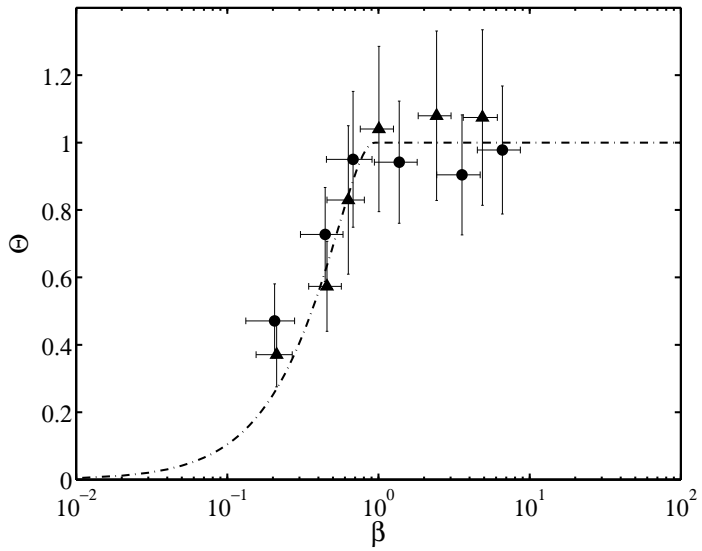

Figure 9.7: Dimensionless threshold curve $\Theta(\beta)$ given by Eq. (9.10). Symbols represent the experimental data for $d_v = 80\ \mu$m and (•) $d_h = 80\ \mu$m or (▲) $d_h = 250\ \mu$m. The conversion from dimensional measurements to dimensionless variables is made through Eq. (9.6).

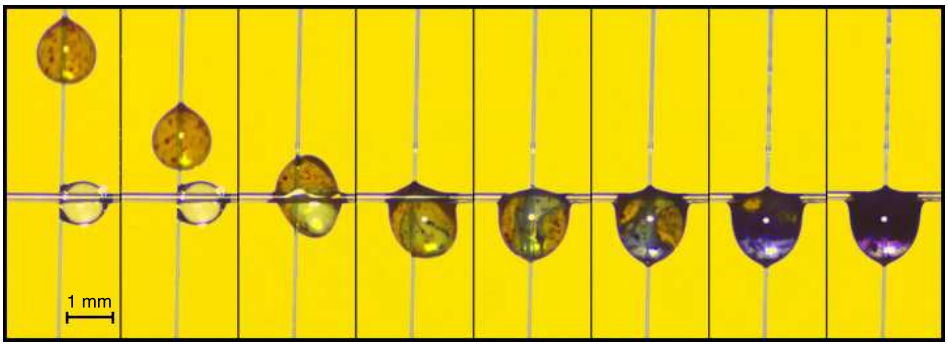

Figure 9.8: A H_2SO_4 droplet (upcoming) fuses with a $NaOH$ droplet on a node. The reaction is revealed by bromomethyl blue. The snapshot length is 0.1 s.

Finally, we note that the parameter c_σ may be related to the critical Bond number Bo_{th}. Indeed, in the overdamped regime, $\Theta_{th} = \kappa$, so

$$Z_2 = 4\pi \frac{\Omega^{*1/3}}{c_\sigma} Bo_{th,\nu\to\infty}. \tag{9.13}$$

Measurements of $Bo_{th}(d_h, d_v)$ (directly from the experiments) and $c_\sigma(d_h, d_v)$ (from the trajectory fitting) suggest that $Z_2 = 0.68\Omega^{1/3}$, whatever d_h and d_v. Therefore,

$$c_\sigma \simeq 9.24 Bo_{th,\nu\to\infty}. \tag{9.14}$$

9.2 Microfluidic operations on fiber networks

We now proceed by showing that the intersection between two fibers may be the basic component of a new fiber-based microfluidic technology, exactly as the "T" junction in microchannels [178]. Indeed, a fiber junction is a perfect place to bring several droplets carrying a biochemical content and make them react together (Fig. 9.8). An efficient and spontaneous mixing occurs when both droplets coalesce together, the reaction is nearly completed after only a few tenths of seconds. The resulting droplet may flow down or remain pinned on the junction, depending on the initial volumes used in the process.

9.2.1 Division

A large droplet spontaneously divides into N small droplets on a network made of N parallel horizontal fibers that cross a single vertical fiber in N points. The large droplet crosses every junction, but coats the intervening vertical segments. The coating film destabilizes and the resulting pearls are collected on the next junction (Fig. 9.9a), giving birth to N localized microdroplets. An experimental prototype has been realized with 44 horizontal fibers (diameter $d_h = 80$ μm, spacing 4 mm) and a vertical fiber ($d_v = 80$ μm) mounted on a LEGO frame. An oil droplet of $\Omega = 2$ μL and $\nu = 5$ cS slides down the vertical fiber, the thin coating film left in its wake destabilizes and forms 44 pearls of volume about 60 nL, collected at the junctions.

By changing the fiber diameter and spacing, this division network can be optimized, e.g. with respect to the number of microdroplets N that are created from a single droplet. This

number obviously depends on the amount of liquid left by coating, which itself varies with the initial droplet velocity. This velocity is about

$$v \sim \frac{Mg}{33\mu\sqrt{d_v\lambda_\sigma}}, \tag{9.15}$$

which means that, according from the coating law of Landau-Levich, the mass loss per unit length is

$$\frac{dM}{dZ} = \pi\rho d_v\delta \sim 0.13\rho d_v^2\left(\frac{Mg}{\sigma\sqrt{d_v\lambda_\sigma}}\right)^{2/3}. \tag{9.16}$$

Remarkably, this mass loss does not depend on μ; approximately the same quantity of liquid is lost by coating, whatever the viscosity of the initial droplet. This fact is of importance since it ensures a strong robustness of the technique to the physical properties of the liquid of interest. The maximum length L that a droplet is able to travel on a vertical fiber before being entirely consumed and transformed in a coating film is

$$L \sim 4\left(\frac{\sigma}{\rho g d_v^2}\right)^{5/6}\Omega^{1/3}, \tag{9.17}$$

which is about 0.5 m for a 2 μL oil droplet on a 80 μm fiber. The droplet can thus travel about a distance equal 360 times its size when $d_v = 80\ \mu$m, and 180000 times when $d_v = 2\ \mu$m ! Since the spacing between fibers needs to be at least 3 times the droplet size, we conclude that about 100 micro-droplets may be generated on a 80 μm fiber network, and 50000 on 2 μm fibers ! Practically, the division factor is less, since a small part of the initial droplet is also directly retained at each junction.

The rate at which the division is performed mainly depends on the time needed by the micro-pearls to reach the next junction. Since the initial droplet is about 1 mm in diameter, a fiber spacing of 4 mm seems to be a reasonable minimum. Pearls of volume $\Omega \simeq 60$ nL and viscosity 5 cS have a velocity $\nu \simeq 10$ mm/s, so they are collected on the node in less than a second, as observed experimentally.

9.2.2 Multiplexing

The division process described here above is of particular interest for multiplexing issues. Multiplexing consists in making biochemical reactions in parallel between a liquid A and N liquids $B_1, B_2, ..., B_N$. One have to divide liquid A in N parts and make every of them react with one of the B_i liquids. For example, the droplet A, released on the vertical fiber of a division network, divides into N parts. Then, the setup is rotated 90°, and the B-droplets are placed on the newly vertical N fibers. The fusion and reaction between A and B occurs on the intersections.

Since the B droplets are made with a syringe, they may be too large to be blocked by the fibers. An improved prototype has been made in LEGO, in order to make a droplet A react with 4 droplets $B_i, i = 1...4$. This setup, schematized in Fig. 9.9(b), consists in a vertical fiber V_{250} (diameter 250 μm), four vertical fibers V_{80} (diameter 80 μm) and 4 horizontal fibers H_{250} (diameter 250 μm). Fibers are shifted in such a way that the H_{250} fibers touch the V_{250}, as well as only one of the V_{80}. An A droplet is released on V_{250}, it slides down the fiber and crosses the four intersections, leaving 4 microdroplets. The B_i droplets are placed on each V_{80}, they cross only one junction where they leave a single microdroplet. The setup is then

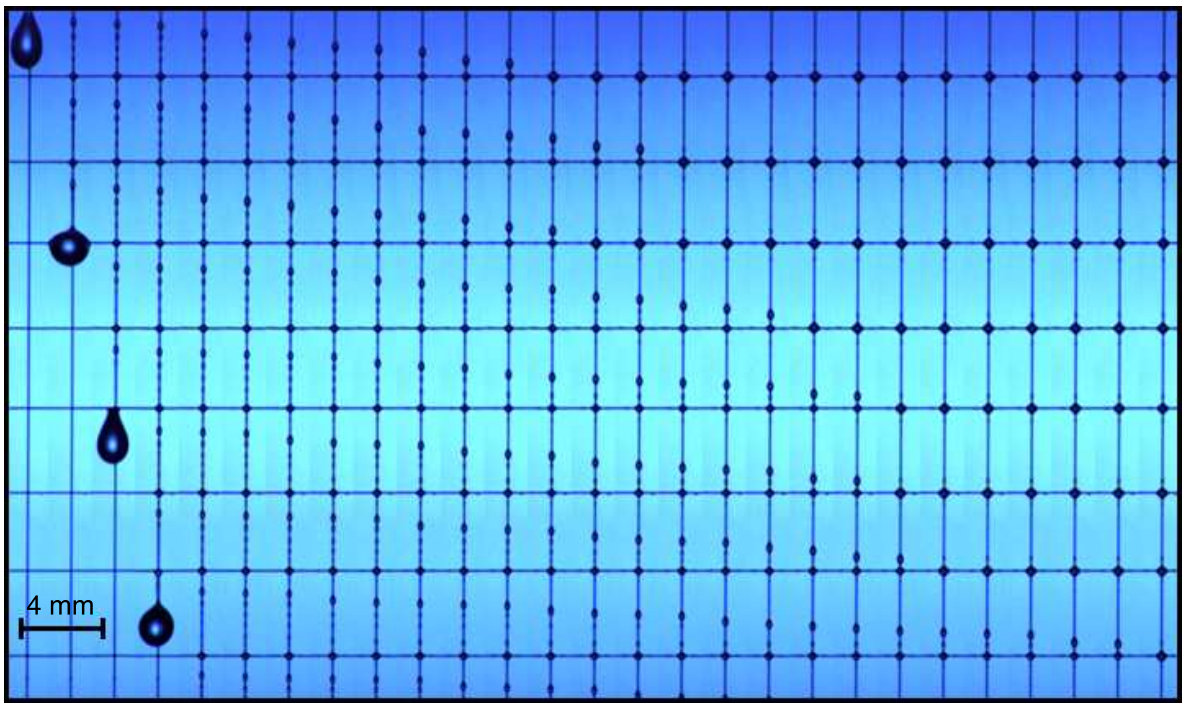

(a)

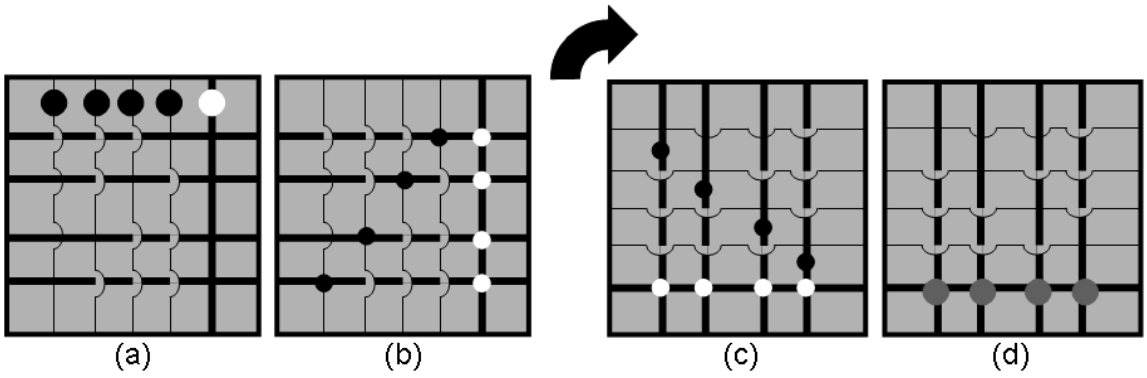

(b)

Figure 9.9: (a) With junctions in series, a droplet of $\Omega = 60$ nL and $\nu = 5$ cS is divided into 44 microdroplets of volume 60 nL. The fluid lost by coating is collected on the nodes. Snapshots are taken every 48 ms. (b) Schematic view of a multiplexing device that make a white droplet react separately with four black droplets.

rotated by 90°, the V_{80} fibers are now horizontal so they cannot sustain the B_i microdroplets. These latter fall down the H_{250} fibers until merging and reacting with the A microdroplets located at the next junction.

9.2.3 Encapsulations

Tiny aqueous droplets evaporate very quickly, only in a few minutes. To prevent evaporation, the droplets may be wrapped with an oil layer. This wrapping can be made at the junction between two fibers (Fig. 9.10). In order to study this phenomenon, a colored water droplet is placed at an intersection, and some oil droplets are left on the vertical fiber. These latter slide down and wrap the water droplet. It is observed that the water droplet may be caught by the oil and carried away from the junction (Fig. 9.10a), or it may be left coated at the junction while the oil keeps sliding down (Fig. 9.10b). The first scenario is of interest in microfluidics since the oil droplet may be seen as "cleaning" the fiber and resetting the system after any operation on the water droplet. The transition between both behaviors has been investigated as a function of the water volume Ω and related Bond number $Bo = \rho\Omega/(2\pi\sigma d_h)$, where $\sigma \simeq 30$ N/m is here the interfacial tension between water and oil. There is a critical Bo_{th} below which the water droplet is left and above which it is caught by the incoming oil droplets (Fig. 9.11a).

9.2.4 Fiber networks in microfluidics

Fiber-based microfluidic devices present numerous advantages over existing technologies (e.g. pressure-driven droplet convection into microchannels, handling on a chip by electrowetting).

- The contact between droplets and solid parts is reduced; the loss of liquid through coating is minimized, especially since the coating pearls are also collected. Therefore, a millimetric droplet can be quickly divided into tens of microdroplets.

- The operations described above are robust to the physico-chemical properties of the liquid of interest. They only require the liquid to wet the fiber, which is easily satisfied by using adequate fiber materials or by adding surfactant molecules. This is of importance in diagnostic applications, where the physical properties of the liquid to be tested are not known in advance. Such a robustness property does not exist in microchannels, where e.g. it is impossible to divide high viscosity droplets [179].

- Contrary to the planar labs-on-a-chip, the geometry of fibers allows the design of fully 3-dimensional networks with many fibers bringing multiple reactants to the same point.

- Channel-based microfluidics [178] often requires synchronisation of the droplets conveyed into various channels, which is achieved through high-tech micropumps. Here, there is no need for any external synchronisation: droplets wait for each other on the nodes.

- Thanks to the sharpness of the blocking/crossing transition, the volume of a droplet that come off a node is accurately controlled.

- There is no risk of denaturing the biochemical content of the droplet due to prohibitive electric fields generated by electronic components.

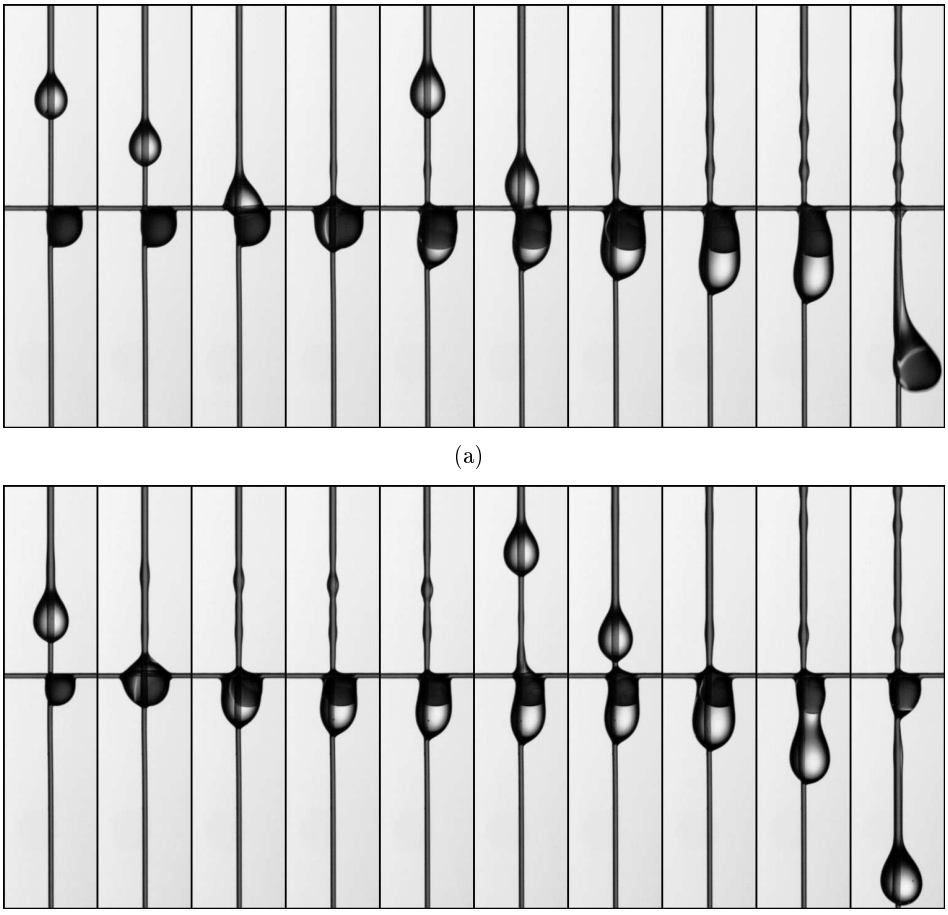

(a)

(b)

Figure 9.10: (a) A large water droplet is wrapped and caught by incoming oil droplets. (b) A small water droplet is wrapped and left by incoming oil droplets. In both cases, the oil viscosity is $\nu = 100$ cS and the diameter of both fibers is $d = 250$ μm.

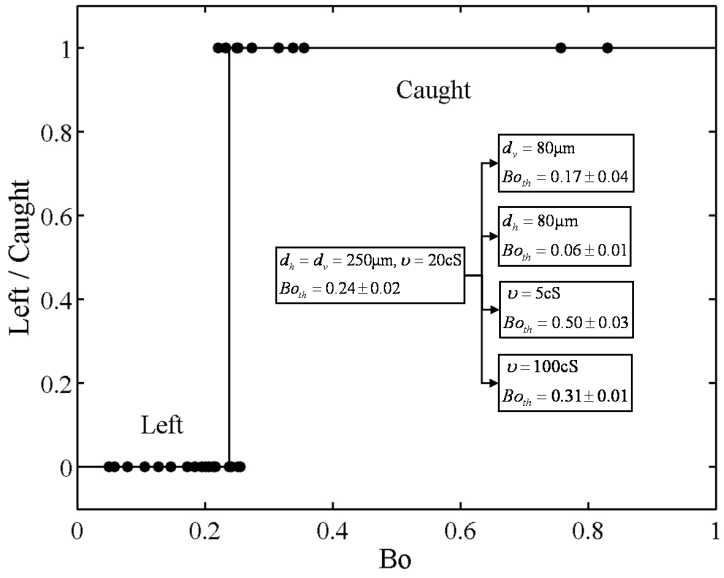

Figure 9.11: Threshold Ω_{th} between the "left" and the "caught" behaviors for $d_h = d_v = 250$ μm and $\nu = 20$ cS. Values of Ω_{th} are mentioned for different fiber radius and oil viscosity.

- Finally, fiber networks are reusable, zero-energy consuming and practically costless. They do not need neither any high-tech device nor any expertise from a research lab. They are also transportable, since microdroplets only unpin from the intersections with extreme inertial forcing. These advantages are crucial because they allow anybody to buy and use this diagnostic device "at home".

The main drawbacks of fiber networks are the risk of evaporation of microdroplets and the operation rate which is not as high as in some other technologies. Nevertheless, evaporation can be avoided by encapsulating droplets, or by placing the setup in a saturated atmosphere. Concerning the rate, which is in fact not so bad, we would argue that most microfluidic operations do not necessarily require the highest achievable rates. It does not matter if a medical diagnostic test is made in 0.1 s with a complex apparatus based on microchannels, or in maybe 1 s thanks to a simple, ergonomic and low-cost fiber network !

9.3 Summary

In this chapter, we have analyzed the behavior of droplets sliding on fibers as they encounter a crossing between two fibers. Large droplets cross the node while small ones remain pinned; the transition between both behaviors occurs for a critical Bond number. The droplet trajectories have been measured. Viscous droplets are observed to experience significant delays in crossing the node. These experimental results are well-rendered by a theoretical model that consists in a truncated harmonic oscillator. Finally, we have shown that simple fiber networks could advantageously perform some basic microfluidic operations.

Conclusions and future work

Conclusion

Although droplets are common objects that may seem perfectly understood, the scientific community is more and more interested in their physics. As explained in chapter 2, droplets are currently considered as very promising objects for microfluidic developments. Indeed, each individual droplet can serve as a support for microscale biochemical reactions. Many processes involved in chemistry, biology and medicine could be miniaturized by handling, mixing, dividing, combining individual droplets of reagent. Nowadays, several techniques of droplet manipulation are already under investigation, e.g. droplets conveyed through a channel network by an immiscible liquid, droplets traveling on a chip by electrowetting, etc. Each application has a series of constraints and requirements that the various techniques can meet more or less easily. Therefore, scientists take advantage to develop every possible way to perform the set of basic operations encountered in digital microfluidics. Hopefully, thanks to the complex action of surface tension, the physics of droplets is extraordinarily rich and we are far from having explored every variant.

The main objective of this thesis was to find some new alternatives to microfluidics and to investigate them through simple experiments and mathematical models. We have mainly focused on the following constraint :
Is it possible to manipulate droplets without touching them with any solid or liquid ? If not, how to minimize the contact ?
These questions are addressed respectively in both parts of the manuscript. In particular, we explain how to handle droplets through bouncing on a bath and on fiber networks.

Usual levitation is definitely expensive and unsuitable for handling individual droplets. Conversely, it is much easier to maintain them in the vicinity of another liquid interface. In particular, we have shown that droplets can be kept bouncing onto a liquid bath, provided this latter is vertically vibrated. While bouncing, the droplets must never touch the liquid beneath, otherwise they would coalesce. A bounce implies a change of direction, which can be achieved only by storing and restoring the kinetic energy of the incoming droplet. In order to understand the underlying mechanisms, we have studied two configurations of bouncing droplets, namely on a soap film (chapter 4) and on a high-viscosity liquid bath (chapter 5). In the first case, the storage is primarily ensured by the soap film. Since its mass is negligible, it instantaneously deforms in response to the droplet, a property which deeply simplifies the corresponding model. On the other hand, the viscous bath cannot restore energy so the droplet must rely on its own deformation. In both cases, permanent bouncing is observed when the liquid support (bath or film) is forced through a vertical sinusoidal motion. More precisely, there is a forcing amplitude threshold above which the droplet bounces indefinitely. Since the bouncing involves a spring mechanism with a related natural frequency, this threshold depends on the forcing frequency. In particular, the threshold may be significantly lowered

by a resonance phenomenon between the forcing and the spring, as well-rendered by the proposed models. Physically, bouncing droplets exhibit some interesting properties such as multi-periodicity and transition to chaos.

To maintain droplets "alive" by making them bounce permanently on a vibrated liquid bath is only the first step. In chapter 6, we have discussed two modes of horizontal self-propulsion of bouncing droplets, namely rollers and walkers. These moving droplets stay at a distance from the edges of the container, so they can be guided when the boundaries form a channel. The walkers also interact together and form orbits, crystalline structures, etc. We have mainly studied the collective motion of a large number of walkers. In this special gas, colliding particles coalesce together until they are so large that they cannot move anymore. Unfortunately, although fusion between droplets is easily achieved, we still do not know how to perform the inverse operation, namely to break up the droplets. In counterpart, as explained in chapter 7, the droplet volume may be controlled in some way. Indeed, low viscosity droplets are shown to experience partial coalescence, i.e. they do not coalesce in one step. Instead, a half-smaller droplet is formed at the end of the coalescence. If sufficiently small, this daughter droplet starts bouncing. Otherwise, it partially coalesces again until it reaches the appropriate size selected by the forcing conditions.

At this stage, the "bouncing-based" microfluidics come close to being fundamental research rather than applied physics. Nevertheless, we can already catch a glimpse of the advantages it would bring over other handling techniques. The first of them is likely the flexibility: manipulations are driven through the forcing parameters, which can be reprogrammed in real-time. This property is of interest for research and development, when one has to deal with a small number of droplets at a time without doing the same operation twice. Since the droplet does never touch another liquid or solid, it is free of unwilled contamination or mass loss by wetting. Finally, as mentioned in the perspective section, some operations can be performed on droplets that are hardly made otherwise, e.g. the spontaneous creation of a micro-emulsion in a bouncing compound droplet.

In the second part of this thesis, we have investigated the behavior of droplets on fiber networks. Fibers are indeed a good compromise since the droplet is touched but the contact area is minimal. First, we have rationalized the motion of a droplet on a vertical fiber (chapter 8). After a short acceleration, the droplet reaches a terminal velocity that results from a balance between gravity and friction forces. The droplet is observed to leave a thin coating film in its wake. Thanks to the Rayleigh-Plateau instability, this film quickly turns into small pearls that also flow down the fiber. Secondly (chapter 9), we have studied what happens when the sliding droplet encounters the basic element of a fiber network, namely a junction with another (horizontal) fiber. Depending on its volume, the droplet may stop or it may keep sliding downwards. This binary behavior turns out to be very interesting for many droplet manipulations. For example, the division of a droplet into a large number of micro-droplets is performed more easily than ever by placing as many nodes in series. Indeed, a large droplet crosses them all while the small pearls resulting from its coating film are blocked. Therefore, each node collects the pearls left in the section just upstream. We have finally studied some other basic operations on fiber networks, such as fusion, multiplexing and encapsulation. As discussed at the end of chapter 9, fiber networks can be advantageously implemented in a number of microfluidic systems, including costless and easy-to-use diagnostic tools.

Future work

The physics of droplets is extraordinarily rich and still shrouded in mystery. These last sections shortly pave the way for new work involving droplets. Some of them can likely be addressed in a few months while others are open questions that may span decades.

Bouncing on a vibrated surface: universal behaviors

Problems related to bouncing on a moving surface share a lot of similarities and universal features. In particular, the corresponding models exhibit common behaviors, such as multi-periodicity and chaos. Moreover, their bifurcation diagrams often seem qualitatively equivalent. Nevertheless, an extensive study of the bifurcations is still lacking, even for the simplest of these systems, i.e. the elastic ball (App. E). Indeed, the involved equations are usually not continuous but piecewise-smooth, so the classical theory of nonlinear systems cannot be directly applied and must be reformulated [180].

Independently from its possible use in microfluidics, the bouncing of objects on a vibrated surface may also be of interest to rationalize some behaviors encountered in nature. For example, flying fishes are observed to bounce onto the sea surface in order to escape predators. Physically, this bouncing is not due to surface tension anymore, but rather to inertial forces, as for skipping stones [181, 182]. Surprisingly, they seem to systematically swim perpendicular to the waves. Would they take advantage of the waves to optimize their trajectory ?

Walkers and rollers

We have discussed two modes of self-propulsion of bouncing droplets on a vibrated bath, namely rollers and walkers. Although a significant work has already been made on walkers [76, 133, 141], both modes need further investigation. In particular, the interactions between droplets must be addressed in details. How does the virtual force they exert on each other scale ? What is the stability of crystalline structures ? Can phase transitions be observed from an ordered to a gas-like state ? What are the similarities with other systems involving collective motion, such as an ideal gas, a colony of bacteria or a fish school ?

Reflection / refraction of droplets

Reflection and refraction are known for centuries in wave theory. In mechanics, macroscopic objects may also be reflected or refracted as they encounter a boundary between two media. While the billiard ball reflection is well-understood, there are a number of

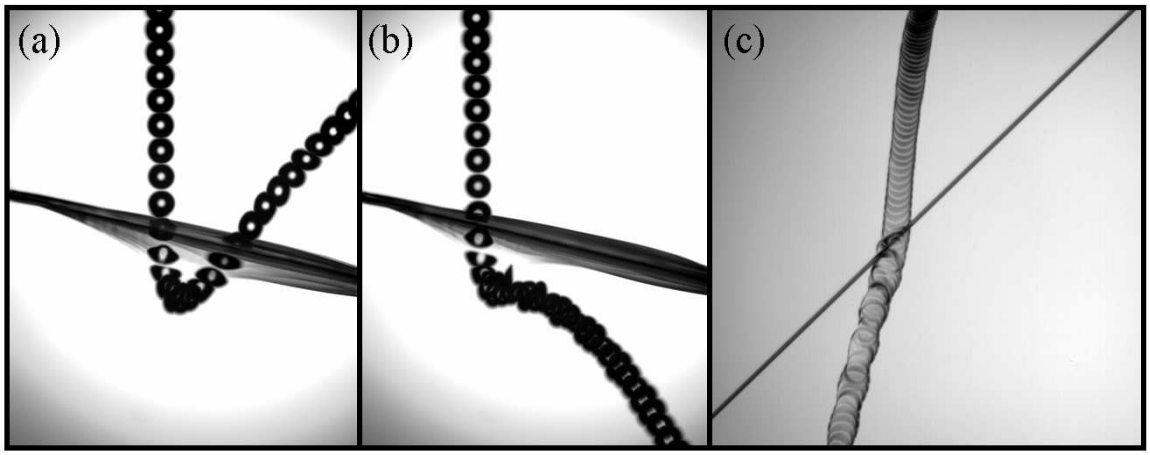

Figure 9.12: (a-b) A water droplet impacts on an inclined soap film. Depending on its velocity, it may bounce on (a) or cross (b) the film. In both cases, the trajectory is deviated, corresponding to a reflection and a refraction respectively. (c) A droplet is also deviated when it impacts an inclined fiber.

reflection/refraction-like motions that still need to be studied, especially in fluid mechanics. In relation with this thesis, droplets that interact with an inclined soap film are deviated so both reflection and refraction are observed (Fig. 9.12a-b). Deviations are also seen when a droplet impacts an inclined fiber (Fig. 9.12c). Can the Snell's laws be extended to these systems ? If not, what are the relevant parameters to scale and rationalize these trajectory deviations ?

Static shape of droplets

In this thesis, we mainly focused on axisymmetric droplets because they are easily observed, characterized and modeled. Nevertheless, it is essential to develop mathematical tools that can efficiently deal with asymmetric shapes. For example, we need to find a convenient way to represent the shape of a droplet hanged on a horizontal or inclined fiber. Nowadays, the only available tool is numerical computation (e.g. Surface Evolver); but we would take advantage in describing these shapes with a relatively small number of parameters, e.g. through spectral methods, perturbations of well-known axisymmetric cases, etc.

Partial coalescence in various configurations

We have investigated the partial coalescence of droplets into a bath. However, partial coalescence may be observed in a variety of configurations. Among others, low viscosity droplets partially coalesce with a soap film. This case is different from the coalescence at a liquid/liquid interface in many respects. First, the droplet usually impacts the soap film with a significant velocity, so the Weber number must be taken into account in the dimensional analysis. The Ψ parameter, namely the size ratio between the final and the initial droplets, is usually much greater than 0.5. Moreover, several satellite droplets may be formed (Fig. 9.13). But the most striking property of coalescence on soap films is that daughter and satellite

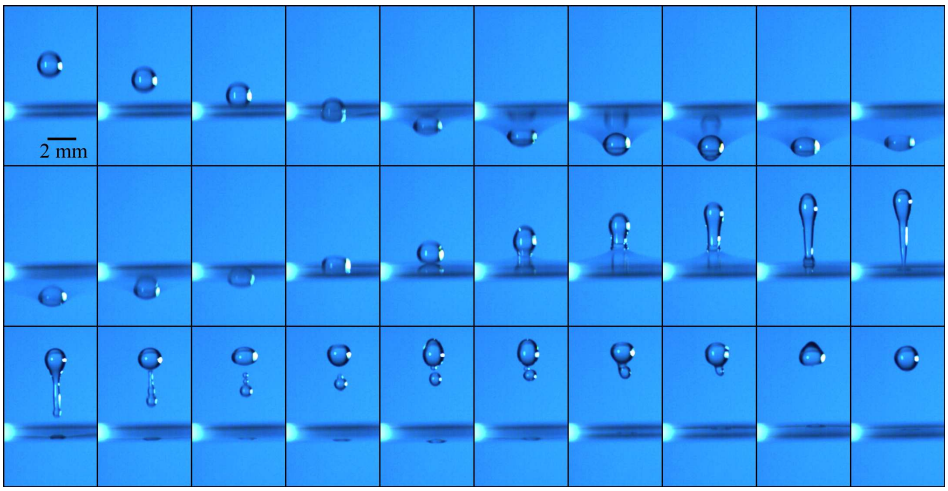

Figure 9.13: Partial coalescence of a droplet on a soap film, with the formation of satellite droplets. Time is indicated in milliseconds.

droplets may be ejected upwards, or downwards (Fig. 4.3d), or both (Fig. 4.3c) ! In that latter case, the soap film splits the droplet in two parts that may evolve independently from each other. Partial coalescence can even be much wilder, as seen with this pure water droplet coalescing into a soapy water bath in Fig. 9.14. Partial coalescence is far from being fully understood and, among others, the conditions of appearance of satellite droplets have still to be addressed. The Ψ function is also of interest for droplet handling, since partial coalescence may be seen as a convenient way to progressively decrease the volume of a droplet.

Compound droplets

An major theme of the droplet physics consists in studying the behavior of compound droplets, typically water droplets wrapped by an oil layer [183]. We have already seen that water droplets may be easily encapsulated on fibers (Chap. 9). There are several other ways to create compound objects [184]. One of the most spectacular consists in making a water droplet impact on a water bath covered with a thin oil layer (Fig. 9.15a). Depending on the layer thickness, the droplet may experience complex motions in which water and oil wrap each other, sometimes resulting in an onion composed of four layers! A similar entrapment and wrapping mechanism is encountered in the creation of antibubbles [62, 84].

Unfortunately, all these exotic objects are unstable; the lighter layers are drained upwards by buoyancy forces, so layers made of the same liquid finally coalesce together and the object disappears. Nevertheless, it is possible to create stable encapsulations of water droplets by carefully choosing the oil phase. For example, diiodomethane is a liquid of especially high density $\rho = 3325$ kg/m^3 and low surface tension $\sigma = 50.8$ mN/m. Consequently, a droplet of diiodomethane released on a water bath shapes as a lens floating on the bath surface. The important thickness of this lens is due to the competition between gravity (that tries to make it sinking) and surface tension (that makes it floating). As seen in Fig. 9.15(b), small water droplets can be placed in these lenses in a stable fashion, which may be of interest for preservation and long-term storage of droplets in a confined volume. Although already investigated (e.g. [185]), the dynamics of lenses is far from explored. What is their exact

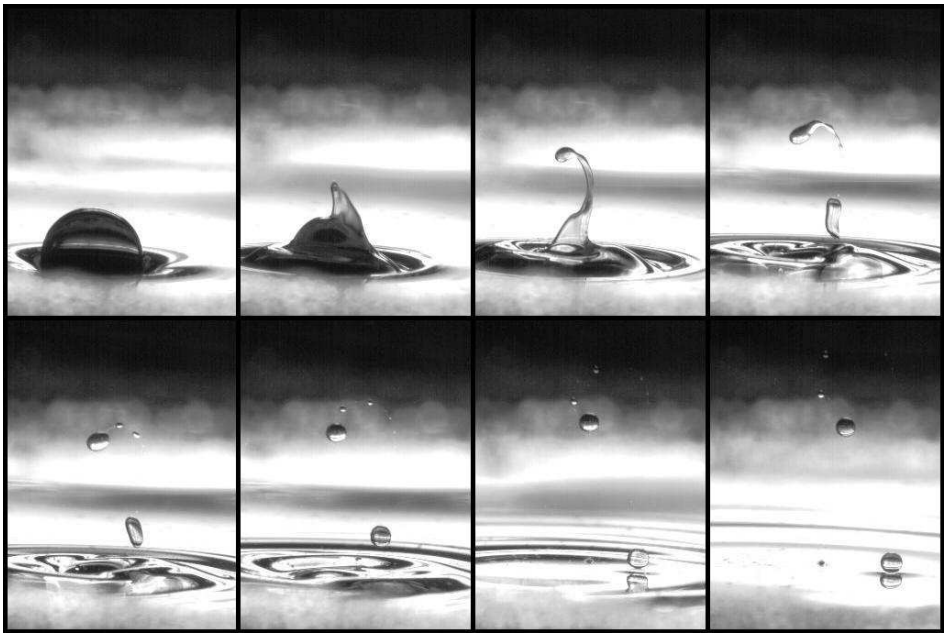

Figure 9.14: Partial coalescence of a plain water droplet into a soapy water bath. The surfactant gradients make the phenomenon much more complex.

shape ? What is the maximum amount of water that can be placed inside ? How do several lenses interact together ? Is it possible to mix two oil lenses without mixing their water content ?

Compound droplets also bounce permanently onto a vibrated liquid bath. Nevertheless, something amazing occurs when a little soap is added: at each impact, the oil layer may be pushed inside the water droplet. Under given conditions, the water pinches the oil layer, resulting in an oil droplet encapsulated in water. The repeated impacts progressively create an oil-in-water micro-emulsion! The exact mechanism is still unknown, though it is thought to have analogies with other experiments involving a similar change in the interface topology [186].

Laser manipulation

Another important direction for applied research is the manipulation of droplets with lasers. We have already mentioned that pulsed lasers may generate wave patterns on a liquid surface that are similar to those emitted by a walking droplet (D. Caballero, private communication). In some sense, the laser may be considered as a virtual droplet. Since walkers interact together, they can be attracted and driven by the laser. The lenses introduced in last section may also be handled with lasers [187], and it is likely that fiber networks can also take advantage of the laser technology.

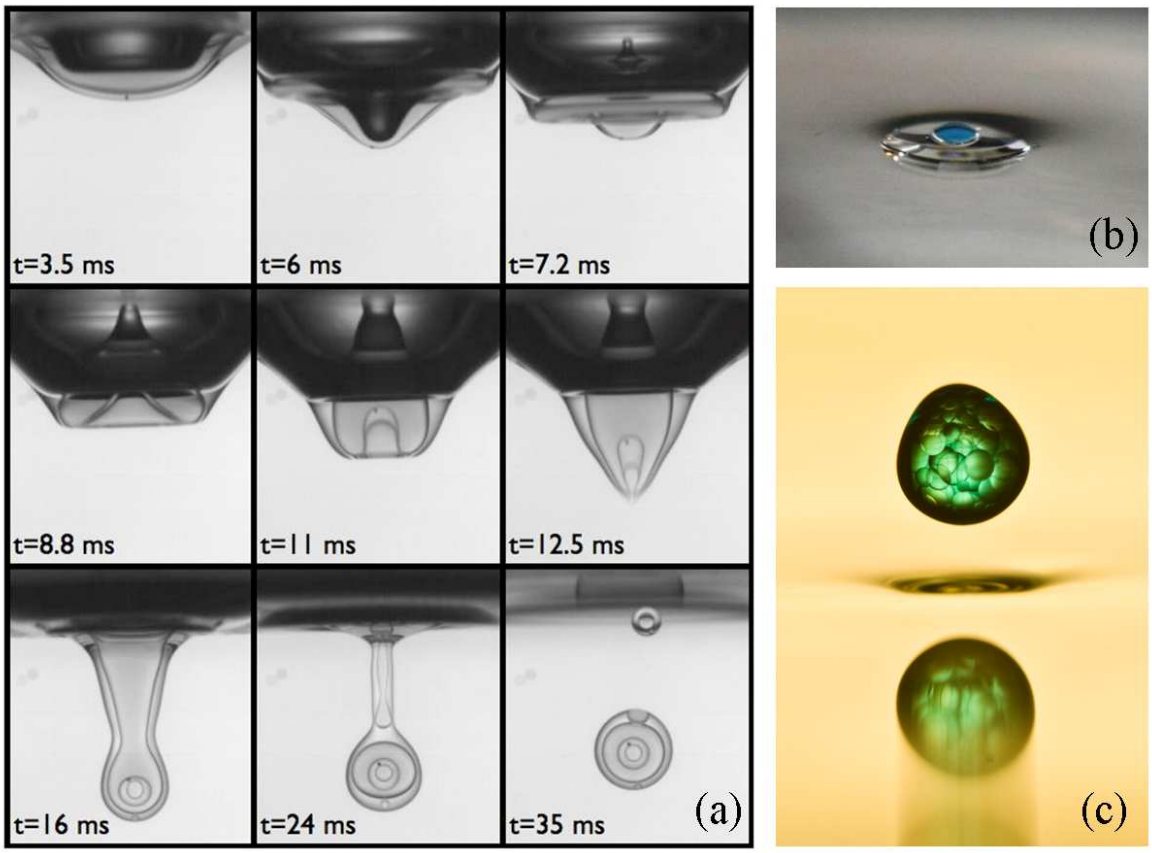

Figure 9.15: (a) By making a water droplet impact a water bath covered with an oil layer, one may create multi-encapsulations, namely water-in-oil-in-water-in-oil-in-water objects ! (Credit: S. Dorbolo) (b) A thick sessile lens is made by releasing a droplet of diiodomethane at the surface of a water bath. A small colored water droplet can be stored for a long time inside the lens. (c) A compound droplet can also experience permanent bouncing on a vibrated bath. At each impact, the oil layer may be trapped and pinched, thus releasing an oil droplet within the water part; an oil-in-water micro-emulsion is spontaneously formed. (Credit: D. Terwagne)

Microfluidics on fiber networks

Finally, the most promising work to undertake is likely the development of smart fiber networks. With an increasing number of capabilities, these latter are expected to provide solutions for practical applications, in particular for biochemical assays and diagnostic tools. Future research may be divided in four axes:

- First, some fundamental questions have to be addressed. Among others, how does a droplet behave as it encounters a node formed with more than two fibers? What is the evaporation timescale of a droplet on a fiber? How efficient is the mixing of two droplets at a node? Is this mixing enhanced by the internal convection created within the resulting droplet when it slides down ? How do these processes scale as the fiber size is decreased down to a few microns or less?

- Fiber nodes are observed to exert a diode-like action on droplets. By analogy with the recently developed bubble computing [32], is it possible to invent a set of logical operations on droplets that may be combined to perform complex fluidic tasks?

- Until now, we have dealt with fishing nylon fibers. Nevertheless, the physics described in this thesis is likely applicable to fibers of any kind. A judiciously chosen material can provide additional capabilities to the network. The fiber could be for example an optical fiber or an electrical wire, possibly textured or chemically coated. The development of electro-wetting on fibers would provide an electronic control of the blocking/crossing transition. The interaction between light/electrical current and the droplet content could allow an in-situ measurement of the droplet properties; micro-reactions would be probed in real time! Moreover, these active fibers may induce chemical reactions within the droplet through heating, UV cross-linkage, etc.

- Finally, droplets can also have a feedback on the fiber network because the fibers are usually elastic. Indeed, liquids exert a capillary action on fibers that may shape them. The best example is the dense network of our hair, which shapes differently if it is wet or not [188]. Elastocapillary phenomena open the way to self-assembly [189]. Droplets are already used in microfabrication, e.g. for the self-alignment of two fibers [12] or for the assembly through drying [190]. Here, the droplets may help designing the network on which they flow ! This increases further the field of application of fiber networks.

Appendix A

Notations

The main notations encountered in the text are summarized in these tables. Note that the appendices have their own notations that may be different from the list below.

Var.	Signification	Eq./Fig.	Var.	Signification	Eq./Fig.
α	Friction coef.	E(8.4)	τ	Dimensionless time	E(4.32)
β	Dimensionless damping	E(7.7-9.6)	τ_σ	Capillary time	E(1.8)
δ	Coating thickness	E(8.9)	ϕ	Phase	
ζ	Max. deflection s.f.	F4.5(a)	φ	Interface angle	F8.2(b)
η	Droplet deformation	F4.5(a)-5.3(a)	χ	Characteristic function	
θ	Inclination angle	F4.5(a)	ω	Dimensionless f	E(4.3)
κ	Dimensionless Z_2	E(9.6)	Δ	Difference	
λ_σ	Capillary length	E(1.4)	$\Delta\rho$	Rel. Diff. of ρ	E(7.1)
μ	Dynamic viscosity		Γ	Dimensionless A	E(4.2)
ν	Kinematic viscosity		Θ	Dimensionless Mg	E(9.6)
ξ	Size ratio	E(4.1)	Φ	Dimensionless freq. fiber	E(9.8)
ρ	Density		Ψ	Size ratio	E(7.2)
σ	Surface tension	E(1.1)	Ω	Droplet volume	

Table A.1: Greek characters.

Subscript	Signification	Subscript	Signification
F	Faraday instability	m	Minimum
M	Maximum	nw	Not walking droplet
a	Air	s	Surrounding immiscible liquid
cw	Capillary waves	sf	Soap film
f	Final state	th	Threshold
h	Horizontal fiber	v	Vertical fiber
i	Initial state	w	Walker

Table A.2: Subscripts.

Var.	Signification	Eq./Fig.	Var.	Signification	Eq./Fig.
A	Forcing amplitude	F4.2(b)	a	Scale Weibull	E(6.7)
Bo	Bond number	E(1.3-9.1)	b	Shape Weibull	E(6.7)
C	Bouncing thres. fun.	E(5.17)	c_D	Dissipation coef.	E(5.6)
$\mathcal{C}$	Mean curvature	E(1.2)	c_K	Kinetic energy coef.	E(5.6)
Ca	Capillary number	E(8.9)	c_{L1}, c_{L2}	Lubrication coef.	E(5.3)
E_σ	Surface energy	E(1.1)	c_T	Transfer coef.	E(4.29)
F_L	Lubrication force		c_k	Stiffness coef.	E(4.4)
F_σ	Capillary force		c_{we}	Wetting coef.	E(8.9)
G	Deformation ampl.	E(5.11)	$c_{\mu 1}$, $c_{\mu 2}$	Friction coef.	E(9.2-9.12)
H	Height drop. summit		$c_{\nu 1}$, $c_{\nu 2}$	Friction coef.	E(8.2-8.6)
$\mathcal{H}$	Heaviside function		c_σ	Surface tension coef.	E(4.4-9.12)
I_i	Mod. Bessel 1st kind	E(5.17)	d	Fiber diameter	
K	Kinetic en. impact		f	Forcing frequency	F4.2(b)
L	Traveling length	E(9.17)	$f_{(\ell,m)}$	Natural freq. of Y_ℓ^m	E(1.7)
M	Droplet mass		g	Gravitational accel.	
N	Number of droplets		h	Film thickness	F5.3(a)
Oh	Ohnesorge number	E(1.9)	j	Index	
P	Pressure		k	Stiffness	E(4.4)
$\mathcal{P}$	Probability		ℓ	Degree of Y_ℓ^m	F1.2
P_D	Dissipated power		m	Order of Y_ℓ^m	F1.2
Q, $\vec{Q}$	Flow rate		p	N. forc. per./boun	
R	Mean radius	F4.2(a)	q	N. boun/per. traj.	
S	Surface area		r	Radial axis	F4.5(a)
U	Dimensionless V	E(4.32)	s	Curvilinear coord.	
V	Vert. vel. impact		t	Time	
W	Droplet width	F8.2(b)	t_c	Contact time	E(3.3)
We	Weber number	E(1.6)	t_L	Lifetime	
X	Droplet extension	F8.2(b)	u, $\vec{u}$	Local velocity	
Y	Short-term average y	E(5.14)	v	Droplet velocity	
Y_ℓ^m	Spherical harmonics	F1.2	x	Dimensionless η	E(5.7)
Z	Vert. pos. drop.	F4.5(a)	y	Dimensionless Z, h	E(4.32-5.7-9.4)
Z_1, Z_2	Truncature	E(9.2)	z	Vertical axis	F4.5(a)

Table A.3: Latin characters.

Appendix B

Physical properties of the liquids

The relevant physical properties of the liquids used in the experiments of this thesis are summarized in Table B.1. The interfacial tension $\sigma_{w/o}$ between aqueous mixtures and silicon oils has been measured by the pendent drop technique. Pure water gives $\sigma_{w/o} \simeq 45 \pm 1$ mN/m, whatever the associated oil. Addition of glycerol decreases the interfacial tension down to $\sigma_{w/o} \simeq 42 \pm 1$ mN/m. On the other hand, a significant variation is observed when ethanol is added:

$$\begin{aligned} \sigma_{w/o}(10\%E) &= 25 \text{ mN/m}, \sigma_{w/o}(20\%E) = 17 \text{ mN/m}, \\ \sigma_{w/o}(30\%E) &= 12 \text{ mN/m}, \sigma_{w/o}(20\%E) = 9 \text{ mN/m} . \end{aligned}$$

Liquid	ρ (kg/m^3)	ν (cS)	σ (mN/m)
W	1000	0.893	72.0
87.5%W + 12.5%G	1030	1.17	70.2
80%W + 20%G	1048	1.47	69.5
75%W + 25%G	1061	1.73	69.0
62.5%W + 37.5%G	1093	2.67	68.0
50%W + 50%G	1127	4.74	67.4
25%W + 75%G	1195	30.9	66.1
90%W + 10%E	983	1.35	46.6
80%W + 20%E	969	1.82	37.7
70%W + 30%E	954	2.23	32.3
60%W + 40%E	934	2.51	29.6
DC-0.65 cS	761	0.65	15.9
DC-1.5 cS	850	1.5	16.8
DC-5 cS	920	5	19.7
DC-10 cS	934	10	20.1
DC-20 cS	949	20	20.6
DC-50 cS	960	50	20.8
DC-100 cS	965	100	20.9
DC-1000 cS	971	1000	21.2

Table B.1: Liquid properties (G=Glycerol, E=Ethanol, W=Water, DC=Dow Corning 200 silicon oil).

Appendix C

Capillary waves on a spherical interface

C.1 Useful formulas in spherical coordinates

The deformations of a sphere can be represented through the surface $\vec{x} = R(\theta, \varphi)\vec{e_r}$, where

$$(\vec{e_r}, \vec{e_\theta}, \vec{e_\varphi}) = \begin{pmatrix} \sin\theta\cos\varphi & \cos\theta\cos\varphi & -\sin\varphi \\ \sin\theta\sin\varphi & \cos\theta\sin\varphi & \cos\varphi \\ \cos\theta & -\sin\theta & 0 \end{pmatrix}. \tag{C.1}$$

These unit vectors form a cartesian coordinate system and satisfy, among others, to $\partial_\theta \vec{e_r} = \vec{e_\theta}$ and $\partial_\varphi \vec{e_r} = \sin\theta \vec{e_\varphi}$.

The main differential operators are written:

$$\boldsymbol{\nabla} F = \vec{e_r}\partial_r F + \vec{e_\theta}\frac{\partial_\theta F}{r} + \vec{e_\varphi}\frac{\partial_\varphi F}{r\sin\theta}, \tag{C.2}$$

$$\boldsymbol{\nabla}\cdot\vec{F} = \frac{\partial_r(r^2 F_r)}{r^2} + \frac{\partial_\theta(\sin\theta F_\theta)}{r\sin\theta} + \frac{\partial_\varphi F_\varphi}{r\sin\theta}, \tag{C.3}$$

$$\boldsymbol{\nabla}\wedge\vec{F} = \frac{\partial_\theta(\sin\theta F_\varphi) - \partial_\varphi F_\theta}{r\sin\theta}\vec{e_r} + \frac{\partial_\varphi F_r - \sin\theta\partial_r(rF_\varphi)}{r\sin\theta}\vec{e_\theta} + \frac{\partial_r(rF_\theta) - \partial_\theta F_r}{r}\vec{e_\varphi}, \tag{C.4}$$

$$\nabla^2 F = \frac{\partial_r(r^2\partial_r F) + \nabla^2_{\theta\varphi} F}{r^2}, \tag{C.5}$$

where the angular component of the Laplacian operator is

$$\nabla^2_{\theta\varphi} F = \frac{\partial_{\varphi\varphi} F + \sin\theta\partial_\theta(\sin\theta\partial_\theta F)}{\sin^2\theta}. \tag{C.6}$$

The eigenfunctions of this operator are the spherical harmonics $Y_\ell^m = P_\ell(\cos\theta)e^{im\varphi}$ obeying to

$$\nabla^2_{\theta\varphi} Y_\ell^m + \ell(\ell+1)Y_\ell^m = 0. \tag{C.7}$$

The outward-pointing normal vector is

$$\vec{n} = \frac{\vec{e_r} - \frac{\partial_\theta R}{R}\vec{e_\theta} - \frac{\partial_\varphi R}{R\sin\theta}\vec{e_\varphi}}{\sqrt{1 + \left(\frac{\partial_\theta R}{R}\right)^2 + \left(\frac{\partial_\varphi R}{R\sin\theta}\right)^2}}. \tag{C.8}$$

C.1.1 Linearization for small deformations

The surface is represented by $R = R_0(1+\eta)$ where $\eta \ll 1$. This yields

$$\vec{n} \simeq \vec{e_r} - \frac{\partial_\theta \eta}{R_0}\vec{e_\theta} - \frac{\partial_\varphi \eta}{R_0 \sin\theta}\vec{e_\varphi}, \tag{C.9}$$

$$\boldsymbol{\nabla}\cdot\vec{n} \simeq \frac{2(1-\eta)}{R_0} - \frac{\nabla^2_{\theta\varphi}\eta}{R_0}, \tag{C.10}$$

$$\vec{n}\cdot\boldsymbol{\nabla} \simeq \partial_r. \tag{C.11}$$

C.2 Dispersion relation

We proceed by establishing the dispersion relation of capillary waves on a spherical droplet immersed in a surrounding liquid (denoted by the subscript $_s$). We suppose that

- the flow is irrotational and incompressible,
- the wavelength is much larger than the viscous length $\sqrt{\nu/f}$, and
- the wave amplitude is small compared to the wavelength.

So the velocity field inside $\vec{u}$ and outside $\vec{u_s}$ may be derived from scalar potentials ψ and ψ_s satisfying to the Laplace equation: $\nabla^2\psi = \nabla^2\psi_s = 0$, so for each mode (ℓ, m),

$$\psi = B(t)\left(\frac{r}{R_0}\right)^{\ell} Y_\ell^m \quad \text{and} \quad \psi_s = B_s(t)\left(\frac{r}{R_0}\right)^{-(\ell+1)} Y_\ell^m. \tag{C.12}$$

The continuity of the normal velocity on the interface $r = R_0(1+\eta)$ implies $\vec{n}\cdot\vec{u}]_{r=R_0} = \vec{n}\cdot\vec{u_s}]_{r=R_0} = R_0\partial_t\eta$, so

$$B = \frac{R_0^2}{\ell Y_\ell^m}\partial_t\eta \quad \text{and} \quad B_s = -\frac{R_0^2}{(\ell+1)Y_\ell^m}\partial_t\eta. \tag{C.13}$$

Finally, the linearized Bernoulli equation gives the pressure within the flow $P = 2\sigma_s/R_0 - \rho\partial_t\psi$ and $P_s = -\rho_s\partial_t\psi_s$. According to the Laplace law, $P - P_s = \sigma_s\boldsymbol{\nabla}\cdot\vec{n}$ on the interface, so

$$\rho\partial_t\psi]_{r=R_0} - \rho_s\partial_t\psi_s]_{r=R_0} = \frac{\sigma_s}{R_0}\left(2\eta + \nabla^2_{\theta\varphi}\eta\right), \tag{C.14}$$

which yields

$$\partial_{tt}\eta = \frac{\sigma_s}{[(\ell+1)\rho + \ell\rho_s]R_0^3}\ell(\ell+1)\left(2\eta + \nabla^2_{\theta\varphi}\eta\right). \tag{C.15}$$

We can now decompose the perturbations into spherical harmonics $\eta = \eta_0(t)Y_\ell^m$ and obtain

$$\ddot{\eta_0} + \frac{\ell(\ell^2-1)(\ell+2)}{(\ell+1)\rho + \ell\rho_s}\frac{\sigma_s}{R_0^3}\eta_0 = 0. \tag{C.16}$$

We define the mean density $\rho_m = (\rho+\rho_s)/2$ and the relative difference of density $\Delta\rho = (\rho-\rho_s)/(\rho+\rho_s)$. Therefore, the natural frequency $f_{(\ell,m)}$ of the mode (ℓ, m) is given by

$$(2\pi f_{(\ell,m)})^2 = \frac{\sigma_s}{\rho_m R_0^3}\frac{\ell(\ell^2-1)(\ell+2)}{2\ell+1+\Delta\rho}. \tag{C.17}$$

We see that this relation dispersion is degenerated, namely it does not depend on m.

When $\rho_s = 0$, Eq. (1.7) is recovered:

$$f^2_{(\ell,m)} = \frac{\sigma}{3\pi M}\ell(\ell+2)(\ell-1). \tag{C.18}$$

The planar case is obtained as the limit when $R_0 \to \infty$, with $\ell = 2\pi R_0/\lambda$:

$$f^2 = \frac{2\pi\sigma_s}{(\rho+\rho_s)\lambda^3}. \tag{C.19}$$

In summary, the general solution is

$$\left\{\begin{array}{ll} R & = R_0(1 + BY_\ell^m \cos(2\pi ft) \\ \psi & = -B\frac{2\pi f R_0^2}{\ell}\left(\frac{r}{R_0}\right)^\ell Y_\ell^m \sin(2\pi ft) \\ \psi_s & = B\frac{2\pi f R_0^2}{\ell+1}\left(\frac{r}{R_0}\right)^{-(\ell+1)} Y_\ell^m \sin(2\pi ft) \\ (2\pi f)^2 & = \frac{\sigma_s}{R_0^3}\frac{\ell(\ell^2-1)(\ell+2)}{\rho(\ell+1)+\rho_s\ell}. \end{array}\right. \tag{C.20}$$

C.3 Viscous dissipation

Although the flow is supposed irrotational (and so inviscid), it is possible to estimate the viscous dissipation on the basis of the velocity gradients provided by the potential solution. The local dissipation D (per unit volume) writes

$$\begin{aligned} D = \; & 2\mu\left[(\partial_r u_r)^2 + \frac{(\partial_\theta u_\theta + u_r)^2}{r^2} + \frac{(\partial_\varphi u_\varphi + u_r\sin\theta u_\theta\cos\theta)^2}{r^2\sin^2\theta}\right] + \left[r\partial_r\left(\frac{u_\theta}{r}\right) + \frac{\partial_\theta u_r}{r}\right]^2 \\ & + \left[\frac{\sin\theta}{r}\partial_\theta\left(\frac{u_\varphi}{\sin\theta}\right) + \frac{\partial_\varphi u_\theta}{r\sin\theta}\right]^2 + \left[\frac{\partial_\varphi u_r}{r\sin\theta} + r\partial_r\left(\frac{u_\varphi}{r}\right)\right]^2. \end{aligned} \tag{C.21}$$

The dissipated power P_D is calculated by integrating this dissipation function over the whole space:

$$\begin{aligned} P_D &= \int_0^{2\pi}\mathrm{d}\varphi\int_0^{\pi}\mathrm{d}\theta\int_0^{R_0}\mathrm{d}r D r^2\sin\theta \\ &= \frac{B^2\mu(2\pi f)^2 R_0^3(\ell-1)(2\ell+1)(1+\delta_{m0})\sin^2(2\pi ft)}{\ell} \\ P_{Ds} &= \int_0^{2\pi}\mathrm{d}\varphi\int_0^{\pi}\mathrm{d}\theta\int_{R_0}^{\infty}\mathrm{d}r D_s r^2\sin\theta \\ &= \frac{B^2\mu_s(2\pi f)^2 R_0^3(\ell+2)(2\ell+1)(1+\delta_{m0})\sin^2(2\pi ft)}{\ell+1}. \end{aligned} \tag{C.22}$$

We observe that $P_D/\mu < P_{Ds}/\mu_s$; the dissipated power per unit viscosity is higher in the surrounding fluid.

The total kinetic energy of the flow is also obtained from the potential solution:

$$\begin{aligned} K &= \int_0^{2\pi} \mathrm{d}\varphi \int_0^{\pi} \mathrm{d}\theta \int_0^{R_0} \mathrm{d}r \frac{u_r^2 + u_\theta^2 + u_\varphi^2}{2} r^2 \sin\theta \\ &= \frac{B^2 \rho (2\pi f)^2 R_0^5 (1+\delta_{m0}) \sin^2(2\pi f t)}{4\ell} \\ K_s &= \int_0^{2\pi} \mathrm{d}\varphi \int_0^{\pi} \mathrm{d}\theta \int_{R_0}^{\infty} \mathrm{d}r \frac{u_r^2 + u_\theta^2 + u_\varphi^2}{2} r^2 \sin\theta \\ &= \frac{B^2 \rho_s (2\pi f)^2 R_0^5 (1+\delta_{m0}) \sin^2(2\pi f t)}{4(\ell+1)}. \end{aligned} \tag{C.23}$$

The kinetic energy per unit density is smaller in the surrounding fluid, $K/\rho > K_s/\rho_s$.

The total mechanical energy E of capillary waves decreases with time as a decreasing exponential of factor β:

$$E = E_{t=0} \mathrm{e}^{-\beta t}, \tag{C.24}$$

where

$$\beta = \frac{P_D + P_{Ds}}{2(K+K_s)} = \frac{2\ell+1}{2R_0^2} \frac{\mu(\ell^2-1) + \mu_s \ell(\ell+2)}{\rho(\ell+1) + \rho_s \ell}. \tag{C.25}$$

Obviously, the shorter are the waves (large ℓ), the more efficient is the damping. Like the dispersion relation, the damping factor does not depend on the parameter m.

For a planar interface, the dissipation is

$$\beta = 4\pi^2 \frac{\mu + \mu_s}{(\rho + \rho_s)\lambda^2}. \tag{C.26}$$

C.4 Axisymmetric progressive waves

The propagation of plane waves is well-described by the solution

$$X = \tilde{X} \mathrm{e}^{2\pi i (x/\lambda - ft)}, \tag{C.27}$$

corresponding to a monochromatic wave of wavelength λ and frequency f. This wave travels at speed λf in the direction of increasing x; it is therefore a progressive wave. Since the physical problem is linearized, every linear combination of two solutions is also a solution. The sum of two waves only differing by their direction give birth to a standing wave

$$X = \tilde{X} \cos(2\pi x/\lambda) \cos(2\pi f t). \tag{C.28}$$

When axisymmetric waves on a sphere are considered, calculations become more complicated. The separation of variables is requested and solutions are

$$X = \tilde{X} P_\ell(\cos\theta) \mathrm{e}^{-2\pi i f t}, \tag{C.29}$$

where $P_\ell(x)$ is the Legendre polynomial of degree ℓ. This solution is already a standing wave, and it seems difficult to deduce the corresponding progressive wave.

However, there is a approximation for progressive waves that is determined hereafter. In order to combine angular and time variables, we need to formulate the angular part as an

amplitude modulation of the cosine. In other words, we need to determine the functions $A_\ell(\theta)$ and $\omega_\ell(\theta)$ satisfying to

$$P_\ell(\cos\theta) = A_\ell(\theta)\cos\Big(2\pi\omega_\ell(\theta)\Big). \tag{C.30}$$

The progressive waves are then given by

$$X = \tilde{X}A_\ell(\theta)\mathrm{e}^{2\pi i(\omega_\ell(\theta)\pm ft)}. \tag{C.31}$$

The equation C.30 would have an infinity of solution if we did not impose $A_\ell(\theta) > 0$. So the zeros of $\cos(2\pi\omega_\ell(\theta))$ must coincide with the zeros of the Legendre polynomials.

C.4.1 Determination of $\omega_\ell(\theta)$

The Legendre polynomial of degree ℓ always has ℓ zeros, so the same is for the cosine. If we observe these zeros as functions of θ, (Fig. C.1a), we see that they are regularly spaced. More exactly, they are approximately at positions

$$\theta_j = \frac{\frac{3\pi}{4} + j\pi}{\ell + \frac{1}{2}}; j \in \Big(\mathbb{Z}\bigcap[0, \ell - 1]\Big). \tag{C.32}$$

The error made with this approximation is represented in the inset of Fig. C.1(a). Since the zeros of the cosine are in $\pi/2 + j\pi$, we deduce the equation for $\omega_\ell(\theta)$.

$$\omega_\ell(\theta) = \left(\ell + \frac{1}{2}\right)\frac{\theta}{2\pi} - \frac{1}{8}. \tag{C.33}$$

C.4.2 Determination of $A_\ell(\theta)$

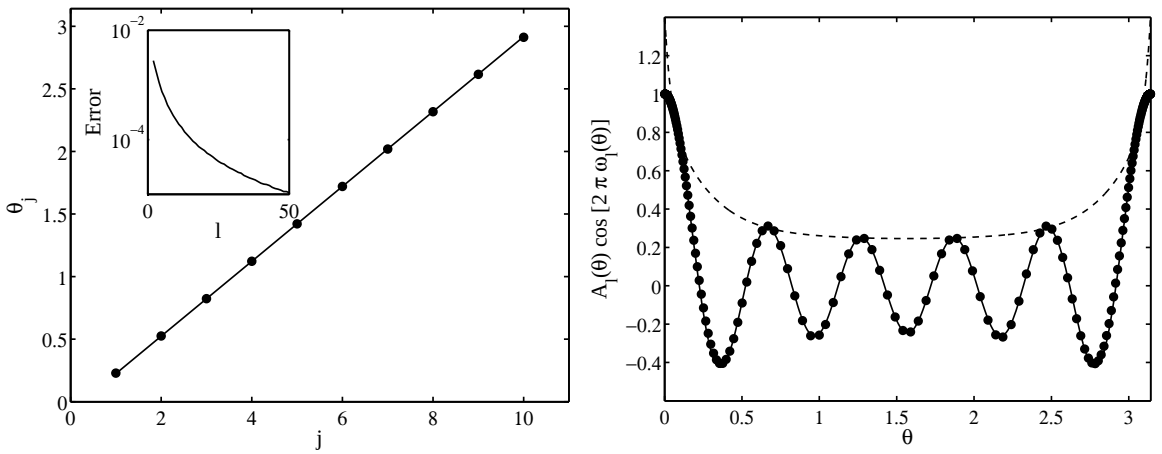

(a) (b)

Figure C.1: (a) (•) Zeros θ_j of the polynomial $P_10(\cos\theta)$, approached by equation (C.32). (Inset) Absolute error of Eq. (C.32) on the the position of zeros in the 50 first Legendre polynomials. (b) (•) Legendre polynomial with $\ell = 10$. The solid line is the approximation $A_{10}\cos(2\pi\omega_{10})$. The dashed line is the function A_{10}.

The amplitude $A_\ell(\theta)$ cannot be obtained by simply dividing the Legendre polynomial by the cosine. Indeed, since the zeros of both functions do not exactly coincide, the error explodes close to these points. We start giving some properties of the function $A_\ell(\theta)$:

1. It is even according to $\pi/2$: $A_\ell(\pi-\theta) = A_\ell(\theta)$. Indeed, both the polynomial and the cosine have the same parity as ℓ.

2. Its first derivative satisfies

$$\frac{\mathrm{d}P_\ell(x=\cos(\theta))}{\mathrm{d}\theta} = -\frac{\mathrm{d}P_\ell}{\mathrm{d}x}\sin\theta = \frac{\mathrm{d}A_\ell}{\mathrm{d}\theta}\cos\left[\left(\ell+\frac{1}{2}\right)\theta-\frac{\pi}{4}\right]-A_\ell\left(\ell+\frac{1}{2}\right)\sin\left[\left(\ell+\frac{1}{2}\right)\theta-\frac{\pi}{4}\right]. \tag{C.34}$$

3. In $\theta = 0$ (and so in $\theta = \pi$),

$$A_\ell(0) = \sqrt{2} \text{ and } \frac{\mathrm{d}A_\ell}{\mathrm{d}\theta}\Big]_{\theta=0} = -\sqrt{2}\left(\ell+\frac{1}{2}\right). \tag{C.35}$$

4. In $\theta = \pi/2$,

   - if ℓ is even,
$$A_\ell\left(\frac{\pi}{2}\right) = (-1)^{\frac{\ell}{2}}P_\ell(x=0). \tag{C.36}$$
   - else
$$A_\ell\left(\frac{\pi}{2}\right) = (-1)^{\frac{\ell-1}{2}}\frac{\ell}{\ell+\frac{1}{2}}P_{\ell-1}(x=0). \tag{C.37}$$

5. $A_\ell(\theta)$ is positive definite, must be minimal in $\theta = \pi/2$ (smallest amplitude because the energy is distributed on the whole equator) and maximal in $\theta = 0$ and $\theta = \pi$ (convergence of the energy on the poles).

We choose to represent $A_\ell(\theta)$ by a polynomial in $(\pi/2-\theta)$:

$$A_\ell(\theta) = c_0 + \sum_{i=1}^{n} c_i\left(\frac{\pi}{2}-\theta\right)^{2i} \tag{C.38}$$

where the coefficients c_i are positive, in order to ensure the positivity of the function. Coefficients are subject to three additional constraints, resulting from the behavior of A_ℓ in $\theta = 0$ and $\theta = \pi/2$:

$$\sum_{i=1}^{n} c_i\left(\frac{\pi}{2}\right)^{2i} = \sqrt{2}-c_0, \tag{C.39}$$

$$\sum_{i=1}^{n} c_i\cdot 2i\left(\frac{\pi}{2}\right)^{2i-1} = \sqrt{2}(l+1/2), \tag{C.40}$$

$$c_0 = \begin{cases} (-1)^{\frac{\ell-1}{2}}\frac{\ell}{\ell+1/2}P_{\ell-1}(0) & \text{when } l \text{ is uneven,} \\ (-1)^{\frac{\ell}{2}}P_\ell(0) & \text{when } \ell \text{ is even.} \end{cases} \tag{C.41}$$

The determination of coefficients c_i is a constrained linear least-square problem which is easily solved numerically. The number of coefficients is arbitrarily chosen to $n = 2\ell$. The result of this optimization is shown in Fig. C.1(b).

C.4.3 Wave convergence

It is possible to estimate the ratio between the amplitudes of waves at the poles and at the equator. This ratio illustrates the convergence of energy in the polar zone, and is given by

$$\frac{A_\ell(\theta = 0)}{A_\ell \theta = \pi/2)} = \frac{2^{\ell+0.5}\left[\left(\frac{\ell}{2}\right)!\right]^2}{\ell!} \tag{C.42}$$

This ratio is increasing with ℓ, so higher modes experience a more important convergence.

Appendix D

Lubrication

In this appendix, we study the axisymmetric quasi-steady flow within the air film located beneath a droplet of radius R. The air film is supposed horizontal has a thickness $h \ll R$ homogeneous according to r. The objective is to estimate the vertical force F_L required to thin the film with a thinning rate $\dot{h}$.

In cylindrical coordinates, the continuity equation writes

$$\frac{\partial_r(ru_r)}{r} + \partial_z u_z = 0. \tag{D.1}$$

The first term scales as u_r/R while the second term scales as u_z/h, so $u_z \sim u_r h/R \ll u_r$ and the flow is mainly in the r direction. The Navier-Stokes equation is greatly simplified under the assumptions $h \ll R$, $\partial_z \gg \partial_r$ and $u_r \ll u_z$, namely

$$\partial_r P = \mu_a \partial_{zz} u_r \text{ and } \partial_z P = 0. \tag{D.2}$$

In order to integrate this equation and find the radial velocity u_r, we need to prescribe boundary conditions. We suppose that the bath beneath the air film (in $z = 0$) is at rest. On the other hand, the internal flows within the droplet make the droplet/air interface ($z = h$) moving with a velocity $c_U r$. That yields

$$u_r = \frac{c_U r}{h} z - \frac{\partial_r P}{2\mu_a} z(h - z). \tag{D.3}$$

The velocity averaged over the film thickness is

$$U = \frac{\int_0^h u_r \mathrm{d}z}{h} = \frac{c_U r}{2} - \frac{\partial_r P}{12\mu_a} h^2. \tag{D.4}$$

We proceed by integrating the continuity equation in the z-direction with the assumption $\partial_r h = 0$,

$$\dot{h} = \frac{-h}{2r} \partial_r (r^2 c_U) + \frac{h^3}{12\mu_a r} \partial_r (r \partial_r P). \tag{D.5}$$

The pressure P is obtained by integrating this equation twice according to r, and by supposing that the pressure is zero in $r = R$.

$$P = -\frac{3\mu_a}{h^2} \left(\frac{\dot{h}}{h} + c_U \right) (R^2 - r^2). \tag{D.6}$$

The resulting vertical force F_L resulting from P is then given by

$$F_L = 2\pi \int_0^R Pr\mathrm{d}r = -\frac{3\pi}{2}\mu_a R^2 \left(\frac{R}{h}\right)^2 \left(\frac{\dot{h}}{h} + c_U\right) \tag{D.7}$$

We note that both the exponent and prefactor of R/h strongly depend on the considered geometry (e.g. spherical instead of cylindrical).

When a droplet is released close to a liquid interface, it thins the air film ($\dot{h} < 0$) and drains it outwards. In the same time, the droplet flattens, which creates an internal motion outwards ($c_U > 0$). Therefore, the internal flows help the air film to drain and decrease F_L. At leading order, c_U is proportional to the droplet deformation $\dot{\eta}$, namely $c_U \sim \dot{\eta}/R$.

The resulting vertical force F_L impacts on the energy balance of the droplet (Eq.5.5) through the term $F_L\dot{\eta}$. Although the resultant of horizontal stresses vanishes, the work they produce does not. It is estimated to

$$2\pi \int_0^R \mu_a \left(\partial_z u_r\right)_{z=h} (c_U r) r\mathrm{d}r = \frac{3\pi}{2}\mu_a c_U R^3 \frac{R}{h}\left(\frac{\dot{h}}{h} + \frac{4c_U}{3}\right) \tag{D.8}$$

This power scales as $F_L\dot{\eta}(h/R)$, which is much smaller than the vertical power $F_L\dot{\eta}$ and may thus be neglected.

Appendix E

The elastic ball

Walker's experiment is based on the old problem of the elastic ball. In this system, a partially elastic bead bounces indefinitely onto a surface vibrated according to a vertical sinusoidal motion of amplitude A and frequency f. The vertical position $z_s(t)$ of the surface is given by $z_s = A\cos 2\pi ft$. In the mathematical model, the bead bouncing is such that the take-off velocity is proportional to the impact velocity; the coefficient of proportionality is called restitution coefficient ϵ. Moreover, the contact time is null, so take-off occurs immediately after landing. Nowadays, the elastic ball is considered as one of the simplest experiments that illustrates chaotic concepts [191]. It obeys to relatively simple equations of motion, that are solved numerically without major issues. Like the logistic map, it seems to experience a cascade of period doubling bifurcations that leads to chaos [111].

In spite of its apparent simplicity, the elastic ball problem is far from being solved. Experimentally, the restitution coefficient is observed to depend on the impact velocity [192], exactly like for droplets on a vibrated soap film (Chap. 4). On the other hand, the chaotic behavior of the system is contested. Indeed, the elastic ball usually experience sticking cascades, namely series of bounces smaller and smaller that converge to rest in a finite time [193]. The ball then sticks on the plate and takes off again when the instantaneous acceleration of the plate is sufficiently low (i.e. less than $-g$). Even if the trajectory seems chaotic, the ball always ends up sticking to the plate [111]. This resets the system in some way, and makes the motion necessarily periodic. The sticking occurrence increases with decreasing ϵ.

The elastic ball problem is involved in various applications in both fundamental physics and engineering. It is directly related to the Fermi model encountered in astrophysics and atomic physics [194]. Shaken granular materials [195] and some optical systems [196] present obvious similarities with the elastic ball. It also provides a theoretical background for many technologies in fields as various as acoustics [197], milling [198] or atomic force microscopy [199]. Finally, the elastic ball is a standard problem in control theory [200], where the goal is to create a continuous signal $z_s(t)$ to drive the bouncing motion. One of the simplest strategies consists in juxtaposing parabolas (one per bounce) which parameters are computed from the data of previous impact. As an analog of the juggling problem [201], the elastic ball is a study case to test the control ability of human brain [202].

E.1 Equations of the elastic ball

The position of the elastic ball relative to the surface beneath is given by

$$Z(t) = c_1 + c_2 t - g\frac{t^2}{2} - A\cos\Big[2\pi f t\Big], \tag{E.1}$$

which can be made dimensionless by defining $y = (2\pi f)^2 Z/g$ and $\phi = 2\pi f t$, so

$$y(\phi) = c_3 + c_4\phi - \frac{\phi^2}{2} - \Gamma\cos\phi, \tag{E.2}$$

where $\Gamma = 4\pi^2 A f^2/g$. The constants c_3 and c_4 are determined by fixing the take-off condition $(y, \dot{y}) = (0, V_n)$ in $\phi = \phi_n$. Moreover, the ball lands in ϕ_{n+1} and takes-off immediately after with a velocity prescribed by $V_{n+1} = -\epsilon\dot{y}(\phi_{n+1})$, so

$$F_1 \equiv \Gamma(\cos\phi_n - \cos\phi_{n+1}) + (\phi_{n+1} - \phi_n)(V_n - \Gamma\sin\phi_n) - \frac{(\phi_{n+1} - \phi_n)^2}{2} = 0, \tag{E.3}$$

$$F_2 \equiv V_{n+1} + \epsilon\Big[\Gamma(\sin\phi_{n+1} - \sin\phi_n) + V_n - (\phi_{n+1} - \phi_n)\Big] = 0. \tag{E.4}$$

The flight time is defined as $T_n = \phi_{n+1} - \phi_n$. For given parameters (Γ, ϵ), the system (E.3) is a 2-dimensional map that calculates (ϕ_{n+1}, V_{n+1}) as a function of (ϕ_n, V_n).

Fixed points are given by the conditions $\phi_{n+1} = \phi_n + 2k\pi$ and $V_{n+1} = V_n$, which yield

$$\phi_n = -\arcsin\left(\frac{1-\epsilon}{1+\epsilon}\frac{k\pi}{\Gamma}\right) \text{ and } V_n = 2k\pi\frac{\epsilon}{1+\epsilon}. \tag{E.5}$$

These points only exist when

$$\Gamma \geq \Gamma_m = \frac{k\pi(1-\epsilon)}{(1+\epsilon)}. \tag{E.6}$$

Their stability is addressed by looking to the amplification of a small perturbation $(\mathrm{d}\phi_n, \mathrm{d}V_n)$ around the fixed point:

$$\begin{pmatrix} \mathrm{d}\phi_{n+1} \\ \mathrm{d}V_{n+1} \end{pmatrix} = J \begin{pmatrix} \mathrm{d}\phi_n \\ \mathrm{d}V_n \end{pmatrix} \text{ with } J = -\begin{pmatrix} \frac{\partial F_1}{\partial\phi_{n+1}} & \frac{\partial F_1}{\partial V_{n+1}} \\ \frac{\partial F_2}{\partial\phi_{n+1}} & \frac{\partial F_2}{\partial V_{n+1}} \end{pmatrix}^{-1} \begin{pmatrix} \frac{\partial F_1}{\partial\phi_n} & \frac{\partial F_1}{\partial V_n} \\ \frac{\partial F_2}{\partial\phi_n} & \frac{\partial F_2}{\partial V_n} \end{pmatrix}. \tag{E.7}$$

At fixed point, J is given by

$$J = \begin{pmatrix} 1 - (1+\epsilon)\Gamma\cos\phi_n & 1+\epsilon \\ \epsilon(1+\epsilon)\Gamma\cos\phi_n(\Gamma\cos\phi_n - 1) & \epsilon^2(1 - \Gamma\cos\phi_n) - \epsilon\Gamma\cos\phi_n. \end{pmatrix} \tag{E.8}$$

The fixed point is stable only when the eigenvalues of J are smaller than 1 in modulus. After calculations, this condition writes

$$\Gamma < \Gamma_M = \sqrt{\frac{4(1+\epsilon^2)^2}{(1+\epsilon)^4} + \Gamma_m^2}. \tag{E.9}$$

Passed this point, the system experience a period doubling bifurcation.

E.2 Inelastic ball

Equations (E.3) may be particularized to the case of a completely inelastic ball, namely $\epsilon = 0$ [203]. At impact, the ball loses any information about its previous velocity, and takes the velocity of the vibrating plate (i.e. $V_n = 0$). Therefore, immediate take-off is observed only when $\Gamma \cos\phi_n \geq 1$. Otherwise, the ball sticks on the plate until the take-off condition is satisfied. The flight time T_n is given by

$$F \equiv \Gamma \cos\phi_n(1 - \cos T_n) - -\Gamma \sin\phi_n(T_n - \sin T_n) - \frac{T_n^2}{2} = 0, \tag{E.10}$$

which is much simple since we only need to determine $T_n(\phi_n)$ with a single parameter Γ instead of two. As easy as this problem may seem, its bifurcation diagram $T_n(\Gamma)$ is complex and contains fractal-like structures, shaped by the interplay of two kinds of bifurcations, repeated a non-denumerable number of times. A more detailed investigation of this case has been made in [204].

Appendix F

Faraday instability

The Faraday instability consists in the destabilization of a planar interface between two fluids, due to a vertical oscillation of the whole system. In a container of finite dimensions, this instability gives birth to standing waves of finite amplitude. Experiments on these waves were reported for the first time by Faraday in 1831 [125]. Although the waves are easily observed by placing a simple container on a speaker, accurate measurements of the threshold require good experimental conditions. In particular, the vibration has to be perfectly vertical [126], and the meniscus at the container edges must be kept horizontal. This can be made by pinning the meniscus into a wedge, or by realizing an overflow. In the case the meniscus is free to move, it starts emitting capillary waves that prematurely trigger the instability [132]. The first analytical model of the Faraday instability was proposed in 1954 by Benjamin and Ursell [126]. These authors assumed inviscid fluids and obtained a Mathieu equation, i.e. a second-order linear homogeneous differential equation where the coefficient of the 0-order term is periodic. According to this equation, the threshold should be zero, and the interface must always be unstable. In reality, the Faraday instability cannot be described without taking viscosity into account.

In this appendix, we present the model firstly introduced by Kumar and Tuckerman in 1994 [129], adapted to a liquid/air interface. We denote by $\vec{v}$ the velocity field, $\vec{u}$ its horizontal component and $w\vec{e_z}$ its vertical component, where $\vec{e_z}$ is the downward-pointing unit vector. Continuity and Navier-Stokes equations are written for the liquid phase, in the frame of the vibrated container,

$$\boldsymbol{\nabla} \cdot \vec{v} = 0 \tag{F.1}$$

$$\partial_t \vec{v} + (\vec{v} \cdot \boldsymbol{\nabla})\vec{v} = -\frac{\boldsymbol{\nabla} P}{\rho} + g(1 - \Gamma \cos \omega t)\vec{e_z} + \nu \boldsymbol{\nabla}^2 \vec{v}, \tag{F.2}$$

where ω is the angular frequency of the vibration. We linearize the second equation around the reference state (planar interface): $\vec{v} = 0$ and $P_0 = \rho g z(1 - \Gamma \cos \omega t)$. We note p the pressure perturbation and keep $\vec{v}$, $\vec{u}$ and w for the velocity perturbations. The vertical velocity w and pressure p are thus obtained by

$$\partial_t \nabla^2 w = \nu \nabla^4 w \tag{F.3}$$

$$\nabla_h^2 p = \rho \partial_{tz} w - \rho \nu \nabla^2 \partial_z w, \tag{F.4}$$

where ∇_h^2 is the horizontal part of the Laplacian operator.

One has now to impose boundary conditions. At the bottom of the container, the velocity must vanish, so$w = 0$ and $\vec{u} = 0$ in $z = h$. At the free surface ($z = \eta(x, y, t)$), the normal velocity of fluid particles has to be equal to the normal velocity of the interface. This condition, once linearized, yields $w = \partial_t \eta$. Moreover, the tangential stress exerted by the air is negligible, which gives $\nabla_h^2 w = \partial_{zz} w$. The normal stress involves pressure, gravity, the normal component of the velocity gradient and surface tension. Balance between these interactions yields

$$\frac{p}{\rho} = g\eta(\Gamma \cos \omega t - 1) + 2\nu \partial_z w + \sigma \nabla_h^2 \eta. \tag{F.5}$$

This equation can be reformulated by using the equation for pressure within the liquid, so

$$\left[\partial_t - 3\nu\nabla_h^2 - \nu\partial_{zz}\right]\partial_z w = \left[g(\Gamma \cos \omega t - 1) + \frac{\sigma}{\rho}\nabla_h^2\right]\nabla_h^2 \eta. \tag{F.6}$$

We note that this equation is the only one where the forcing term $\Gamma \cos \omega t$ appears. In a media of infinite horizontal extension, we may assume that the horizontal part of the solution is proportional to $\sin(k_x x + k_y y)$. We can therefore replace ∇_h^2 by $-k^2$ with $k^2 = k_x^2 + k_y^2$. By the way, we do not need anymore to prescribe boundary conditions on the lateral walls. Practically, the spectrum of k_x and k_y is discretized by the lateral walls, an effect which is significant only when the wavelength is of the order of the horizontal extension of the container. We thus obtain a system of equations for unknowns $w(z, t)$ and $\eta(t)$:

$$(\partial_t + \nu k^2 - \nu\partial_{zz})(\partial_{zz} - k^2)w = 0 \qquad \forall z, \tag{F.7}$$

$$w = \partial_z w = 0 \qquad \text{in } z = h, \tag{F.8}$$

$$w = \partial_t \eta \qquad \text{in } z = 0, \tag{F.9}$$

$$(\partial_{zz} + k^2)w = 0 \qquad \text{in } z = 0, \tag{F.10}$$

$$\left[\partial_t + 3\nu k^2 - \nu\partial_{zz}\right]\partial_z w = \left[g(1 - \Gamma \cos \omega t) + \frac{\sigma}{\rho}k^2\right]k^2\eta \qquad \text{in } z = 0. \tag{F.11}$$

According to the Floquet theory, we should expect

$$w(z, t) = \mathrm{e}^{(\mu + i\alpha)t} \sum_{n=-\infty}^{\infty} w_n(z)\mathrm{e}^{in\omega t}, \tag{F.12}$$

$$\eta(t) = \mathrm{e}^{(\mu + i\alpha)t} \sum_{n=-\infty}^{\infty} \eta_n \mathrm{e}^{in\omega t}, \tag{F.13}$$

$$\tag{F.14}$$

with $\alpha \in [0, \omega/2]$. The solutions are stable when $\mu < 0$ and unstable otherwise. The solution is harmonic when $\alpha = 0$, while it is subharmonic when $\alpha = \omega/2$. Defining $q_n^2 = 1 + \frac{\mu + i(\alpha + n\omega)}{\nu k^2}$ yields

$$w_n(z) = a_n \cosh kz + b_n \sinh kz + c_n \cosh q_n kz + d_n \sinh q_n kz. \tag{F.15}$$

The four first boundary conditions are

$$\begin{bmatrix} \cosh kh & \sinh kh & \cosh q_n kh & \sinh q_n kh \\ \sinh kh & \cosh kh & q_n \sinh q_n kh & q_n \cosh q_n kh \\ 2 & 0 & 1 + q_n^2 & 0 \\ 1 & 0 & 1 & 0 \end{bmatrix} \begin{bmatrix} a_n \\ b_n \\ c_n \\ d_n \end{bmatrix} = \nu k^2 (q_n^2 - 1)\eta_n \begin{bmatrix} 0 \\ 0 \\ 0 \\ 1 \end{bmatrix}. \tag{F.16}$$

Inverting this system leads to the coefficients a_n, b_n, c_n and d_n:

$$\begin{cases} a_n = \nu k^2(1+q_n^2)\eta_n, \\ b_n = \frac{(q_n - \tanh kh \tanh q_n kh)a_n + \frac{q_n c}{\cosh kh \cosh q_n kh}}{\tanh q_n kh - q_n \tanh kh}, \\ c_n = -2\nu k^2 \eta_n, \\ d_n = \frac{(q_n \tanh kh \tanh q_n kh - 1)c - \frac{a}{\cosh kh \cosh q_n kh}}{\tanh q_n kh - q_n \tanh kh}. \end{cases} \tag{F.17}$$

The last boundary condition writes

$$2\left[1 + \frac{\sigma k^2}{\rho g} - \frac{\nu^2 k^3}{g} F(q_n, kh)\right]\eta_n = \Gamma(\eta_{n+1} + \eta_{n-1}), \tag{F.18}$$

where

$$F(q_n, kh) = \frac{(q_n^5 + 2q_n^3 + 5q_n) - (q_n^4 + 6q_n^2 + 1)\tanh kh \tanh q_n kh - 4\frac{q_n + q_n^3}{\cosh kh \cosh q_n kh}}{\tanh q_n kh - q_n \tanh kh}. \tag{F.19}$$

We note that this condition couples η_{n+1} and η_{n-1} to η_n through the forcing term, so the solution cannot be obtained analytically. The condition F.18 is a system with an infinity of complex equations, that has to be truncated by only computing η_n with $n \in [0, N]$. Real perturbations η satisfy $\eta_{-n} = \eta_n^*$ in the harmonic case ($\alpha = 0$) and $\eta_{-n-1} = \eta_n^*$ in the subharmonic case ($\alpha = \omega/2$).

Usually, in stability analysis, k and Γ are fixed, so μ and α are determined and the observed mode is the most unstable, namely the mode of largest μ. Here, we proceed backwards and compute the marginal stability curves ($\mu = 0$) for both harmonic and subharmonic cases (which fix α). These tongue-like curves are plotted in Fig. F.1(a) for the following parameters: $g = 9.81$ m/s^2, $\sigma = 20$ mN/m, $\rho = 965$ kg/m^3, $h = 0.1$ m, $\nu = 50$ cS and $\omega = 100\pi$ rad/s. The solution in unstable and Faraday waves appear within the tongues. The instability threshold Γ_F is the minimum of these stability curves; its abscissa k_F indicates the wavelength observed just above the threshold. The predicted threshold is in relatively good agreement with the experimental measurements at $h = 9$ mm (Fig. F.1b). Finally, we note that, by equalling Γ to zero in Eq. (F.18), we recover the dispersion relation of gravity/capillary waves with a finite depth and the inclusion of viscosity effects,

$$1 + \frac{\sigma k^2}{\rho g} = \frac{\nu^2 k^3}{g} F(q_n, kh). \tag{F.20}$$

F.1 Instability in a container of infinite depth

When the liquid bath is sufficiently deep, namely when $k_S h \gg 1$, the function $F(q_n, kh)$ is notably simplified,

$$F(q_n) = -(q_n^4 + 2q_n^2 + 4q_n + 1). \tag{F.21}$$

Figure F.2 represents the threshold Γ_F computed by Eq. (F.18) as a function of viscosity ν and frequency $f = \omega/2\pi$. Scaling laws are observed for both Γ_F and k_F:

$$\begin{cases} \omega \simeq 2\Omega(k_F), \\ \Gamma_F \simeq 3.5\frac{\nu k_F \omega}{g}, \end{cases} \tag{F.22}$$

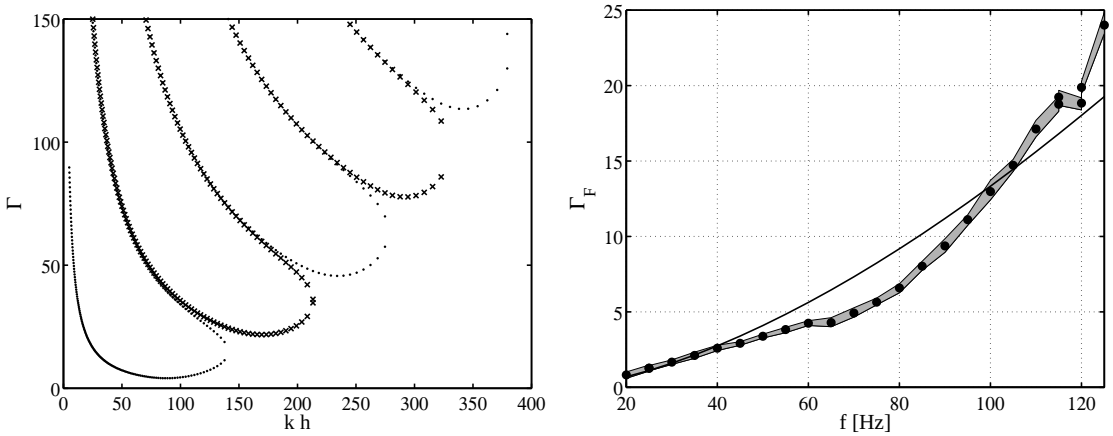

Figure F.1: (a) Marginal stability curves: (•) subharmonic, and (×) harmonic solutions. Within the tongues, the system is unstable and Faraday waves appear. (b) Comparison between the model results and the experimental measurements for $\nu = 50$ cS, $h = 9$ mm, $\sigma = 20$ mN/m and $\rho = 965$ kg/m^3.

where $\omega = \Omega(k)$ is the dispersion relation of gravity/capillary waves given by Eq. (F.20). The first equation indicates that the selected wave number corresponds to half the forcing frequency, which is coherent for the subharmonic case. As seen in Fig. F.2, these scaling laws correctly represent the threshold curves in a large range of parameters. Predictions are good provided $k_F h > 2$, which is coherent with our hypothesis of infinite depth.

We conclude by establishing the dispersion relation $\Omega(k)$ for the viscous gravity/capillary waves. First, we define

$$1 + x = q_n^2 = 1 + \frac{\mu(k) + i\Omega(k)}{\nu k^2}, \tag{F.23}$$

in Eq. (F.20) and

$$\alpha = \frac{gk + \sigma k^3}{\nu^2 k^4}, \tag{F.24}$$

so

$$x^4 + 8x^3 + (24 + 2\alpha)x^2 + (16 + 8\alpha)x + \alpha(\alpha + 8) = 0. \tag{F.25}$$

This equation has four complex solutions. Nevertheless, the polynomial is convex, namely the second derivative is positive everywhere, and the function is both positive and increasing in $x = 0$, whatever α. So we can state that every real solution is necessarily negative or zero. But in reality, waves correspond to not-real solutions, for which $\Omega(k) \neq 0$. To find them, we have to set $x = a + ib$, which yields

$$\begin{cases} b^2 = \frac{a^3+6a^2+(12+\alpha)a+4+2\alpha}{a+2}, \\ a^6 + 12a^5 + (60+\alpha)a^4 + 8(20+\alpha)a^3 + 4(59+6\alpha)a^2 + 16(11+2\alpha)a + 4(11+4\alpha) = 0. \end{cases} \tag{F.26}$$

This polynomial of degree 6 has a fixed point according to α in $a = -2$. In this point, the polynomial is negative and experience a local maximum. This maximum should be the only one since the fourth derivative is positive semi-definite. So the polynomial cannot have more than two distinct real roots a, which are shown to be negative. Practically, we can show that when $\alpha < 0.546$, Eq. (F.25) has two real roots that do not correspond to waves, and a pair

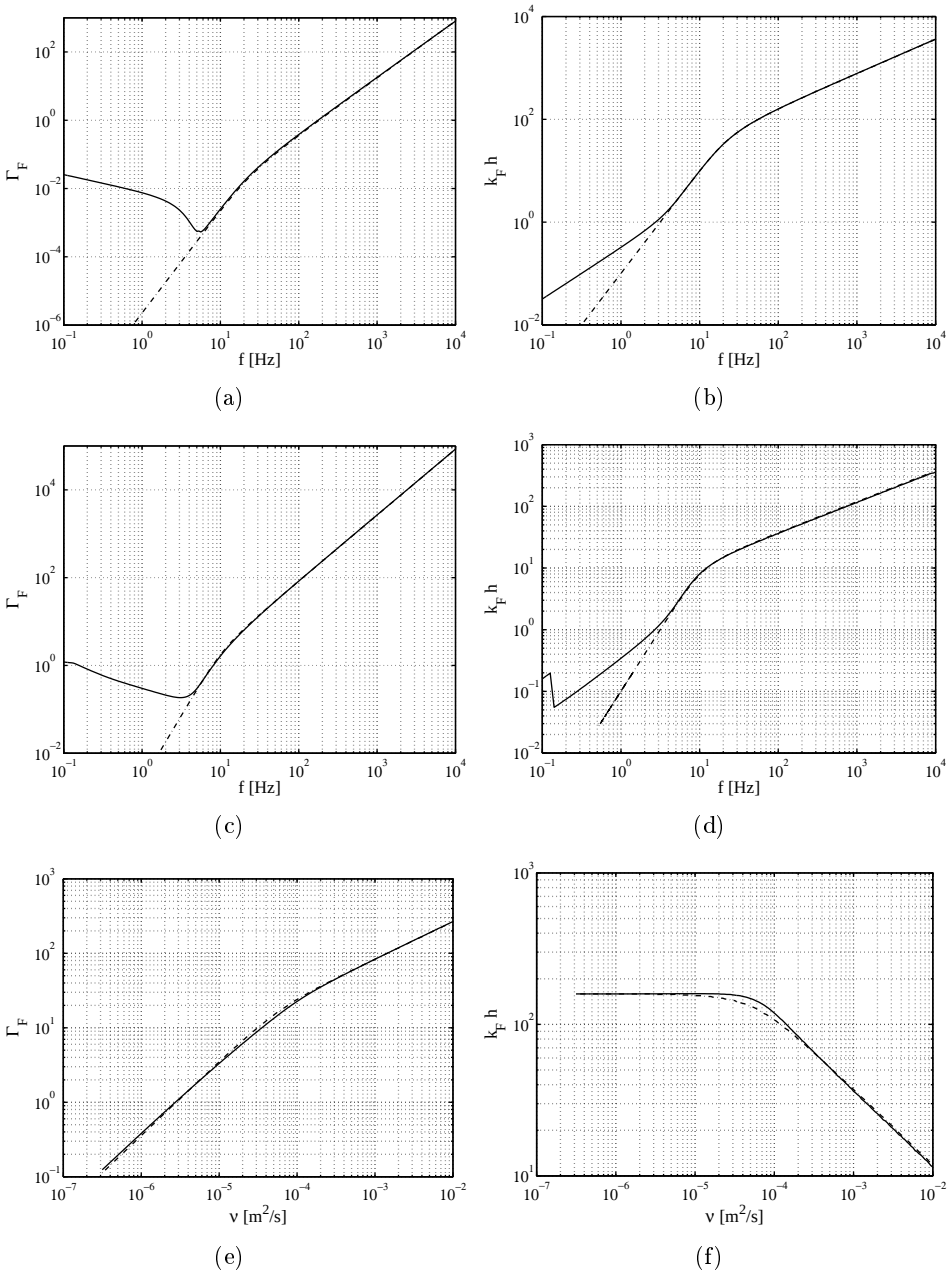

Figure F.2: Threshold acceleration Γ_F and wavelength k_F of the Faraday instability for a container of infinite depth. Parameters are $h = 0.1$ m, $\rho = 965$ kg/m^3 and $\sigma = 20$ mN/m. The solid lines correspond to the numerical resolution of Eq. (F.18) while the dashed lines represent the relation (F.22). (a-b) Variation with f for $\nu = 1$ cS, (c-d) variation with f for $\nu = 1000$ cS, and (e-f) variation with ν for $f = 100$ Hz.

of complex conjugate roots corresponding to damped waves. When $\alpha > 0.546$, there are two pairs of complex conjugate roots, so two distinct frequencies satisfy to the dispersion relation for the same k. This transition between one and two frequencies corresponds to the change of regime non-viscous/viscous observed in Fig. F.2(e-f).

Appendix G

Droplets on fibers

G.1 Static shape of a droplet on a fiber

In this section, we propose to solve Eq. (8.1) introduced in chapter 8 to describe the axisymmetric shape of a droplet of volume Ω wetting a fiber of diameter d_v. We neglect the influence of gravity, so equations are

$$\left\{\begin{array}{lll} \frac{\mathrm{d}r}{\mathrm{d}s} & = & \cos\varphi, \\ \frac{\mathrm{d}z}{\mathrm{d}s} & = & \sin\varphi, \\ \frac{\mathrm{d}\varphi}{\mathrm{d}s} & = & \frac{\Delta P}{\sigma} - \frac{\sin\varphi}{r}, \end{array}\right. \tag{G.1}$$

where ΔP is the overpressure within the droplet, at location $z = 0$. These equations cannot be solved analytically in the general case, but asymptotic solutions may be inferred when the droplet volume Ω is either much smaller or much bigger than d_v^3.

Large droplets (typically $\Omega/d_v^3 > 10^4$) tend to keep their spherical shape when hanged on a fiber. The sphere of radius R, described by $(r_0, z_0, s_0) = R(\sin\varphi, 1 - \cos\varphi, \varphi)$ satisfies Eq. (8.1) for $\Delta p = 2\sigma/R \ll 1$, but not matching conditions on the fiber. Next to these matching points, the curvature still need to be $1/R$, which is much smaller than the fiber curvature $2/d_v$. Therefore, the droplet may be locally approximated by a catenoid (zero-curvature surface) of equation

$$r_1 = \frac{d_v}{2\sin\varphi}, \qquad z_1 = \frac{d_v}{2}\ln\left(\frac{\sin\varphi}{1-\cos\varphi}\right) \quad \text{and} \quad s = \frac{d_v}{2}\cot\varphi. \tag{G.2}$$

Both solutions match each other when $r_0 = r_1$ for the same angle φ, so when $\sin\varphi = \sqrt{d_v/2R}$ and $r = \sqrt{Rd_V/2} \ll R$. The droplet volume is roughly equal to the volume of the sphere, the catenoidal contribution being negligible. Therefore, we infer

$$\frac{W}{d_v} \simeq \left(\frac{3\Omega}{4\pi d_v^3}\right) \quad \text{and} \quad X = 2W. \tag{G.3}$$

These scalings are similar to those discussed in [171].

When the droplet size is smaller than d_v, the droplet spreads on the fiber in such a way that the curvature of its interface is only slightly lower than the fiber curvature $2/d_v$. Therefore, we can infer the asymptotic solution by perturbing the solution $(r_0, z_0, \varphi_0) = (d_v/2, s, \pi/2)$ when

$\Omega = 0$ (corresponding to the fiber itself). Supposing $\Delta p = 2\sigma(1-\varepsilon)/d_v$ and perturbations denoted by tilted variables, we obtain

$$\left\{ \begin{array}{ll} \frac{\mathrm{d}\tilde{r}}{\mathrm{d}s} & \simeq -\tilde{\varphi}, \\ \frac{\mathrm{d}\tilde{z}}{\mathrm{d}s} & \simeq 0, \\ \frac{\mathrm{d}\tilde{\varphi}}{\mathrm{d}s} & \simeq \frac{4\tilde{r}}{d_v^2} - \frac{2\varepsilon}{d_v}, \end{array} \right. \tag{G.4}$$

from which we find the droplet shape

$$\begin{pmatrix} r \\ z \\ \varphi \end{pmatrix} = \begin{pmatrix} \frac{d_v}{2}\left[1 + \varepsilon\left(1 - \cos\frac{2s}{d_v}\right)\right] \\ s \\ \frac{\pi}{2} - \varepsilon \sin\frac{2s}{d_v} \end{pmatrix}. \tag{G.5}$$

The droplet shape is therefore close to a sinusoid. The vertical extension X is equal to πd_v, which corresponds to the fiber perimeter. The thickness and volume of the droplet are easily computed,

$$\frac{W}{d_v} = \varepsilon = \frac{8\Omega}{\pi^2 d_V^3} \quad \text{and} \quad \frac{X}{d_v} = \pi. \tag{G.6}$$

It is seen in figure 8.4 that both small and large droplets are well described by the proposed asymptotic behaviors.

G.2 Rayleigh-Plateau instability

A film of liquid covering a fiber spontaneously turns into a string of droplets, i.e. an unduloidal shape, due to the Rayleigh-Plateau instability. The related calculation is detailed in this section. We first suppose that the thickness of the film h is much smaller than the fiber diameter d, so the lubrication equations can be applied,

$$\partial_z P = \mu \partial_{rr} u_z \quad \text{and} \quad \partial_r P = 0, \tag{G.7}$$

where the z-axis (resp. r-axis) is parallel (resp. normal) to the fiber. Boundary conditions are $u_z(d/2) = 0$ (no-slip condition) and $\partial_r u_z(d/2 + h) = 0$ (free surface). The velocity field thus writes

$$u_z = -\frac{\partial_z P}{\mu}\left(r - \frac{d}{2}\right)\left(h - \frac{2r-d}{4}\right), \tag{G.8}$$

so the flow rate in a z-section is

$$Q(z) = 2\pi \int_{d/2}^{h+d/2} u_z r \mathrm{d}r = -\frac{\pi d h^3 \partial_z P}{3\mu}\left(1 + \frac{5h}{4d}\right). \tag{G.9}$$

The continuity equation yields

$$\partial_z Q = -\pi d\left(1 + \frac{2h}{d}\right)\partial_t h, \tag{G.10}$$

so

$$3\mu d\left(1 + \frac{2h}{d}\right)\partial_t h = \partial_z\left[\left(1 + \frac{5h}{4d}\right) d h^3 p_z P\right]. \tag{G.11}$$

The pressure gradient is found through the Laplace law,

$$\frac{P}{\sigma} = -\frac{\partial_{zz}h}{\left[1+(\partial_z h)^2\right]^{3/2}} + \frac{2}{(2h+d)\left[1+(\partial_z h)^2\right]^{1/2}}. \tag{G.12}$$

Both equations (G.11) and (G.12) are considerably simplified under the assumptions $h \ll d$ and $\partial_z h \ll 1$,

$$3\mu\partial_t h = \partial_z\left(h^3\partial_z P\right) \tag{G.13}$$

$$\frac{P}{\sigma} = -\partial_{zz}h + \frac{2}{d+2h}, \tag{G.14}$$

so

$$\frac{3\mu}{\sigma}\partial_t h = -h^3\partial_{zzzz}h - \frac{4h^3}{d^2}\partial_{zz}h - 3h^2\partial_z h\partial_{zzz}h - 3\frac{4h^2}{d^2}(\partial_z h)^2. \tag{G.15}$$

We proceed by linearizing this equation and considering a small perturbation of the initial uniform film $h = h_i$, namely

$$h = h_i + \varepsilon \mathrm{e}^{ikz}\mathrm{e}^{-\beta t}. \tag{G.16}$$

Substituting this expression into (G.15) leads to the damping factor

$$\beta = \frac{\sigma}{3\mu}\frac{h_i^3}{d^4}k^2d^2\left(k^2d^2-4\right). \tag{G.17}$$

The instability occurs when $\beta < 0$, which corresponds to a wavelength $\lambda = 2\pi/k > \pi d$. Therefore, any perturbation of wavelength greater than the fiber diameter is unstable. The observed wavelength is the most unstable one, i.e. $\lambda = \pi\sqrt{2}d$. The related characteristic time of the instability is

$$t_{RP} = \frac{1}{\beta} = \frac{3\mu d^4}{4\sigma h_0^3}. \tag{G.18}$$

Bibliography

[1] Larousse, ed., Le Larousse de poche (Larousse-Bordas, 1998).

[2] L. Rayleigh, *The principle of similitude*, Nature **95**, 66 (1915).

[3] E. Guyon, J-P. Hulin and L. Petit, Hydrodynamique physique (EDP Sciences / CNRS Editions, 2001).

[4] P.G. de Gennes, F. Brochard-Wyart and D. Quéré, Gouttes, bulles, perles et ondes (Belin, 2002).

[5] D.L. Hu and J.W.M. Bush, *Meniscus-climbing insects*, Nature **437**, 733 (2005).

[6] A. Yarin, *Drop impact dynamics : Splashing, spreading, receding, bouncing...*, Annu. Rev. Fluid Mech. **38**, 159 (2006).

[7] J.W.M. Bush and A.E. Hasha, *On the collision of laminar jets: fluid chains and fish-bones*, J. Fluid Mech. **511**, 285 (2004).

[8] R. Savino, D. Paterna and M. Lappa, *Marangoni flotation of liquid droplets*, J. Fluid Mech. **479**, 307 (2003).

[9] S.T. Thoroddsen, T.G. Etoh and K. Takehara, *High-speed imaging of drops and bubbles*, Annu. Rev. Fluid Mech. **40**, 257 (2008).

[10] L.T. Elkins-Tanton, P. Aussillous, J. Bico, D. Quéré and J.W.M. Bush, *A laboratory model of splash-form tektites*, Meteoritics **38**, 1331 (2003).

[11] P. Dell'Aversana and G.P. Neitzel, *When liquids stay dry*, Phys. Today **51**, 38 (1998).

[12] S. N. Reznik, W. Salalha, A. Yarin and E. Zussman, *Microscale fibre alignment by a three-dimensional sessile drop on a wettable pad*, J. Fluid Mech. **574**, 179 (2007).

[13] C. Py, P. Reverdy, L. Doppler, J. Bico, B. Roman and C. Baroud, *Capillary origami*, Phys. Fluids **19**, 091104 (2007).

[14] http://www.physorg.com/news308.html, *Philips' fluid lenses bring things into focus : unique variable-focus with no mechanical moving parts.*

[15] D. Psaltis, S.R. Quake and C. Yang, *Developing optofluidic technology through the fusion of microfluidics and optics*, Nature **442**, 381 (2006).

[16] H. Song, D.L. Chen and R.F. Ismagilov, *Reactions in droplets in microfluidic channels*, Angew. Chem. Int. Ed. **45**, 7336 (2006).

[17] Y. Fouillet and J.-L. Achard, *Microfluidique discrète et biotechnologie*, C.R. Physique **5**, 577 (2004).

[18] D.R. Meldrum and M.R. Holl, *Microscale bioanalytical systems*, Science **297**, 1197 (2002).

[19] G. Whitesides, *The origins and the future of microfluidics*, Nature **442**, 368 (2006).

[20] J. Knight, *Honey, i shrunk the lab*, Nature **418**, 474 (2002).

[21] T.M. Squires and S.R. Quake, *Microfluidics : fluid physics at the nanoliter scale*, Rev. Mod. Phys. **77**, 977 (2005).

[22] H.A. Stone, A.D. Stroock and A. Ajdari, *Engineering flows in small devices: Microfluidics toward a lab-on-a-chip*, Annu. Rev. Fluid Mech. **36**, 381 (2004).

[23] H.A. Schifter and G. Lee, *Protein spray drying: single droplet drying kinetics via acoustic levitation.*

[24] L. Mangin, *Sphères moléculinaires*, Pour la Science **Juillet** (2008).

[25] M. Joanicot and A. Ajdari, *Droplet control for microfluidics*, Science **309**, 887 (2005).

[26] A.V. Anilkumar, C.P. Lee and T.G. Wang, *Stability of an acoustically levitated and flattened drop: an experimental study*, Phys. Fluids A **5**, 2763 (1993).

[27] A.L. Yarin, M. Pfaffenlehner and C. Tropea, *On the acoustic levitation of droplets*, J. Fluid Mech. **356**, 65 (1998).

[28] C. Coirault, J.-C. Pourny, F. Lambert and Y. Lecarpentier, *Les pinces optiques en biologie et en médecine*, Medecine/sciences **19**, 364 (2005).

[29] E. Brandt, *Levitation in physics*, Science **243**, 249 (1989).

[30] R. Papen, R. Ellson and J. Olechno, *Sound effects*, American Laboratory **December** (2004).

[31] D.L. Chen, L. Li, S. Reyes, D.N. Adamson and R.F. Ismagilov, *Using three-phase flow of immiscible liquids to prevent coalescence of droplets in microfluidic channels: criteria to identify the third liquid and validation with protein crystallization*, Langmuir **23**, 2255 (2007).

[32] M. Prakash and N. Gershenfeld, *Microfluidic bubble logic*, Science **315**, 832 (2007).

[33] T. Lincoln, *Do-it-yourself microfluidics*, Nature **452**, 421 (2008).

[34] F. Su, K. Chakrabarty and R.B. Fair, *Microfluidics-based biochips: technology issues, implementation platforms, and design-automation challenges*, IEEE Trans. Comput.-Aid. Des. Integr. Circ. Syst. **25** (2006).

[35] P. de Gennes, *Wetting: statics and dynamics*, Rev. Mod. Phys. **57**, 827 (1985).

[36] J. Bico and D. Quéré, *Self-propelling slugs*, J. Fluid Mech. **467**, 101 (2002).

[37] N. LeGrand, A. Daerr and L. Limat, *Shape and motion of drops sliding down an inclined plane*, J. Fluid Mech. **541**, 293 (2005).

[38] F. Mugele, A. Klingner, J. Buehrle, D. Steinhauser and S. Herminghaus, *Electrowetting: a convenient way to switchable wettability patterns*, J. Phys.: Condens. Matter **17**, 559 (2005).

[39] M. Gunji and M. Washizu, *Self-propulsion of a water droplet in an electric field*, J. Phys. D: Appl. Phys. **38**, 2417 (2005).

[40] U. Thiele, K. John and M. Bär, *Dynamical model for chemically driven running droplets*, Phys. Rev. Lett. **93**, 027802 (2004).

[41] M. Callies, Splendeur et misère de l'effet Lotus, Ph.D. thesis, Université Paris VI (2007).

[42] M. Reyssat and D. Quéré, *L'effet lotus*, Pour la Science **347**, 34 (2006).

[43] R. Blossey, *Self-cleaning surfaces - virtual realities*, Nature Materials **2**, 301 (2003).

[44] H. Linke, B.J. Aleman, L.D. Melling, M.J. Taormina, M.J. Francis, C.C. Dow-Hygelund, V. Narayanan, R.P. Taylor and A. Stout, *Self-propelled leidenfrost droplets*, Phys. Rev. Lett. **96**, 154502 (2006).

[45] P. Aussillous and D. Quéré, *Liquid marbles*, Nature **411**, 924 (2001).

[46] P. Aussillous and D. Quéré, *Shapes of rolling liquid drops*, J. Fluid Mech. **512**, 133 (2004).

[47] J.W.M. Bush, D.L. Hu and M. Prakash, *The integument of water-walking arthropods: form and function*, Adv. Insect Physiol. **34**, 117 (2008).

[48] P. Brunet, J. Eggers and R.D. Deegan, *Vibration-induced climbing of drops*, Phys. Rev. Lett. **99**, 144501 (2007).

[49] P. Brunet, J. Eggers and R.D. Deegan, *Motion of a drop driven by substrate vibrations*, Eur. Phys. J. Special Topics **166**, 11 (2008).

[50] M. Prakash, D. Quéré and J.W.M. Bush, *Surface tension transport of prey by feeding shorebirds: the capillary ratchet*, Science **320**, 931 (2008).

[51] L. Rayleigh, *The influence of electricity on colliding water drops*, Proc. R. Soc. London Ser.A **28**, 406 (1879).

[52] L. Rayleigh, *Further observations upon liquid jets, in continuation of those recorded in the royal society's proceedings for march and may, 1879*, Proc. R. Soc. London Ser.A **34**, 130 (1882).

[53] J. Qian and C.K. Law, *Regimes of coalescence and separation in droplet collision*, J. Fluid Mech. **331**, 59 (1997).

[54] G. Brenn, D. Valkovska and K.D. Danov, *The formation of satellite droplets by unstable binary drop collisions*, Phys. Fluids **13**, 2463 (2001).

[55] O.W. Jayaratne and B.J. Mason, *The coalescence and bouncing of water drops at an air/water interface*, Proc. R. Soc. London, Ser. A **280**, 545 (1964).

[56] B. Ching, M.W. Golay and T.J. Johnson, *Droplet impacts upon liquid surfaces*, Science **226**, 535 (1984).

[57] A. Worthington, *On impact with a liquid surface*, Proc. Roy. Soc. **25**, 261 (1882).

[58] M. Rein, *The transitional regime between coalescing and splashing drops*, J. Fluid Mech. **306**, 145 (1996).

[59] A. Prosperetti and H.N. Oguz, *The impact of drops on liquid surfaces and the underwater noise of rain*, Annu. Rev. Fluid Mech. **25**, 577 (1993).

[60] M. Thrasher, S. Jung, Y.K. Pang, C-P. Chuu and H.L. Swinney, *Bouncing jet: a newtonian liquid rebounding off a free surface*, Phys. Rev. E **76**, 056319 (2007).

[61] E. Reyssat, Gouttes, films et jets: quand les écoulements modèlent les interfaces, Ph.D. thesis, Université Paris VII (2007).

[62] S. Dorbolo, H. Caps and N. Vandewalle, *Fluid instabilities in the birth and death of antibubbles*, New J. Phys. **5**, 161 (2003).

[63] K.L. Pan and C.K. Law, *Dynamics of droplet-film collision*, J. Fluid Mech. **587**, 1 (2007).

[64] D. Legendre, C. Daniel and P. Guiraud, *Experimental study of a drop bouncing on a wall in a liquid*, Phys. Fluids **17**, 097105 (2005).

[65] D. Richard, C. Clanet and D. Quéré, *Contact time of a bouncing drop*, Nature **417**, 811 (2002).

[66] D. Bartolo, F. Bouamrirene, E. Verneuil, A. Buguin, P. Silberzan and S. Moulinet, *Bouncing or sticky droplets: impalement transitions on micropatterned surfaces*, Europhys. Lett. **74**, 299 (2006).

[67] D. Bartolo, C. Josserand and D. Bonn, *Singular jets and bubbles in drop impact*, Phys. Rev. Lett. **96**, 124501 (2006).

[68] E. Boucher, *Capillary phenomena : properties of systems with fluid/fluid interfaces*, Rep. Prog. Phys. **43**, 497 (1980).

[69] X.D. Shi, M.P. Brenner and S.R. Nagel, *A cascade of structure in a drop falling from a faucet*, Science **265**, 219 (1994).

[70] C. Clanet and J.C. Lasheras, *Transition from dripping to jetting*, J. Fluid Mech. **383**, 307 (1999).

[71] H. Dong, W.W. Carr and J.F. Morris, *An experimental study of drop-on-demand drop formation*, Phys. Fluids **18**, 072102 (2006).

[72] P. Coullet, L. Mahadevan and C.S. Riera, *Hydrodynamical models for the chaotic dripping faucet*, J. Fluid Mech. **526**, 1 (2005).

[73] D. Bogy, *Drop formation in a circular liquid jet*, Annu. Rev. Fluid Mech. **11**, 207 (1979).

[74] J. Plateau, Statique expérimentale et théorique des liquides soumis aux seules forces moléculaires (Paris: Gauthier-Villars, 1873).

[75] L. Rayleigh, *On the capillary phenomena of jets*, Proc. Roy. Soc. London **29**, 71 (1879).

[76] S. Protiere, A. Boudaoud and Y. Couder, *Particle-wave association on a fluid interface*, J. Fluid Mech. **554**, 85 (2006).

[77] C.L. Goodridge, W.T. Shi and D.P. Lathrop, *Threshold dynamics of singular gravity-capillary waves*, Phys. Rev. Lett. **76**, 1824 (1996).

[78] J. Eggers, *Nonlinear dynamics and breakup of free-surface flows*, Rev. Mod. Phys. **69**, 865 (1997).

[79] J. Eggers, J.R. Lister and H.A. Stone, *Coalescence of liquid drops*, J. Fluid Mech. **401**, 293 (1999).

[80] P. Dell'Aversana, V. Tontodonato and L. Carotenuto, *Suppression of coalescence and of wetting : the shape of the interstitial film*, Phys. Fluids **9**, 2475 (1997).

[81] O. Reynolds, *On drops floating on the surface of water*, Chem. News **44**, 211 (1881).

[82] O. Reynolds, *On the theory of lubrication*, Philos. Trans. R. Soc. London Ser.A **177**, 157 (1886).

[83] G. Debrégeas, P.-G. de Gennes and F. Brochard-Wyart, *The life and death of bare viscous bubbles*, Science **279**, 1704 (1998).

[84] S. Dorbolo, E. Reyssat, N. Vandewalle and D. Quéré, *Aging of an antibubble*, Europhys. Lett. **69**, 966 (2005).

[85] I.B. Ivanov and T.T. Traykov, *Hydrodynamics of thin liquid films. rate of thinning of emulsion thin films of pure liquids*, International Journal of Multiphase Flow **2**, 397 (1976).

[86] T.D. Hodgson and J.C. Lee, *The effect of surfactants on the coalescence of a drop at an interface*, J. Colloid Interface Sci. **30**, 94 (1969).

[87] Y. Amarouchene, G. Cristobal and H. Kellay, *Noncoalescing drops*, Phys. Rev. Lett. **87**, 206104 (2001).

[88] Y. He, T. Howes, J.D. Litster and G.H. Ko, *Experimental study of drop-interface coalescence in the presence of polymer stabilisers*, Coll. Surf. A Physico-chem. Eng. Aspects **207**, 89 (2002).

[89] Y. Leblanc, Étude des mécanismes de la coalescence partielle d'une goutte à unr interface liquide-liquide (Mechanisms of partial coalescence of a drop on a liquid-liquid interface), Ph.D. thesis, Université Paris VII (1993).

[90] G.E. Charles and S.G. Mason, *The coalescence of liquid drops with flat liquid/liquid interfaces*, J. Colloid Sci. **15**, 236 (1960).

[91] G.P. Neitzel and P. Dell'Aversana, *Noncoalescence and nonwetting behavior of liquids*, Annu. Rev. Fluid Mech. **34**, 267 (2002).

[92] Y. Cai, *Phenomena of a liquid drop falling to a liquid surface*, Exp. Fluids **7**, 388 (1989).

[93] P. Dell'Aversana, J.R. Banavar and J. Koplik, *Suppression of coalescence by shear and temperature gradients*, Phys. Fluids **8**, 15 (1996).

[94] K.R. Sreenivas, P.K. De and J.H. Arakeri, *Levitation of a drop over a film flow*, J. Fluid Mech. **380**, 297 (1999).

[95] A.-L. Biance, C. Clanet and D. Quéré, *Leidenfrost drops*, Phys. Fluids **15**, 1632 (2003).

[96] A.-L. Biance, F. Chévy, C. Clanet, G. Lagubeau and D. Quéré, *On the elasticity of an inertial liquid shock*, J. Fluid Mech. **554**, 47 (2006).

[97] B. Derjaguin and P. Prokhorov, *On the cause of noncoalescence of liquid drops upon impact*, Reprinted in Prog. Surf. Sci. **43**, 273 (1993).

[98] J. Walker, *Drops of liquid can be made to float on the liquid. what enables them to do so ?*, Sci. Am. **238**, 123 (1978).

[99] W. González-Viñas and J. Salán, *Drops on a resonantly forced interface*, Europhys. Lett. **41**, 159 (1998).

[100] K. Okumura, F. Chevy, D. Richard, D. Quéré and C. Clanet, *Water spring: a model for bouncing drops*, Europhys. Lett. **62**, 237 (2003).

[101] L. Courbin, A. Marchand, A. Vaziri, A. Ajdari and H. A. Stone, *Impact dynamics for elastic membranes*, Phys. Rev. Lett. **97**, 244301 (2006).

[102] L. Courbin and H. A. Stone, *Impact, puncturing and the self-healing of soap films*, Phys. Fluids **18**, 091105 (2006).

[103] A. LeGoff, L. Courbin, H. A. Stone and D. Quéré, *Energy absorption in a bamboo foam*, Europhys. Lett. **84**, 36001 (2008).

[104] T. Gilet and J.W.M. Bush, *The fluid trampoline : droplets bouncing on a soap film*, J. Fluid Mech. **625**, 167 (2009).

[105] T. Gilet and J.W.M. Bush, *Chaotic bouncing of a droplet on a soap film*, Phys. Rev. Lett. **102**, 014501 (2009).

[106] N. LeGrand-Piteira, P. Brunet, L. Lebon and L. Limat, *Propagative wave pattern on a falling liquid curtain*, Phys. Rev. E **74**, 026305 (2006).

[107] A. Boudaoud, Y. Couder and M. Ben Amar, *Self-adaptation in vibrating soap films*, Phys. Rev. Lett. **82**, 3847 (1999).

[108] D. Richard and D. Quéré, *Bouncing water drops*, Europhys. Lett. **50**, 769 (2000).

[109] C. Clanet, C. Béguin, D. Richard and D. Quéré, *Maximal deformation of an impacting drop*, J. Fluid Mech. **517**, 199 (2004).

[110] J. B. McLaughlin, *Period-doubling bifurcations and chaotic motion for a parametrically forced pendulum*, J. Stat. Physics **24**, 375 (1981).

[111] J. M. Luck and A. Mehta, *Bouncing ball with a finite restitution : Chattering, locking, and chaos*, Phys. Rev. E **48**, 3988 (1993).

[112] D. Terwagne, T. Gilet, N. Vandewalle and S. Dorbolo, *From bouncing to boxing*, Chaos **18**, 041104 (2008).

[113] S. Dorbolo, D. Terwagne, N. Vandewalle and T. Gilet, *Resonant and rolling droplets*, New J. Phys. **10**, 113021 (2008).

[114] Y. Couder, E. Fort, C.-H. Gautier and A. Boudaoud, *From bouncing to floating: non-coalescence of drops on a fluid bath*, Phys. Rev. Lett. **94**, 177801 (2005).

[115] X. Noblin, A. Buguin and F. Brochard-Wyart, *Vibrated sessile drops: transition between pinned and mobile contact line oscillations*, Eur. Phys. J. E **14**, 395 (2004).

[116] S. Courty, G. Lagubeau and T. Tixier, *Oscillatinf droplets by decomposition on the spherical harmonics basis*, Phys. Rev. E **73**, 045301 (2006).

[117] F. Celestini and R. Kofman, *Vibration of submillimeter-size supported droplets*, Phys. Rev. E **73**, 041602 (2006).

[118] M. Perez, Y. Brechet, L. Salvo, M. Papoular and M. Suery, *Oscillation of liquid drops under gravity: influence of shape on the resonance frequency*, Europhys. Lett. **47**, 189 (1999).

[119] E. Becker, W.J. Hiller and T.A. Kowalewski, *Experimental and theoretical investigation of large amplitude oscillations of liquid droplets*, J. Fluid Mech. **231**, 189 (1991).

[120] R.E. Apfel, Y. Tian, J. Jankovsky, T. Shi, X. Chen, R.G. Holt, E. Trinh, A. Croonquist, K.C. Thornton, A. Sacco, Jr., C. Coleman, F.W. Leslie and D.H. Matthiesen, *Free oscillations and surfactant studies of superdeformed drops in microgravity*, Phys. Rev. Lett. **78**, 1912 (1997).

[121] T. Gilet, D. Terwagne, N. Vandewalle and S. Dorbolo, *Dynamics of a bouncing droplet onto a vertically vibrated interface*, Phys. Rev. Lett. **100**, 167802 (2008).

[122] D. Terwagne, N. Vandewalle and S. Dorbolo, *Lifetime of a bouncing droplet*, Phys. Rev. E **76**, 056311 (2007).

[123] D. Terwagne, T. Gilet, N. Vandewalle and S. Dorbolo, *Metastable bouncing droplets*, Physics of Fluids, in press (2009).

[124] Y. Couder, S. Protière, E. Fort and A. Boudaoud, *Walking and orbiting droplets*, Nature **437**, 208 (2005).

[125] M. Faraday, *On a peculiar class of acoustical figures, and on certain forms assumed by groups of particles upon vibrating elastic surfaces*, Phil. Trans. R. Soc. Lond. **52**, 299 (1831).

[126] T.B. Benjamin and F. Ursell, *The stability of the place free surface of a liquid in vertical periodic motion*, Proc. R. Soc. Lond. A **255**, 505 (1954).

[127] M. Perlin and W.W. Schultz, *Capillary effects on surface waves*, Annu. Rev. Fluid Mech. **32**, 241 (2000).

[128] W.S. Edwards and S. Fauve, *Patterns and quasi-patterns in the faraday experiment*, J. Fluid Mech. **278**, 123 (1994).

[129] K. Kumar and L.S. Tuckerman, *Parametric instability of the interface between two fluids*, J. Fluid Mech. **279**, 49 (1994).

[130] B. Christiansen, P. Alstrom and M.T. Levinsen, *Dissipation and ordering in capillary waves at high aspect ratios*, J. Fluid Mech. **291**, 323 (1995).

[131] S. Protiere, Y. Couder, E. Fort and A. Boudaoud, *The self-organization of capillary wave sources*, J. Phys.: Condens. Matter **17**, 3529 (2005).

[132] S. Douady, *Experimental study of the faraday instability*, J. Fluid Mech. **221**, 383 (1990).

[133] Y. Couder and E. Fort, *Single-particle diffraction and interference at a macroscopic scale*, Phys. Rev. Lett. **97**, 154101 (2006).

[134] S. Protiere, S. Bohn and Y. Couder, *Exotic orbits of two interacting wave sources*, Phys. Rev. E **78**, 036204 (2008).

[135] N. Vandewalle, D. Terwagne, K. Mulleners, T. Gilet and S. Dorbolo, *Dancing droplets onto liquid surfaces*, Phys. Fluids **18**, 091106 (2006).

[136] S.I. Lieber, M.C. Hendershott, A. Pattanaporkratana and J.E. Maclennan, *Self-organization of bouncing oil drops: two dimensional lattices and spinning clusters*, Phys. Rev. E **75**, 056308 (2007).

[137] P.A. Kralchevsky and K. Nagayama, *Capillary interactions between particles bound to interfaces, liquid films and biomembranes*, Adv. Colloid Interf. Sci. **85**, 145 (2000).

[138] P. Singh and D.D. Joseph, *Fluid dynamics of floating particles*, J. Fluid Mech. **530**, 31 (2005).

[139] D. Vella, P.D. Metcalfe and R.J. Whittaker, *Equilibrium conditions for the floating of multiple interfacial objects*, J. Fluid Mech. **549**, 215 (2006).

[140] G. Liger-Belair and P. Jeandet, *Capillary-driven flower-shaped structures around bubbles collapsing in a bubble raft at the surface of a liquid of low viscosity*, Langmuir **19**, 5771 (2003).

[141] A. Eddi, D. Terwagne, E. Fort and Y. Couder, *Wave propelled ratchets and drifting rafts*, Europhys. Lett. **82**, 44001 (2008).

[142] C. Becco, Tracking et modélisation de bancs de poissons, Master's thesis, University of Liege (2004).

[143] S. Hartland, *The coalescence of a liquid drop at a liquid-liquid interface / part iii: film rupture*, Trans. Inst. Chem. Eng. **45** (1967).

[144] A.F. Jones and S.D.R Wilson, *The film drainage problem in droplet coalescence*, J. Fluid Mech. **87**, 263 (1978).

[145] C. Hanson and A.H. Brown, *Secondary droplet formation during drop coalescence*, Solvent Extraction Chemistry **522** (1967).

[146] B.S. Dooley, A.E. Warncke, M. Gharib and G. Tryggvason, *Vortex ring generation due to the coalescence of a water drop at a free surface*, Experiments in Fluids **22**, 369 (1997).

[147] A.V. Anilkumar, C.P. Lee and T.G. Wang, *Surface-tension induced mixing following coalescence of initially stationary drops*, Phys. Fluids A **3**, 2587 (1991).

[148] P.N. Shankar and M. Kumar, *Vortex rings generated by drops just coalescing with a pool*, Physics of Fluids **7**, 737 (1995).

[149] R.W. Cresswell and B.R. Morton, *Drop-formed vortex rings - the generation of vorticity*, Physics of Fluids **7**, 1363 (1995).

[150] L. Mahajan, *The effect of the surrounding medium on the life of floating drops*, Phil. Mag. **10**, 383 (1930).

[151] G.E. Charles and S.G. Mason, *The mechanism of partial coalescence of liquid drops at liquid/liquid interfaces*, Journal of Colloid Science **15**, 105 (1960).

[152] S.T. Thoroddsen and K. Takehara, *The coalescence cascade of a drop*, Physics of Fluids **12**, 1265 (2000).

[153] Z. Mohamed-Kassim and E.K. Longmire, *Drop coalescence through a liquid/liquid interface*, Physics of fluids **16**, 2170 (2004).

[154] S. Thoroddsen, *Droplet genealogy*, Nature Physics **2**, 223 (2006).

[155] F. Blanchette and T.P. Bigioni, *Partial coalescence of drops at liquid interfaces*, Nature Physics **2**, 1 (2006).

[156] F. Blanchette and T.P. Bigioni, *Dynamics of drop coalescence at fluid interfaces*, J. Fluid Mech. **620**, 333 (2009).

[157] E.M. Honey and H.P. Kavehpour, *Astonishing life of a coalescing drop on a free surface*, Physical Review E **73**, 027301 (2006).

[158] H. Aryafar and H.P. Kavehpour, *Drop coalescence through planar surfaces*, Phys. Fluids **18**, 072105 (2006).

[159] X. Chen, S. Mandre and J.J. Feng, *Partial coalescence between a drop and a liquid-liquid interface*, Phys. Fluids **18**, 051705 (2006).

[160] X. Chen, S. Mandre and J.J. Feng, *An experimental study of the coalescence between a drop and an interface in newtonian and polymeric liquids*, Phys. Fluids **18**, 092103 (2006).

[161] P. Yue, C. Zhou and J.J. Feng, *A computational study of the coalescence between a drop and an interface in newtonian and viscoelastic fluids*, Phys. Fluids **18**, 102102 (2006).

[162] T. Gilet, K. Mulleners, J.P. Lecomte, N. Vandewalle and S. Dorbolo, *Critical parameters for the partial coalescence of a droplet*, Physical Review E **75**, 036303 (2007).

[163] T. Gilet, N. Vandewalle and S. Dorbolo, *Controlling the partial coalescence of a droplet on a vertically vibrated bath*, Physical Review E **76**, 035302.

[164] I.L. Kliakhandler, S.H. Davis and S.G. Bankoff, *Viscous beads on vertical fibre*, J. Fluid Mech. **429**, 381 (2001).

[165] R. Craster and O. Matar, *On viscous beads flowing down a vertical fibre*, J. Fluid Mech. **553**, 85 (2006).

[166] C. Duprat, C. Ruyer-Quil, S. Kalliadasis and F. Giorgiutti-Dauphiné, *Absolute and convective instabilities of a viscous film flowing down a vertical fiber*, Phys. Rev. Lett. **98**, 244502 (2007).

[167] B. Carroll, *The accurate measurement of contact angle, phase contact areas, drop volume, and laplace excess pressure in drop-on-fiber systems*, J. Colloid Interface Sci. **57**, 488 (1976).

[168] G. McHale and M. Newton, *Global geometry and the equilibrium shapes of liquid drops on fibers*, Colloids and Surfaces A: Physicochem. Eng. Aspects **206**, 79 (2002).

[169] A. Kumar and S. Hartland, *Shape of a drop on a vertical fiber*, J. Colloid Interface Sci. **124**, 67 (1988).

[170] A. L. Yarin, W. Liu and D. H. Reneker, *Motion of droplets along thin fibers with temperature gradient*, J. Appl. Phys. **91**, 4751 (2002).

[171] E. Lorenceau and D. Quéré, *Drops on a conical wire*, J. Fluid Mech. **510**, 29 (2004).

[172] S. Dawar, H. Li, J. Dobson and G. Chase, *Drag correlation of drop motion on fibers*, Drying technology **24**, 1283 (2006).

[173] L. Landau and B. Levich, *Dragging of a liquid by a moving plate*, Acta Physicochim. USSR **17**, 42 (1942).

[174] D. Quéré, *Fluid coating on a fiber*, Annu. Rev. Fluid Mech. **31**, 347 (1999).

[175] P. Aussillous and D. Quéré, *Quick deposition of a fluid on the wall of a tube*, Phys. Fluids **12**, 2367 (2000).

[176] E. Lorenceau and D. Quéré, *Drops impacting a sieve*, J. Colloid Interface Sci. **263**, 244 (2003).

[177] E. Lorenceau, C. Clanet and D. Quéré, *Capturing drops with a thin fiber*, J. Colloid Interface Sci. **279**, 192 (2004).

[178] D.R. Link, S.L. Anna, D.A. Weitz and H.A. Stone, *Geometrically mediated breakup of drops in microfluidic devices*, Phys. Rev. Lett. **92**, 054503 (2004).

[179] J. Eggers and M.A. Fontelos, *Isolated inertialess drops cannot break up*, J. Fluid Mech. **530**, 177 (2005).

[180] M. di Bernardo, C.J. Budd, A.R. Champneys and P. Kowalczyk, Piecewise-smooth dynamical systems (Springer, 2008).

[181] C. Clanet, F. Hersen and L. Bocquet, *Secrets of successful stone-skipping*, Nature **427**, 29 (2004).

[182] L. Rosellini, F. Hersen, C. Clanet and L. Bocquet, *Skipping stones*, J. Fluid Mech. **543**, 137 (2005).

[183] R.E. Johnson and S.S. Sadhal, *Fluid mechanics of compound multiphase drops and bubbles*, Annu. Rev. Fluid Mech. **17**, 289 (1985).

[184] N. Vandewalle, D. Terwagne, T. Gilet, H. Caps and S. Dorbolo, *Antibubbles, liquid onions and bouncing droplets*, Colloid Surf. A: Physicochem. Eng. Aspect, in press (2009).

[185] R. Stocker and J.W.M. Bush, *Spontaneous oscillations of a sessile lens*, J. Fluid Mech. **583**, 465 (2007).

[186] M.C. Sostarecz and A. Belmonte, *Dynamics inside polymer drops: from dimple to rayleigh instability to torus*, Phys. Fluids, Gallery of Fluid Motion **15**, 5 (2003).

[187] S. Rybalko, N. Magome and K. Yoshikawa, *Forward and backward laser-guided motion of an oil droplet*, Phys. Rev. E **70**, 046301 (2004).

[188] J. Bico, B. Roman, L. Moulin and A. Boudaoud, *Elastocapillary coalescence in wet hair*, Nature **432**, 690 (2004).

[189] C. Py, R. Bastien, J. Bico, B. Roman and A. Boudaoud, *3d aggregation of wet fibers*, EuroPhys. Lett. **77**, 44005 (2007).

[190] I.U. Vakarelski, D.Y.C. Chan, T. Nonogushi, H. Shinto and K. Higashitani, *Assembly of gold nanoparticles into microwire networks induced by drying liquid bridges*, Phys. Rev. Lett. **102**, 058303 (2009).

[191] N.B. Tufillaro and A.M. Albano, *Chaotic dynamincs of a bouncing ball*, Am. J. Phys. **54**, 939 (1986).

[192] E. Falcon, C. Laroche, S. Fauve and C. Coste, *Behavior of one inelastic ball bouncing repeatedly off the ground*, Eur. Phys. J. B **3**, 45 (1998).

[193] Z.J. Kowalik, M. Franaszek and P. Pieranski, *Self-reanimating chaos in the bouncing-ball system*, Phys. Rev. A **37**, 4016 (1988).

[194] E. Fermi, *On the origin of the cosmic radiation*, Phys. Rev. **75**, 1169 (1949).

[195] J.M. Pastor, D. Maza, I. Zuriguel and A. Garcimartin, *Time-resolved particle dynamics in granular convection*, Physica D **232**, 128 (2007).

[196] V. Milner, J.L. Hanssen, W.C. Campbell and M.G. Raizen, *Optical billiards for atoms*, Phys. Rev. Lett. **86**, 1514 (2001).

[197] S. Ramachandran and G. Lesieutre, *Dynamics and performance of a harmonically excited vertical impact damper*, J. Vibr. Acoust. - Trans. ASME **130**, 021008 (2008).

[198] Y. Chen, M. Bibole, R. Le Hazif and G. Martin, *Ball-milling-induced amorphization in nixzry compounds: a parametric study*, Phys. Rev. B **48**, 14 (1993).

[199] N.A. Burnham, A.J. Kulik and G. Gremaud, *Nanosubharmonics: the dynamics of small nonlinear contacts*, Phys. Rev. Lett. **74**, 5092 (1995).

[200] R. Ronsse and R. Sepulchre, *Feedback control of impact dynamics : the bouncing ball revisited*, Proceedings of the 45th IEEE conference on Decision and Control 4807 (2006).

[201] R. Ronsse, P. Lefèvre and R. Sepulchre, *Robotics and neuroscience : a rhythmic interaction*, Neural Networks **21**, 577 (2008).

[202] H. Katsumata, V. Zatsiorsky and D. Sternad, *Control of ball-racket interactions in rhythmic propulsion of elastic and non-elastic balls*, Exp. Brain Res. **149**, 17 (2003).

[203] A. Mehta and J.M. Luck, *Novel temporal behavior of a nonlinear dynamical system: the completely inelastic bouncing ball*, Phys. Rev. Lett. **65**, 393 (1990).

[204] T. Gilet, N. Vandewalle and S. Dorbolo, *Completely inelastic ball*, Phys. Rev. E, in press (2009).